# Electrode Processing and Microstructure Formation of Lithium- and Sodium-Ion-Battery Electrodes: Material-Process-Microstructure-Property Relationships

Zur Erlangung des akademischen Grades eines
DOKTORS DER INGENIEURWISSENSCHAFTEN (DR.-ING.)

von der KIT-Fakultät für Chemieingenieurwesen und Verfahrenstechnik des
Karlsruher Instituts für Technologie (KIT)
genehmigte

DISSERTATION

von
Julian Klemens, M.Sc.
aus Karlsruhe

Tag der mündlichen Prüfung: 16.07.2026

Erstgutachter: Prof. Dr.-Ing. Dr. h.c. Wilhelm Schabel
Zweitgutachter: Prof. Dr. rer. nat. Jens Tübke

# Preface

The present work was carried out during my research as a scientific assistant in the Thin Film Technology (TFT) research group at the Institute for Thermal Process Engineering (TVT) at the Karlsruhe Institute of Technology (KIT) between 2019 and 2024.

I would like to express my sincere gratitude to all those who accompanied me and supported me in various ways during this period. My particular thanks go to Prof. Dr.-Ing. Dr. h. c. Wilhelm Schabel and Dr.-Ing. Philip Scharfer, who supervised my work in the TFT group. They provided excellent working conditions and placed their trust in me, enabling my personal and scientific development throughout my time in the group. I am grateful for the opportunity to present my findings at numerous national and international conferences. I also extend my gratitude to Prof. Dr. rer. nat. Jens Tübke for his interest in my work and for serving as the second reviewer of this thesis.

I would like to express my gratitude to my colleagues at TFT, who played a significant role in creating a positive and supportive working environment. They consistently offered support and valuable ideas during professional discussions. I especially appreciate the countless and unforgettable moments during and outside of work, through which colleagues became friends. I am also grateful to my former students Nadine Zimmerer, David Burger, and Linus Janning, who continued with PhD studies following the completion of their master's theses. It was a distinct privilege to contribute to your development, and I am confident that you benefited from our time together as much as I did. Your contributions in the form of work, ideas, and discussions led to publications presenting a wide range of findings and interpretations that are reflected in this thesis. In this context, I would particularly like to highlight the contributions of David, whose exceptional dedication was evident in his extensive research, discussions, interpretation of the literature, and critical engagement with the subject matter. Maintain your curiosity to explore the unknown. Furthermore, I would like to thank my colleagues and friends Andreas Altvater, Sandro Spiegel, Thilo Heckmann, Victor Gracia, and Philipp Quarz for the many moments outside of work that enhanced my motivation and endurance and were always a source of great enjoyment.

I gratefully acknowledge the financial support pf the German Research Foundation (DFG). I also thank the Excellence Cluster POLiS (post-Lithium Storage Cluster of Excellence) for the opportunity to further my education within the graduate school “Electrochemical Energy Storage” (GS-EES) and for funding my research stay at the research institution CIDETEC Energy Storage in Spain. I am particularly grateful to Luca Schneider, Ann-Kathrin Wurba, Marcus Müller, Werner Bauer and Anna Smith for their collaboration within the POLIS research cluster. Through discussions with you, the development of new ideas, and the establishment of novel investigation and measurement techniques, this work was brought to completion. Luca and Ann-Kathrin deserve special mention, as we also

became close friends during our time together. Luca, your dissertation made impedance measurement an important component of this work as well.

Finally, I would especially like to thank my parents, my grandmother Brundhilde, my brother Fabian, his wife Mona, and my nephew Finn for their unconditional support and the trust they have always placed in me and my abilities. My deepest thanks go to my wife Sarah for her endless patience, motivation, and support throughout my studies and doctoral research. Without you, this path would never have been possible.

Leinfelden-Echterdingen, July 2026 Julian Klemens

# Kurzfassung

Elektrochemische Energiespeichersysteme stellen eine zentrale Schlüsseltechnologie für die globale Transformation hin zu einer nachhaltigen Energieversorgung und elektrifizierten Mobilität dar. Unter den verschiedenen Batterietechnologien dominieren derzeit Lithium-Ionen-Batterien (LIBs) den Markt, was auf ihre hohe gravimetrische und volumetrische Energiedichte, ihre hohe Zellspannung sowie ihre lange Lebensdauer zurückzuführen ist. Die rasche Ausweitung der LIB-Produktion geht jedoch mit einer steigenden Nachfrage nach kritischen Rohstoffen wie Lithium, Kobalt, Nickel und Graphit einher, was zu Umweltbedenken, Versorgungsrisiken und zunehmendem Kostendruck führt.

Natrium-Ionen-Batterien (SIBs) haben sich als vielversprechende komplementäre Technologie etabliert, da sie auf reichlich verfügbaren und breit zugänglichen Ressourcen basieren. Trotz ihres technologischen Potenzials befindet sich die industrielle Herstellung von SIB-Elektroden noch in einem frühen Entwicklungsstadium. Aufgrund von Ähnlichkeiten im Zelldesign und in den Prozessrouten wird die SIB-Technologie häufig als Drop-in-Lösung für bestehende LIB-Produktionslinien betrachtet. Die verwendeten Aktivmaterialien unterscheiden sich jedoch erheblich in ihrer chemischen Zusammensetzung sowie in ihrer spezifischen Partikelmorphologie. Die Annahme einer Drop-in-Fähigkeit von SIB wurde bislang nicht systematisch validiert und vernachlässigt aktivmaterialspezifische Wechselwirkungen, die die Elektrodenherstellungsprozesse maßgeblich bestimmen. Folglich sind die materialspezifischen Herausforderungen und Potenziale beim Übergang von LIB zu SIB bislang unzureichend verstanden.

Die Elektrodenproduktion umfasst mehrere zentrale Prozessschritte: Das Aktivmaterial wird zusammen mit Leitadditiv, Dispersionsmittel, Binder und Lösemittel zu einem Slurry gemischt, auf eine metallische Stromableiterfolie aufgetragen und anschließend getrocknet. Sowohl die Auswahl des Lösemittels und des Bindersystems als auch der Trocknungsprozess sind für das jeweilige Aktivmaterial spezifisch zu optimieren. Insbesondere die Trocknung ist aufgrund des industriellen Energiebedarfs ein kostenbestimmender Prozessschritt und zusätzlich von entscheidender Bedeutung für die Eigenschaften der Elektroden. Hohe Trocknungsraten, die für eine wirtschaftliche Produktion notwendig sind, fördern die Migration des Binders. Dies führt zur inhomogenen Verteilung des Binders und damit zu einer Verschlechterung der mechanischen, elektrischen und elektrochemischen Elektrodeneigenschaften. Ein umfassendes mechanistisches Verständnis der Mikrostrukturausbildung und der Bindermigration in Abhängigkeit unterschiedlicher Aktivmaterialien und Partikelmorphologien für LIB und SIB liegt bislang nicht vor.

Vor diesem Hintergrund verfolgt die vorliegende Dissertation das übergeordnete Ziel, Material-Prozess-Mikrostruktur-Eigenschaftsbeziehungen systematisch aufzuklären und damit die Drop-In Fähigkeit der SIB-Technologie fundiert zu bewerten und den aktuellen

Kenntnisstand im Bereich der Elektrodenproduktion in Abhängigkeit des Aktivmaterials zu erweitern. Die zugrundeliegende Hypothese lautet, dass die Drop-in-Fähigkeit nicht durch die nominelle Prozesskompatibilität bestimmt wird, sondern davon abhängt, ob materialspezifische Wechselwirkungen unter identischen Prozessbedingungen zu vergleichbarer Mikrostrukturentwicklung und Elektrodenperformance führen. Ziel ist es, generalisierbare Zusammenhänge abzuleiten, die sowohl für SIB- als auch für LIB-Materialien gelten.

Die vergleichenden Untersuchungen erfolgen unter kontrollierten Bedingungen, einschließlich identischer Elektrodenformulierungen, standardisierter Mischprozesse und konsistenter Trocknungsbedingungen. Darüber hinaus wird eine umfassende Datenbasis zu Partikel- und Elektrodeneigenschaften aufgebaut, um quantitative Analysen und zukünftige Modellierungen zu ermöglichen. Auf Grundlage einer systematischen Auswahl relevanter Materialsysteme werden zwei komplementäre Forschungsbereiche definiert:

**Forschungsbereich 1: Wasserbasierte Elektrodenverarbeitung mit CMC/SBR Bindersystem und der Einfluss von Partikeleigenschaften**

Ziel ist es, den Einfluss der Materialeigenschaften auf Prozessparameter und Prozessierungseigenschaften, wie Slurryeigenschaften, Produktionsgeschwindigkeit, Trocknungszeiten sowie den Trocknungsmechanismus und die Bindermigration zu quantifizieren und in verallgemeinbare Zusammenhänge zu überführen. Dafür wurde für die LIB als Kathodenmaterial Lithium-Eisen-Phosphat (LFP) und als Anodenmaterial Graphit (Gr) sowie für die SIB als Kathodenmaterial Prussian-Blue-Analoge (PBA) und als Anodenmaterial Hard Carbon (HC) ausgewählt.

Der mechanistische Ablauf der Mikrostrukturausbildung bei der Trocknung von Batterieslurry lässt sich phänomenologisch in Filmschrumpfung und Porenentleerung unterteilen. Der Beginn der Porenentleerung bezeichnet auch den Beginn der Bindermigration. In der Literatur wird angenommen, dass der zeitliche Übergang zwischen diesen beiden Phasen materialabhängig sein kann und wesentliche Auswirkungen auf die Bindermigration besitzt. Zur Überprüfung dieser Hypothese wurde ein neuartiger experimenteller Versuchsaufbau entwickelt, der eine simultane Messung von Filmschrumpfung und Porenentleerung ermöglicht. Entgegen bisherigen Annahmen zeigen die Ergebnisse, dass der Beginn der Porenentleerung unabhängig vom Aktivmaterial stets mit dem Ende der Filmschrumpfung zusammenfällt. Dies definiert einen universellen Übergangspunkt, der die Binder-Migration bestimmt und eine Vorhersage ihres Beginns für verschiedene Materialsysteme ermöglicht.

Während der Beginn der Binder-Migration materialunabhängig ist, hängt deren Ausprägung stark vom jeweiligen Aktivmaterial ab. Eine zentrale Erkenntnis dieser Arbeit ist, dass eine Reduzierung der Partikelgröße des Aktivmaterials die Wechselwirkung zwischen Partikel und Binder verstärkt und dadurch die Bindermigration unterdrückt. Zur gezielten

Analyse dieses Effekts wurde die Trocknung eines spezifischen Aktivmaterials (Hard Carbon) mit unterschiedlichen Partikelgrößen untersucht. Es konnte gezeigt werden, dass mit kleineren Partikeln Elektroden mit einer Flächenkapazität von 2.3 mAh $cm^{-2}$ bei einer Trocknungszeit von nur ca. 12 s ohne negative Auswirkungen der Bindermigration auf die Elektrodeneigenschaften hergestellt werden können. Im Vergleich zu einer State-of-the-Art-Elektrodenproduktion mit ca. einer Minute Trocknungszeit bei gleicher Beladung stellt dies eine signifikaten Beschleunigung des Trocknungsprozesses dar und eröffnet Potenziale zur Reduktion der erforderlichen Trocknerlänge in zukünftigen Produktionsanlagen.

**Forschungsbereich 2: Prozessierung von porös, nanostrukturierten Kathodenpartikeln und Mechanismus der Mikrostrukturausbildung**

Porös, nanostrukturierte Aktivmaterialpartikel ermöglichen eine für den Elektrolyten offen zugängliche Porenstruktur, wodurch Diffusionswege innerhalb des Aktivmaterials reduziert, die Schnellladefähigkeit erhöht sowie die Zyklenstabilität verbessert werden. Solche Partikelmorphologien werden beispielsweise bei Natrium-Vanadium-Phosphat (NVP) in SIBs eingesetzt. Zur systematischen Untersuchung des Einflusses der internen Porosität auf das Verarbeitungsverhalten wurde Lithium-Nickel-Manganoxid (NCM) als Modellaktivmaterial ausgewählt, da es sowohl in kompakter (kommerziell verfügbarer) als auch in modifizierter, poröser Partikelmorphologie vorliegt.

Im Rahmen der Untersuchung wurde gezielt der Unterschied zwischen herkömmlichem, kompaktem Aktivmaterial und porös, nanostrukturiertem Aktivmaterial in der Mikrostrukturausbildung sowie dem Trocknungsverhalten bei schneller Trocknung herausgestellt. Elektroden bestehend aus porös, nanostrukturiertem Aktivmaterial, die bei hohen Trocknungsraten hergestellt wurden, zeigen keinen negativen Einfluss auf die elektrochemischen Eigenschaften. Der Trocknungsmechanismus wird so erklärt, dass das Lösemittel in den Partikeln erst nach der Porenentleerung der umliegenden Mikrostruktur verdampft. Der Binder verbleibt in den Partiklen und ist über den gesamten Querschnitt der Elektrode verteilt, ohne die Poren zwischen den Partikeln zu blockieren. Dies verbessert die elektrochemische Performance, geht jedoch mit einer verringerten mechanischen Stabilität einher.

Zur Kombination der Vorteile beider Partikelmorphologien wurden mehrlagige Elektrodenarchitekturen hergestellt. Es konnte gezeigt werden, dass kompakte Partikel in stromableiternahen Schichten die Haftfestigkeit erhöhen, während poröse Partikel in oberen Schichten in Richtung des Separators die Schnellladefähigkeit verbessern. Damit wird ein materialeffizientes und prozessrobustes Elektrodendesign ermöglicht.

Zusammenfassend liefert diese Dissertation erstmals einen systematischen Vergleich von LIB- und SIB-Materialien aus Sicht der Elektrodenfertigung. Sie schafft ein mechanistisches Verständnis der Binder-Migration, quantifiziert den Einfluss der Partikelmorphologie auf das Trocknungsverhalten und stellt eine wissenschaftlich validierte Methodik zur Bewertung der Drop-in-Fähigkeit der SIB-Technologie bereit. Die Ergebnisse zeigen, dass eine erfolgreiche industrielle Umsetzung einen Paradigmenwechsel von chemiebasierten

Annahmen hin zu einem materialgetriebenen Prozessdesign erfordert. Die gewonnenen Erkenntnisse bilden die Grundlage für eine rationale Prozessentwicklung und tragen dazu bei, die Lücke zwischen Materialentwicklung und industriell skalierbarer Elektrodenfertigung zu schließen.

# Abstract

Electrochemical energy storage systems are a central enabling technology for the global transition to sustainable energy supply and electrified mobility. Among the various battery technologies, lithium-ion batteries (LIBs) currently dominate the market due to their high gravimetric and volumetric energy density, high cell voltage, and long cycle life. However, the rapid expansion of LIB production is associated with increasing demand for critical raw materials such as lithium, cobalt, nickel and graphite, leading to environmental concerns, supply risks, and cost pressure.

Sodium-ion batteries (SIBs) have emerged as a promising complementary technology based on abundant and widely available resources. Despite their technological potential, the industrial-scale manufacturing of SIB electrodes remains in an early stage. Due to similarities in cell design and processing routes, SIB technology is frequently assumed to be a drop-in solution for existing LIB production lines. However, the active materials used differ considerably in their chemical composition as well as in their specific particle morphology. The assumption of drop-in capability of SIB has not been systematically validated and neglects active-material-specific interactions that governs electrode manufacturing processes. Consequently, the material-specific challenges and opportunities associated with the transition from LIB to SIB remain insufficiently understood.

Electrode manufacturing consists of several key process steps: the active material is mixed with conductive additive, dispersing agent, binder, and solvent to form a slurry, which is then applied to a metallic current collector and subsequently dried. Both the choice of solvent and binder system as well as the drying process itself must be optimized for the respective active material. Drying is a cost-determining step due to its high energy demand and plays a critical role in defining electrode properties. High drying rates, which are essential for economically viable manufacturing, promote binder migration. This leads to an inhomogeneous binder distribution and, thus, to deteriorated mechanical, electrical, and electrochemical electrode properties. A comprehensive mechanistic understanding of microstructure formation and binder migration as a function of different active materials and particle morphologies for LIB and SIB electrodes is still required.

The central objective of this dissertation is to systematically elucidate material-process-microstructure-property relationships and thereby provide a scientifically grounded evaluation of the drop-in capability of SIB technology, while also expanding the current state of knowledge on electrode manufacturing as a function of the active material. The underlying hypothesis is that drop-in capability is not governed by nominal process compatibility, but by whether material-specific interactions result in comparable microstructure formation and electrode performance under identical processing conditions. The aim is to derive generalizable correlations applicable to both SIB and LIB materials.

Comparative investigations are conducted under controlled conditions, including identical electrode formulations, standardized mixing procedures, and identical drying conditions. In addition, a comprehensive database of particle and electrode properties is established to support quantitative analysis and future development. Based on a systematic selection of relevant material systems, two complementary research areas and specific research questions are defined:

**Research area 1: Water-based electrode processing using CMC/SBR binder system and the influence of active material properties**

The aim is to quantify the influence of material properties on process parameters such as slurry characteristics, production speed, drying time, drying mechanism, and binder migration, and to translate these findings into generalizable relationships. For this purpose, lithium-iron phosphate (LFP, cathode) and graphite (Gr, anode) were selected as LIB materials, while Prussian-blue analogues (PBA, cathode) and hard carbon (HC, anode) were chosen as SIB materials.

The mechanistic progression of microstructure formation during slurry drying can be phenomenologically divided into film shrinkage and pore emptying. The onset of pore emptying marks the beginning of binder migration. The literature assumes that the temporal transition between these phases may depend on the active material and significantly affect binder migration. To examine this hypothesis, a novel experimental setup was developed that enables the simultaneous measurement of film shrinkage and pore emptying. The results show, contrary to previous assumptions, that the onset of pore emptying always coincides with the end of film shrinkage, independent of the active material, establishing a universal transition point governing binder migration. This allows the beginning of binder migration to be calculated for different material systems and used for the design and optimization of industrial dryers.

Furthermore, a key working hypothesis of this work states that smaller active material particles can suppress binder migration due to enhanced interaction with the binder system. To analyze this effect, the drying behavior of a specific active material (Hard Carbon) with different particle sizes was systematically investigated. It is demonstrated that reducing particle size enables drying times of 12 seconds for electrodes with an areal capacity of 2.3 mAh $cm^{-2}$ without detrimental effects associated with binder migration on electrode properties. Compared to state-of-the-art production, which requires around one minute of drying time for the same areal loading, this represents a substantial reduction in drying time, enabling shorter dryer length in future production facilities.

**Research area 2: Influence of porous, nanostructured cathode particles on microstructure formation and binder migration behavior**

Porous, nanostructured active-material particles offer an accessible pore structure for the electrolyte, reducing diffusion pathways within the active material and thereby enhancing

fast-charging capability and cycling stability in both LIB and SIB systems. Such particle morphologies are, for example, employed for Sodium-Vanadium Phosphate (NVP) in SIBs. To systematically assess the influence of internal porosity on processing behavior, Lithium-Nickel-Manganese Oxides (NCM) was selected as a model active material, as it is available as compact (commercially available) and modified porous particle morphologies

The investigations highlight the differences between conventional, compact active materials and porous, nanostructured materials with respect to microstructure formation and drying behavior under higher drying rates. Electrodes consisting of porous, nanostructured particles and produced at high drying rates exhibit no deterioration in electrochemical performance. The drying mechanism is governed by delayed solvent evaporation within the particles, which occurs only after the surrounding pore network has been emptied. The binder remains inside the particles and is distributed across the entire electrode cross-section, without blocking the pores between the particles. This enhances electrochemical performance but introduces trade-offs, including reduced adhesion strength.

To combine the advantages of both particle morphologies, a multilayer electrode architecture was developed. It was demonstrated that compact particles in layers near the current collector increase adhesion strength, while porous particles in the upper layers toward the separator enhance fast-charging capability. This enables a material-efficient and process-robust electrode design.

Overall, this dissertation provides the first systematic comparison of LIB and SIB materials from an electrode manufacturing perspective. It establishes a mechanistic understanding of binder migration, quantifies the impact of particle morphology on drying behavior, and delivers a scientifically validated methodology for assessing the drop-in capability of SIB technology. The results demonstrate that successful industrial implementation requires a paradigm shift from chemistry-driven assumptions toward material-driven process design. The insights gained provide a foundation for rational process adaptation and contribute to bridging the gap between material development and industrial-scale electrode manufacturing.

# Table of Contents

# Symbols and Abbreviations

### Latin Letters

| Symbol | Unit | |
|---|---|---|
| $c$ | mAh cm$^{-2}$ | Areal capacity |
| $C$ | h$^{-1}$ | C rate |
| $c_{\mathrm{p}}$ | J kg$^{-1}$K$^{-1}$ | Heat capacity |
| $G'$ | Pa | Storage module |
| $G''$ | Pa | Loss module |
| $\Delta h_{\mathrm{v}}$ | J kg$^{-1}$ | Enthalpy evaporation |
| $K_{\mathrm{A}}$ | - | Ackermann correction factor |
| $K_{\mathrm{S}}$ | - | Stefan correction factor |
| $m_{electrode}$ | g m$^{-2}$ | Areal mass loading; dry electrode |
| $\widetilde{M}_i$ | g mol$^{-1}$ | Molar mass |
| $\dot{m}_s$ | g m$^{-2}$s$^{-1}$ | Specific drying rate |
| $p_i^*$ | Bar | Vapor pressure component *i* |
| $p_i$ | Bar | Partial pressure component *i* |
| $p$ | Bar | Pressure |
| $\dot{q}$ | W m$^{-2}$ | Specific heat flux |
| $R$ | Ω | Resistance |
| $t$ | s | Drying time |
| $T_{dryer}$ | °C | Temperature of the gas in the dryer |
| $T_{film}$ | °C | Temperature of the drying film |
| $U_R$ | V | Current |
| $U_{23}$ | V | Voltage between two points |
| $\mathrm{v_i}$ | cm$^3$ | Diffusion volume |
| $x_{50}$ | µm | Mean particle diameter; diameter at 50 % in cumulative distribution |
| $X$ | g g$^{-1}$ | Solvent loading |
| $X_{EOFS}$ | g g$^{-1}$ | Solvent loading at the end of the film shrinkage phase |
| $\tilde{y}_{s,dryer}$ | - | Molar fraction of solvent in the gas phase |
| $\tilde{y}_{s,surface}$ | - | Molar fraction of solvent at the liquid-gas surface |

## Greek Letters

| Symbol | Unit | |
|---|---|---|
| $\alpha$ | W $m^{-2}K^{-1}$ | Heat transfer coefficient |
| $\beta$ | m $s^{-1}$ | Mass transfer coefficient |
| $\delta$ | ° | Phase shift angle; Rheology |
| $\delta_{s,g}$ | $m^2$ $s^{-1}$ | Diffusion coefficient of solvent in gas |
| $\varepsilon$ | - | Particle or electrode porosity |
| $\eta$ | Pa s | Dynamic viscosity |
| $\dot{\gamma}$ | $s^{-1}$ | Shear rate; Rheology |
| $\lambda$ | W $m^{-1}K^{-1}$ | Heat conductivity |
| $\nu$ | $m^2$ $s^{-1}$ | Kinematic viscosity |
| $\rho$ | kg $m^{-3}$ | Density |
| $\sigma$ | S $m^{-1}$ | Electrical resistance |
| $\tau$ | - | Tortuosity |
| $\tau_A$ | N $m^{-2}$ | Shear stress; Rheology |
| $\varphi$ | - | Volume fraction |

## Subsricpts

| | |
|---|---|
| active material | Property related to active material |
| Anode | Property related to anode |
| Cathode | Property related to cathode |
| dry | Dry film or dry electrode |
| dryer | Property within dryer |
| EOFS | End of film shrinkage |
| film | Property related to film or electrode |
| g | Property related to gas phase |
| i | Component i related to dry electrode |
| j | Component j related to slurry |
| OCV | Open circuit voltage |
| practical | Property related to practical value |
| s | solvent |
| slurry | Property related to the slurry |
| surface | Property at solvent-gas phase boundary |
| theoretical | Property related to theoretical value |
| transport | Property related to transport of ions and electrons |

## Dimensionless Numbers

| | |
|---|---|
| Ca | Capillary number |
| $Le_i$ | Lewis number; component i |
| Nu | Nusselt number |
| Pr | Prandtl number |
| Re | Rynolds number |
| Sc | Schmidt number |
| $Sh_i$ | Sherwood number; component i |

## Abbrevations

| | |
|---|---|
| Al | Aluminium |
| BET | Brunauer-Emmett-Teller |
| CMC | Carboxymethyl cellulose |
| CRM | Critical raw materials |
| Cu | Copper |
| DMC | Dimethyl carbonate |
| EC | Ethylene carbonate |
| EMC | Ethyl methyl carbonate |
| HC | Hard Carbon |
| KIT | Karlsruhe Institute of Technology |
| Li | Lithium |
| LFP | Lithium iron phosphate |
| LIB | Lithium-ion battery |
| $LiPF_6$ | Lithium hexafluorophosphate |
| LVE | Linear viscoelastic range |
| Na | Sodium |
| NCA | Lithium nickel cobalt aluminium oxide |
| NCM | Lithium nickel manganese cobalt oxide |
| NCM111 | $LiNi_{0.33}Mn_{0.33}Co_{0.33}O_2$ |
| NCM622 | $LiNi_{0.6}Mn_{0.2}Co_{0.2}O_2$ |
| NFP | Sodium iron phosphate |
| NMO | Sodium manganese oxide |
| NMP | N-Methyl-2-pyrrolidone |
| NVP | Sodium vanadium phosphate |
| PBA | Prussian blue analogues |
| PVDF | Polyvinylidene difluoride |
| SBR | Styrene-butadiene rubber |
| SEI | Solid electrolyte interphase |
| SIB | Sodium-ion battery |

# 1 Introduction

Electrochemical energy storage systems are a key enabling technology for the global transition towards sustainable energy supply and electrified mobility. Among the various battery technologies, lithium-ion batteries (LIB) currently dominate the market due to their high gravimetric and volumetric energy density, high cell voltage, and long cycle life. These characteristics have led to their widespread application in portable electronics, electric vehicles, and stationary energy storage systems. Moreover, the versatility of LIBs allows performance characteristics to be tailored to specific applications through the selection of active materials and electrode design.[1,2]

However, the rapid expansion of LIB production is accompanied by a growing demand for critical raw materials such as lithium, cobalt, nickel and graphite. Their extraction and production are often associated with environmental and social concerns and strong geographical concentration, resulting in vulnerable supply chains and increasing cost pressure for battery manufacturers. In particular, the dominance of a small number of countries in the mining and processing of lithium and graphite highlights the strategic risk, inherent to current battery technologies.[3–5]

In response to these challenges, alternative battery technologies based on abundant and widely available elements are being intensively investigated to improve battery sustainability and reduce the use of critical raw materials.[6] Sodium-Ion Batteries (SIB) represent a particularly promising alternative, as they rely on the same fundamental working principles as LIBs while utilizing sodium, one of the most abundant elements in the Earth's crust (2.36 wt-% of the Earth's crust is sodium, compared to 0.0017 wt-% for lithium)[7].[8] In addition, sodium carbonate ($Na_2CO_3$) is ~99 % cheaper at a price of 0.4 € compared to lithium carbonate ($Li_2CO_3$) at a price of 35.3 €, which are used for the production of active materials.[9] Owing to their similar functional principles, cell architecture, and manufacturing, SIBs can potentially be manufactured using existing LIB production infrastructure and equipment, positioning them as a viable drop-in technology.[10,11]

Although early SIB generations exhibited substantially lower energy densities than state-of-the-art LIBs, recent advances in active materials and cell design have substantially narrowed this gap. In particular, the practical energy densities of advanced SIB systems now approach those of commercially relevant lithium-iron-phosphate (LFP)-based LIBs. This development indicates that further improvements in battery performance and commercialization are increasingly governed not by intrinsic electrochemical material limitations, but by electrode architecture and industrial manufacturing processes. At the same time, the transfer of promising material properties from laboratory-scale studies to industrial-scale electrode manufacturing remains a critical challenge as limited understanding of electrode processing exists, particularly with respect to particle morphology of the active material.[14]

In this context, electrode processing emerges as a key factor for both battery performance and production efficiency. The coating and drying of electrode slurries determine the formation of the electrode microstructure, including porosity and spatial distribution of binder and conductive additives. Process-induced inhomogeneities such as binder migration during drying, can deteriorate mechanical integrity, electrical conductivity, and electrochemical performance, while simultaneously limiting production speed. Despite its industrial relevance, the interplay of active material properties, such as particle size, porosity, and chemistry, on microstructure evolution during electrode processing is not yet sufficiently understood for either LIB or SIB systems.

This dissertation therefore aims to systematically investigate the interrelationships between active material characteristics, electrode processing conditions, microstructure development, and resulting electrode properties for LIB and SIB.[a]

## 1.1 Motivation

The long-term scalability and sustainability of battery technologies increasingly depend on reducing reliance on critical raw materials while maintaining high performance and cost efficiency. Although SIBs offer clear advantages in terms of material availability and potential cost reduction, their large-scale commercialization remains limited. One major reason lies in the limited availability of active materials with sufficient performance, consistency, and large-scale producibility.[12,13]

Another central challenge lies in transferring advances in active material development to industrial electrode manufacturing process. While material-level performance has improved significantly, the processing of these materials into electrodes with reproducible and optimized microstructures remains insufficiently understood. This challenge is particularly pronounced for emerging SIB materials, whose particle morphology, and surface characteristics can differ substantially from established LIB materials and thus lead to distinct processing behavior.[14]

Within battery electrode production, the continuous coating and drying of slurries represent a decisive and cost-intensive step.[15–17] During drying, complex transport phenomena govern microstructure formation and binder redistribution, directly influencing electrode properties. At the same time, industrial requirements demand high drying rates to ensure economic viability, which can induce inhomogeneities due to binder migration, resulting in

[a] Main parts of this work have been performed within the Post-Lithium-Storage Cluster of Excellence (POLiS) in cooperation with the Institute for Applied Materials (IAM-ESS), the Institute of Production Engineering (wbk) and the Battery Technology Center at the Karlsuhe Institute of Technology (KIT). The publications as first author were generated in the course of the project and contribute to the identification of *material-process-microstructure-properties relationships*. As a second author, further manuscripts on the evaluation of SIB as a drop-in technology have been published. The participation concerned the conception, experimental implementation, evaluation and interpretation of the investigations.

reduced adhesion, increased ionic and electric resistance, and degraded electrochemical performance.[18,19]

As a consequence, insufficient control and understanding of process-microstructure-property relationships constitute a major bottleneck in translating promising active materials into scalable, high-performance battery technologies. In particular, a mechanistic understanding of how material characteristics interact with processing parameters to determine electrode microstructure is still lacking, especially for SIB systems.

Addressing this knowledge gap is essential for enabling the ratinal deisgn of electrode manufacturing processes that simultaneously achieve high performance, reproducibility, and cost efficiency. Providing this understanding constitutes the central motivation of the present work.

## 1.2 Lithium-Ion and Sodium-Ion Battery

LIBs and SIBs are both based on the reversible insertion and extraction of the respective alkali ions ($Li^+$ or $Na^+$) into and out of host structures within the active materials during charge and discharge.[20]. Despite their chemical differences, the two technologies share similar cell architectures and operating principles, enabling a direct comparison of materials, performance, and manufacturing processes.

The properties of the alkali ions themselves play a decisive role in battery operation, influencing ion transport, electrode potentials, and achievable energy density. A detailed comparison of both ions is given in the Appendix 11.2. While lithium offers advantages in terms of smaller ionic radius and higher operating voltages, sodium provides significant benefits in terms of abundance. Through appropriate particle and electrode design, the disadvantages can be partially compensated, enabling competitive energy densities for SIB systems.

The following sections introduce the structure and functioning of LIB and SIB cells, discuss transport resistances arising from electrode microstructure, and provide an overview of active materials and achievable energy densities.

### 1.2.1 Structure and Functioning

As the structure, components, and charge storage mechanisms are very similar, Figure 1.1 presents a schematic representation of the structure of a LIB, accompanied by a comparison of the similarities and differences of LIB and SIB.

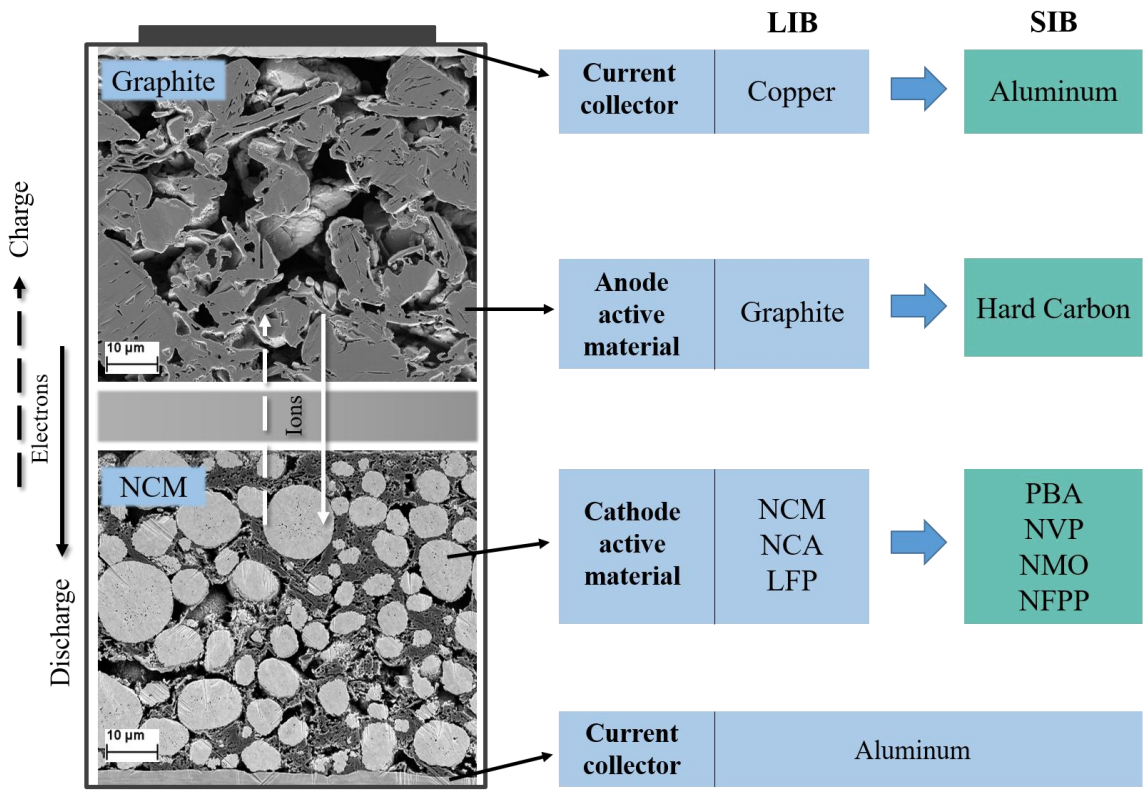


Figure 1.1: Schematic representation of the operation of a LIB. A SIB operates on the same principle as a LIB, with ion inter- and deintercalating into the structure of active materials. However, different active materials are used on the anode and cathode sides, and the electrolyte composition is adjustet. The abbreviations for the various materials are explained in Section 1.2.2. Aluminum (Al) can also be used as a current collector on the anode side for a SIB, which reduces the costs of the cell.

Both LIB and SIB cells consist of a cathode electrode, an anode electrode, a separator, and an electrolyte. Each electrode consists of a metallic current collector coated with a porous composite layer containing the active material, a polymeric binder, and conductive additives. The binder provides mechanical cohesion and adhesion to the current collector, while the conductive additive forms an electrically percolating network, connecting active material particles to the current collector. The anode and cathode electrodes are separated by an electronically insulating but ion-permeable separator soaked with electrolyte. During battery operation, electrons are transported through the external circuit, while ions migrate through the electrolyte-filled pore structure of the electrodes and separator.[1]

At the cell level, a key difference between LIB and SIB lies in the choice of current collector materials. In LIBs, lithium forms an alloy with aluminum at low potentials, necessitating the use of copper current collector on the anode side. In contrast, sodium does not alloy with aluminum under battery operating conditions, allowing aluminum to be used as the current collector for both electrodes in SIBs, thereby reducing cost and weight.[21]

In the charged state of a LIB or SIB, the alkali ions are stored in the anode's active material. Once the battery is connected to a consumer, electrons flow from the anode to the cathode through the closed external circuit. The electrodes serve as electron conductors and the electrolyte within the pore structure and between the electrodes serves as an ion conductor. During the discharge process, $Li^+$ or $Na^+$ ions are released (deintercalated) from the anode's active material to maintain charge neutrality. These ions diffusively reach the active material of the cathode through the electrolyte and are then stored (intercalated) in the cathode material. The reverse process occurs during charging, enabling reversible energy storage.

**Transport resistances**

During charging and discharging, ion and electron transport within the battery is opposed by a series of resistances that collectively reduce usable capacity and operating cell voltage, particularly at high current rates (C-rate). Detailed information on capacity and the impact of transport resistances can be found in the Appendix 11.1. These transport resistances arise from ionic diffusion in the electrolyte and solid phase, electronic conduction through the electrode matrix, and interfacial charge-transfer processes.

The electrode microstructure plays a central role in governing theses resistances. Active material particles size and morphology influence ion diffusion lengths and accessible surface area, while the spatial distribution of binder and conductive additives determines electronic connectivity and ionic transport pathways. Inhomogeneities in microstructure, such as binder accumulation near the electrode surface, can significantly impair transport properties. Optimizing transport resistances therefore requires a detailed understanding of how material properites and processing conditions interact to form the final electrode microstructure and component distribution.

### 1.2.2 Active Materials and Energy Density

To enable a realistic comparison between LIBs and SIBs, this section provides an overview of the most relevant anode and cathode active materials and their achievable energy densities. A comparison of the possibilities, developments, and current status of SIB can be made, although not all active materials are fully covered. While the material landscape is broader, the focus is placed on reference materials, representative of the current technological state. Detailed material descriptions and performance data are provided in the Appendix 11.2.

The specific energy density $w$ (Wh $kg^{-1}$) can be calculated from the specific capacities $q$ (Ah $kg^{-1}$) and the potentials $U$ (V) of the anode and cathode materials (Equation (1.1)).[9]

$$w = \frac{q_{\text{Cathode}} \cdot (U_{\text{Cathode}} - U_{\text{Anode}})}{1 + \frac{q_{\text{Cathode}}}{q_{\text{Anode}}}} \tag{1.1}$$

It is evident that high capacities of the materials combined with large potential difference between the anode and cathode are therefore essential to achieve high energy densities.

**Anode active materials**

Graphite is the state-of-the-art anode material for LIBs. The intercalation of Li-ions into the graphene layers of the graphitic structure results in a high practical capacity of 360 mAh $g^{-1}$.[9] In contrast to LIB, graphite is not suitable as an anode material for SIB, because the formation of a Na-graphite intercalation bond is energetically unfavorable and has a very low capacity of 35 to 130 mAh $g^{-1}$.[22–24] Instead, Hard Carbon (HC) has emerged as the reference anode material for SIBs. Although the sodium storage mechanism in HC is still under discussion,[25] practical capacities against metallic sodium in half-cells reported in the literature typically range from 200 to 450 mAh $g^{-1}$, while the majority of values reported average at 300 to 330 mAh $g^{-1}$.[9,14]

**Cathode active materials**

Cathode active materials for LIBs and SIBs can be grouped into layered oxides, phosphates, and polyanion-based compounds.[9] Lithium-based layered oxides such as Lithium-Nickel-Cobalt-Aluminium Oxide (NCA) and Lithium-Nickel-Manganese Oxides (NCM) dominate the LIB market due to their high capacities and operating voltages.[1,26,27] Sodium-based layered oxides, for example Sodium-Manganese Oxide (NMO), exhibit comparable practical capacities but operate at lower voltages, resulting in reduced energy densities.

Phosphate-based cathodes represent a second important material class. Lithium-Iron-Phosphate (LFP) is widely used in LIBs due to its electrochemical properties, durability, safety, and the use of non-toxic and non-critical raw materials.[28,29] Sodium analogues such as Sodium-Iron Phosphate (NFP) and Sodium-Vanadium Phosphate (NVP) show moderate capacities and voltages but are characterized by high cycle stability.[12,14,30,31] Prussian Blue Analogues (PBA) constitute a particularly promising class for SIBs due to their three-dimensional lattice structure, which facilitates efficient sodium-ion transport and enables high conductivity.[32,33] Although practical capacities and cycle life are still being optimized, PBA represents a cost-effective alternative.[13]

Beyond intrinsic electrochemical properties of the active materials, particle morphology plays a decisive role. For layered oxide materials, in both LIB and SIB systems, tailored particle architectures are used to mitigate kinetic limitations, as ion diffusion within the solid phase is significantly slower than in the electrolyte.[43] Hierarchically structured secondary particles with internal porosity enable improved electrolyte penetration and reduced diffusion pathways.[43–45] Similar strategies are applied to phosphate-based cathodes such as LFP and NVP, where intrinsically low electronic and ionic conductivities necessitate nanoscaling, carbon coating, and formation of nanosized primary particles into micrometer-sized secondary particles.[1,12,46] PBA represents a distinct case, with a characteristic cubic

particle morphology and challenges in terms of electronic conductivity and volumetric energy density.[11,13,47] However, the impact of these different particle morphologies on electrode manufacturing and microstructure formation it not yet fully understood.

Table 1.1 summarizes the theoretical and practical capacities, as well as average operating potentials of the main LIB and SIB materials. Overall, LIB cathodes currently offer higher voltages and practical capacities, whereas SIB cathodes are still under development but show substantial potential for future applications.

Table 1.1: Overview of the cathode active materials for LIB and SIB. Theoretical and practical capacities are compared, as well as the average potential.[9]

| | | $q_{theoretical}$ / mAh $g^{-1}$ | $q_{practical}$ / mAh $g^{-1}$ | Average Potential / V |
|---|---|---|---|---|
| LIB | NCA | 279 | 188 | 3.7 |
| | NCM | 276 | 170 | 3.7 |
| | LFP | 170 | 165 | 3.5 |
| SIB | NMO | 175 | 175 | 2.8 |
| | NFP | 154 | 152 | 2.7 |
| | NVP | 118 | 112 | 3.4 |
| | PBA | 171 | 149 | 3.0 |

Based on practical specific capacities of the cathode and anode materials, the corresponding practical energy densities were calculated using Equation (1.1) and are shown in the following.

**Energy density based on cathode active materials compared to commercial products**

The calculated energy densities represent a realistic maximum achievable energy density at the active material-level and therefore serve as a benchmark for evaluating the maturity of current battery technologies. As these calculations exclude inactive cell components such as binders, current collectors, electrolyte, separator, or cell housing, they systematically overestimate the energy densities achievable in practical cells.[9]

To place the calculated material-level energy densities into context, Figure 1.2 compares the calculated energy densities with achieved or announced energy densities of commercial LIB and SIB cells.

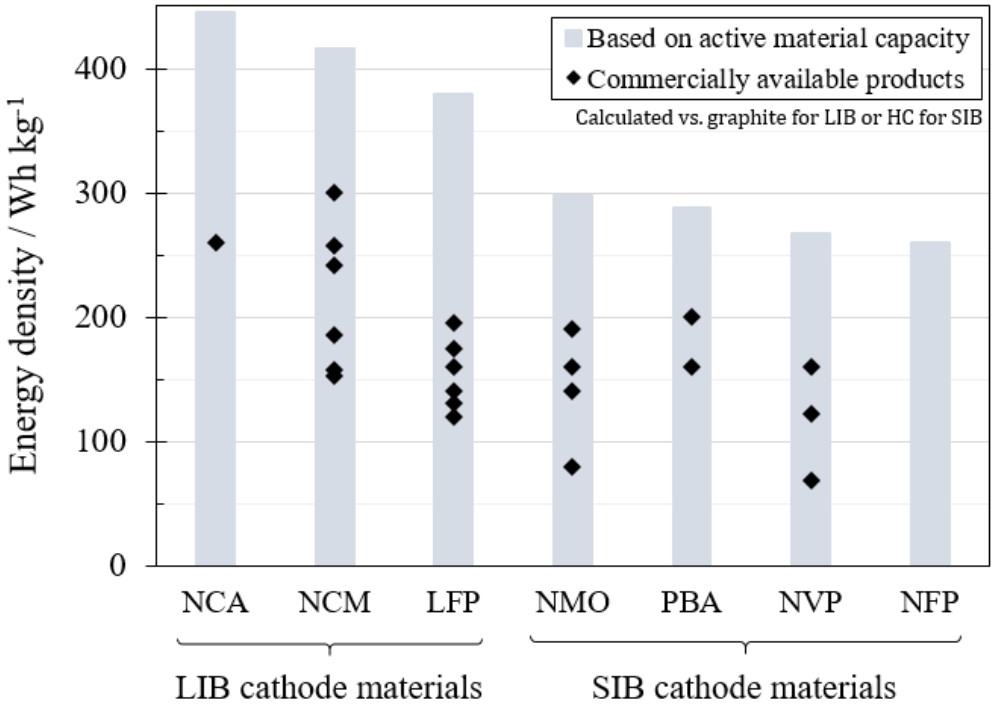


Figure 1.2: Calculated energy densities based on practical capacities for LIB and SIB cathode materials (Equation (1.1)). Also data about practical energy densities from available and next generation full cells are given for a realistic comparison.[10,34–41] The different energy densities within a material class also reflect the historical development. While early LIB systems exhibited relatively low energy densities, decades of incremental improvements have enabled modern cells to approach their material-level potential. The products shown are assigned to the material class of the cathode material specified, as the exact composition is not known.

This comparison highlights the historical and technological development of LIB technology, from early commercial cells based on lithium cobalt oxide vs. graphite with approximately 90 Wh $kg^{-1}$ (Sony in 1991) to modern NCM- and NCA-based systems reaching energy densities between 150 and 300 Wh $kg^{-1}$.[35–38] More recently, LFP-based LIB cells have achieved 140 to 160 Wh $kg^{-1}$, with further increases up to 195 Wh $kg^{-1}$ expected for next-generation systems.[10,39]

A similar development trend is observed for SIBs. First-generation SIB cells introduced around 2015 from Faradion (layered oxide vs. HC) achieved energy densities of approximately 80 Wh $kg^{-1}$. Subsequent material and cell-level developments have increased this value to 140 to 160 Wh $kg^{-1}$ at 4.2 V,[10,36,40] with next-generation SIB systems from Faradion projected to reach up to 190 Wh $kg^{-1}$.[41] The next-generation SIB from CATL (PBA vs. HC) will deliver energy densities of up to 200 Wh $kg^{-1}$.[34,42]

Overall, the results in Figure 1.2 demonstrate that SIB technology has rapidly narrowed the energy density gap to LIBs, highlighting its strong potential for future energy storage ap-

plications. Notably, the projected energy densities of next-generation SIB systems approach those of contemporary LIB technologies, indicating that the remaining performance differences are less constrained by intrinsic material properties and increasingly driven by electrode engineering and process design optimization. In this context, the successful commercialisation of battery technologies depends critically on industrial electrode manufacturing, including the influence of particle morphology, electrode microstructure, and process parameters. As battery technologies mature, the ability to reproducibly fabricate electrodes with tailored microstructure at high throughput and low cost becomes a key determinant of industrial viability.

Understanding and controlling electrode manufacturing and drying behavior during fast drying therefore represents a key challenge for next-generation battery production. Consequently, the following sections focus on electrode manufacturing and, in particular, on the influence of the drying process on electrode structure and performance (Section 1.3). The role of the active materials within this context is addressed within the overarching objectives of this work (Section 1.4).

## 1.3 Electrode Production: Limitations and Microstructure Formation

In addition to the comparative energy density of battery systems, cell production cost represents a decisive factor for commercial viability of current and emerging battery technologies. SIBs are frequently described as a potential drop-in technology, as their manufacturing is, in principle, based on the same process chain and equipment used for LIBs. From an industrial perspective, the incentive to transition toward novel battery chemistry, such as SIB or innovative active material morphology, is therefore driven by reductions in the final costs and improvements in the overall carbon footprint.[14,48]

Battery cell manufacturing can be broadly devided into three main stages: electrode production, cell assembly, and cell finishing. A representative breakdown of manufacturing costs for LIBs is shown in Figure 1.3. Among these stages, electrode production constitutes a major cost driver and plays a pivotal role in determining the final electrochemical performance of the battery cell.

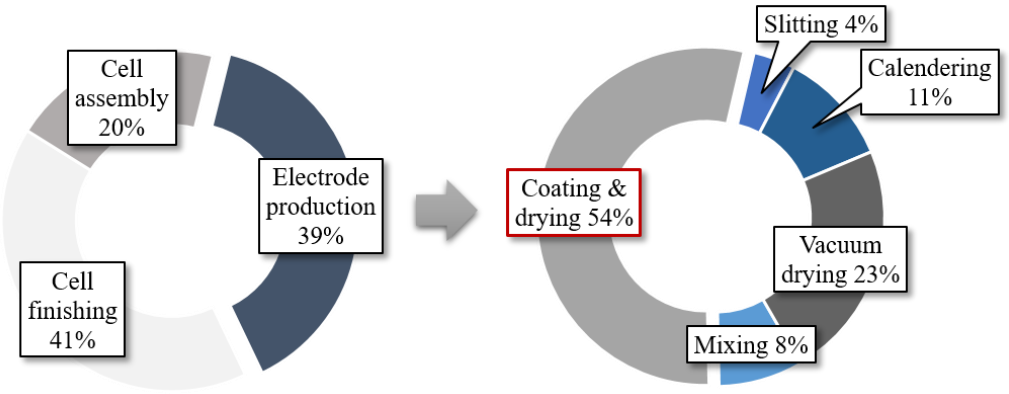


Figure 1.3: Distribution of the battery cell production costs for the individual process categories for LIB cells: electrode production, cell assembly, and cell finishing.[49] The present dissertation is dedicated to the study of electrode production, which represents a significant cost factor in the overall process chain. The production of electrodes involves a series of operations, such as the mixing of the slurry, the coating of the homogeneous wet film, the drying and microstructure formation, the cutting of the electrode tracks, the calendering, and the post-drying. In terms of cost, the coating and drying processes assume a pivotal role. Another publication on cost distribution estimates 53 % for electrode production, of which 69 % is for coating and drying.[50]

The electrode manufacturing typically involves slurry preparation by mixing and dispersing active material, conductive additive, dispersing agent, binder, and solvent, followed by coating onto a metallic current collector foil in a roll-to-roll process. Subsequent drying removes the solvent, after which the electrodes are calendered to adjust porosity and improve electrical contact between particles and the current collector. Finally, the electrodes are slit and further processed by stacking or winding, electrolyte filling, and cell sealing.[1,51,52]

Beyond energy and material costs, process stability and yield are critical determinants of overall production costs. Reject or scrap rates vary significantly depending on manufacturer, cell design, and process maturity, typically ranging from 5 to 30 %[53–55] and oftern exceeding these values during production ramp-up phases[56]. Advances in measurement technology, process analytics, and quality assurance are expected to reduce scrap rates to below 10 % by 2026, with further reductions to below 5 % considered feasible through increased digitalization.[55]

However, these improvements are largely based on established LIB manufacturing processes. When transitioning to new active materials or alternative particle morphologies, such as those employed in SIB electrodes, existing process windows may no longer be directly applicable. Changes in material properties can significantly affect slurry behavior, microstructure formation, and drying behavior, thereby increasing the risk of coating defects, unknown impact of binder migration, and elevated scrap rates. This uncertainty represents a major barrier for industrial adoption and contributes to manufacturers' restraint to implement new battery chemistries despite their potential advantages.

Therefore, a central objective of this thesis is to systematically investigate electrode production depending on the active material used. While accelerating production, particularly by increasing drying rates, offers a direct pathway to reducing manufacturing costs, such acceleration is fundamentally limited by drying-induced binder migration. Binder migration can compromise electrode homogeneity and deteriorate electrical and mechanical properties, as discussed in Section 1.3.1. Since binder migration originates from microstructure formation during slurry drying, Section 1.3.2 focuses on elucidating the underlying mechanisms governing microstructure evolution as a function of process parameters.

### 1.3.1 Limitation during Drying: Binder Migration

Drying the applied slurry is one of the most expensive steps in roll-to-roll electrode manufacturing, both in terms of investment and energy consumption. Industrial coating lines typically comprise dryers with total lengths between 50 and 100 m, subdivided into multiple segments that allow individual adjustments of drying conditions. The construction of suitable production facilities represents a substantial investment, which may even exceed the cost of the coating and drying equipment itself. Consequently, increasing throughput and reducing dryer length are key levers for lowering cell manufacturing costs.[57] In industrial practice, production speeds typically range between 50 and 100 m $min^{-1}$, resulting in average dwell times or drying times of about one minute (dryer length of about 50 – 100 m). At a constant drying rate, higher production speeds directly translate into longer required dryer lengths and thus increased investment costs. In addition, extending the dryer requires increased control of process parameters and web tension.[51] Increasing the drying rate after coating is therefore an attractive strategy to shorten drying times or reducing dryer length and enhance production efficiency.

However, accelerated drying is well known to promote binder migration, leading to a depletion of binder near the current collector and an accumulation toward the top of the electrode facing the separator (see Figure 1.4).[18,45,58,59]

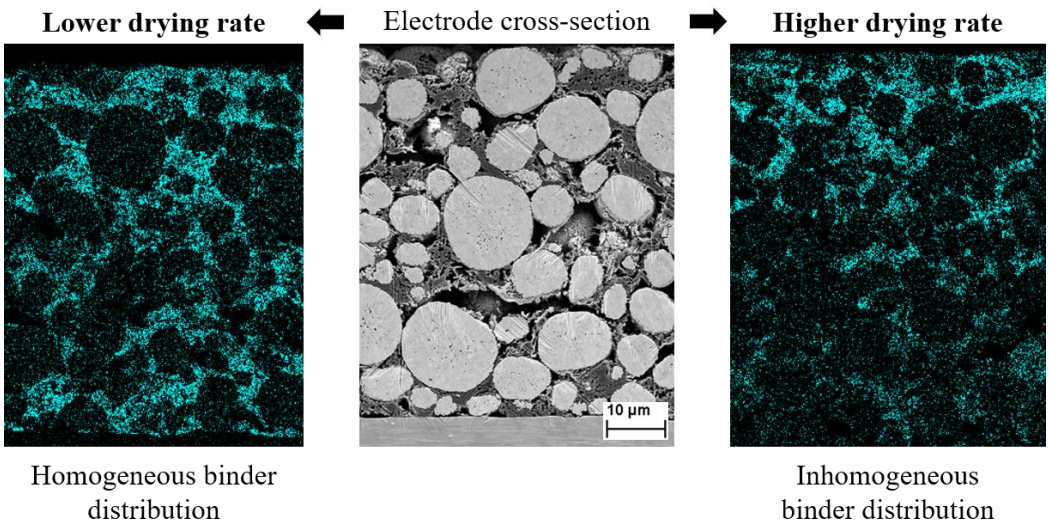


Figure 1.4: Cross-sectional scanning electron microscopy (SEM) images of an NCM-622 cathode produced within the context of this thesis. The images on the left and right are energy-dispersive X-ray spectroscopy (EDS) maps that illustrate the distribution of fluorine (polyvinylidene fluoride, PVDF binder) within the electrode. The PVDF binder is located between the active material particles and in conjunction with the conductive carbon. The migration of the binder during the drying of battery slurries results in an inhomogeneous distribution of the binder. The depletion of binder near the current collector and the increase of binder concentration in the pore network near the separator affect the adhesion, electrical, ionic and electrochemical properties of the electrodes.

This inhomogeneous binder distribution can severely deteriorate electrode performance.[17–19,60–62] Binder accumulation in the pores and on the active materials' surfaces in the upper electrode region increases ionic resistance,[63] which in turn affects both the cycling stability and the C-rate capability. Moreover, insufficient binder content near the current collector reduces adhesion strength and may cause partial or complete delamination of the electrode coating, which can result in reduced battery lifetime or high scrap rates during manufacturing.[51,64–66] Ensuring sufficient mechanical integrity of the dried electrode is particularly critical, as the coating must withstand cyclic mechanical stresses induced by the expansion and contraction of electrochemically active materials during ion intercalation.[67,68]

To ensure optimal battery electrode performance, it is imperative to minimize binder migration. Consequently, a comprehensive understanding of the underlying physical mechanisms governing binder transport during drying and of how these mechanisms are influenced by ative material and the process parameters must be established. The following section will elucidate the origin of the binder migration effect.

## 1.3.2 Microstructure Formation during Drying

The final properties of battery electrodes are strongly governed by the drying process and the associated formation of the electrode microstructure. Drying parameters not only determine the overall drying time but also critically influence the spatial distribution of binder and conductive additives within the dried electrode. The drying process from slurry application to the formation of the dry electrode is schematically illustrated in Figure 1.5., following the conceptual framework introduced by Jaiser et al..[60,69]

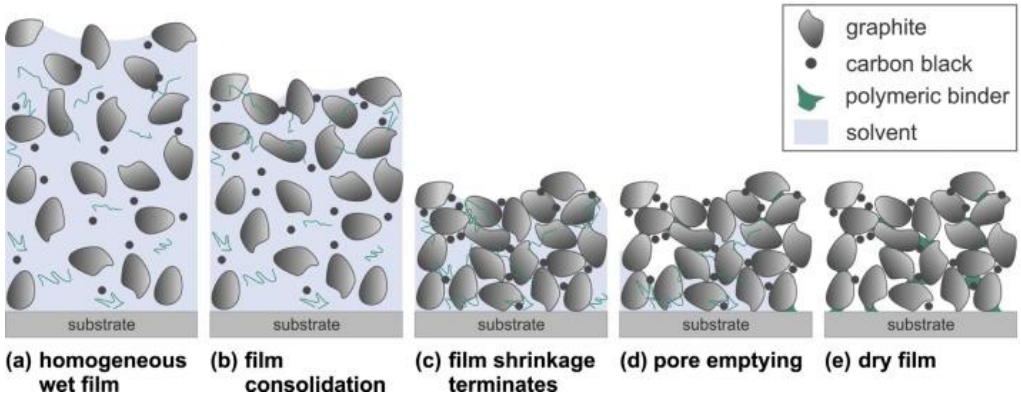


Figure 1.5: The formation of microstructure occurs through a series of processes, beginning with the homogeneous wet film and continuing through the pore emptying process until the final dry film is achieved. Reprinted from Experimental investigation into battery electrode surfaces: The distribution of liquid at the surface and the emptying of pores during drying, 494, S. Jaier, L-Funk, M. Baunach, P. Scharfer, W. Schabel, 22-31, © (2017).[69] The film shrinks due to evaporation of the solvent, reaching its final thickness when the microstructure is fully formed. The entire porosity is filled with solvent, resulting in a complete saturation of the microstrucutre. The solvent is removed from the pores between the active material particles (pore emptying), with the drying rate and film temperature remaining constant. If the surface of the microstructure is no longer kept wet through capillary action, the drying rate will decrease while the film temperature reaches a maximum of that of the surrounding air temperature.

Immediately after coating, solvent evaporation leads to a reduction in wet film thickness. After a short transient phase, a steady-state drying regime is reached, characterized by a constant drying rate and a constant wet-bulb temperature of the slurry. During this phase, particles approach each other as solvent evaporates, resulting in film shrinkage until the final electrode thickness and porosity are established. Jaiser et al. demonstrated for graphite anodes processed with a polyvinylidene fluoride (PVDF) binder and N-Methyl-2-pyrrolidone (NMP) as a solvent that, during this film shrinkage phase, the active material particles remain homogeneously distributed within the slurry matrix.[70]

Once film shrinkage is complete, a fully saturated and interconnected pore network is formed within the electrode microstructure. As long as capillary transport is sufficient to maintain a wet surface, the drying rate and the wet-bulb temperature remain constant. Ac-

cording to Schlünder's "Wet Surface Model", maintaining wetting over as little as approximately 1 % of the surface area is sufficient to sustain about 90 % of the drying rate.[71,72] This behavior is characteristic for many porous material systems.[71–76]

Capillary transport arises from the heterogeneous pore size distribution within the electrode microstructure, which generates capillary pressure gradients.[69,70,74,75,77] Solvent is transported through the formed pore network towards the electrode surface, where evaporation occurs. The liquid menisci are drawn back into the pore structure until they reach the current collector, which is known as pore breakthrough. The interconnected pores gradually empty, starting with the larger ones. Larger pores empty out towards the current collector foil, while smaller pores remain liquid-filled for longer time due to their higher capillary pressure. This hierarchical pore emptying enables continued solvent supply to the surface and sustains the drying rate.

Binder migration is instrinsically coupled to this capillary-driven solvent transport. The binder is transportet within the liquid phase, moving ultimately towards the evaporation front at the electrode surface. Higher drying rates intensify capillary flow and thus accelerate binder migration. Opposing this transport, viscous friction within the pore network induces a pressure drop, counteracting capillary driving forces.

Pore network modeling studies provide important insights into this interplay between capillary and viscous forces. Metzger et al. demonstrated through discrete pore network simulations that capillary forces generally dominate liquid transport during drying, while viscous friction plays a secondary role, even at elevated viscosities, depending on pore structure and connectivity.[77,78] Similarly, Lehmann et al. showed that characteristic length scales and pore size distributions critically determine evaporative drying behavior, with pore geometry exerting a stronger influence than liquid viscosity.[79] Shokri et al. further highlighted that layered pore structures and heterogeneities can shift the location of evaporation fronts, without fundamentally altering the dominance of capillary transport.[80]

Nevertheless, some studies suggest that pore breakthrough and the onset of capillary transport may occur before the end of film shrinkage, depending on active material properties or increased coating thickness.[69,81,82] In these studies, drying rate measurements and pore breakthrough observations were conducted separately, introducing uncertainty in correlating the two phenomena. Consequently, the causal relationship between particle properties, pore structure, layer thickness, viscosity within the capillaries, and the timing of pore breakthrough remains insufficiently understood. Clarifying this relationship is of decisive importance for industrial dryer design, as an earlier or delayed onset of pore emptying could significantly affect binder migration behavior depending on active material. One of the central objectives of this thesis is therefore the systematic investigation of pore breakthrough as a function of active material properties, with particular emphasis on its role in governing binder migration and its implication for industrial drying process.

If capillary effects become insufficient to maintain surface wetting, liquid menisci retract deeper into the porous structure, resulting in a transition to a falling-rate drying regime. This leads to a reduced drying rate due to additional mass transfer resistance, as solvent must evaporate from isolated liquid clusters within the microstructure and must then be transported via the gas phase.[70,71,74,75,82]

**Drying Rate**

The drying rate is a key parameter for comparing electrode drying across laboratory, pilot, and industrial scales. It is defined as the mass transfer rate of solvent in the gas-phase, $\dot{m}_s$ (g $m^{-2}s^{-1}$), and can be expressed for unilateral diffusion in a binary system as:

$$\dot{m}_s = \beta_{s,g} \cdot \tilde{\rho}_g \cdot \widetilde{M}_s \cdot \ln\left(\frac{1-\tilde{y}_{s,dryer}}{1-\tilde{y}_{s,surface}}\right) \tag{1.2}$$

The drying rate depends on the mass transfer coefficient $\beta_{s,g}$ (m $s^{-1}$), the molar density of the gas phase $\tilde{\rho}_g$ (mol $m^{-3}$), the molar mass of the solvent $\widetilde{M}_s$ (g $mol^{-1}$), as well as the molar solvent fraction in the surrounding gas phase $\tilde{y}_{s,dryer}$ and at the gas-liquid phase boundary of the drying film $\tilde{y}_{s,surface}$. The mass transfer coefficient can be calculated by the Lewis analogy and the connection to the heat transfer coefficient $\alpha$ in W $m^{-2}K^{-1}$.[64] The latter depends on dryer geometry, gas flow conditions, and gas temperature (drying air).[83]

Accordingly, the drying rate can be controlled through temperature, airflow conditions, and the solvent loading of the drying air. A detailed description of the methodology employed to calculate the drying rate and the film temperature during the drying process is provided in Section 2.3.1.

## 1.4 Aim of this Work

SIBs are increasingly emerging as a significant complement to the established LIBs. SIB technology has rapidly narrowed the energy density gap to LIB, underlining its substantial potential for future energy storage applications. The projected energy densitites of next-generation SIB systems approach those of contemporary LIB technologies, indicating that further performance improvements are no longer primarly constrained by the instrinsic properties of the active materials. Despite their technological potential, the industrial-scale manufacturing of SIBs is still in an early stage of development. One reason for the limited industrial application of SIB could be the insufficient understanding of the manufacturability and processing behavior of electrodes with different active materials and particle morphologies.

Although the scientific literature frequently assumes that electrode processing for SIBs and LIBs is largely analogous, leading to the notion that SIBs may serve as a drop-in technol-

ogy, no systematic and experimentally validated comparison between the two systems existed prior to this work. As a consequence, material-specific challenges and opportunities associated with the transition from LIB to SIB remain poorly understood. Manufacturers therefore need to empirically investigate processing behavior of new materials and optimized particle morphologies in either system and redefine process parameters, resulting in significant development costs and substantial scrap rates. From an industrial perspective, the successful implementation of SIB technology requires a paradigm shift away from chemistry-based drop-in assumptions towards a material-driven process design. Consequently, systematic investigations linking active material characteristics, processing conditions, and resulting electrode properties therefore form the central aim of this work.

A more profound understanding of how changes in active material properties or particle morphology affect slurry rheology, coating and drying behavior, binder migration, production speed, and dryer design is thus of fundamental importance. This becomes even more evident when considering that high drying rates, which are required for enhanced production throughput, promote binder migration and thereby strongly influence electrode structure and performance. Consequently, investigating the underlying mechanisms and correlations along the process chain in relation to the active materials and their particle properties is imperative for developing robust and cost-efficient manufacturing processes for battery electrode.

Therefore, the overarching objective of this thesis is to systematically identify active material-process-microstructure-property relationships in order to evaluate the drop-in capability of SIB technology. This thesis aims to provide a mechanistic basis for assessing the true drop-in capability of SIB technology and for enabling rational, material-aware process design in industrial electrode manufacturing for LIB and SIB. Using deliberately selected characterization methods (see Chapter 2), the influence of the active material on material properties throughout the electrode manufacturing process is investigated (see Figure 1.6).

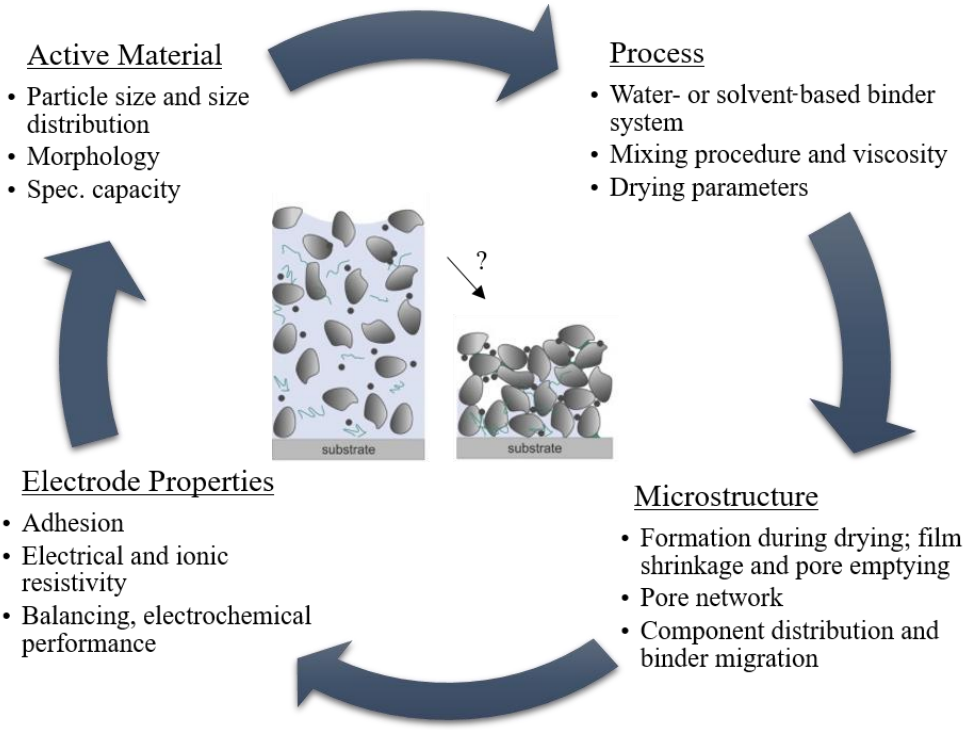


Figure 1.6: Schematic illustration of the relationships between active material, process, microstructure, and resulting properties. To systematically investigate the influence of the active material on the process chain, key active material properties are analyzed. The active material affects the selection of both the binder system and the solvent. In order to enable a meaningful comparison of different active materials or particle morphologies with respect to microstructure formation and binder migration, constant mixing procedures and drying parameters are applied. The resulting electrode properties are subsequently used to assess the influence of the active material on the final product, therby closing the loop between active material-process-microstructure-property relationships.

The aim of this work is to identify critical parameters, universally applicable correlations, and mechanisms govering the microstructure formation and binder migration. The comparative studies rely on strict process comparability by employing constant mixing procedures, identical electrode compositions, and uniform drying conditions. In addition, this work provides a comprehensive database of particle and electrode parameters to support future research.

The results from this work provide the first direct comparison between SIB and LIB active materials from the perspective of electrode manufacturing, thereby enabling a scientifically validated evaluation of the drop-in capability of SIBs. For this investigation of the capability and the quantifying of the impact of particle morphology on drying mechanisms and deeper understanding of binder migration behavior, the selection of suitable active materials is essential (see Section 2.1). A systematic analysis of available material systems led to the identification of two central research areas and specific research questions as shown in Figure 1.7.

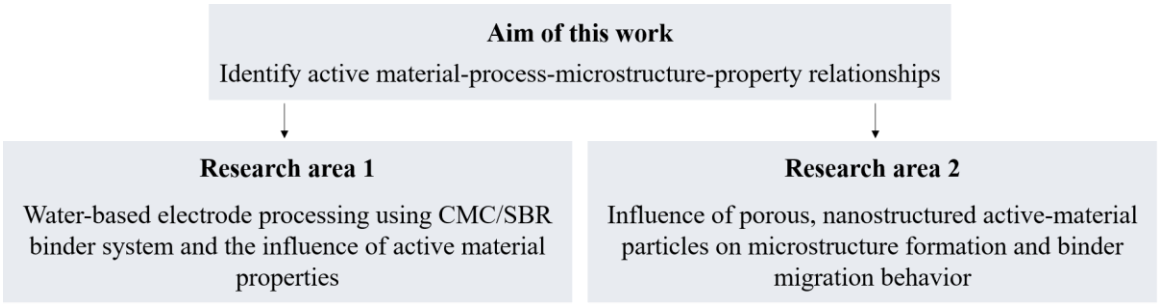


Figure 1.7: Conceptual framework of this work illustrating the methodological approach used to establish material-process-microstructure-property relationships in electrode manufacturing. Two complementary research areas were defined to decouple and systematically assess the influence of active material characteristics on electrode processing and structure formation. Research area 1 focuses on water-based electrode processing with a CMC/SBR binder system and investigates process-governed phenomena, including slurry rheology, film formation, drying, and binder migration mechanisms. Research area 2 addresses the process-structure coupling by analyzing the resulting electrode microstructure with emphasis on pore architecture, component and binder distribution, and a controlled comparison between compact and porous active material particles.

**Water-based electrode processing using CMC/SBR binder system and the influence of active material properties**

The objective of this research area is to elucidate how material properties influence process dimensioning (production speed and dryer length), slurry behavior, drying mechanisms and binder migration, and to derive generalizable active material-process-microstructure-property relationships (see Chapter 3).

A central hypothesis is that the separation of the two phases of microstructure development, film shrinkage and pore emptying, is active material dependent, which could influence the binder migration behavior. To examine this, a novel experimental setup has been developed within this thesis to simultaneously measure film shrinkage and the onset of pore emptying as the onset of binder migration during capillary transport. The aim is to determine the onset of binder migration as a function of particle parameters and to derive generally valid conclusions. Additionally, an overarching hypothesis is postulated, asserting that the particle size in particular has a dominant influence on the interaction between the binder system and the active material. The hypothesis is that smaller particles interact more strongly with the binder system and, consequently, exhibit less binder migration at higher drying rates. To isolate the effect of particle size from chemical composition of the active materials, different particle-size fractions of a single active material are investigated (see Chapter 4).

**Influence of porous, nanostructured active-material particles on microstructure formation and binder migration behavior**

Porous, nanostructured particle morphology for active materials represents a targeted strategy for improving long-term stability and electrochemical performance of both LIB and

SIB systems. However, their use introduces challenges, including decreased adhesion strength to the current collector and reduced volumetric energy density.

This research area examines the processing, drying and binder migration behavior of porous, nanostructured cathode particles relative to compact particles (see Chapter 5). The solvent-based PVDF binder is being used in this investigation. It is assumed that the solvent and binder penetrate into the particle structure during slurry production, remaining there and thus reducing the adhesion strength of the electrodes. The central hypothesis states that the solvent remains within the small pores of the particles for an extended time and evaporates only after the surrounding pore network has been emptied. Consequently, the binder is also retained inside the particles, resulting in a homogeneous binder distribution across the entire cross-section of the electrode. However, the question of whether the behavior described affects binder migration remains open.

The investigation additionally considers multilayer electrode architectures as a promising approache for an enhanced and material-efficient electrode design and for mitigating the drawbacks associated using porous particles (see Chapter 6). Although preliminary concepts exist for both aqueous and solvent-based multilayer-electrode processing, the underlying mechanisms remain insufficiently understood. This work aims to close this gap by enabling the targeted integration of such structures into production, thereby supporting higher manufacturing throughput while improving electrode performance.

Against this background, the following sections focus on electrode manufacturing as a key enabling factor for high-performance battery systems. Particular emphasis is placed on the drying process and its influence on electrode properties. The role of active materials is addressed within the overarching objectives of this work, which aim to systematically elucidate active material-process-microstructure-property relationships and to provide a basis for evaluating the drop-in capability of SIB technology. The material systems, experimental approaches, and characterization methods employed to address the research questions and hypotheses outlined in this thesis are descriped in detail in the following section.

# 2 Materials, Methods and Characterization

In line with the aim of this work to investigate and elucidate active material-process-microstructure-property relationships during electrode processing, with a particular focus on slurry drying using different active materials, this chapter presents the materials, experimental procedures, and characterization techniques employed throughout this dissertation.

The introduction of new active materials requires a systematic investigation of their influence on quantifiable process and electrode parameters. In particular, the complex interdependencies between particle properties, slurry characteristics, microstructure formation mechanisms, and binder migration behavior must be comprehensively analyzed. Given the large number of influencing factors and their coupled effects on processability, microstructure development, and binder redistribution, targeted experimental investigations are essential to minimize confounding variables and to isolate the influence of particle-related effects.

To address the defined aims of this work, a deliberate selection of active materials was carried out. Based on a conceptual framework (see Figure 1.7), the overall research objective was structured into two distinct research areas. Figure 2.1 provides an overview of the experimental matrix, illustrating the assignment of the selected active materials to the respective research areas as well as to the overarching research questions.[b]

[b] At the beginning of this work (year 2019), only Hard Carbon[85] could be acquired with different particle sizes as the active material for the anode of the SIB. Other SIB materials were the subject of research or have been developed and produced by emerging companies for their own use. It is only in recent years that materials (e.g. PBA) have become available in smaller quantities.[14]

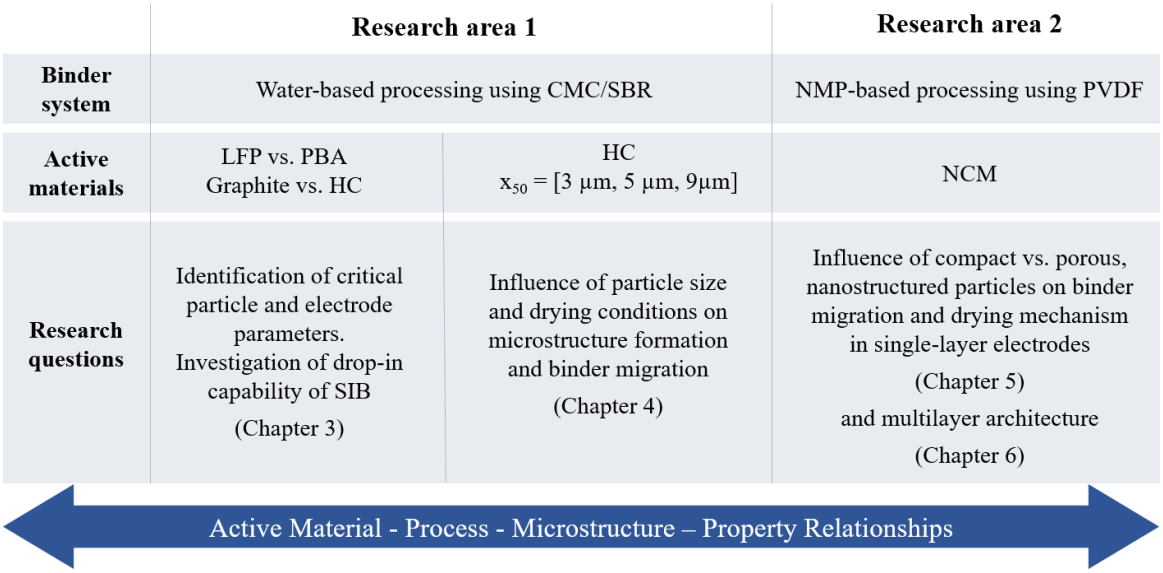


Figure 2.1: Structured overview of the experimental matrix and research questions addressed within the two research areas of this work. Research area 1 focuses on water-based electrode processing using a CMC/SBR binder system and investigates the influence of different active materials (LFP vs. PBA; graphite vs. hard carbon) and particle size (hard carbon with varying particle size) on slurry rheology, microstructure formation, and binder migration. Research area 2 addresses NMP-based electrode processing with PVDF and examines the influence of compact versus porous, nanostructured active material particles on drying mechanisms, pore formation, and the resulting electrode microstructure, including multilayer architectures as an optimization strategy. The combined investigation enables a systematic analysis of active material-process-microstructure-property relationships across different processing routes.

To ensure comparability between different active materials, all electrodes are manufactured under strictly controlled and constant process conditions. This includes fixed mixing procedures, identical electrode compositions, and well-defined coating and drying parameters. This standardized approach enables a direct comparison of material-specific effects and, in particular, allows for an assessment of the drop-in capability of SIB electrodes within established processing routes.

Accordingly, this chapter describes the experimental framework of the dissertation, including the characterization methods for the active materials (Section 2.1), slurry preparation and mixing procedures (Section 2.2), electrode compositions (Section 2.2.1) and slurry rheology (Section 2.2.4), coating and drying setups used (Section 2.3), and the applied electrode characterization methods (Section 2.4). To achieve a deeper understanding of processing behavior and microstructure evolution during drying, the systematic selection of active materials and characterization techniques is complemented by the development and implementation of novel experimental methods.

On the one hand, a dedicated coating and drying setup was developed. The distinctive feature of the developed measurement setup is the in-situ determination of film shrinkage and the onset of pore emptying, which has not been experimentally investigated simultaneously to date (see Section 2.3.2). This approach enables a direct validation of the end-of-film shrinkage (EOFS) by comparing the measurements with the experimentally observed beginning of pore emptying for different active materials, thereby providing a more comprehensive understanding of battery slurry drying behavior depending on the active materials used.

On the other hand, electrochemical impedance spectroscopy (EIS) was established as an additional measurement method for assessing binder migration effects in water-based electrodes. Its applicability was validated through comparison with the established adhesion strength measurement (see Section 2.4.3), thereby extending the methodological toolbox for characterizing binder redistribution in dried electrodes.

The following section outlines the selection of the active materials and the characterization methods applied to quantify their relevant particle properties, thereby enabling the correlation of processing behavior with material characteristics.

## 2.1 Active Material Selection and Characterization of Particle Properties

For aqueous electrode processing using a CMC/SBR binder system within *Research area 1*, the active materials lithium iron phosphate (LFP), Prussian blue analogue (PBA), graphite, and hard carbon (HC) were selected. This material set enables the assessment of drop-in capability using two anode and two cathode materials and allows for a systematic investigation of processing behavior as a function of different active materials and particle characteristics (see Chapter 3). One key hypothesis regarding water-based electrode processing is that particle size significantly influences binder migration behavior. Thus, hard carbon of various particle sizes was used to investigate this hypothesis in detail. Beyond the evaluation of drop-in capability, this selection facilitates the derivation of generalized correlations between particle-related properties and processing behavior, particularly with respect to binder migration, independent of a direct comparison between LIBs and SIBs, which represents a central objective of this work.

Active materials such as NVP for SIB and NCM for LIB were excluded from the aqueous processing study, as slurry preparation using water as a solvent is not readily feasible. Although aqueous processing of NCM has been demonstrated in literature, it is typically accompanied by capacity losses due to water-induced side reactions and subsequent aluminum current collector corrosion caused by an increased slurry pH value.[84] Nevertheless, general implications regarding processing behavior as a function of active material parameters are discussed where appropriate throughout this work.

Within *Research area 2*, the processing behavior and binder migration of porous, nanostructured cathode particles are investigated in comparison to compact particle morphologies. Porous, nanostructured active materials represent a targeted optimization strategy to improve long-term stability and electrochemical performance in both LIB and SIB systems. Such particle morphologies are, for example, employed for NVP in SIBs and are characterized by shortened diffusion pathways within the particles. To systematically assess the influence of internal porosity on processing behavior, NCM was selected as a model active material, as it is available as compact (commercially available) and modified porous particle morphologies.[c] The processing behavior of porous particles was investigated using NCM111[18] and NCM622[62] and compared to their respective commercial counterparts with compact particle morphology. It is assumed that the findings obtained for porous, nanostructured NCM particles can be transferred to the processing behavior of NVP, which has also porous and nanostructured particles. Complementary investigations on the processing and influence of the particle structure on the electrochemical performance of electrodes using NVP were conducted by a project partner within the Cluster of Excellence POLiS.[12]

To generate porous particle morphologies, compact NCM particles were subjected to a subsequent treatment process, resulting in internally porous structures. Due to the complexity of the synthesis route and limited material availability, NCM111 was selected for fundamental investigations on microstructure formation and drying behavior. Details of the production process and its impact on electrochemical performance are discussed in Chapter 5. The subsequent optimization of electrode architectures through multilayer designs was carried out using NCM622 (see Chapter 6). The fundamental effects observed for NCM111 were also reproduced for NCM622, confirming that the observed processing behavior is predominantly governed by the internal porosity of the active material.

The experimental workflow begins with the quantitative characterization of the active materials, as particle-related properties constitute the primary input parameters for slurry preparation, drying behavior, and microstructure evolution.

**Characterization of active material particle properties**

Active materials differ in chemical composition, particle size, particle size distribution, and particle morphology. Identifying the critical particle parameters and understanding their influence on slurry behavior, microstructure formation, and resulting electrode properties is therefore essential. Accordingly, this section describes the characterization methods applied to determine the relevant particle size characteristics, specific surface area, density, and morphological features required for the interpretation in the subsequent processing chapter.

[c] The porous, nanostructured particles are produced by the Institute for Applied Materials.

In the context of this work, the active materials were characterized with respect to their particle size distribution, specific surface area, and particle density. Particle size distributions were determined by laser diffraction (Horiba LA950, Retsch Technology) after dispersing the powders in 2-propanol. The specific surface area was measured by nitrogen adsorption using the Brunauer-Emmett-Teller (BET) method (Gemini VII 2390, Micromeritics). Particle densities, corresponding to the pure or true density, were obtained by helium pycnometry (AccuPyc 1330, Porotec). In addition, scanning electron microscopy (SEM; Zeiss Supra 55 from Carl Zeiss AG, Oberkochen, Germany) was employed to visualize and compare the characteristic particle morphologies of the investigated active materials.

To ensure comparability of the processing studies, all comparative investigations were conducted using identical slurry preparation protocols, mixing procedures, and electrode processing parameters. To systematically evaluate the influence of particle properties on electrode processing, the analysis follows the electrode manufacturing process chain, starting with the impact of particle characteristics on slurry properties. This approach enables subsequent conclusions regarding drying behavior and binder migration phenomena.

## 2.2 Slurry Mixing and Rheology

To ensure comparability across all investigations, the slurry mixing procedures were kept strictly constant for each experimental series. The standardized mixing protocols described below were applied to all active materials within the respective research area. This approach allows the influence of the selected active materials and their particle-related properties on processing behavior to be isolated and systematically evaluated. In order to reveal material-specific effects, the rheological behavior of the slurries was determined using identical preparation procedures and comparable solid contents.

### 2.2.1 Binder Systems

A variety of binders, solvents, and additives are employed in battery electrode manufacturing. Within the scope of this work, two fundamentally different slurry systems were investigated: a water-based slurry employing a two-component binder system consisting of CMC and SBR, and an NMP-based slurry using only PVDF. PVDF fulfills a dual function, acting both as a dispersant during slurry preparation and as a binder in the dried electrode. In contrast, water-based slurries rely on CMC as dispersant and rheology modifier, while SBR serves as the primary binder.

Only selected active materials are directly compatible (without using additional slurry-formulation additives) with aqueous processing. Table 2.1 provides an overview of the investigated active materials and the corresponding binder-solvent systems used in this work. In addition, the influence of the binder system on the drying behavior of hard carbon with varying particle sizes was explicitly examined by processing HC with both CMC/SBR and

PVDF to show the impact of the binder system on binder migration behavior as a function of the particle size.

Table 2.1: Overview of the active materials and the binder system used.

| Active Material | CMC/SBR | PVDF |
|---|---|---|
| Graphite | x | |
| HC | x | x |
| LFP | x | |
| PBA | x | |
| NCM | | x |

For the calculation of slurry density, the composition and density of the individual components were used according to Equation (2.1).

$$\rho_{slurry} = \left( \sum \frac{x_{j,slurry}}{\rho_{\mathrm{j}}} \right)^{-1} \tag{2.1}$$

### 2.2.2 Water-based Slurries with CMC/SBR Binder System

Water-based slurries consist of the active material, conductive Carbon Black (CB) additive, CMC as dispersant and thickening agent, SBR as binder, and water as solvent. Figure 2.2 illustrates the materials used for aqueous slurry preparation.


Figure 2.2: Materials used for water-based slurry preparation. Conductive carbon black is supplied as a powder and is commonly characterized by its BET surface area (e.g., C65 corresponds to BET surface area of 65 $m^2\ g^{-1}$). CMC is supplied as powder and forms a viscous solution upon dispersion in water, enabling effective particle stabilization. SBR is provided as an aqueous dispersion with a solid content of 40 wt-% and a typical particle size of approximately 200 nm.

Since CMC only develops its dispersing and thickening properties after hydration, a CMC-water solution was prepared prior to slurry mixing. Carbon black particles exhibit strong agglomeration due to their small primary particle size and high surface energy. To ensure homogeneous distribution within the slurry and to avoid coating defects caused by residual

agglomerates, an energy-intensive dispersing step is required.[17,51,86] Dispersing the dry mixture, consisting of the active material and the conductive additive, or the conductive additive in the dispersing agent including a portion of the solvent, can be carried out. Increased dust formation occurs during dry mixing. In this work, Carbon Black was deagglomerated in a dry mixing step.

The dry mixtures and slurries containing HC (Kuranode, kuraray), graphite (SMGA, Hitachi Chemical Co. Ltd., Japan), PBA (Gelon LIB Co., Ltd.), and LFP (ibu-Tec, Germany) were prepared using a dissolver (Dispermat SN-10, VMA Getzmann GmbH Verfahrenstechnik, Germany). The slurry composition was selected such that the resulting dry electrode composition corresponded to that listed in Table 2.2**.**

Table 2.2: Composition of dry LIB and SIB electrodes.

| Composition | Active Material | CB | CMC | SBR |
|---|---|---|---|---|
| Dry electrode $x_i^{dry}$/ wt-% | 93.00 | 1.40 | 1.87 | 3.73 |

Carbon Black (Super C65, Imerys) and the active material were added to the container and dispersed at 200 rpm for 10 min. A 2 wt-% CMC (Sunrose MAC500LC, Nippon Paper Industries, Japan) solution was added to 1/3 of the mixed particles and dispersed at 500 rpm for 10 min. The container was cooled during the dispersing process. The remaining active material particles were added in two equal steps and further dispersed. Additional water was added to reach the final solid content. The slurries were then mixed for 45 min at 1500 rpm. In the final step, SBR (Zeon Europe GmbH, Japan) was added and the slurry was mixed for 10 min at 500 rpm. The container was degassed during the final mixing step.

For targeted investigations, HC electrodes were additionally prepared using PVDF as binder and NMP as solvent, while maintaining the same overall dry electrode composition and mixing procedure. In this case, the PVDF content corresponds to the combined mass fraction of CMC and SBR listed in Table 2.2.

### 2.2.3 NMP-based Cathode Slurries with PVDF Binder

NMP-based slurries for NCM111 cathodes (NM-3100, Toda Kogyo Corp.) were prepared in a dissolver (Dispermat SN-10, VMA Getzmann GmbH Verfahrenstechnik, Germany). Both compact and porous NCM particle morphologies were processed with the same mixing procedure. Conductive additives Carbon Black Super C65 and graphite KS6L (Imerys), a PVDF (Solef 5130, Solvay) solvent solution (7.5 wt-% in NMP), and approximately 50 % of the required NMP (Carl Roth, Germany) were dispersed at 1000 rpm for 30 min. Subsequently, the active material and the remaining NMP were added to adjust the solid content to 50.5 wt-% followed by dispersion at 1000 rpm for additional 30 min.

Table 2.3: Composition of dry electrode cathode NCM111.

| Active Material / wt-% | CB / wt-% | KS6L / wt-% | PVDF / wt-% |
|---|---|---|---|
| 89.29 | 3.57 | 3.57 | 3.57 |

During the course of this work, the porous, nanostructuring approach was successfully transferred to NCM622. In addition, the formulation was adjusted to reduce the content of conductive additives and to increase the solid content. The corresponding composition is summarized in Table 2.4. The mixing procedure remained identical to that described for NCM111.

Table 2.4: Composition of dry electrodes with NCM622.

| Active Material / wt-% | CB / wt-% | KS6L / wt-% | PVDF / wt-% |
|---|---|---|---|
| 90.50 | 3.00 | 2.00 | 4.5 |

The characterization of the prepared slurries is based on their rheological behavior, while maintaining constant electrode compositions and comparable solid contents. This approach allows the influence of active material type and particle properties on slurry flow behavior to be systematically evaluated.

### 2.2.4 Rheology

Rheological measurements represent a key link between particle-related properties and subsequent processing steps, as they provide essential insight into slurry processability, slurry structural properties, coating and drying behavior, and binder migration phenomena. In this work, the rheological behavior of the slurries was characterized using rotational and oscillatory rheometry in order to capture their flow behavior and structural stability.

**Rotational viscosimetry**

The viscosity profile of a slurry provides valuable information on particle-particle and particle-binder system interactions as a function of shear rate. Rotational viscosity measurements were carried out using a rotational viscometer (Physica MCR 101, Anton Paar, Germany) equipped with a plate-plate geometry (PP25-SN30563, plate-diameter 25 mm). The measurement gap was set to 0.5 mm (500 µm). During measurement, the slurry was placed between the stationary lower plate and the rotating upper plate, while the temperature of the lower plate was maintained at 25 °C.

Viscosity measurements were conducted by increasing the shear rate from 0.01 to 1,000 $s^{-1}$, and the corresponding shear rate stress and viscosity were recorded. For an ideal Newtonian fluid, the shear stress $\tau$ (Pa) is directly proportional to the applied shear rate $\dot{\gamma}$ ($s^{-1}$), as described by the Newtonian shear stress law of viscosity:

$$\tau = \eta\,\dot{\gamma} \tag{2.2}$$

Where $\eta$ denotes the dynamic viscosity (proportionality factor in Pa s).[87] In Newtonian fluids, viscosity is independent of shear rate. In contrast, battery slurries typically exhibit non-Newtonian behavior, for which the viscosity depends on the applied shear rate:

$$\tau = \eta(\dot{\gamma})\,\dot{\gamma} \tag{2.3}$$

As observed for most battery slurries and polymer-containing solutions, the viscosity decreases with increasing shear rate, a behavior commonly referred to as shear thinning. Several rheological models are available to describe shear-thinning behavior. The Power-Law model could be used as a phenomenological description:

$$\eta = \kappa\,\dot{\gamma}^{n-1} \tag{2.4}$$

where $\kappa$ represents the consistency index and $n$ the flow behavior index. Values of n < 1 indicate shear-thinning behavior.

**Oscillatoric viscosimetry**

Oscillatory rheometry was used to characterize the viscoelastic properties and structural stability of the battery slurries. The stability of the slurry provides information about the interaction of the particles and the additives. In oscillatory measurements, the upper plate is subjected to a sinusoidal deformation (periodic motion), generating non-steady shear conditions. When a sinusoidal shear deformation is applied (maximum deformation, $\gamma_A$),

$$\gamma(t) = \gamma_A\,sin\,(\omega t) \tag{2.5}$$

a viscoelastic fluid responds with a shear stress that is phase-shifted (delay) by an phase-shift angle $\delta$:

$$\tau(t) = \tau_A\,sin\,(\omega t + \delta) \tag{2.6}$$

Here, $\gamma_A$ denotes the strain amplitude, $\tau_A$ the shear stress amplitude, $\omega$ the angular frequency, and $\delta$ the phase shift angle between stress and strain as a delay of the reponse of the fluid.

The elastic contribution to the deformation behavior of the battery slurry is described by the storage modulus G´, while the viscous contribution is represented by the loss modulus G´´. The moduli take into account the maximum deformation and the amplitude of the shear stress as well as the phase shift angle and are calculated according to:

$$G' = \frac{\tau_A}{\gamma_A} \cos(\delta) \tag{2.7}$$

$$G'' = \frac{\tau_A}{\gamma_A} \sin(\delta) \tag{2.8}$$

The ratio of viscous to elastic bevahior is expressed by the loss factor $\tan(\delta)$:

$$\tan(\delta) = \frac{G''}{G'} \tag{2.9}$$

Oscillatory deformation behavior provides insight into slurry structure and stability. A phase-shift angle $\delta$ greater than 45° (tan(δ) > 1) indicates predominantly liquid-like behavior, whereas $\delta$ values below 45° (tan(δ) < 1) are characteristic for gel-like behavior. At $\delta = 45°$ (tan(δ) = 1), the storage and loss moduli are equal, corresponding to the sol-gel-transition region.

Oscillatory measurements were performed using both amplitude and frequency sweeps. During amplitude sweep tests, the strain amplitude was varied at a constant frequency to determine the linear viscoelastic (LVE) range, within the internal structure of the slurry remains intact. The resulting storage G´ and loss moduli G´´ are typically plotted as a function of deformation on a double-logarithmic scale.

If the storage modulus is located above the loss modulus, the fluid exhibits a gel-like behavior (G´ > G´´). If the storage modulus is below the loss modulus, this indicates that the fluid exhibits liquid-like behavior (G´ < G´´). Exceeding the LVE range leads to irreversible changes in the substance structure of the sample being tested. Up to the limit $\gamma_{\text{limit}}$, no significant structural changes occur in the material during deformation. When this limit is exceeded, the structure changes irreversibly. The limit deformation at which the LVE range ends was used as a fixed parameter for subsequent frequency sweep measurement.

In frequency sweep tests, the frequency was varied while maintaining a constant strain amplitude (deformation) within the LVE range. The frequency measurements reveal the time-dependent deformation behavior. Low frequencies describe the long-term behavior of the sample. By examining the storage modulus at low frequencies, a statement can be made about the stability of a measured sample. Samples with a storage modulus of approximately 10 Pa or higher exhibit stable long-term behavior, while suspensions with a storage modulus below 1 Pa tend to sediment.[87] The colloid network's strength is demonstrated by an almost constant storage modulus across the frequency range.[88]

The question arises as to whether, depending on the slurry behavior, there is a change in drying behavior or a change in relation to binder migration.

## 2.3 Drying Process

Following slurry preparation, the electrodes are coated and dried under well-defined and controlled conditions. Since both microstructure formation and binder migration are governed by the complex interplay between material properties and drying kinetics, a central hypothesis of this work is that differences in drying behavior can be primarily attributed to active material-related parameters, provided that the external drying conditions are kept constant.

Accordingly, all drying experiments were conducted under strictly identical boundary conditions in order to isolate the influence of particle properties on microstructure evolution and binder redistribution. This section therefore first outlines the key parameters governing the drying process and describes the experimental framework used to ensure constant and reproducible drying conditions.

Building on this foundation, a novel experimental approach is introduced that enables the simultaneous in-situ determination of film shrinkage and pore emptying. This methodology provides direct experimental access to mechanistically relevant drying phenomena and allows for a quantitative evaluation of material-dependent drying mechanisms.

### 2.3.1 Drying Conditions

Precise control of drying conditions is essential for the reproducible fabrication of battery electrodes and for generating reliable and comparable experimental data. As the drying process decisively affects electrode microstructure and performance-relevant properties, a mechanistic investigation requires a systematic separation and evaluation of all relevant influencing parameters. The present section therefore focuses on identifying the process parameters that fundamentally govern the drying process.

The drying rate represents a key variable, as it is directly influenced by temperature, gas-phase conditions, and heat and mass transfer limitations (see Equation (1.2)). Its dependence on these parameters can be derived analytically and thus provides a suitable basis for controlled experimental variations.

**Film Temperature and Drying Rate**

The film temperature during drying is calculated as a function of the gas temperature and the heat transfer coefficient using a steady-state enthalpy balance (adiabatic wet-bulb temperature).[64,89] During evaporation, solvent removal occurs at the surface of the slurry, while the film temperature remains constant.

Under steady-state conditions, the heat flux into the film $\dot{q}$ (W m$^{-2}$) equals the enthalpy flux associated with solvent evaporation $\dot{h}$ (W m$^{-2}$), which is determined by the mass flux of the evaporating solvent $\dot{m}_s$ (g m$^{-2}$s$^{-1}$) and the enthalpy of evaporation at the film temperature:

$$\dot{q} = \dot{m}_s \cdot \Delta h_{\mathrm{v}}(T_{\mathrm{film}}) \tag{2.10}$$

The convective heat input depends on the temperature gradient between the drying air and the film, as well as on the heat transfer coefficient, and can be described by Equation (2.11). The Ackermann correction factor $K_A$ adjusts for the decreased heat flux into the film caused by the heating of the evaporation mass flux to the temperature of the ambient air in the gas phase.

$$K_A\, \alpha \left(T_{dryer} - T_{film}\right) = \beta_{s,g}\, \rho_{\mathrm{g}} \ln\left(\frac{1-\tilde{y}_{s,dryer}}{1-\tilde{y}_{s,surface}}\right) \Delta h_{\mathrm{v}}(T_{\mathrm{film}}) \tag{2.11}$$

The film temperature must be calculated implicitly (equation (2.11)), as the enthalpy of evaporation $\Delta h_{\mathrm{v}}$, the gas-phase heat capacity $c_{\mathrm{p,g}}$, the molar mass fraction at the phase boundary $\tilde{y}_{\mathrm{s,surface}}$, and the Lewis number $Le$ all depend on the film temperature. The Lewis analogy establishes a relationship between the heat transfer coefficient and the mass transfer coefficient:

$$\frac{\alpha}{\beta_{\mathrm{s,g}}} = \rho_{\mathrm{g}}\, c_{\mathrm{p,g}}\, Le^{1-n} \tag{2.12}$$

with the dimensionless Lewis number defined as:

$$Le = \frac{Sc}{Pr} = \frac{\lambda_{\mathrm{g}}}{\rho_{\mathrm{g}}\, c_{\mathrm{p,g}}\, \delta_{s,g}} \tag{2.13}$$

The diffusion coefficient $\delta_{s,g}$ is calculated according to Fuller et al.[90] and depends on temperature and pressure:

$$\delta_{s,g} = \frac{0.00143 \left(\frac{T_{\mathrm{g}} + T_{\mathrm{film}}}{2}\right)^{1.75} \left[\left(\frac{1}{\widetilde{M}_{\mathrm{s}}}\right) - \left(\frac{1}{\widetilde{M}_{\mathrm{g}}}\right)\right]^{0.5}}{p_{\mathrm{ges}} \sqrt{2} \left[\mathrm{v}_{\mathrm{s}}^{\frac{1}{3}} - \mathrm{v}_{\mathrm{g}}^{\frac{1}{3}}\right]^2} \tag{2.14}$$

with the diffusions volumes of the solvent (e.g., water) $\mathrm{v}_{\mathrm{s,water}} = 10.7\ cm^3$ and for air as the gas phase $\mathrm{v}_{\mathrm{g}} = 19.7\ cm^3$. The molar mass fraction of the solvent in the gas phase depends on the saturated vapor pressure at the dew-point temperature and the ambient pressure in the dryer:

$$\tilde{y}_{\mathrm{s,dryer}} = \frac{p_s^*\left(T_{dew\ point}\right)}{p_{dryer}} \tag{2.15}$$

The molar mass fraction of the solvent at the phase boundary depends on the saturated vapor pressure at the film temperature and the ambient pressure in the dryer.

$$\tilde{y}_{\mathrm{s,surface}} = \frac{p_s^*\left(T_{film}\right)}{p_{dryer}} \tag{2.16}$$

Figure 2.3 illustrates the relationship between drying rate and film temperature as a function of dryer temperature for different heat transfer coefficients.

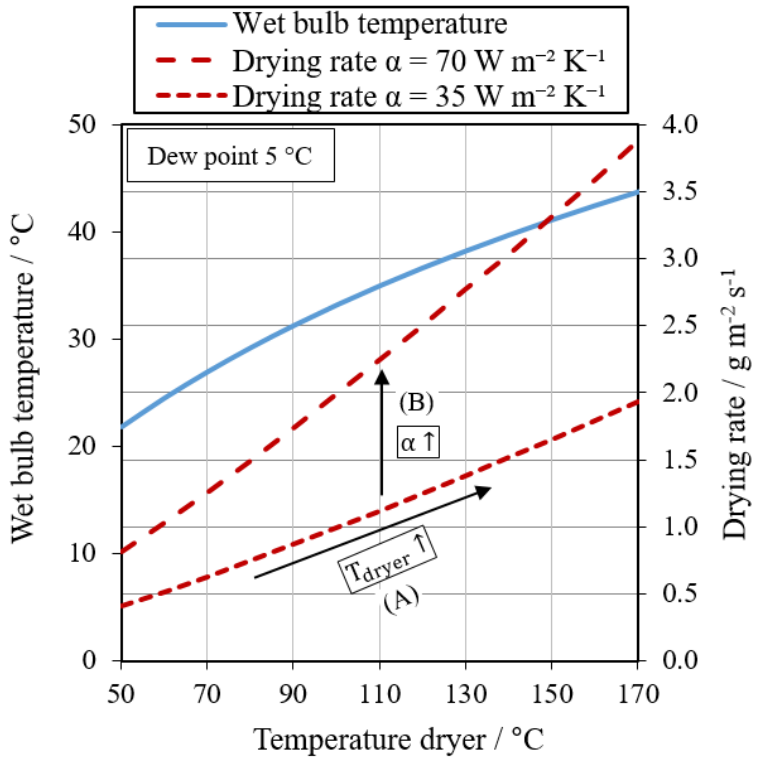


Figure 2.3: Dependence of drying rate and film temperature on dryer temperature for heat transfer coefficients of α = 35 W m$^{-2}$ K$^{-1}$ and α = 70 W m$^{-2}$ K$^{-1}$. Since the vapor pressure of the solvent in the gas phase, and thus the molar fraction in the gas phase $\tilde{y}_{s,dryer}$, depend on the dew point, the diagram is valid only for the dew point of 5 °C.

For a constant water dewpoint in the gas phase, the drying rate can be increased either by raising the drying temperature ((A): $T_{dryer}$ ↑, $T_{film}$ ↑) or by increasing the heat transfer coefficient at constant film temperature ((B): α ↑, $T_{film}$ = const.). Conversely, the influence of film temperature at constant drying rate can be investigated ($\dot{m}$ = const., $T_{film}$ ↓). The Figure shows that the steady-state temperature at a constant dew point does not depend on air flow conditions.

**Comparison of Water and NMP as solvents**

As NMP remains state-of-the-art solvent for cathode electrode production, the drying conditions of water- and NMP-based slurries is compared with respect to their film temperature and drying rate dependence (Figure 2.4).

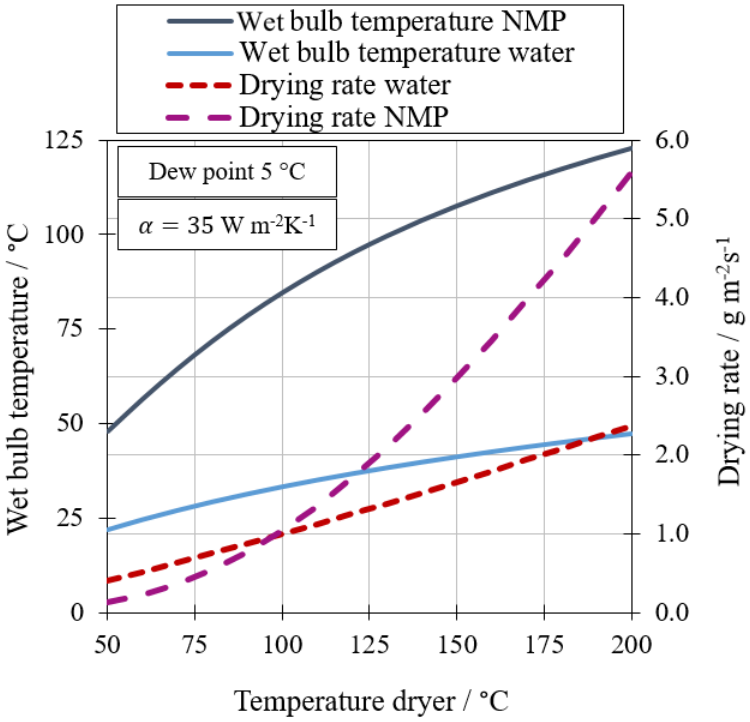


Figure 2.4: Comparison of wet-bulb temperature and drying rate as a function of the gas temperature for water and NMP. The drying rate increases faster with increasing gas temperature of the dryer when NMP is used as the solvent. The data applies to a dew point of 5 °C and a heat transfer coefficient of 35 W $m^{-2}K^{-1}$.

Using NMP as a solvent instead of water results in a faster increase in drying rate for increasing dryer temperature. Figure 2.3 and Figure 2.4 show that the drying rate can be adjuste by several factors and that the wet-bulb temperature is influenced by the solvent system used.

Previous studies have demonstrated that electrode properties differ depending on whether the drying rate is increased by raising the gas temperature or by enhancing the heat and mass transfer coefficients. Building on theoretical considerations, an experimental setup is presented that enables electrode fabrication under strictly defined drying conditions. This approach facilitates the isolation of individual process variables, thereby providing a basis for interpreting the resulting microstructural changes, binder migration behavior and the governing drying mechanisms.

**Coating and Drying Setup – Isothermal electrode drying**

The anode and cathode slurries were coated and dried using a discontinuous process, following the description of Baunach et al.[64] with a temperature-controlled plate and an impingement dryer hood (air-nozzle dryer). All experiments were conducted using isothermal drying conditions. The isothermal drying temperature equaled steady-state temperature as long as drying took place during the constant rate period, which was proven to be true for

battery slurries.[60,91] The drying rate was adjusted by controlling the plate and air temperature, taken the heat transfer coefficient and the dew point into account.

The temperature-controlled plate was used to attach either a 10 µm copper current collector foil (Civen Metal Material Co. Ltd., China) or a 20 µm aluminum current collector foil (Schlenk, Germany). The anode and cathode slurries were coated using a doctor blade or knife coater ZUA 2000.60 or ZUA 2000.100 (Screening Eagle Technologies AG, Switzerland). The knife coater is vertically positioned over the coating plate and the slurry is applied. Due to the substrate's movement, the slurry is uniformly coated. The thickness of the coating, whether wet or dry, is dependent upon the slurry parameters and the height of the blade. The desired dry or wet film thickness to be used is determined by the desired areal mass loading or areal capacity for the battery electrode. A detailed description of the calculation of the wet and dry film thickness can be found in Section 11.4.1.

The coating on the plate was periodically moved under the dryer hood to ensure uniform drying. Due to the heat input by means of heat conduction, the coating dries quasi-isothermally at a temperature close to the plate temperature.

Since the wet-bulb temperature for NMP is significantly higher than that of water (see Figure 2.4), higher isothermal drying temperatures are required to achieve comparable drying rates. This imposes stricter thermal constraints on the drying system, making its operational limits a critical factor. For isothermal drying, the heating plate temperature is therefore typically limited to 85 to 90 °C. Under these conditions, a maximum drying rate of up to 3.5 g $m^{-2}s^{-1}$ can be achieved for NMP-based slurries, assuming a heat transfer coefficient of 70 W $m^{-2}K^{-1}$.

In addition to the manufacturing of battery electrodes under constant drying conditions and the investigation of the individual factors influencing binder migration, a mechanistic understanding of the microstructure formation process is required. The apparatus utilized for the simultaneous measurement of film shrinkage and pore emptying was developed in this dissertation and is outlined in the next section.

### 2.3.2 Simultaneous Measurement of Film Shrinkage and Pore Breakthrough

Besides the drying conditions, the mechanism of microstructure formation could be a function of the particle properties of the active material. A mechanistic understanding of microstructure formation requires direct experimental access to film shrinkage and pore emptying during drying. Under the influence of different active materials, the end of film shrinkage and the onset of pore emptying may not coincide, which has important implications for binder migration.

As drying proceeds, the wet film thickness decreases until a saturated pore network forms. Equation (2.17) calculates the film shrinkage profile, which is dependent on the wet film thickness, drying rate, and solvent density.

$$h(t) = h_{wet} - v \cdot t = h_{wet} - \frac{\dot{m}_s}{\rho_s} \cdot t \tag{2.17}$$

The rate at which the applied wet film hight decreases is, for example, $v \approx 1$ µm $s^{-1}$ with a drying rate of 1 g $m^{-2}s^{-1}$ and water as the solvent.

The final film thickness of the saturated network corresponds to the dry film thickness, which can be calculated using equation (2.18).

$$h_{dry} = h_{wet} \frac{1 - \varphi_{s,t=0}}{1 - \varepsilon} \tag{2.18}$$

Knowledge of electrode porosity enables the calculation of dry film thickness based on solvent volume fraction after slurry preparation $\varphi_{s,t=0}$. Estimating porosities on a theoretical basis can be challenging, as noted by Lippke et al..[92] Therefore, experimentally determined porosities are needed.

Similar to the film shrinkage, the reduction in solvent loading $X(t)$ can be calculated by considering the initial solvent loading, drying rate, and areal mass loading of the dry electrode.

$$X(t) = X_0 - \frac{\dot{m}_s}{m_{areal}^{dry}} \cdot t \tag{2.19}$$

The solvent loading at the end of film shrinkage is calculated according to equation (2.20). It can be calculated from the porosity of the dry electrode $\varepsilon$ and the ratio of the density of the solvent $\rho_s$ to the average density of the dry mixture $\rho_{\text{dry mixture}}$.

$$X_{EOFS} = \frac{\varepsilon}{1 - \varepsilon} \frac{\rho_s}{\rho_{\text{dry mixture}}} = \frac{\rho_s \, \varepsilon \, h_{dry}}{m_{areal}^{dry}} \tag{2.20}$$

The solvent mass fraction during drying $x(t)$ can be calculated from the solvent loading $X(t)$ (equation (2.21)).

$$x(t) = \frac{X(t)}{1 + X(t)} \tag{2.21}$$

Figure 2.5 shows the new experimental drying setup, which enables simultaneous measurement of film thickness reduction and the detection of the first pore breakthrough at the substrate interface.

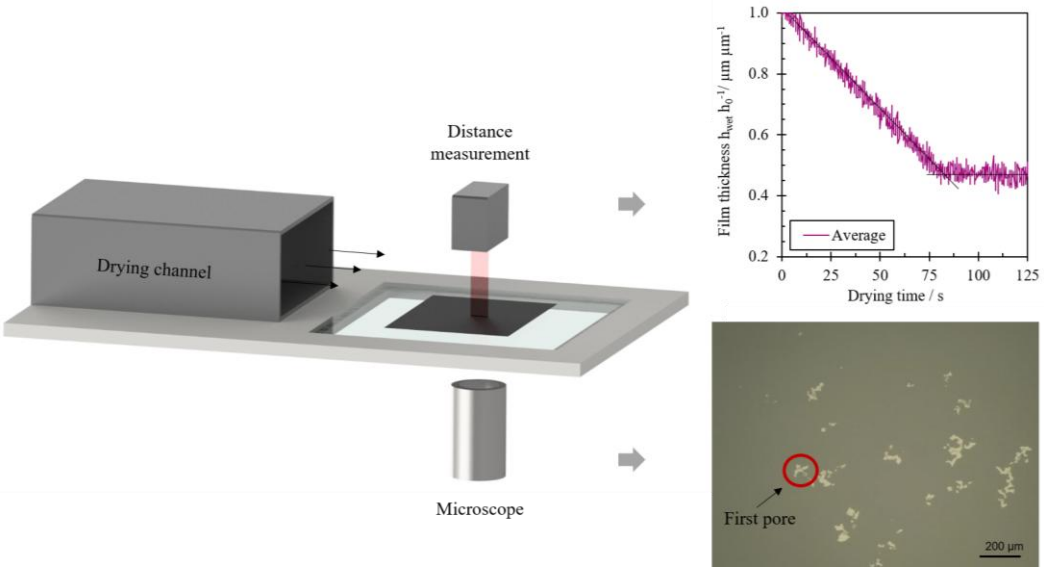


Figure 2.5: New experimental drying setup for simultaneous measurement of film shrinkage and pore emptying during drying. At the same time, the decrease in layer thickness is measured and the first visible pore at the bottom of the microstructure is detected. The time at which the first pore appears is compared to the experimental determination of the end of film shrinkage. The film is subjected to a lateral hot-air flow, resulting in initially position-dependent local heat and mass transfer coefficients due to boundary layer development. Beyond the entrance region, this dependence becomes negligible and quasi-constant coefficients are established. Measurements were therefore carried out at a position where both coefficients are approximately constant.

The slurry is exposed to lateral flow of drying air, which initially can lead to spatial variations in the local heat and mass transfer coefficients along the flow direction (moving drying front) due to the development of thermal and concentration boundary layers. With increasing downstream distance (entrance or start-up region), this dependence gradually diminishes, and the local heat and mass transfer coefficients approach quasi-constant values. To minimize the influence of these entrance effects, measurements were deliberately conducted at a position where both coefficients can be considered approximately constant. A detailed analytical evaluation of this behavior is provided in the Appendix 11.3.

The film thickness reduction is measured through distance measurement, and the point at which the film stops shrinking is determined by the intersection of the linear regression of the film shrinkage and constant film thickness. The appearance of the first pore, which breaks through to the glass substrate, is detected using a microscope from underneath (underside of the electrode). The point in time at which the first pore becomes visible during the drying process can be determined by observing the underside of the applied wet film ($t_{1st\ pore}$), and the point in time at which the shrinkage is complete is determined from the measurement of the film shrinkage ($t_{EOFS}$). Furthermore, the film shrinkage curve allows for the calculation of the drying rate. The drying rate is determined by the withdrawal speed of the film surface and the density of the solvent $\dot{m}_{\text{film shrinkage}} = v\ \rho_{\text{solvent}}$.

In order to investigate the influence of microstructure formation and drying conditions on binder migration as a function of the active material, the resulting electrode properties must be systematically characterized.

## 2.4 Electrode Characterization

The characterization methods were selected to identify the influence of particle properties, material systems, and process conditions on the electrode microstructure and the distribution of binder during the drying process of LIB and SIB slurries. Particular emphasis is placed on methods that enable conclusions about binder migration during drying. Depending on the choice of active material, it may be necessary to use a specific measurement method or to combine different measurement methods.

As direct imaging techniques for analyzing binder distribution are only limitedly applicable to electrodes using the CMC/SBR binder system, the development and validation of indirect measurement methods are required to enable conclusions about the component distribution as a function of process conditions. A key approach for indirectly determining the binder distribution is the measurement of the adhesion strength between the active layer and the current collector. In addition, structural properties of the electrodes, such as porosity, are determined to show the influence of different active materials on the microstructure.

Electrochemical impedance spectroscopy under blocking conditions also represents an indirect evaluation method for binder migration and has already been successfully applied to electrodes with inhomogeneous PVDF binder distributions. In the present work, the results obtained from this method for CMC/SBR electrodes are compared with adhesion strength measurements in order to evaluate the validity of both approaches for assessing binder migration.

Furthermore, electrochemical characterization is conducted for selected cathode materials in order to investigate potential effects of the microstructure, particularly in the case of nanoporous particles, on electrochemical performance.

### 2.4.1 Adhesion Strength

The adhesion strength between the active layer and the current collector represents an established method for indirectly assessing binder migration. During the drying process, binder may migrate from the vicinity of the current collector towardss the electrode surface, which results in a reduced binder concentration at the interface between the active layer and the current collector. This decrease in binder concentration leads to weaker mechanical adhesion of the coating to the current collector. Consequently, the measured adhesion strength can be interpreted as an indicator of the binder distribution within the electrode.

The adhesion strength was determined using a 90° peel test. For this purpose, a universal testing machine (AMETEK LS1, Lloyd Instruments Ltd., UK) equipped with a 10 N load cell was used (Figure 2.6).

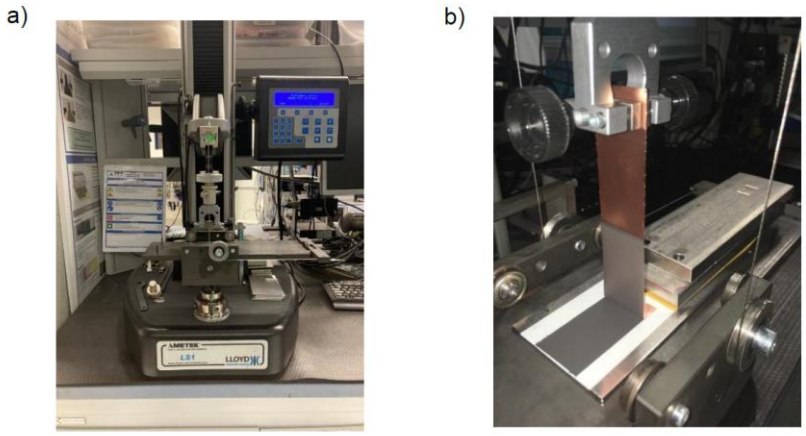


Figure 2.6: Adhesion strength measurement via 90° peel test using an AMETEK LS1 universal testing maschine a). Electrode during adhesion strength measurement b).

The dried electrodes were all cut to a width of 30 mm and attached with the coated side to an adhesive tape. To ensure uniform contact between the coating and the adhesive tape, a weight of 10 kg was applied prior to the measurement. Subsequently, the coating was peeled from the current collector at a constant speed and at an angle of 90°, while the resulting force was recorded.

The investigated NCM electrodes were analyzed at the Institute for Applied Materials (IAM-ESS) using specialized safety procedures for material analysis. In this case, a universal testing machine from Zwick was used. Electrodes with a width of 17 mm were cut and pressed onto an adhesive strip with a weight of 200 kg using a hand press (MP150D, Maassen). The coating was then peeled off the current collector foil at a constant speed of 600 mm $min^{-1}$ and at a 90° angle using the testing machine. The resulting pull-off force was measured and divided by the sample width to obtain a line adhesion force.

Besides adhesion strength, the porosity of the dried electrodes represents an important structural parameter.

### 2.4.2 Porosity and Tortuosity

The porosity characterizes the electrode microstructure and was calculated from the areal mass loading divided by the dry coating thickness and the density of the dry mixture of the components.

$$\varepsilon = 1 - \frac{m_{electrode}}{\rho_{dry\ mixture}\ h_{dry}} \tag{2.22}$$

The electrode thickness was measured using a thickness gauge (ID-H0530, Mitutoyo) equipped with a flat measuring head. The density of the dry mixture is given by the mass fractions in the dry electrode and the density of all solid materials.

$$\rho_{dry\ mixture} = \left(\sum \frac{x_{i,electrode}}{\rho_i}\right)^{-1} \tag{2.23}$$

The geometric tortuosity can be calculated using the electrodes' porosity according to the empirical correlations from Bruggeman (equation (2.24))[96] or Zehner-Bauer-Schlünder (equation (2.25))[97,98].

$$\tau_{\text{geometric,Bruggeman}} = \varepsilon^{-0.5} \tag{2.24}$$

$$\tau_{\text{geometric, ZBS}} = \frac{\varepsilon}{1-(1-\varepsilon)^{-1.5}} \tag{2.25}$$

In this case, tortuosity describes the actual path length $l_{\text{real}}$ divided by the ideal path length $l_{\text{ideal}}$ through an electrode.

$$\tau_{\text{geometric}} = \frac{l_{\text{real}}}{l_{\text{ideal}}} \tag{2.26}$$

As shown in Figure 2.7, geometric tortuosity describes the elongation of the effective transport pathway within the porous microstructure compared to the ideal straight path through the electrode.

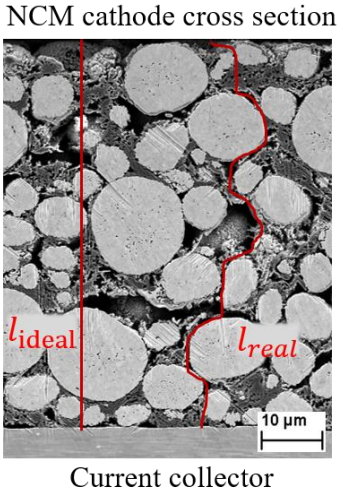


Figure 2.7: Illustration of the geometric tortuosity. The ideal path corresponds to the electrode thickness. The real path describes the path between the particles and through the network of conductive additives.

The ideal path corresponds to the electrode thickness, whereas the real transport path follows the interconnected network between active material particles and conductive additives.

The shown relationship between the length of a real path and an ideal path (electrode thickness) can be used to describe the heat transfer[93] or mass transfer in the gas phase of the microstructure of an electrode[94,95]. However, experimental studies have shown that ionic transport in real electrodes is additionally influenced by the distribution of binder.[99,100] This was also confirmed in a joint publication with the Institute for Applied Materials (KIT IAM-ESS).[45] As a result, the actual transport tortuosity for a given species (e.g. liquid or gaseous solvent, ion) can deviate significantly from the purely geometric estimate.

### 2.4.3 Impedance Spectroscopy Measurements (Ionic Resistance)

To experimentally determine the ionic transport resistance within the electrode microstructure, electrochemical impedance spectroscopy (EIS) under blocking conditions was applied. Analogous to the concept of geometric tortuosity, electrical tortuosity is defined as a ratio of the effective conductivity $\kappa_{\text{effective}}$ (that is, the ionic conductivity in a porous electrode structure) and the unaffected conductivity of the electrolyte $\kappa$ (equation (2.27)).[45]

$$\tau_{\text{electrical}} = \varepsilon \frac{\kappa}{\kappa_{\text{effective}}} \tag{2.27}$$

The ionic transport resistance within the electrode microstructure in the electrolyte is strongly influenced by the amount, type, and spatial distribution of the binder. Changes in these parameters therefore affect the ion transport resistance or the distribution of ion transport resistances within the electrode.[63,100,101] Considering the electrode geometry, the electrical tortuosity can be calculated from measured ionic resistance $R_{ion}$.

$$\tau_{electrical} = \frac{R_{\text{ion}}\, A\, \kappa\, \varepsilon}{2\, h_{\text{dry}}} \tag{2.28}$$

If only porosity is used to estimate electrical tortuosity, it will be greatly underestimated. Section 11.5.6 provides a more detailed explanation of this when examining HC electrodes.

Ionic resistance $R_{ion}$ was measured in a symmetric cell configuration in which two identical electrodes were separated by glass fiber separators. The setup was implemented in CR2032 coin cells. Two glass fiber separators (GF/C, Whatman) were placed between the electrodes. The electrodes and separators were punched to a diameter of 1.6 cm, corresponding to an electrode area of A = 2.01 cm². Cell assembly was performed in a glove box.

As electrolyte, 200 µL of 10 mM tetrabutylammonium perchlorate ($TBAClO_4$) in EC:DMC (1:1 by volume) was added. The conductivity of this electrolyte is $\kappa = 0.3505 \pm 0.0011$ mS cm$^{-1}$. Electrodes and separators were punched out with a diameter of 1.6 cm corresponding to an area $A = 2.01$ cm$^2$. EIS measurements were performed in a temperature-controlled chamber (BTZ-175, Espec) at 25 °C using a coin cell holder (Dual CR2032 Coin Cell Holder, Gamry Instruments) with a potentiostat (VSP-300, Biologic). The measuring parameters were 10 mV perturbation and a frequency range from 200 kHz to 100 mHz. The resulting impedance spectra were fitted using the EIS software RelaxIS 3 (rhd instruments)

with a transmission line model (TLM) in order to determine the ionic transport resistance $R_{\mathrm{ion}}$. The electrical tortuosity was calculated by equation (2.28) with the dry film thickness and the porosity of the electrode as described by Landesfeind et al.[101]. The results obtained from the EIS measurements under blocking conditions will be used to compare them against the adhesion strength measurements in order to evaluate the method for assessing binder migration.

As mentioned earlier, the choice of active material may limit the use of certain measurement methods. Particularly when using nanoporous, structured active materials, it has been shown that using the adhesion strength to interpret drying effects could be insufficient, as the absolute adhesion strength is very low. For this reason, and to gain a deeper understanding of the drying behavior and binder distribution, parameters such as electrical resistivity or electrochemical performance can be determined.

### 2.4.4 Electrical Resistivity and Electrochemical Characterization of NCM Cathode Electrodes

Electrical and electrochemical analyses were performed on selected NCM cathodes. These investigations were conducted at the Institute for Applied Materials (IAM-ESS) under specialized safety conditions for material analysis.

The electrical through-plane resistance of the electrodes was measured between cylindrical copper electrodes using an ohmmeter (RM3544, HIOKI E.E. Corp.). For this purpose, circular electrode samples were placed between polished copper cylinders with a diameter of 14 mm and compressed with a force of 9.81 N. The measured resistance was used to calculate the specific electrical resistivity of the electrode, taking into account the electrode area and thickness.

Electrochemical characterization of the cathodes was carried out in coin cells against a lithium-metal counter electrode. The electrolyte used was 200 µL LP30 (BASF) with the conductive salt 1M LiPF6 in an EC/DMC (1:1) mixture. The separator was a glass microfiber fleece (GF/C, Whatman) with a diameter of 16 mm. Cell assembly was performed in a glove box, and the cells were sealed using a crimping press (MSK-11, MTI, KJ Group) at a pressure of 750 psi. The cycling was carried out in a BT2000 battery cycler from Arbin Instruments in constant current mode in a voltage window of 3 to 4.3 V. Identical C-rates were used for charging and discharging. After two formation cycles at a C-rate of C/20, the C-rate was gradually increased to 5C. Two more steps were carried out, at C/2 and 1C.

# 3 Drop-In Capability: Material-Dependent Electrode Manufacturing of LIB vs. SIB

The electrode manufacturing of SIBs is frequently regarded as being largely analogous to that of LIBs, leading to the widespread assumption that SIBs may be implemented as a potential drop-in technology. Despite this perception, systematic and experimentally validated studies comparing the manufacturing behavior of SIB and LIB electrodes have been lacking. Consequently, the extent to which differences in active material properties and particle charactersitics affect electrode processing and microstructure formation has remained unclear.

A comprehensive understanding of how active material properties and particle characteristics influence electrode processing is of fundamental importance. In particular, the implementation of new battery materials or particle morphologies requires the identification of their impact on slurry behavior, drying process design, and electrode microstructure formation mechanism, based on quantifiable material and process parameters. This need becomes even more critical under high drying rates, which are essential for economically viable production throughput but simultaneously promote binder migration, thereby strongly influencing electrode microstructure and performance.

Consequently, the results presented in this chapter focus on elucidating the mechanisms governing microstructure formation along the electrode manufacturing process chain, with particular emphasis on the role of active material properties. The overarching objective of this thesis is to identify material-process-microstructure-property relationships that allow for an evaluation of the drop-in capability of SIB technology.

The results presented here constitue the first direct, manufacturing-oriented comparison of SIB and LIB active materials. Based on a systematic screening of available material systems, this chapter focuses on water-based electrode processing using the CMC/SBR binder system. The influence of active material properties on slurry behavior, process dimensioning (i.e., production speed and dryer length), drying mechanism, and binder migration is systematically examined with the aim of deriving generalizable material-process-microstructure-property relationships that are applicable across battery chemistries.[d]

[d] The results and discussion in this chapter are part from the following publication by the author:[14]
J. Klemens, A. Wurba, D. Burger, M. Müller, W. Bauer, S. Büchele, O. Leonet, J.A. Blázquez, I. Boyano, E. Ayerbe, H. Ehrenberg, J. Fleischer, A. Smith, P. Scharfer, W. Schabel, Challenges and Opportunities for Large-Scale Electrode Processing for Sodium-Ion and Lithium-Ion Battery, Batteries & Supercaps (2023). https://doi.org/10.1002/batt.202300291.

To place the investigation of the active-material-dependent drop-in capability, drying mechanisms, and binder migration into the context of electrode manufacturing, the following section outlines the motivation of this chapter and reviews the current state of the art.

## 3.1 Motivation and State of the Art

To evaluate the drop-in capability of SIBs in comparison to LIBs, it is first necessary to outline the machine- and process-relevant parameters of industrial LIB electrode manufacturing reported in the literature. Key indicators for industrial electrode production are production speed and plant footprint, which is largely determined by the length of the drying section.

Reported production speeds for industrial LIB electrode manufacturing, including coating and drying machines, typically range from approximately 25 to 50 m $min^{-1}$ [51], with upper values of up to 80 to 100 m $min^{-1}$.[15,102,103] Dryer lengths are commonly reported to be between 10 and 20 m, but may reach up to 100 m, particularly for electrodes with high areal loadings and/or higher production speeds. With increasing machine length, however, the complexity of web handling and the control of individual dryer zones increases significantly.[51] The values reported in the literature vary widely depending on production scale and are therefore used in this work primarily to estimate realistic drying times. Assuming a production speed of 60 m $min^{-1}$ and a dryer length of 60 m, an effective drying time of one minute can be derived. The drying time, production speed and dryer length are dependent on the areal loading or areal capacity of the electrode to be produced and the drying rate.

Against this background, a comparison of drying times as a function of areal capacity and drying rate is particularly suitable for analyzing differences between LIB and SIB anode and cathode electrodes. Such a comparison is therefore investigated in the subsequent results section of this study.

Enhancing the efficiency of industrial electrode manufacturing fundamentally requires strategies that enable accelerated drying in order to either increase production throughput or reduce the required dryer length.[57] Numerous studies have shown, however, that fast drying promotes binder migration, which in turn negatively affects electrode mechanical and electrochemical properties. In industrial practice, this trade-off results either in the need for slower drying process or in a targeted adaption of individual drying zones to the underlying mechanisms of microstructure formation.

The mechanistic development of electrode microstructure formation during slurry drying can be phenomenological divided into two phases: film shrinkage and pore emptying. After slurry application, solvent evaporation leads to a reduction in wet film thickness, causing particles to approach each other until the final electrode thickness and porosity are reached. At the end of film shrinkage, a fully saturated microstructure with a complex network of

solvent-filled pores or capillaries is formed. Due to the heterogeneous pore size distribution, capillary pressure gradients arise, inducing capillary transport of the solvent towards the electrode surface, where evaporation occurs.[69,70,74,75,77] As the liquid menisci retreat through the pore structure towards the current collector, pore breakthrough occurs, marking the onset of pore emptying and the beginning of binder migration.

The literature suggests that the temporal transition between film shrinkage and pore emptying depend on the active material and has a decisive influence on binder migration.[69,81] Indications exist that, depending on particle properties, viscosity in the pore network, drying rate or coating thickness, pore breakthrough may occur before the end of film shrinkage, which has the potential to impact the binder migration process.[82] Since drying rates and pore breakthrough have typically been investigated separately, the causal relationship between active material properties, early pore breakthrough, and binder migration remains unclear.

For a reliable evaluation of the drop-in capability of SIBs relative to LIBs, it is therefore essential to quantify the influence of different active materials on drying behavior, microstructure formation, and binder migration. This approach is crucial for deriving reliable conclusions regarding process design, acceptable drying rates, and their impact on electrode properties.

This chapter addresses this research gap through a systematic investigation of the drying process LIB vs. SIB with particular emphasis on material-dependent effects. The objective is to identify the relevant influencing parameters and to derive generalizable material-process-microstructure-property relationships that enable an assessment of the industrial transferability of SIB electrode manufacturing process and thereby provide a key contribution to the evaluation of their drop-in capability. The results contribute to an improved understanding of drying process design and electrode microstructure formation, thereby advancing the current state of the art in battery electrode manufacturing.

## 3.2 Results and Discussion

To enable a systematic comparison between SIB and LIB electrode manufacturing, all comparative investigations presented in this chapter were conducted under strictly controlled and identical processing conditions. Constant mixing procedures, identical electrode compositions, and uniform drying parameters were applied throughout the study to ensure the process comparability. This experimental approach provides the basis for identification of universally valid correlations as well as material-specific effects. The comparative results are structured along four central aspects of electrode manufacturing. First, the influence of active material properties on process dimensioning is analyzed, with particular emphasis on drying time, production speed, and dryer length. Second, differences in slurry viscosity behavior are examined and related to particle characteristics. Third, the drying-induced mi-

crostructure evolution is investigated through a phenomenological analysis of film shrinkage, including the relationship between the end of film shrinkage and the onset of pore breakthrough. Finally, electrode adhesion strength and binder migration behavior are evaluated in the context of material-dependent drying mechanisms.

Since the processing behavior and drying response of electrodes are intrinsically linked to the properties of the active materials, this chapter builds upon a systematic characterization of the selected materials. The relevant particle properties are introduced first and subsequently correlated with the observed processing behavior, microstructure formation and binder migration. This structure enables a coherent interpretation of the comparative results and supports the derivation of material-process-microstructure-property relationships across both battery chemistries.

### 3.2.1 Active Materials and Particle Properties

For the comparative investigation of LIB and SIB electrode processing and manufacturing parameters, graphite and hard carbon were selected as anode materials, while LFP and a PBA were used as cathode materials. All selected active materials are compatible with water-based electrode processing using CMC/SBR binder system, thereby ensuring process comparability between LIB and SIB electrodes. In addition, it is evident that nowadays the practical energy densities of SIB using PBA can compete with LIB using LFP (see Section 1.2.2).

To provide a qualitative impression of the active materials, Figure 3.1 presents scanning electron microscopy images of the particle powders employed for slurry preparation and drying experiments.

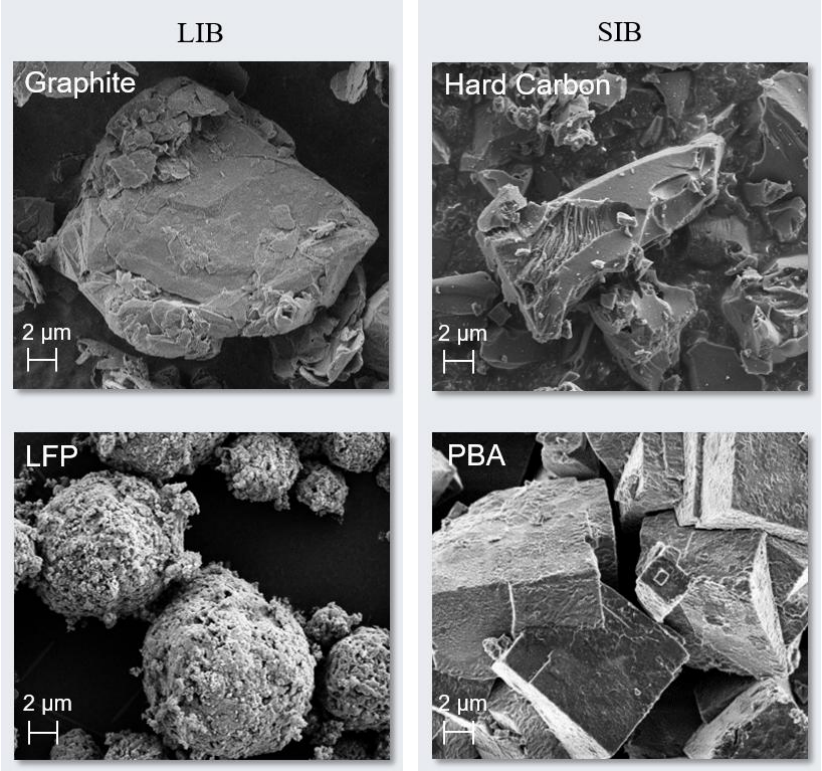


Figure 3.1: SEM images of the investigated active materials: Graphite particles exhibit a plate-like morphology, whereas HC shows an irregular, granular to angular shape. LFP particles are predominantly spherical and contain conductive carbon incorporated to enhance electrical conductivity. In contrast, PBA particles display a characteristic cubic morphology.

The anode and cathode active materials for LIB and SIB investigated in this section differ significantly in terms of particle morphology. Graphite particles show a plate-like shape, whereas HC particles display an irregular, granular, or angular morphology. Among the cathode materials, LFP particles predominantly exhibit a spherical shape and possess an internal pore structure that is not visible in the SEM images. In addition, the particle framework is modified by the incorporation of conductive carbon to enhance electrical conductivity. In contrast, PBA particles exhibit a well-defined cubic morphology, which is characteristic for this class of cathode materials.

A quantitative overview of the active materials investigated in this chapter is given in Table 3.1, which summarizes the particle characterization of the median particle size, BET surface area, and particle density of the anode and cathode materials.

Table 3.1: Overview of the characteristic particle properties of the anode and cathode active materials investigated in this study. Density values correspond to the true density determined by gas pycnometry. The hard carbon powder used in this study is identical to the material employed in the subsequent particle-size investigation and is denoted as HC-C therein (see Section 4.2.1).

| Anode or Cathode / - | LIB or SIB / - | Name /- | Median particle size $x_{50}$ / µm | BET / $m^2\ g^{-1}$ | Density / $kg\ m^{-3}$ |
|---|---|---|---|---|---|
| Cathode | LIB | LFP | 13 | 24.0 | 3350 |
| | SIB | PBA | 12 | 1.0 | 2049 |
| Anode | LIB | Graphite | 18 | 2.7 | 2260 |
| | SIB | HC | 9 | 3.5 | 2062 |

The mean particle diameter of graphite is about two-times higher than for HC. LFP and PBA show almost the same measured mean particle diameter.

The BET surface area describes specific surface area of the particles as the ratio of the particle surface area to the particle volume. For non-porous spherical particles, it is inversely proportional to the characteristic particle diameter. However, the comparison of the four active materials investigated here shows that the idealized relationship between particle size and BET surface area is not strictly consistent. In particular, the LFP particles exhibit a comparatively high BET surface area due to their composite structure, which includes carbon and open porosity, thereby providing additional accessible surface area beyond geometric scaling.

In addition to these particle-related properties, the active materials differ in their specific capacities, as discussed in Section 1.2.2. For the comparison of the calculated areal mass loading, drying time, and production speed, literature values of the specific capacities are used in order to provide practically relevant reference data. These values are summarized in Table 3.2.

Table 3.2: Overview of the specific capacities considered from the literature for the calculation of the areal mass loading and drying time of anode and cathode materials for LIB and SIB.

| | LFP | PBA | Graphite | HC |
|---|---|---|---|---|
| Spec. capacity / $mAh\ g^{-1}$ | 165 | 149 | 360 | 300 |

The results about the particle and active material characteristics form the basis for the subsequent process-related analysis.

### 3.2.2 Process Dimensioning (Drying Time, Production Speed, Dryer Length)

To evaluate the drop-in capability of SIBs in comparison to LIBs, the required drying times, production speeds, and dryer lengths for anode and cathode electrodes are calculated in the following. The objective is to identify critical active material and process parameters and to derive preliminary estimates of their influence on industrial electrode manufacturing.

The drying time is calculated according to Equation (3.1) as the ratio of the areal solvent mass loading in the slurry to the applied drying rate.

$$t = \frac{m_s}{\dot{m}_s} \tag{3.1}$$

The areal solvent mass loading $m_s$ in g m$^{-2}$ is determined using Equation (3.2).

$$m_s = m_{electrode}\,\frac{x_s}{1 - x_s} = m_{electrode}\,X \tag{3.2}$$

For all water-based slurries, a solvent content of 57 wt-% is assumed, corresponding to a solvent loading X = 1.33 in $g_{solvent}\,g^{-1}_{dry\ electrode}$. The areal mass loading of the dry electrode $m_{electrode}$ (g m$^{-2}$) is calculated according to Equation (3.3) based on the target areal capacity $c_{areal}$ (mAh cm$^{-2}$), the specific capacity $q$ (mAh g$^{-1}$) of the active material, and active material fraction in the dry electrode $x_{AM,electrode}$ (kg $kg^{-1}_{solid}$). For all investigated water-based slurries an active material content in the dry electrode of 93 wt-% was used.

$$m_{electrode} = \frac{c}{q\ x_{AM,electrode}} \tag{3.3}$$

According to Equation (3.4), the drying time scales proportionally with the areal mass loading and thus the required areal capacity t ~ $m_{electrode}$ ~ $c_{areal}$ and inversely with the applied drying rate t ~ $\dot{m}_s^{-1}$.

$$t = \frac{m_s}{\dot{m}_s} = m_{electrode}\,X\,\frac{1}{\dot{m}_s} = \frac{c}{q\ x_{AM,electrode}}\,X\,\frac{1}{\dot{m}_s} \tag{3.4}$$

Figure 3.2 shows the linear relationship of the required areal mass loading of the dry electrodes and the drying time for a constant drying rate as a function of the areal capacity for all investigated materials. The constant drying rate of 1.5 g m$^{-2}$s$^{-1}$ is considered industrially relevant and is therefore used as a reference for comparison.[51,89]

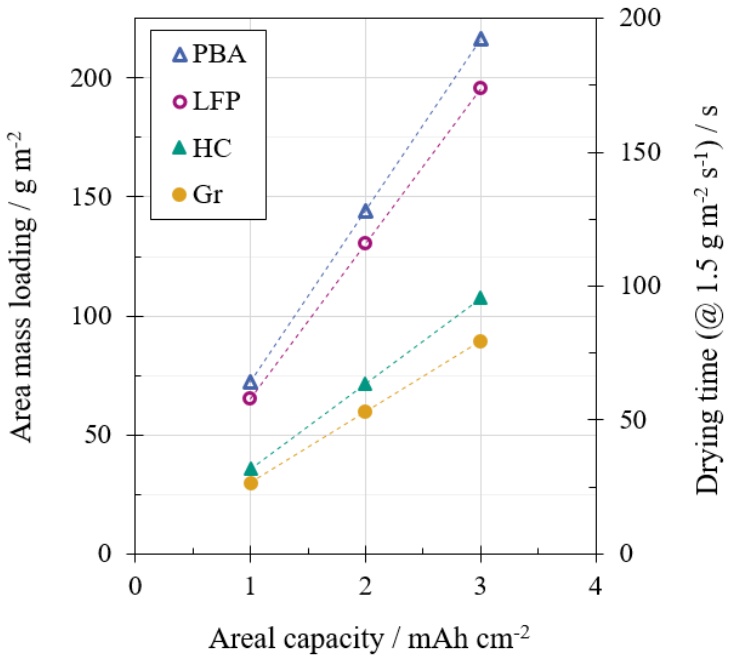


Figure 3.2: Linear relationship of the required areal mass loading of the dry electrodes and the drying time for a constant drying rate as a function of the areal capacity for all investigated materials. The constant drying rate of 1.5 g $m^{-2}s^{-1}$ is considered industrially relevant and is therefore used as a reference for comparison.[51,89] The areal mass loading and drying time were calculated based on the areal capacity for identical proportion of active material in the dry electrode of 93 wt-% identical proportion of solvent in the slurry of 57 wt-%.

Due to their lower specific capacities, cathode materials exhibit a higher mass loading than anode materials at identical areal capacity. Furthermore, as the areal capacity increases, the absolute difference in areal mass loading between LIB and SIB materials increases for both anodes and cathodes, which affects the drying time. Consistent with the differences in areal mass loading, cathode materials exhibit longer drying times than anode materials due to their lower specific capacities. Moreover, at identical areal capacity and slurry composition, SIB active materials require longer drying times than their LIB counterparts. This effect becomes more pronounced at higher areal capacities, as the absolute differences in areal mass loading increases accordingly.

It should be noted that the desired areal mass loading determines the required wet film thickness during coating. A comparison of the necessary wet film thickness is therefore provided in Appendix 11.4.1. While the relationship between areal capacity and wet film thickness remains linear, the differences between materials become more pronounced compared to the areal mass loading. This is attributed to the dependence of wet film thickness

on slurry density, which is influenced by the density of the active material.[e] The role of active material density is further discussed in the context of slurry viscosity in Section 3.2.3.

To highlight the influence of drying rate on the comparison between LIB and SIB electrodes, Figure 3.3 shows the drying time as a function of drying rate for anodes and cathodes at an identical areal capacity of 2 mAh $cm^{-2}$.

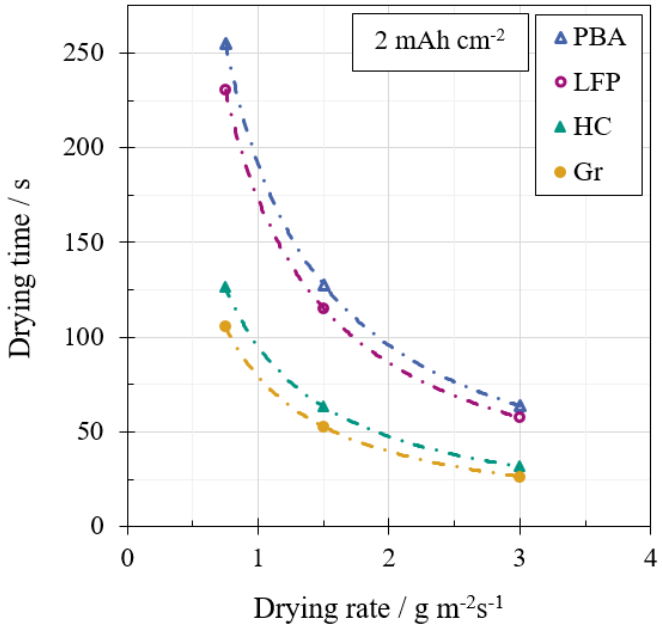


Figure 3.3: Calculated drying time as a function of the drying rate for 2 mAh $cm^{-2}$. The difference in drying time between LIB and SIB materials becomes smaller as the drying rate increases.

For all investigated materials, higher drying rates significantly reduce drying time. While the relative differences in drying time between LIB and SIB materials remain constant across different drying rates, the absolute differences decrease at higher drying rates and are reduced to only a few seconds. Consequently, achieving comparable drying times for LIB and SIB electrodes requires higher drying rates for SIB materials. Under the given boundary conditions, SIB electrodes can only reach drying times equal to or shorter than those of LIB electrodes if higher drying rates are applied.

Although the absolute differences in drying time appear small at a drying rate of 3 g $m^2s^{-1}$, they translate into substantial differences in production speed or required dryer length. To provide a practically relevant comparison, the maximum achievable production speed for

[e] Higher wet film thickness may require additional investment in larger mixers, feed tanks, and pumping system. If a production line has been configured for high-capacity electrodes, producing larger volumes or pumping higher volume flows should not be a challenge. In general, a reduction in wet film thickness for the same areal mass loading of the electrode can be achieved by increasing the active material content, solid content, specific capacity, or density of the active material.

a fixed dryer length and, conversely, the minimum required dryer length for a target production speed are evaluated for all materials. Table 3.3 compares the production speed achievable with a dryer length of 60 m and the required dryer length at a production speed of 60 m $min^{-1}$.

Table 3.3: Overview of two case studies for electrodes with an areal capacity of 2 mAh $cm^{-2}$ and dried at a constant drying rate of 3 g $m^{-2}s^{-1}$ for Graphite vs. HC and LFP vs. PBA: Electrodes' manufacturing speed for a fixed dryer length of 60 m or, on the other hand, expected dryer length for a fixed production speed of 60 m $min^{-1}$.

| | Graphite | HC | LFP | PBA |
|---|---|---|---|---|
| Max. production speed / m $min^{-1}$ @ fixed dryer length of 60 m | 136 | 114 | 63 | 56 |
| Min. dryer length / m @ fixed production speed of 60 m $min^{-1}$ | 26 | 32 | 58 | 64 |

At a production speed of 60 m $min^{-1}$, a difference of one second in drying time corresponds to a difference of one meter in dryer length. Conversely, at a fixed dryer length, small differences in drying time lead to significant variations in achievable production speed.

Overall, the results show that drying times, production speeds or dryer lengths for LIB and SIB electrodes at the same areal capacity and slurry composition can only be achieved if the applied drying rate for SIB is increased relative to that of LIB. The required increase in drying rate is directly proportional to the ratio of specific capacities. In the present case, the specific capacity of LFP is approximately 1.2 times higher than that of PBA, and the specific capacity of graphite is approximately 1.1 times higher than that of HC. Accordingly, the drying rate for SIB materials must be increased by these factors to achieve comparable production speeds or dryer lengths.

An alternative approach to compensate for the longer drying times associated with SIB electrodes is to increase the solid content of the slurry, as indicated by Equation (3.4). While this strategy effectively reduces the solvent load, consequently, the required drying time, it directly affects slurry viscosity. As a result, the apparent mitigation of drying related limitations is accompanied by additional process constraints, particularly with respect to slurry processability. Both strategies discussed, higher drying rates and increased solid contents, therefore necessitate non-trivial adjustments to the established LIB manufacturing process window. In this context, slurry viscosity emerges as a critical parameter that governs the feasibility of these process adaptions.

Slurry viscosity is strongly influenced by the intrinsic properties of the active material. Consequently, the following section systematically examines the influence of active material properties on slurry viscosity behavior to assess their implications for process design and the drop-in capability of SIB electrode manufacturing.

### 3.2.3 Slurry Viscosity

To isolate the influence of the active material and to enable a direct comparison between LIB and SIB on processing behavior, slurries were prepared with identical solid contents and processed using the same mixing procedure. Despite these strictly controlled conditions, pronounced differences in viscosity behavior are expected among the investigated slurries, as particle size, particle size distribution, and particle morphology are known to strongly influence slurry rheology, particularly at lower shear rates.[87]

Figure 3.4 presents the viscosity profiles as a function of shear rate in a double logarithmic scale.

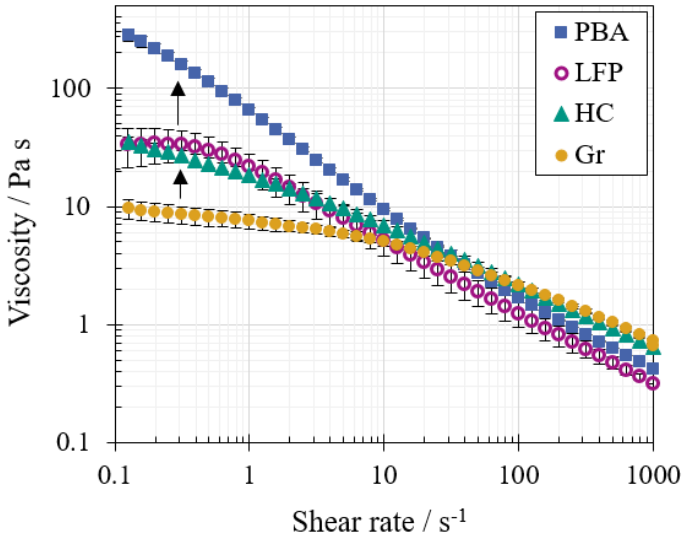


Figure 3.4: The viscosity profiles of the anode and cathode slurries for LIB and SIB were measured as a function of shear rate. The slurries had identical water-based compositions, mixing procedures, and solid contents. At low shear rates, the viscosity of the anode and cathode slurries of SIB is found to be higher than that of LIB slurries. The increase in viscosity in the low shear rate region is a result of the increase in particle interactions.

At low shear rates (0.1 – 10 $s^{-1}$), both SIB anode and cathode slurries exhibit higher viscosities than their LIB counterparts. For the anode materials, this behavior can be illustrated by the comparison of HC and graphite. HC is characterized by a smaller particle size and a higher specific surface area than graphite, which promotes stronger particle-particle and particle-binder interactions and consequently results in an increased viscosity at lower shear rates.[85,87]

A similar trend is observed for the cathode materials. Particle morphology plays an additional role: spherical particles tend to slide past each other more easily, whereas irregular shaped particles promote mechanical interlocking.[87] Accordingly, the spherical LFP particles exhibit lower viscosity at low shear rates than the cubic PBA particles.[104]

To further rationalize the observed viscosity differences, the volume fraction of the active material in the slurry is considered. Equation (3.5) defines the relationship between particle density and volume fraction, indicating that a lower particle density results in a higher active material volume fraction in the slurry ($\varphi_{\mathrm{AM}}^{\mathrm{slurry}} \sim \rho_{\mathrm{AM}}^{-1}$).

$$\varphi_{\mathrm{AM}}^{\mathrm{slurry}} = \frac{x_{\mathrm{AM}}^{\mathrm{dry}}}{\rho_{\mathrm{AM}}} \cdot \rho^{slurry} \qquad (3.5)$$

As summarized in Table 3.4, the lower densities of the SIB active materials lead to higher volume fractions compared to the LIB materials at identical solid contents. This increased volume fraction raises flow resistance within the slurry and contributes to the higher viscosity observed for the SIB systems, particularly at low shear rates.

Table 3.4: Overview of the volume fraction of the active material in the slurry.

| Name | Volume fraction active material / % ($m^3\ m^{-3}$) |
|---|---|
| Graphite | 23 |
| HC | 25 |
| LFP | 17 |
| PBA | 25 |

It is important to note that the viscosity profiles reflect a superposition of several contributing factors, including, particle size, morphology, surface area, and density. Consequently, the viscosity measurements alone do not allow a direct attribution of the LIB-SIB differences to a single parameter. For this reason, Section 4.2.2 provides a more detailed investigation of the influence of particle size on viscosity behavior and its implications for electrode drying.

From a processing perspective, an elevated viscosity at low shear rates is not inherently detrimental. On the contrary, higher low-shear viscosity limits particle movement and thereby lowers the susceptibility to sedimentation. At higher shear rates (> 10 $s^{-1}$), the viscosities of all investigated slurries converge and exhibit pronounced shear-thinning behavior. This indicates that both LIB and SIB slurries are, in principle, equally suitable for established coating technologies such as slot-die coating.[15,105] Moreover, shear-thinning slurries with higher low-shear viscosity are known to reduce edge elevation during electrode manufacturing and therefore minimize scrap rates.[15,105–107]

However, the viscosity results also highlight important challenges with respect to the drop-in capability of SIB technology. As discussed previously, longer drying times off SIB electrodes may be compensated by increasing the solid content of the slurry. The present viscosity analysis demonstrates that such an approach inevitably leads to a further increase in viscosity, particularly at low shear rates. Excessively high viscosities can pose challenges for slurry pumping and complicate air bubble removal, which causes negative effects on

coating quality. This can also affect the design of the coating equipment for homogeneous distribution of the slurry on the current collector and may result in the need for new coating equipment.[108] These effects may require adjustments to coating equipment or process parameters and thus represent a deviation from a true drop-in implementation.

In summary, while SIB slurries remain compatible with established coating technologies, their distinct viscosity behavior requires material-specific process adjustments. Moreover, slurry viscosity behavior defines the initial conditions for subsequent drying and thus could directly influence pore network development and the onset of pore breakthrough. The following section therefore examines the drying behavior of LIB and SIB electrodes, with particular emphasis on elucidating how active material properties govern microstrucutre formation and pore breakthrough and their implications for binder migration.

### 3.2.4 Pore Breakthrough Depending on Active Material

The drying-induced formation of electrode microstructure is commonly described as a sequence of film shrinkage followed by pore emptying. While solvent evaporation initially leads to particle consolidation and macroscopic shrinkage, the establishment of a continuous pore network enables capillary transport, marking the onset of pore emptying and initiating binder migration.

Based on previous studies in the literature, it has been assumed that the temporal relationship between these two phases depends on active material properties, viscosity in the pore network, drying rate, and electrode characteristics, potentially leading to early or delayed pore breakthrough and altered binder migration behavior (see Section 1.3.2). However, experimental validation of this assumption has been limited, as drying kinetics and pore breakthrough have predominantly been investigated separately. Therefore, the causal relationships and the underlying mechanisms remain insufficiently understood. The present work directly addresses this gap to identify critical parameters.

This section therefore examines the influence of active material on microstructure formation. A novel experimental approach is employed that allows simultaneous measurement of film shrinkage and pore breakthrough, enabling the identification of parameters governing the onset of pore emptying.

As presented in Section 3.1, pore emptying is influenced by a multitude of interacting parameters, including the active material influence, complex three-dimensional pore network, slurry viscosity, and potential superposition of effects. This complexity complicates the formulation of clear a priori hypotheses. Nevertheless, it could be expected that an increased viscosity at the end of film shrinkage would lead to higher friction losses and thus delay pore emptying.

To quantify this effect, a methodology for estimating the viscosity of the CMC solution within the pore structure at the end of film shrinkage is developed and presented in the

Appendix 11.4.3. It is shown that the end of film shrinkage varies with active material density and microstructure porosity, resulting in different solvent contents and consequently, significantly different viscosities within the pore network. The viscosity in the pore network at the end of film shrinkage is, for example, higher for electrodes with LFP than with Graphite. A comparatively higher viscosity of the liquid in the capillary network could increase the flow resistance.[f] However, these considerations are predominantly based on idealized pore network structures and therefore do not capture the superposition of effects that occur in real electrode microstructures. Based on the examination of the viscosity of the CMC-water solutions at the end of film shrinkage, this could mean that the pore breakthrough for slurries containing LFP occurs with a delay than for slurries containing graphite.

To this end, the influence of the active material on the onset of pore emptying and thus the initiation of binder migration is examined in the following. The onset of pore breakthrough is determined by observing the underside of the applied wet film and identifying the time at which the first pore becomes visible ($t_{1st\ pore}$). The end of film shrinkage ($t_{EOFS}$) is obtained from film shrinkage measurements, which also allow calculation of the drying rate (described in 2.3.2). Figure 3.5 shows the ratio $t_{1st\ pore}\ t_{EOFS}^{-1}$ for a dry film thickness of approximately 100 µm for the different material systems.

[f] Similarly, a relatively large coating thickness as well as a narrow pore size distribution have been reported to promote a later onset of pore emptying (see Section 1.3.2).

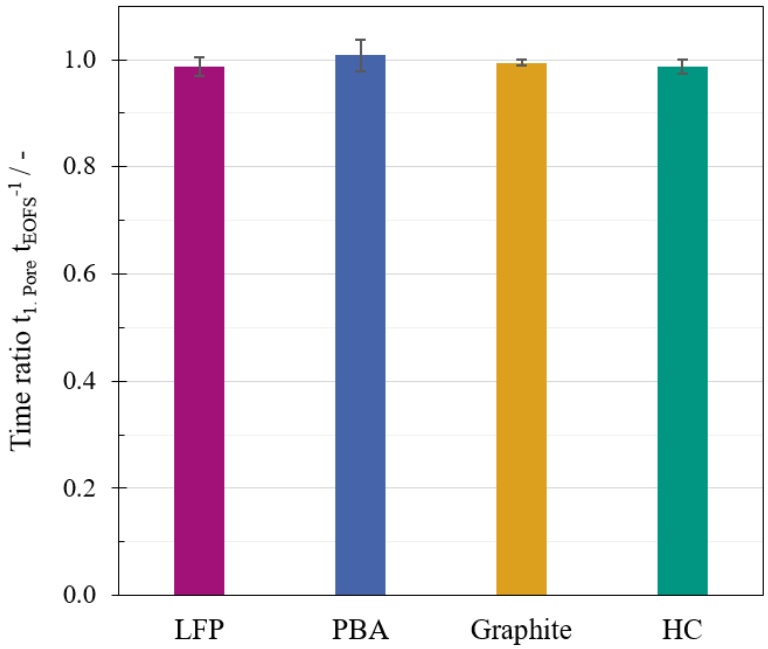


Figure 3.5: Ratio of the time of first visible pore emptying on the underside of the wet film ($t_{1st\ pore}$) to the time at which film shrinkage is completed ($t_{EOFS}$) for a dry film thickness of approximately 100 µm for the different active material systems. The drying rate was approximately 1 g $m^{-2}s^{-1}$ for all experiments presented.[gh] For all investigated active materials, pore breakthrough coincides with the end of film shrinkage ($t_{1st\ pore} = t_{EOFS}$), demonstrating that the pore breakthrough is independent of material system and slurry viscosity.

For all investigated material systems, the first pore becomes visible precisely at the end of film shrinkage. This demonstrates that pore breakthrough and the completion of film shrinkage occur simultaneously, independent of the active material system. Consequently, the onset of capillary transport during drying coincides with the end of film shrinkage, allowing a clear separation of the drying process into film shrinkage and pore emptying phases.

These findings challenge the assumption from the literature that slurry viscosity plays a decisive role in determining pore breakthrough timing during the drying of water-based electrodes. These findings indicate that capillary forces dominate the drying process and effectively overcome viscous resistance within the pore network. This interpretation is supported by literature about drying in porous media.[77–80] Metzger et al. demonstrate through simulations that, depending on the pore size distribution, capillary forces can significantly

[g] The PBA electrodes tend to develop cracks on the surface of the electrode structure. The cracks appeared at the time of the end of film shrinkage.

[h] Additional results obtained at different drying rates and dry film thicknesses are provided in the Appendix 11.4.4. In all cases, the same relationship as discussed here was consistently observed.

dominate over liquid friction, which means that a higher viscosity in the pore network does not play a significant role.[78]

As a direct consequence of the results shown in Figure 3.5, a material-dependent shift in the onset of pore breakthrough and the associated onset of binder migration can be excluded. The subsequent analysis thus focuses on quantifying binder migration for different active materials, evaluated via adhesion strength measurements as a function of drying rate.

### 3.2.5 Adhesion and Binder Migration

To investigate the influence of different active materials on binder migration and to derive material-process-microstrucutre-property relationships, the adhesion strength of the electrodes is examined in the following. Adhesion strength is defined as the force required to induce failure at the interface between the first particle layers and the substrate, and can be used as an indirect measure of binder migration.[17,19,81,82,91] By decoupling absolute adhesion strength from drying-rate-induced changes, material-dependent binder migration mechanisms can be systematically evaluated.

It can be hypothesized that a correlation exists between the absolute adhesion strength and the sensitivity to binder migration at increased drying rates. A higher absolute adhesion strength could mean better fixation and thus a lower sensitivity to binder migration. To test this assumption, adhesion strength is first evluated at a constant low drying rate, followed by systematic variation of the drying rates.

Figure 3.6 presents the adhesion strength of LIB and SIB anode and cathode electrodes with an areal capacity of 2 mAh $cm^{-2}$, manufactured at a constant drying rate of 0.75 g $m^{-2}s^{-1}$.

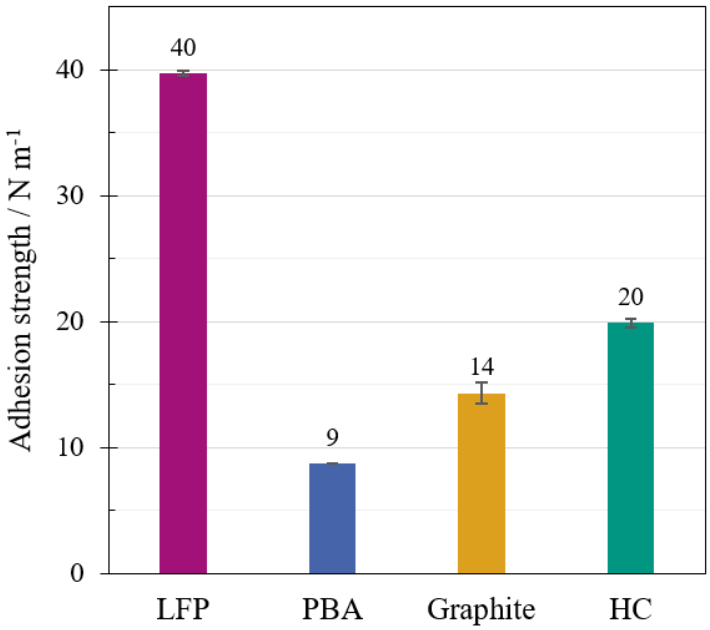


Figure 3.6: Adhesion strength of water-based processed electrodes with LFP, PBA, Graphite, and HC as active material, measured for electrodes with an areal capacity of 2 mAh $cm^{-2}$. LFP electrodes exhibit the highest adhesion strength, whereas PBA electrodes show the lowest values. This trend is consistent across different areal capacities (see Appendix 11.4.6). All electrodes were manufactured using identical slurry mixing procedure, a constant drying rate of 0.75 g $m^{-2}s^{-1}$, and identical dry electrode compositions. Note that PBA electrodes show initial cracking and that absolute adhesion strength is only directly comparable between HC and LFP due to different current collector materials.

Significant differences in adhesion strength are observed among the investigated active material systems. LFP exhibits the highest adhesion strength, whereas PBA electrodes show the lowest adhesion values. This trend is consistent for electrodes with different areal capacities (see Appendix 11.4.6). However, PBA electrodes display initial cracking, indicating cohesion-related issues and limiting the direct comparability of adhesion strength values. In addition, only HC and LFP electrodes can be directly compared in terms of absolute adhesion strength, as graphite electrodes are coated on copper substrate rather than aluminum.

A direct correlation between adhesion strength and particle ize cannot be consistently identified across all investigated materials. While a particle size dependence may be present within the anode materials, particularly between HC and graphite, this trend does not extend to the cathode materials. The influence of particle size on electrode processing is further addressed in Chapter 4.

When considering the specific surface area, an apparent correlation with adhesion strength emerges, with lower BET values corresponding to lower adhesion and vice versa. However, this relationship is not physically robust. In the case of LFP, the high BET surface area is

party attributed to internal porosity, which does not necessarily contribute to binder accessible surface area. As a result, the BET value may overestimate the effective interfacial area relevant for adhesion. That high BET surface area does not necessarily result in increased adhesion is also shown in the literature and in Chapter 5 using NCM active material with high porosity of the particles and the binder PVDF.[18,109]

In this context, a more plausible explanation is given by an additional superposition effect arises from differences in particle density. Due to its higher particle density, LFP exhibits an increased SBR volume fraction compared to the other materials, which have similar densities and thus more comparable binder volume fractions (see Table 3.5).

Table 3.5: Overview of the SBR volume fraction in the dry electrode for the investigated active material systems. Since adhesion strength is primarily governed by the SBR binder, the corresponding binder volume fraction reported to enable a direct comparison between materials. Differences in active material density result in notable variations of the SBR volume fraction in the dry electrode.

| Name | Volume fraction SBR binder / % ($m^3$ $m^{-3}$) |
|---|---|
| LFP | 11 |
| PBA | 7 |
| Graphite | 8 |
| HC | 7 |

This increased binder availability likely contributes to the higher adhesion strength of LFP and may additionally reduce the sensitivity to binder migration during drying. In the context of industrial electrode production, where high drying rates are required (see Section 3.2), it is therefore essential to distinguish between material-independent and material-specific effects on binder migration. In particular, the identification of relevant particle properties governing these effects remains a key objective.

Figure 3.7 shows the normalized adhesion strength as a function of drying rate for electrodes with fixed areal capacity. Normalization is based on the reference adhesion strength shown in Figure 3.6 to isolate the effect of binder migration.

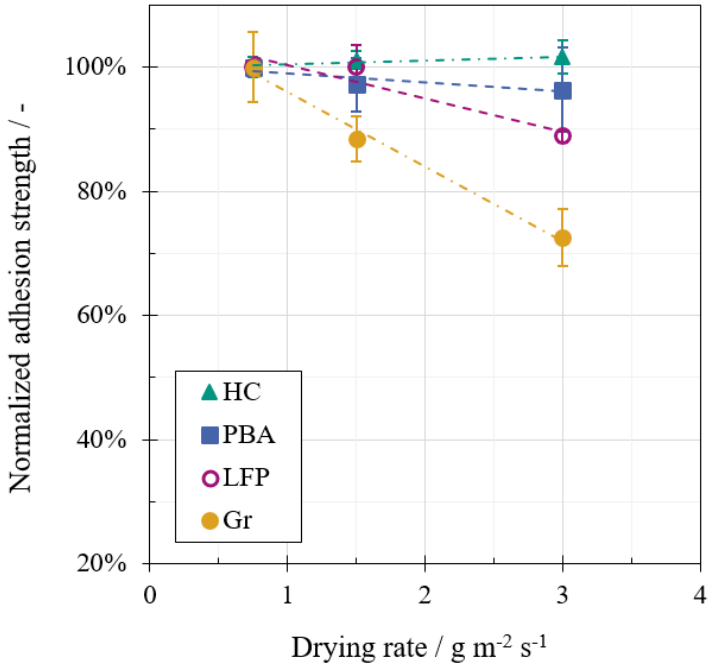


Figure 3.7: Normalized adhesion strength for electrodes containing different active materials and increasing drying rate. The drying rate was adjusted by varying the temperature of the heated plate and the drying air, while maintaining a constant heat-transfer coefficient of the slot nozzle dryer. The impact of binder migration varies depending on the material system used. Graphite shows the often observed phenomenon of decreasing adhesion strength with increasing drying rate (binder migration). In particular, electrodes with HC as the active material do not show decreasing adhesion strength with increasing drying rate.

When increasing the drying rate, the material-dependent nature of binder migration becomes evident. For graphite and LFP electrodes, increasing drying rates result in a pronounced reduction in adhesion strength, indicating significant binder migration. In contrast, HC electrodes do not exhibit a reduction in adhesion strength, despite having a lower absolute adhesion strength than LFP (see Figure 3.6). This demonstrates that absolute adhesion strength alone is not a sufficient indicator of binder fixation. Furthermore, HC and graphite exhibit similar SBR volume fractions, yet show markedly different behavior with respect to binder migration, indicating that the influence of binder volume fraction can be considered negligible in this context.

In addition, for LFP electrodes binder migration occurs once a critical drying rate is exceeded, suggesting that capillary forces must surpass a threshold to overcome binder fixation. These findings emphasize that binder migration sensitivity is governed by the balance between capillary transport and binder fixation rather than by adhesion strength alone. This supports the hypothesis that affinity between binder and active material plays a decisive role in determining binder migration sensitivity.

Furthermore, the results suggest a particle-size-dependent mechanism. The smaller particle size of HC compared to LFP and graphite appears to reduce sensitivity to binder migration,

requiring higher drying rates to induce binder transport. This result leads to the hypothesis that decreasing particle size increases the resistance of binder transport. To investigate this effect systematically, HC electrodes with particle size variations are examined in the subsequent Chapter 4. This approach additionally ensures that superimposed effects arising from differences in active material density are excluded.

## 3.3 Conclusion

This chapter systematically evaluates the extent to which SIBs can be regarded as a drop-in technology relative to LIBs under realistic manufacturing conditions. The focus is on manufacturing-oriented analysis that examines the role of active material properties along the electrode production chain. The objective is to identify material-dependent process limitations and to consolidate them into consistent active material-process-microstructure-property relationships.

Starting from industrial LIB electrode manufacturing practice, it is shown that key performance indicators such as production speed, drying time, and plant footprint are largely limited by the drying process. Even small differences in required drying time directly translate into significant changes in dryer length or achievable line speed. Against this background, the widely held assumption that LIB process conditions can be directly transferred to SIB electrode manufacturing is critically assessed.

The comparative analysis is based on strictly controlled and identical processing conditions for LIB and SIB electrodes. Graphite and hard carbon are investigated as anode materials, while LFP and a PBA are studied as cathode materials, all processed using a water-based CMC/SBR binder system. This systematic approach ensures that observed differences can be unambiguously attributed to intrinsic active material properties.

One central finding is that the specific capacity of the active materials constitutes a dominant process parameter. Due to their lower specific capacities, the investigated SIB materials require higher areal mass loadings at identical areal capacities, which inevitably results in longer drying times. This relationship is fundamental and independent of the applied drying rate. Although higher drying rates reduce absolute differences in drying time, the material-related process disadvantage of SIB electrodes persists. From an industrial perspective, this necessitates either higher drying rates or longer dryers, thereby challenging the notion of true drop-in capability already at the level of process dimensioning.

Increasing the solid content of the slurry is discussed as an alternative strategy to compensate for longer drying times, as it reduces solvent loading. However, this approach directly increases slurry viscosity, highlighting slurry rheology as a critical link between active material properties and process feasibility. Despite identical solid contents, SIB slurries exhibit significantly higher viscosities at low shear rates than their LIB counterparts. These differences are attributed to a combination of lower particle density, smaller particle size, higher

specific surface area, and less favorable particle morphology, all of which increase the active material volume fraction and flow resistance.

From a processing perspective, these viscosity differences are ambivalent. On the one hand, all investigated slurries remain processable due to pronounced shear-thinning behavior. On the other hand, elevated low-shear viscosities restrict pumpability, degassing, and process stability, potentially requiring adaptations in equipment design or operating conditions. Consequently, even seemingly straightforward process adjustments intended to mitigate drying-related limitations introduce additional manufacturing constraints.

With regard to drying-induced microstructure evolution, the chapter provides a key generalizable result: for all investigated material systems, pore breakthrough occurs exactly at the end of film shrinkage. Despite pronounced differences in solvent content and pore-network viscosity at the end of film shrinkage, no material-dependent temporal shift in the onset of pore breakthrough is observed. This demonstrates that capillary forces dominate over viscous resistance during drying, and that the initiation of binder migration is not governed by slurry or pore-network viscosity. This finding experimentally challenges a common assumption in the literature.

While the onset of binder migration is thus shown to be material-independent, the extent of binder migration is strongly material-dependent. Adhesion strength measurements reveal that absolute adhesion strength alone is not a reliable indicator of binder migration sensitivity. LFP electrodes, despite exhibiting high adhesion strength, show pronounced binder migration once a critical drying rate is exceeded, whereas hard carbon electrodes display little sensitivity to increased drying rates. Since differences in binder volume fraction cannot explain this behavior, binder-active material affinity and particle size are identified as decisive parameters. This insight provides the conceptual basis for the systematic investigation of particle size effects presented in the subsequent chapter.

In summary, this chapter demonstrates that the drop-in capability of SIB electrode manufacturing is not limited by individual process parameters, but by interconnected active material-process-microstructure-property relationships. Due to their intrinsic material properties, SIB electrodes require adapted process strategies, and a direct transfer of established LIB manufacturing conditions under drying-limited regimes is not feasible.

The findings of this chapter clearly indicate that the industrial implementation of SIB technology is less a question of machine compatibility than of material-specific process design. Future work should therefore focus on developing process windows that explicitly account for active-material-dependent constraints rather than pursuing a uniform transfer of LIB manufacturing strategies.

A key lever lies in the targeted modification of particle properties, particularly particle size, to reduce sensitivity to binder migration without excessively compromising slurry processability. This represents a promising design space at the interface between active material engineering and process optimization.

In the long term, the active material-process-microstructure-property relationships identified in this chapter extend beyond LIB and SIB systems. For future post-lithium battery technologies characterized by lower specific capacities and increasingly complex particle architectures, the coupled design of active materials and manufacturing processes will become a decisive competitive factor. The framework established here provides a robust conceptual foundation for such developments.

The subsequent chapter builds directly on these insights by systematically isolating and varying individual material parameters, most notably particle size, and investigating their specific impact on drying behavior, binder migration, and resulting electrode properties. This marks the transition from comparative analysis towards targeted material and process optimization.

# 4 Influence of Particle Size and Fast Drying on Binder Migration

Enhancing the efficiency of industrial electrode manufacturing requires strategies that enable accelerated drying, thereby increasing production throughput or reducing the necessary dryer length. However, existing literature demonstrates that fast drying can induce binder migration, which in turn leads to degradation of electrode properties (see Section 1.3.1). As a result, either slower drying must be employed, or the individual drying zones must be specifically adapted to the mechanisms governing microstructure formation.

The preceding sections have shown that the intensity of binder migration is not universal but strongly depends on the active material used. In particular, the investigations conducted in Section 3.2.5 indicate that particle size exerts a key role. Nevertheless, this phenomenon may additionally be affected by other material-specific factors, such as chemical composition or particle morphology. It is evident that further systematic research is required in order to establish a more comprehensive understanding of the interrelations between active material properties, process conditions, and resulting electrode microstructure and properties.

Given this background, the objective of this section is to analyze the correlation between particle size and binder migration under fast drying conditions for water-based slurries with the CMC/SBR binder system. To isolate the particle-size effect and mitigate influences from differing active materials or particle morphologies, the investigation focuses exclusively on HC as active material. The broader applicability of the identified particle-size effects is further demonstrated for LFP in the Appendix 11.6. This targeted approach enables a deeper understanding of the complex interplay between material, process conditions, and the resulting microstructure formation and binder migration. The findings provide novel insights into the drying mechanism as a function of the particle size, drying conditions, and particle-binder interactions, thereby extending the current state of knowledge. Moreover, this work presents the first systematic comparison of ionic resistance and adhesion strength as a function of drying rate for water-based electrodes.[i]

[i] The results and discussion in this chapter are part from the following publication by the author:[14] Klemens, J.; Schneider, L.; Burger, D.; Zimmerer, N.; Müller, M.; Bauer, W.; Ehrenberg, H.; Scharfer, P.; Schabel, W. (2023): *Process and Drying Behavior Toward Higher Drying Rates of Hard Carbon Anodes for Sodium-Ion Batteries with Different Particle Sizes: An Experimental Study in Comparison to Graphite for Lithium-Ion-Batteries.* In: Energy Technol., DOI: 10.1002/ente.202300338.

## 4.1 Motivation and State of the Art

The existing literature identifies a range of potential factors that may affect binder migration as a function of active-material properties. Reported influences include changes in pore-emptying behavior, variations in particle shape and size, and the complex interactions between CMC, SBR, and the particles present in the slurry. However, it is important to note that previous studies often involve and discuss multiple overlapping effects, making it difficult to isolate the contribution of individual parameters.

Therefore, the aim of this chapter is to investigate the influence of particle size in an isolated manner and thereby identify a key mechanism underlying binder migration. A particularly promising hypothesis attributes the material-dependent migration behavior to variations in the interactions between CMC and SBR, which therefore serve as the conceptual foundation of the following analysis.

To develop a mechanistic understanding, this chapter first examines the interactions between CMC and SBR in the absence of additional particles, with particular emphasis on the relevance of the CMC overlap concentration. The overlap concentration describes the critical polymer concentration at which a polymer solution begins to form an interconnected network. Below this threshold, polymer chains behave largely independently in the dilute regime, whereas above the overlap concentration significant chain entanglement and cooperative interactions occurs, leading to pronounced changes in rheological and transport properties.

Subsequently, the analysis demonstrates how the introduction of active-material particles modifies these interactions and how particle-binder interactions influence binder migration. This systematic approach highlights the scientific importance of the investigations presented in this work.

**Interaction between CMC and SBR and the significance of CMC-overlap concentration**

The use of the multicomponent binder system consisting of CMC and SBR significantly increases the complexity of slurry interactions compared with the single-component PVDF binder, as both CMC and SBR can move independently and exhibit distinct interaction mechanisms. A key contribution to the fundamental understanding of these processes is provided by Lim et al.[110], who investigated the drying of CMC-water solutions while varying the CMC concentration and adding SBR-like latex particles (without active material).

To assess the potential accumulation of latex particles before the end of film shrinkage, the authors employed the dimensionless Peclet number as well as the sedimentation number. The Peclet number, calculated using the Stokes-Einstein relation[111], estimates particle diffusivity in liquids.[112–114] However, this approach is only valid for highly dilute polymer solutions and fails at higher polymer concentrations due to macromolecular effects such as

chain entanglement. While an accumulation of latex at the film surface was shown to be theoretically possible, experimental observations revealed that this behavior strongly depends on the CMC concentration. Once the overlap concentration is exceeded, entanglement of the CMC chains leads to immobilization of the latex particles, indicating strong interactions between CMC and latex.

In the context of battery-electrode slurries, however, the inherent capillary network formed by the active material must also be considered. Lim et al. demonstrated therefore that the addition of graphite particles and the resulting porous microstructure induce latex migration even when the CMC-water solution is above the overlap concentration. Although the binder is immobilized by CMC-polymer entanglement, it can become remobilized through capillary-driven flow within the porous network. Whether CMC itself undergoes significant movement in drying slurries remains an open question.[115]

In this context, the following section examines how binder migration can be suppressed despite capillary flow and clarifies the role of CMC-active material interactions in this process.

**Suppressed binder migration by binder-system and particle interactions**

One possible explanation for the resistance to binder migration in water-based electrode formulations is the specific interaction of CMC under the influence of active material particles. Studies on the microstructure formation of graphite anodes demonstrate that polymeric CMC forms a network within the dried electrode, and that its immobilization is strongly affected by the surface chemistry of the active material.[17,116,117] Chang et al.[118] showed that CMC can be immobilized depending on the surface properties, suggesting that functional groups of the polymer form specific bonds with the particle surface during drying.[118]

Rheological investigations of graphite slurries further indicate that increasing the CMC concentration enhances the amount of CMC adsorbed onto graphite particles.[119] Factors influencing this adsorption include the degree of substitution of hydrogen in the hydroxyl groups by carboxymethyl groups and the molecular weight of the polymer.[120] Cryogenic broad ion beam scanning electron microscopy (cryo BIB SEM) images consistently show that CMC adsorbs onto active material surfaces and simultaneously SBR binder adheres to the fixated CMC.[119] These findings align with the results of Lim et al.[110], who demonstrated that latex particles can be immobilized within the CMC network depending on the polymer concentration.

In the context of binder migration in battery slurries, additional studies investigated the drying behavior of graphite slurries with varying particle morphologies and mixing intensities.[17] These studies revealed that spherical, comparatively smaller particles as well as intensively mixed slurries (e.g., prepared with a kneader) exhibit reduced binder migration

as the drying rate increases. Proposed explanations include stronger particle-CMC interactions and a higher number of particle contacts, both of which increase the potential bonding sites between the CMC/SBR network and the active material. Thus, resulting in less pronounced SBR binder migration during drying.[17] However, these studies did not allow for universal conclusions, as several influencing factors, such as particle morphology, mixing procedures, and material properties, were superimposed.

Building on the limitations identified in previous studies, particularly the overlap of multiple influencing factors, the present work aims to isolate the specific effect of particle size on binder migration in water-based systems. For this purpose, Hard Carbon from the same manufacturer was selected in distinct particle size classes, ensuring a controlled comparison without material-specific variability. Electrode fabrication was carried out using identical slurry formulations, consistent mixing procedures, controlled drying conditions, and standardized characterization methods to eliminate additional sources of variation.

To further substantiate that the observed phenomena arise from the synergistic behavior of the CMC/SBR binder system, complementary drying experiments were conducted using PVDF as a reference binder (see Appendix 11.5.5). This reference system offers a crucial benchmark for differentiating between particle-size-driven effects and binder-chemistry-driven mechanisms.

The following section presents results of these systematically designed experiments and discusses how particle size governs rheological behavior, binder migration, adhesion strength, and ionic resistance under well-defined drying conditions. Additionally, the investigation extends to the exploration of whether the sensitivity to binder migration can be influenced by the particle size of the material system utilized. The study will examine whether the use of smaller particle sizes of the active material can shift the threshold of drying rate that is needed to move the binder. These findings would imply a substantial role for particle size. The following section presents the experimental methodology and results that form the basis for evaluating this hypothesis.

## 4.2 Results and Discussion

The processing of HC active material with systematically varied particle sizes is investigated. The central objective is to determine how different particle sizes influences electrode processing, from rheological behavior to microstructure formation and binder migration during fast drying.

To address this question, rheological investigation is complemented by stability measurements, enabling a quantitative correlation between slurry properties and binder migration behavior. To facilitate a more comprehensive comparison, measurements of the rheological behavior of graphite slurry and the adhesion strength of graphite electrodes at increasing drying rates are also included. This methodological approach allows a comparative analysis

of the influence under identical electrode compositions, solid contents, and drying conditions. The combined evaluation of rheological, stability, and adhesion strength data provides the basis for identifying correlations and facilitate predictive trends for binder migration behavior.

To further elucidate the relationship between particle characteristics, slurry flow behavior, and binder migration, a detailed analysis of the active material particle properties is presented in the following section. An analysis of graphite particles and a comparison with HC particles has already been prodived in Chapter 3.

### 4.2.1 Particle Properties

For the comparative investigation of different particle sizes on electrode processing and binder migration behavior, HC active materials were obtained from the same manufacturer and differ primarily in their particle size and size distribution. The SEM images below illustrate the variation in particle size.

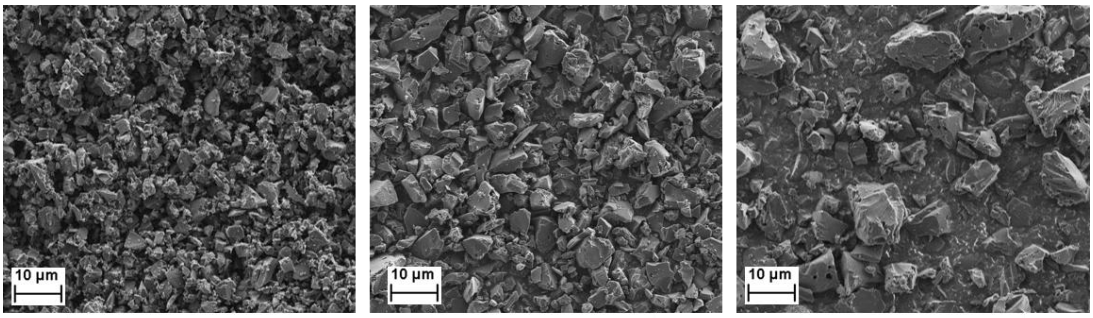


Figure 4.1: SEM images of three HC active material powders with systematically varied particle sizes.[85] All HC materials exhibit an irregular, granular particle morphology. The corresponding particle size distributions are shown in Appendix 11.5.1.

The HC particles have an irregular, granular shape and differ in particle size. The particle size, the specific surface area, and the density (measured by gas pycnometry) of the particles are shown in Table 4.1. The specific surface area decreases as the particle diameter increases. In addition to electrode processing and binder migration, the size and specific surface area of the particles have a significant impact on the electrochemical performance.[j]

[j] The influence of SEI formation on the electrochemical performance for graphite with different particle sizes is discussed in the literature. Due to a higher active surface area, the performance of the cell is affected by a non-reversible lithium-loss during the formation of the Solid Electrolyte Interphase (SEI).[121] The smaller particle size of HC-A particles leads as well to a higher capacity loss due to SEI formation compared to HC-C particles (see Appendix 11.5.9). In turn, the larger particles show a higher overpotential. More detail on the influence of particle size on the voltage profile during charging and discharging of HC electrodes in half cells against sodium metal can be found in the Appendix 11.5.9.

Table 4.1: Overview of the particle properties of the investigated HC materials. The distribution of particle size is illustrated in the Appendix 11.5.1.

| Name | Median particle size $x_{50}$ / µm | Specific surface area BET / $m^2\ g^{-1}$ | Material density / $kg\ m^{-3}$ |
|---|---|---|---|
| HC-A | 3.7 | $9.83 \pm 0.12$ | $1949 \pm 3$ |
| HC-B | 5.0 | $4.99 \pm 0.05$ | $2069 \pm 2$ |
| HC-C | 9.4 | $3.46 \pm 0.04$ | $2062 \pm 2$ |

These morphological differences form the basis for the particle size–dependent rheological behavior discussed in the following section, and, given the comparable particle shape and density of the three HC materials, the rheological investigation is designed to isolate particle size effects.

### 4.2.2 Slurry Viscosity Profile and Slurry Stability

The influence of HC particle size on rheology was systematically investigated using slurries with identical solid content, electrode composition, manufacturing procedures, and mixing parameters. This approach ensured that observed differences in rheology, electrode microstructure, and binder migration could be attributed primarily to particle size effects.

**Viscosity profile**

Figure 4.2 presents the viscosity of HC slurries containing different HC particle sizes as a function of shear rate in a double logarithmic plot, along with a graphite slurry as a reference.

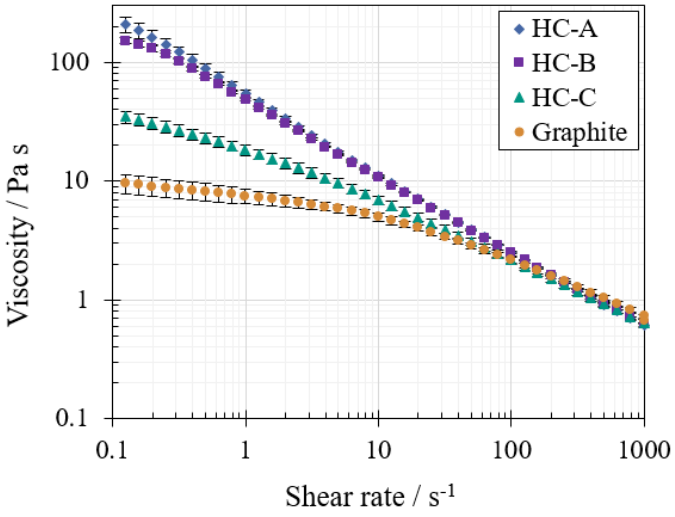


Figure 4.2: Viscosity as a function of shear rate for HC slurries with different mean particle sizes (HC-A: $x_{50}$ = 3.7 µm, HC-B: $x_{50}$ = 5.0 µm, HC-C: $x_{50}$ = 9.4 µm) and a graphite slurry ($x_{50}$ = 18.4 µm), prepared with identical dry composition, water content, and mixing procedure. Smaller particle sizes lead to higher viscosities at low shear rates (0.1 $s^{-1}$), while the viscosities of all slurries converge and become nearly identical at higher shear rates (> 50 $s^{-1}$), indicating a negligible influence of particle size in this regime.

Distinct differences are evident in the low shear-rate regime, where the HC-A slurry exhibits the highest viscosity, followed by HC-B and HC-C. The increased viscosity of HC-A can be attributed to its smaller particle size and correspondingly higher specific surface area, which intensifies particle-particle and particle-polymer interactions.[87]

In contrast, the lower viscosity of the HC-C slurry at low shear rates is likely related not only to its larger particle size but also to its broader particle size distribution, which likely facilitates more efficient particle packing and contributes to the lower viscosity observed at low shear rates. At shear rates above 50 $s^{-1}$, the viscosities of all HC slurries and the graphite slurry converge, indicating shear-induced structure breakdown and reflecting the identical solid content and CMC concentration.

A further distinction between HC-A and HC-B in comparison to HC-C and graphite may relate to the stability behavior of the slurries, which can subsequently affect viscosity. This has been investigated by frequency sweep measurements.

**Slurry stability**

To further assess slurry stability, oscillatory rheological measurements were conduced. These analyses were conducted to evaluate the tendency for sedimentation and to characterize the slurry's structural strength. The objective of this analysis is to illustrate the impact of varying particle sizes on the polymer-particle network that is formed in water-based CMC/SBR electrode slurries, which could be particularly relevant for evaluating binder migration effects.

Prior to the frequency sweeps, amplitude sweeps at an angular frequency of 1 $s^{-1}$ were performed to determine the linear viscoelastic range. Based on these results, an appropriate deformation amplitude was selected. During the frequency sweep, the loss modulus G‘‘ and the storage modulus G‘ were determined. The phase shift angle as a function of frequency is presented in Figure 4.3.

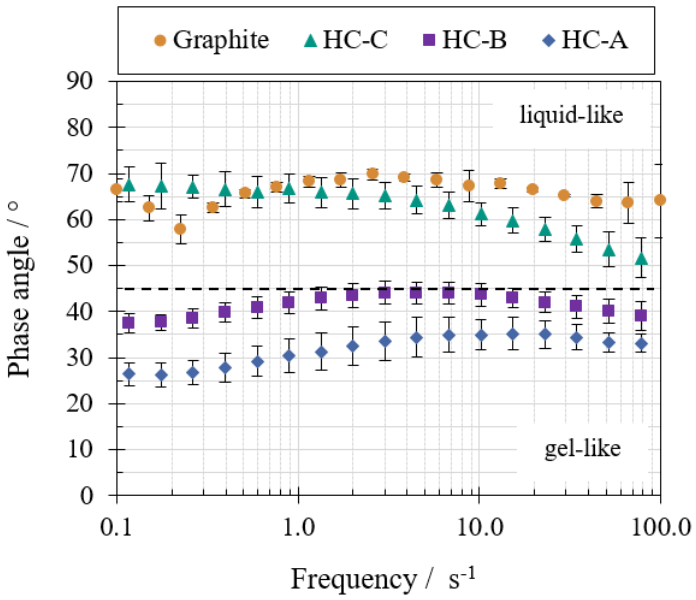


Figure 4.3: Phase angle as a function of frequency measured at a deformation of 1 % for all investigated slurries (Graphite, HC-A, HC-B, HC-C). The phase angle derived from the ratio of storage and loss moduls is used to classify the rheological behavior as gel-like (phase angle <45°) and liquid-like (phase angle >45°).

The rheological characterization reveals a clear distinction between the investigated slurries. HC-A and HC-B slurries exhibit gel-like behavior, while HC-C and graphite slurries show predominantly liquid-like characteristics. The gel-like behavior of HC-A and HC-B is accompanied by increased viscosity at low shear rates and lower phase angles. This behavior is attributed to pronounced particle-particle interactions and an increased number between CMC-polymer and the active material particles.

The observed particle-size-dependent trend for HC slurries is consistent across both viscosity and phase angle analysis. Smaller particles promote the formation of a more interconnected polymer-particle network, which suggests enhanced bridging of the CMC between neighboring particles within the slurry. In contrast, larger particles reduce the nuber ob available interaction sites per unit volume, resulting in a weaker network structure and a more liquid-like response.

From a drying perspective, such an enhanced bridging of the CMC network may limit the mobility of the SBR binder, assuming attractive interactions between CMC and SBR. As a result, capillary-driven binder migration during drying is expected to be suppressed for slurries exhibiting more gel-like behavior, particularly in the case of HC-A and HC-B. This

discussion will be expanded upon in Section 4.2.4 within the context of binder migration investigation.

In assessing binder migration as a function of mean particle size, it is first necessary to determine whether an increase in drying rate induce changes in electrode microstructure. Very high drying rates intensify the driving forces during solvent evaporation and microstructure formation and could potentially alter pore network formation and pore-size distribution.

### 4.2.3 Electrode Microstructure: Influence of Particle Size and Drying Rate

To characterize the microstructure in this section and binder migration during fast drying in Section 4.2.4, the HC electrodes were produced under identical processing conditions. The drying rate during electrode manufacturing was systematically varied between 0.75 and 9 g $m^{-2}s^{-1}$. For an average areal mass loading of about 81 g $m^{-2}$ for the dry HC electrodes (see Table 4.2), the drying time can be reduced from 142 s to only 12 s in the drying rate range investigated. This represents a reduction in drying time of more than 90 %, highlighting the substantial potential for increasing production throughput, as long as the electrode properties remain unaffected.

The present investigation addresses two central aspects: the influence of particle size and the effect of very high drying rate on the resulting electrode microstructure. Theoretical considerations for monodisperse spherical packings suggest that macroscopic structural parameters such as porosity are independent of particle size. However, real electrode systems deviate from this idealization due to particle-size distribution, irregular particle shapes and interparticle interactions (e.g., agglomeration). Consequently, no general prediction of porosity as a function of particle size can be made.

Table 4.2 summarizes the dry film thickness, areal mass loading, and electrode porosity of HC electrodes. The geometric porosity was calculated from the areal mass loading, the density of the dry mixture, and dry film thickness and was validated by mercury intrusion porosimetry (Appendix 11.5.3).[kl] The values listed in Table 4.2 represent the mean values derived from all electrodes produced across the investigated drying-rate range. As shown in Appendix 11.5.3, the porosity of the electrodes and the pore-size distribution do not change by drying with increasing drying rate.

[k] The data reveals a significant deviation, which can be attributed to the presence of closed pores in the active material.[122] These findings are further supported by the observation of SEM cross-sectional images (see Appendix 11.5.3).
[l] In the context of monodisperse spherical packings, it can be deduced from geometric principles that porosity is independent of particle size. The ratio of sphere volume to intersphere space remains constant when the sizes of the spheres are scaled.

Table 4.2: Dry film thickness, areal mass loading, and electrode porosity of non-calendered HC electrodes. The electrode thickness was kept approximately constant to exclude thickness effects on binder migration.[82,91] Values represent averages over all electrodes produced at drying rates of 0.75 to 9 g $m^{-2}s^{-1}$.

| Name | Dry film thickness / µm | Areal mass loading / g $m^{-2}$ | Electrode porosity / % |
|---|---|---|---|
| HC-A | 93 ± 1 | 84 ± 1 | 52 ± 1 |
| HC-B | 93 ± 1 | 80 ± 1 | 56 ± 1 |
| HC-C | 94 ± 1 | 79 ± 1 | 58 ± 1 |

In contrast, the results in Table 4.2 reveal a clear increase in electrode porosity with increasing particle size. SEM cross-sectional images of the HC electrodes (Figure 4.4) further issultrate these differences: HC-A forms a dense packing with small pores, whereas the larger particles of HC-B and HC-C lead to increasingly larger pores and higher porosity.

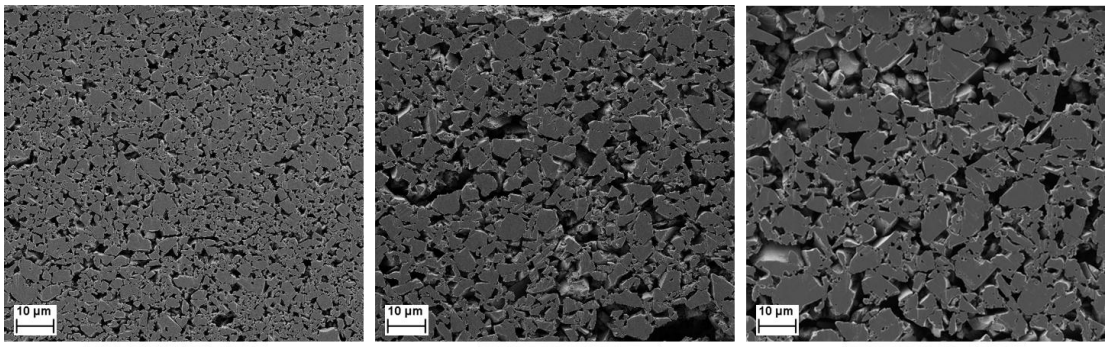


Figure 4.4: SEM cross-sectional images of HC-A, HC-B, and HC-C elelctrodes prepared with systematically increasing active material particle size under otherwise identical processing conditions. All electrodes were fabricated using the same electrode composition, solid content, and mixing procedure. The images illustrate the effect of systematically increasing particle size on electrode microstructure. While HC-A forms a dense packing with small pores, HC-B and HC-C exhibit increasingly larger pores and higher porosity. The pore size distribution is given in Appendix 11.5.3.

The microstructural analysis confirms that the electrode microstructure is primarily governed byparticle morphology, while the drying rate does not lead to significant structural changes in porosity or pore-size distribution.

Previous studies have suggested that variations in porosity or pore size of battery electrodes influence the onset of pore emptying and thus the extent of binder migration during drying.[69,81] However, the results presented in Section 3.2.4 demonstrate that this hypothesis cannot be generalized across different active material systems. The pore-breakthrough process was shown to occur simultaneously with the end of film shrinkage and to be independent of the active material used.

This finding is corroborated by the comparative evaluation of HC electrodes with different particle sizes presented in the Appendix 11.5.4. Although pronounced differences in microstructure are observed, no corresponding shift in pore-emptying behavior is detected.

Consequently, these results indicate that particle size-induced microstructural differences do not directly control the onset of pore emptying and therefore cannot fully account for binder migration effects. This separation of microstructural and transport-related phanomena enables a focused investigation of binder migration depending on particle size of the active material, which is given in the following section.

### 4.2.4 Binder Migration: Influence of Particle Size, Drying Rate and Film Temperature

In this section, binder migration is analyzed using adhesion strength measurements, which provide a quantitative measure of particle-size-dependent binder redistribution in the dried electrodes.[60,65,91] The objective is to evaluate the sensitivity of different active material systems to binder migration as a function of drying rate and particle size, and to establish a link to the previously discussed rheological behavior.

Previous investigations (Section 3.2.5) indicated that HC-C electrodes did not exhibit detectable binder migration within a limited drying-rate range. This observation led to the hypothesis that a reduced sensitivity to binder migration reflects stronger binder fixation within the evolving electrode microstructure. If this assumption holds, substantially higher drying rates should be required to overcome this binder immobilization and induce migration. Therefore, HC-based slurries are dried at significantly increased drying rates in the present study.

The drying conditions were precisely controlled to enable a systematic investigation of drying-rate effects. The drying rate was adjusted by varying the temperature of the heated plate and the drying air, while maintaining a constant heat-transfer coefficient of the slot nozzle dryer. The dew point of the drying air was monitored to ensure comparable drying conditions across all experiments. An overview of the applied drying rates and corresponding drying temperatures is provided in Table 4.3. Further experimental details on the drying setup are given in Section 2.3.1.

Table 4.3: Overview of the applied drying rates and corresponding drying temperatues at a constant heat-transfer coefficient of 35 W $m^{-2}K^{-1}$. The dew point of the supplied air ranged from 9 to 13 °C and was taken into account when setting the drying temperature for each electrode fabrication.

| Drying rate / g $m^{-2}s^{-1}$ | Film temperature / °C |
|---|---|
| 0.75 | 31 |
| 1.5 | 40 |
| 3 | 51 |
| 6 | 63 |
| 9 | 70 |

The analysis of the adhesion strength depending on the drying rate first focuses on HC-C electrodes, with graphite electrodes included for comparison (Figure 4.5). Adhesion strength values are normalized to reference values of 9 N $m^{-1}$ for HC-C and 14 N $m^{-1}$ for graphite[91].

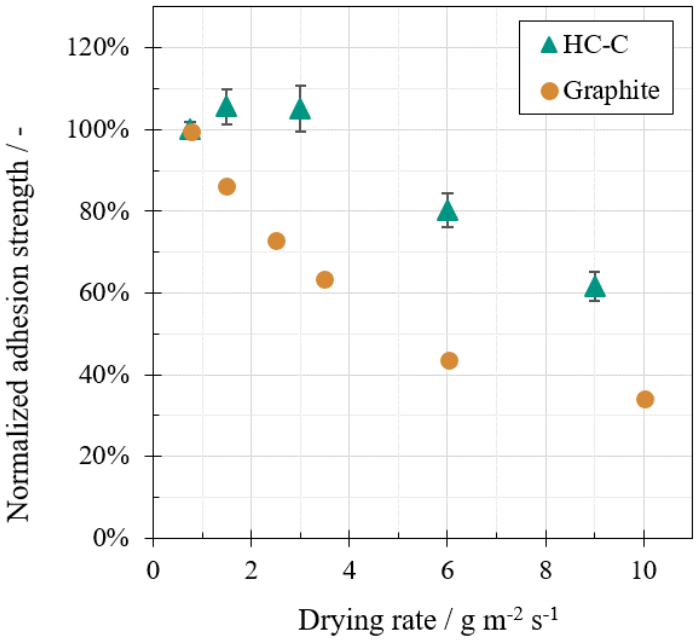


Figure 4.5: Normalized adhesion strength as a function of drying rate for HC-C and graphite electrodes at a constant heat transfer coefficients of 35 W $m^{-2}K^{-1}$. The drying rate was varied by adjusting the isothermal drying temperature. Graphite electrode data is taken from the literature.[91] Both graphite and HC-C electrodes exhibit a decrease in adhesion strength with increasing drying rate, indicating binder migration under accelerated drying conditions. HC-C electrodes show a delayed onset of adhesion degradation, indicating a moderate resistance to binder migration compared to graphite.

Both graphite and HC-C electrodes show a decrease in adhesion strength with increasing drying rate, indicating the occurrence of binder migration under accelerated drying conditions. For graphite electrodes, this reduction occurs already at comparatively low drying rates, reflecting a high sensitivity to capillary-driven binder transport. At higher drying

rates, the decline in adhesion strength becomes less pronounced, suggesting that a fraction of the binder remains immobilized and cannot be detached by further increases in capillary transport. This behavior can be interpreted as an effective depletion of mobile binder in the lower regions of the electrode, such that further increases in drying rate no longer lead to additional binder redistribution. Consequently, the system approaches a limiting state in which the remaining binder is either immobilized within the network structure or has already been transported away from the substrate-near region.

In contrast, HC-C electrodes exhibit a delayed onset of adhesion strength degradation, with binder migration occuring only at higher drying rates. For moderate drying rates up to approximately 3 g $m^{-2}s^{-1}$, no negative influence on the adhesion strength can be observed. Only at higher drying rates does capillary transport become sufficient to mobilize the SBR binder. Despite the liquid-like rhelogical behavior of HC-C slurry, this response indicates a moderate resistance to binder migration compared to graphite, likely arising from differences in particle size and binder-particle interactions.

Subsequently, the influence of particle size is examined by comparing HC-A, HC-B, and HC-C electrodes. Figure 4.6 shows the adhesion strength as a function of drying rate for all HC variants and graphite[91]. Adhesion strength values are normalized to reference values of 9 N $m^{-1}$ for all HC electrodes and 14 N $m^{-1}$ for graphite[91]. The absolute adhesion strength of the HC electrodes shows no dependence on particle size.

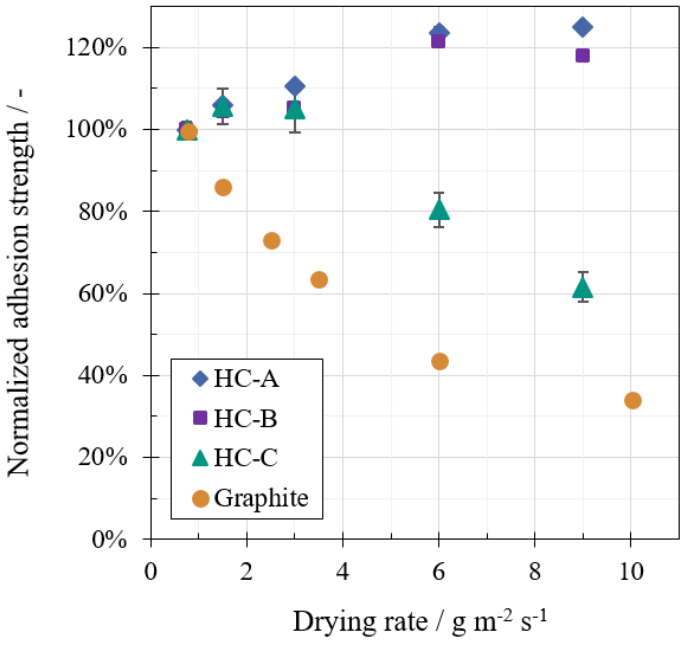


Figure 4.6: Normalized adhesion strength as a function of drying rate for graphite and HC-based electrodes at a constant heat transfer coefficients of 35 W $m^{-2}K^{-1}$. The drying rate was varied by adjusting the isothermal drying temperature. Graphite electrode data are taken from the literature.[91] HC-A and HC-B electrodes exhibit no reduction in adhesion strength over the investigated drying-rate range, demonstrating that a reduction in active material particle size effectively suppressed binder migration and shifts its onset to higher drying rates.

A fundamentally different behavior is observed for HC-A and HC-B electrodes. Despite increasing drying rates, no reduction in adhesion strength is detected. This confirms the hypothesis that reducing particle size suppresses binder migration and shifts its onset to significantly higher drying rates.

This finding is consistent with the gel-like rheological behavior observed for HC-A and HC-B slurries. Smaller partilce sizes promote the formation of a highly interconnected CMC network through increased particle-polymer contact points, resulting in enhanced polymer bridging and mechanical stabilization of the binder phase. Consequently, capillary-driven binder transport during drying is effectively restricted, even at elevated drying rates, enabling a broader drying process window without compromising adhesion strength.

Active material particle morphology governs slurry rheology and network formation, which in turn determine the sensitivity of the electrode to drying-induced capillary transport and binder migration. While gel-like rheology is an indicator of structural stabilization, the results also show that rheological descriptors alone cannot predict binder migration at a given drying rate, as they compete with the magnitude of capillary forces induced during drying.

Additional experiments shown in Appendix 11.5.5 using PVDF as binder demonstrate that binder migration occurs for both HC-A and HC-C at increased drying rates, confirming that the suppression of binder migration observed for HC-A (and HC-B) is specific to the water-based CMC/SBR binder system. This highlights the critical role of the combined interaction between drying rate, particle size, CMC, and SBR in stabilizing and suppression of binder migration.

As dicussed previously, adhesion strength measurements provide a quantitative measure of binder redistribution in dried electrodes. To further substantate these findings, impedance measurements under blocking conditions were performed. The impedance results confirm the trends observed in the adhesion strength measurements (see Appendix 11.5.7). Changes in ionic transport resistance reflect changes in the binder distribution associated with the presence or suppression of binder migration. The combined analysis of adhesion strength and impedance measurements establishes, for the first time, a direct correlation between mechanical adhesion and ionic resistance for water-based-processed electrodes as a function of drying rate. This correlation provides independent evidence for drying-induced binder migration or its suppression and highlights impedance spectroscopy as a complementary tool for assessing microstructural changes induced during electrode drying. Beyond binder migration, the impedance spectroscopy results also reveal a particle-size-dependent effect on ionic transport. Electrodes based on smaller particles exhibit lower ionic resistance, which can be attributed to an increased number of pores and available ion transport pathways. However, the higher specific surface area generally also promotes irreversible ion consumption during SEI formation.[121] Accordingly, HC-A electrodes with smaller particle size exhibit a higher capacity loss during formation compared to HC-C electrodes (see Appendix 11.5.9). To exploit the advantages of reduced binder migration in

CMC/SBR-based electrodes and improved fast drying capability while mitigating the adverse effects of increased surface area, processing of HC multilayer electrode architecturs were investigated (see Appendix 11.5.8). This approach reduces the overall active material surface area while preserving the favorable drying behavior and suppressing binder migration under elevated drying rates.

In summary, the overall findings establish a comprehensive material-microstructure-process-property relationship for water-based electrode processing. This highlights the importance of tailoring active material properties and electrode architecture for achieving robust, high-throughput electrode fabrication under fast-drying conditions.

Notably, HC-A and HC-B electrodes show in Figure 4.6 an increase in adhesion strength with increasing drying rate, indicating an additional mechanism related to film temperature during drying. Higher drying rates are accompanied by elevated film temperatures (see Table 4.3), which may enhance the interaction between CMC and the active material during the drying process[17], and potentially also affect the interaction with the SBR binder. The following section focuses on the role of film temperature during drying depending on the active material particle size.

**Influence of Film Temperature During Drying**

Previous studies on graphite anodes have shown that higher temperatures and low heat transfer coefficient during isothermal drying can have positive effect on adhesion strength.[89,91,121] This effect has not previously been reported for electrodes exhibiting suppressed binder migration and is therefore investigated. The film temperature of the drying slurry was systematically adjusted by varying the heat and mass transfer coefficients, while maintaining the same overall drying rate. Figure 4.7 shows the different temperatures as a function of the drying rate for different applied heat transfer coefficients.

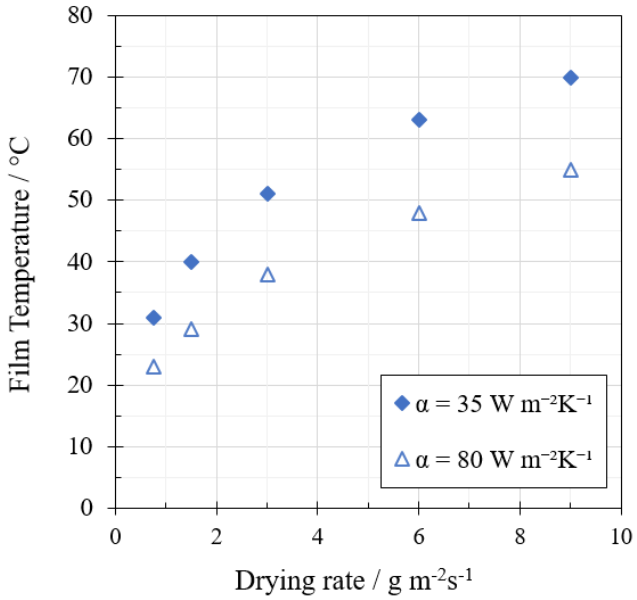


Figure 4.7: Overview of the applied drying rates and corresponding drying temperatures for constant heat transfer coefficients of 35 W $m^{-2}K^{-1}$ and 80 W $m^{-2}K^{-1}$. The dew point of the supplied drying air ranged from 9 to 13 °C and was considered when adjusting the drying temperatures for each electrode fabrication.

The figure indicates a variation in film temperature of more than 10 °C at identical drying rates. Figure 4.8 shows the effect of changing film temperature at identical drying rates on adhesion strength, comparing HC-A, HC-C and graphite electrodes[91].

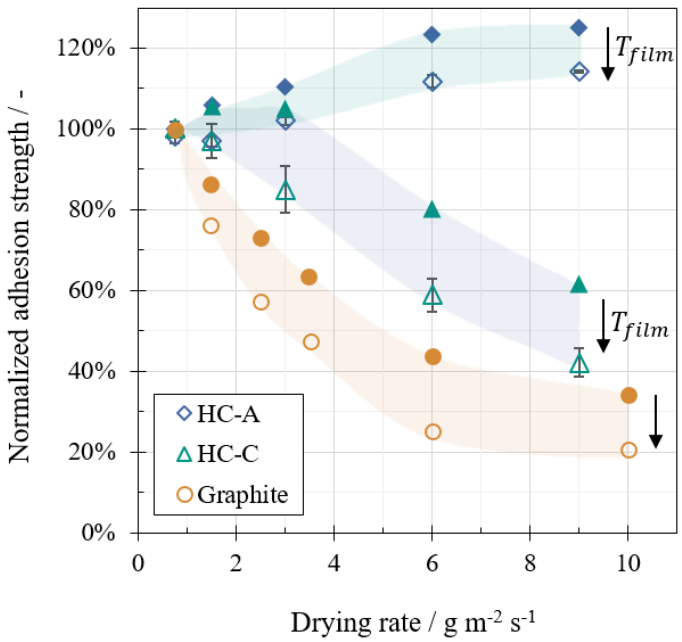


Figure 4.8: Effect of film temperature on adhesion strength at identical drying rates for graphite[91] and HC electrodes. A systematic reduction in adhesion strength is observed at lower film temperatures for all electrodes. Notably, HC-C electrodes no longer exhibit the previously observed suppression of binder migration at reduced film temperatures, with adhesion strength decreasing already at moderate drying rates. This demonstrates that binder migration resistance is not solely governed by drying rate and active material particle characteristics, but is strongly influenced by film temperature during drying.

A systematic reduction in adhesion strength is observed at lower film temperatures for all electrodes. Particularly noteworthy is the behavior of HC-C electrodes, which no longer exhibit the previously observed suppression of binder migration when dried at comparatively lower film temperatures within the investigated drying-rate range. Under these conditions, a decrease in adhesion strength occurs already at moderate drying rates, indicating that the resistance to binder migration is not exclusively governed by drying rate and the influence of the particle system or particle morphology on the interaction with the binder system, but is strongly influenced by film temperature. This finding emphasizes the role of temperature-dependent interactions in controlling binder fixation during electrode drying.

To exclude annealing effects as a potential cause of the increased adhesion strength observed at higher film temperatures, HC-A and HC-C electrodes were subjected to post-drying annealing at different temperatures and subsequently characterized (Appendix 11.5.4). These results demonstrate that the observed increase in adhesion strength cannot be attributed to annealing.

Consequently, the results in Figure 4.8 demonstrate that the film temperature during drying represents an independent and critical process parameter. In addition to capillary transport induced by drying rate, temperature-dependent interactions during drying significantly influence binder mobility and adhesion development. Importantly, these temperature effects

are observed regardless of whether binder migration occurs or is suppressed, highlighting the distinct and yet complementary roles of drying rate and film temperature in electrode processing.

## 4.3 Conclusion

The electrode processing of HC particles with different particle sizes was systematically investigated at varying drying rates and comparatively analyzed with graphite electrodes reported in the literature under comparable conditions, including electrode compositions, slurry preparations, electrode fabrication, and drying conditions.

The results demonstrate that binder migration during electrode drying is governed by a coupled material-microstructure-process-property relationship. Adhesion strength measurements reveal that graphite electrodes are highly sensitive to drying-rate-induced binder migration, while HC-C electrodes exhibit a delayed onset of adhesion loss, indicating a moderate resistance to capillary-driven binder transport. In contrast, HC-A and HC-B electrodes show no degradation in adhesion strength over a wide range of drying rates, demonstrating that binder migration can be effectively suppressed by reducing active material particle size for CMC/SBR-based electrodes. This behavior is directly linked to the gel-like rheology of the corresponding slurries, which arises from enhanced particle-polymer interactions and the formation of a highly interconnected CMC network in the water-based CMC/SBR binder system.

However, the study also shows that rheological descriptors alone are insufficient to predict binder migration at a given drying rate. Binder transport results from the competition between the drying-rate-induced capillary driving force and binder immobilization within the evolving microstructure.

In addition to drying rate, the film temperature during drying was identified as a key process parameter. Independent of material system and particle size, higher film temperatures lead to increased adhesion strength at identical drying rates. This effect may be attributed to improved binder fixation to both the active material and the current collector and is not related to annealing phenomena. These findings suggest that temperature-controlled drying strategies may provide an additional lever to enhance electrode adhesion without promoting binder migration.

Impedance measurements under blocking conditions further confirm the trends observed by adhesion strength results. Variations in ionic transport resistance or electrical tortuosity reflect the presence or suppression of binder migration. For the first time, a direct correlation between adhesion strength and ionic resistance during the processing of water-based slurry as a function of drying rate could be demonstrated.

Overall, the results of this work show that tailoring active material particle size and binder-particle interactions enables a significant extension of the drying process window without

compromising adhesion strength. These findings provide a mechanistic basis for the robust processing of water-based battery electrodes under fast-drying conditions and highlight the importance of integrating material design with process optimization.

Future investigations should focus on quantitatively linking the relationship between CMC network formation and SBR affinity to this network to enable predictive descriptions of binder migration. In addition, it is also recommended to investigate radiation-based drying methods to achieve higher film temperatures during drying and further enhance electrode adhesion in industrial roll-to-roll production.

# 5 Porous, Nanostructured Cathodes: Microstructure Development

Post-lithium batteries are attracting increasing interest as low-cost and sustainable alternatives to LIBs and represent a promising application field for porous, nanostructured, and hierarchically structured active materials. Due to the larger ionic radii of post-lithium charge carriers, intercalation and deintercalation processes induce increased mechanical stresses within the active material. In addition, multivalent ions typically exhibit low diffusion coefficients, limiting their penetration depth into bulk materials. Consequently, nanoscale and hierarchically structured particles are required to achieve high energy densities and sufficient cycle life, thereby representing a viable pathway towards the commercial implementation of postl-lithium systems.[43]

Porous, nanostructured particle morphologies are therefore a targeted strategy to enhance the long-term stability and electrochemical performance of both LIB and SIB systems. However, these morphologies introduces new challenges at the electrode level, most notably reduced adhesion strength to the current collector and a decrease in volumetric energy density.[109]

Nanostructured particles with accessible porosity have been shown to significantly enhance both durability and fast-charging capability. Accordingly, such morphologies are widely employed not only in LIB cathode materials, such as NCM and LFP, but especially in post-lithium battery systems, including SIB cathodes based on NVP or layered oxides. The performance enhancement is primarly attributed to an enlarged electrolyte-active material interface and shortened diffusion paths within the particles. Furthermore, the porous structure architecture reduces mechanical stresses during intercalation and deintercalation, thereby improving cycle stability.[12]

Despite these advantages, the electrode processing of porous active materials differs from that of compact particles, particularly when using PVDF as binder and NMP as solvent. A

systematic understanding of the resulting processing-related effects is therefore essential for the successful implementation of porous particles in practical battery electrodes.[mno]

To exploit the full potential of porous particles for SIBs and other post-lithium batteries, it is therefore necessary to systematically investigate their processing behavior and to understand component redistribution during drying in comparison to compact particles. In this work, the relationship between drying conditions and binder distribution is analyzed by combining adhesion strength measurements, component distribution characterization, and electrochemical testing. Based on these results, the existing understanding of electrode drying mechanisms is extended to explicitly account for the influence of porous active materials and summarized in the form of a sequential drying mechanism.

## 5.1 Motivation and State of the Art

Unlike compact particles, porous active materials enable ion transport not only via solid-state diffusion within the active material but also through the electrolyte-filled pore network inside the particles. This distinction is partciluarly relevant when considering diffusion kinetics. For example, lithium-ion diffusion in NCM occurs at diffusion coefficients on the order of $10^{-10}$ - $10^{-11}$ $cm^2$ $s^{-1}$,[45,123] whereas ion transport in typical battery electrolytes such as LP30 reaches approximately $10^{-6}$ $cm^2$ $s^{-1}$ [124,125]. The presence of electrolyte-filled pores therefore significantly enhances effective ion transport within porous particles.

Porous particle morphologies can be generated either by top-down or bottom-up approaches. Using a top-down strategy, Wagner et al.[44] optimized NCM111 by milling the compact material to a primary particles size of approximately 450 nm, followed by spray drying and calcination to form porous secondary particles. By tailoring the particle morphology, the fast-charging capability was increased from 20 mAh $g^{-1}$ for the original active material to 100 mAh $g^{-1}$ at a C-rate of 5C.

[m] The results and discussion in this chapter are part from the following publication by the author:[18]
Klemens, J.; Schneider, L.; Herbst, E. C.; Bohn, N.; Müller, M.; Bauer, W.; Scharfer, P.; Schabel, W. Drying of NCM Cathode Electrodes with Porous, Nanostructured Particles Versus Compact Solid Particles: Comparative Study of Binder Migration as a Function of Drying Conditions. *Energy Technology* **2022**, 2100985. https://doi.org/10.1002/ente.202100985.

[n] A collaborative publication followed, investigating the ionic transport properties:[45]
Schneider, L.; Klemens, J.; Herbst, E. C.; Müller, M.; Scharfer, P.; Schabel, W.; Bauer, W.; Ehrenberg, H. Transport Properties in Electrodes for Lithium-Ion Batteries: Comparison of Compact versus Porous NCM Particles. *J. Electrochem. Soc.* **2022**, *169* (10), 100553. https://doi.org/10.1149/1945-7111/ac9c37.

[o] Results on material production, electrode processing, characterization and an outlook on post-lithium systems were summarized in an article:[43]
Bauer, W.; Müller, M.; Schneider, L.; Häringer, M.; Bohn, N.; Binder, J. R.; Klemens, J.; Scharfer, P.; Schabel, W.; Ehrenberg, H. Using Hierarchically Structured, Nanoporous Particles as Building Blocks for NCM111 Cathodes. *Nanomaterials* **2024**, *14* (2), 134. https://doi.org/10.3390/nano14020134.

While the electrochemical benefits of porous particles are well reported in the literature, their impact on electrode processing has received considerably less attention. Müller et al.[109] demonstrated that electrodes composed of porous NCM exhibit significantly reduced adhesion strength. This reduction was attributed to the penetration of binder into the porous secondary particles. As a result, the binder is no longer fully available for adhesion at the electrode-current collector interface. It has been demonstrated that adhesion strength can be increased by increasing the binder content and calendering the electrodes. The binder that infiltrated the particles holds them together, even if cracks form in the porous secondary particles during calendering. Therefore, the particles exhibit quasi-plastic deformation behavior.[43]

Despite these observations, the effect of binder penetration during slurry production and the resulting drying behavior and component redistribution have not been systematically investigated.[18]

Within the POLiS research cluster, these findings motivated the investigation of SIB cathode materials with optimized particle morphologies. In particular, NVP exhibits low intrinsic electronic conductivity, requiring either particle size reduction or the incorporation of conductive carbon networks within the particle structure. Hierarchically structured particles provide a promising route to combine both strategies within a single material system. Due to ongoing optimization of NVP synthesis and limited material availability, NCM was selected as a model system in this thesis, enabling a direct and controlled comparison between compact and porous particle morphologies.

This work therefore focuses on the processing, drying, and binder migration behavior of porous, nanostructured cathode particles relative to compact particles. A solvent-based PVDF binder system is employed throughout the study. It is hypothesized that during slurry preparation, both the solvent and the dissolved binder infiltrate the internal pore structure of the porous particles and remain there during drying. As a consequence, the effective binder concentration near the electrode–current collector interface is reduced, leading to decreased adhesion strength and fundamentally altered drying behavior.

Prior to the author's study, it was unknown how particle morphology and the penetration of the solvent-binder solution into the particles affect the processing of slurry and drying behavior at higher drying rates. The aim of this investigation is to determine the differences in processing between the use of compact and porous particles and to expand the mechanism of drying and microstructure formation taking into account particle morphology.

## 5.2 Results and Discussion

The comparative investigations presented in this chapter were conducted under strictly controlled and identical processing conditions to isolate the influence of particle morphology. Mixing procedures, electrode compositions, and drying parameters were kept constant

throughout the investigations. This experimental approach enables the identification of both universal correlations and material-specific effects. The comparative results are structured along four central aspects of electrode manufacturing. First aim is the investigation of the two different particle structures to link the particle properties with the latter processing and drying behavior. Second, the influence of the open porosity of the active material on slurry viscosity behavior is examined. Third, the binder migration behavior is investigated using adhesion strength, electrical resistivity, electrochemical tests, and visualization method to show the effect of binder redistribution during drying. Fourth, the investigations are summariezed and implement an additional understanding of material-dependent drying mechanisms. This structure enables a coherent interpretation of the comparative results and supports the derivation of material-process-microstructure-property relationships.

### 5.2.1 Particle Properties

For the systematic comparison of compact and porous, nanostructured particles with respect to electrode processing and binder migration behavior, NCM111 was selected as cathode material. A porous, nanostructured variant NCM-porous was derived from the compact reference material NCM-compact in order to isolate the influence of particle morphology while maintaining identical chemical composition.

The porous NCM111 particles were prepared by the Institute for Applied Materials at the KIT following a top-down approach as described by Wagner et al.[44]. The compact starting material was first milled in a stirred ball mill to achieve an average primary particle size of approximately 297 nm. The resulting suspension was subsequently processed by spray drying to form spherical secondary particles. To enhance mechanical stability and establish a defined internal pore structure, the spray-dried particles were calcined in hot air at 850 °C for 5 h, during which partial sintering of the primary particles occurred.

Figure 5.1 illustrates the morphological differences between compact and porous NCM111 particles.

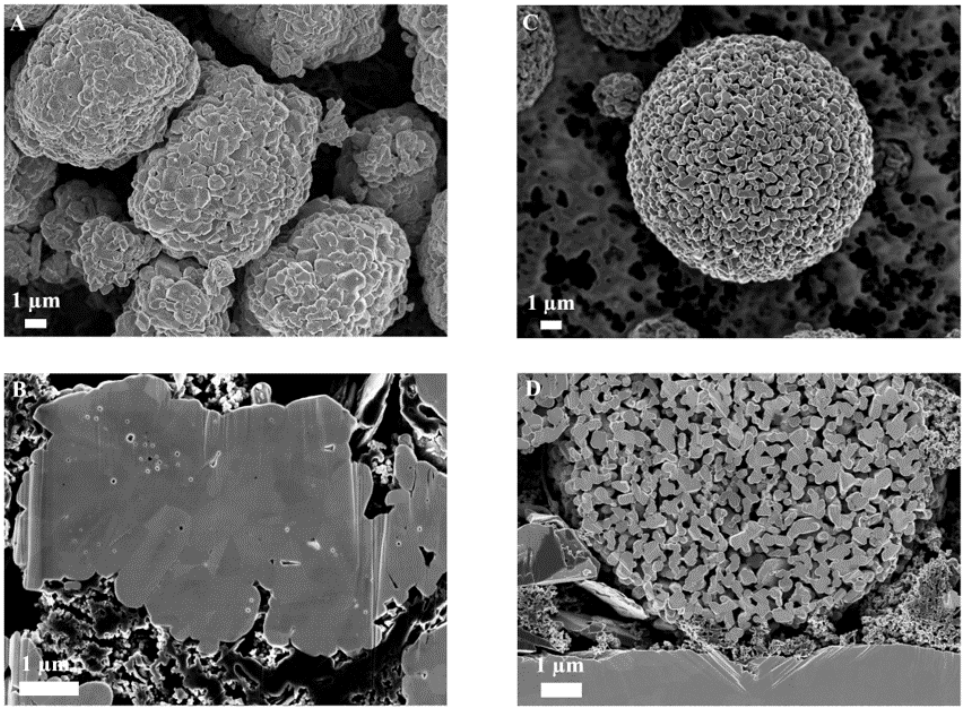


Figure 5.1: SEM images of the secondary particles of the compact NCM (A, B) and the porous NCM (C, D). For the compact NCM, the secondary particles are granular and have a rough surface. In addition, they show a compact structure in which the primary particles (crystal grains) are hardly recognizable. The porous NCM shows an internally accessible porosity and the particles have a rounded shape due to the spray drying process.

While both particle systems exhibit comparable secondary particle sizes and similar particle densities, the internal structure differs fundamentally. The porous secondary particles exhibit an open internal pore network with an intraparticle porosity of approximately 48 %. This internal porosity leads to a substantial increase in the specific surface area from 0.4 $m^2 g^{-1}$ for NCM-compact to 2.9 $m^2 g^{-1}$, corresponding to an increase by a factor of 7.25. Despite this pronounced difference in internal structure, the particle density determined by gas pycnometry remains within the same order of magnitude for both materials, indicating that the post-treatment primarily affects the internal microstructure rather than the macroscopic particle dimensions. An overview of the relevant particle parameters is provided in Table 5.1.

Table 5.1: Overview of the particle parameters of NCM111 with compact or porous particles.

| | Mean particle diameter / µm | BET surface area / $m^2 g^{-1}$ | Density / $kg m^{-3}$ | Secondary particle porosity / % |
|---|---|---|---|---|
| NCM111 compact | 7 | 0.4 | 4520 | - |
| NCM111 porous | 10 | 2.9 | 4700 | 48 |

The comparable particle size and density ensure that differences observed during slurry preparation, drying, and electrode performance can be attributed predominantly to the presence of intraparticle porosity rather than to geometric or compositional effects.

To enable interpretation of the subsequent drying behavior and binder migration results, it is essential to consider the implications of this internal porosity for slurry processing. If the solvent penetrates into the intraparticle pore network during slurry preparation, the effective free solvent volume in the surrounding slurry phase is reduced. Consequently, the effective solids volume fraction increases, which is expected to directly affect slurry viscosity and flow behavior. Moreover, since the PVDF binder is dissolved in the solvent, binder infiltration into the porous particles is inherently coupled to solvent penetration. This effect forms the basis for the hypotheses regarding altered drying behavior and binder immobilization discussed in the following sections.

The internal porosity and surface characteristics of the particles are expected to directly influence slurry rheology through solvent uptake and increased particle–particle interactions. Therefore, the effect of particle morphology on slurry viscosity is examined in the following section.

### 5.2.2 Slurry Viscosity Profile

To assess the influence of particle morphology on slurry processing, cathode slurries containing either compact (NCM-C) or porous (NCM-P) active material particles were prepared using identical compositions, mixing procedures, and solid contents of 51 wt-%. The rheological behavior of the slurries was characterized over a wide shear rate range in order to identify morphology-induced differences relevant for coating and drying (see Figure 5.2).

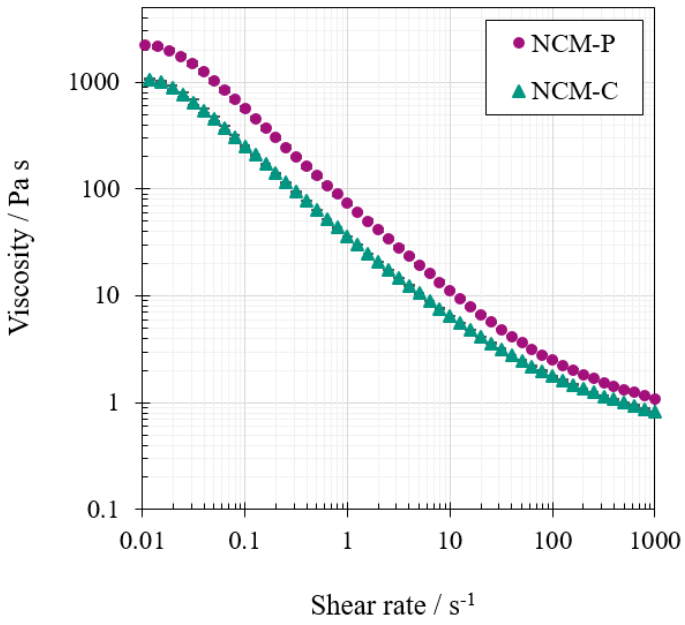


Figure 5.2: Viscosity profile as a function of the shear rate for NCM-C with compact particles and NCM-P slurry with porous nanostructured particles. Due to the morphology of the NCM-P particles, the viscosity increases throughout the entire range of shear rate.

Both slurries exhibit pronounced shear-thinning behavior, which is characteristic for battery slurries. At low shear rates (0.01 $s^{-1}$), the viscosity of the slurry containing porous particles is significantly higher (2203 ± 54 Pa s) than that of the slurry with compact particles (1060 ± 8 Pa s). With increasing shear rate, the viscosities of both systems decrease and approach each other; however, even at high shear rates of 1000 $s^{-1}$, the viscosity of the NCM-P slurry remains approximately 30 % higher.

Since the particle size distributions and solid contents are comparable, the observed viscosity increase must originate from differences in particle morphology. The porous NCM-P particles possess a substantially larger specific surface area and an internal pore volume of approximately 47 %, which enables capillary infiltration of the solvent during slurry preparation. As a consequence, part of the solvent is immobilized within the intraparticle pores, effectively increasing the solids volume fraction in the surrounding slurry phase. Due to the porosity of the particles of almost 50 %, the relevant volume fraction of the active material in the slurry increases by a factor of about two. This leads to enhanced particle-particle interactions and increased internal friction, thereby increasing slurry viscosity across the entire shear rate range.

SEM cross-sectional images of dried electrodes further confirm the presence of PVDF-binder bridges within the porous secondary particles, supporting that the solvent-binder solution penetrates the intraparticle pore network during slurry preparation (see Figure 5.3).

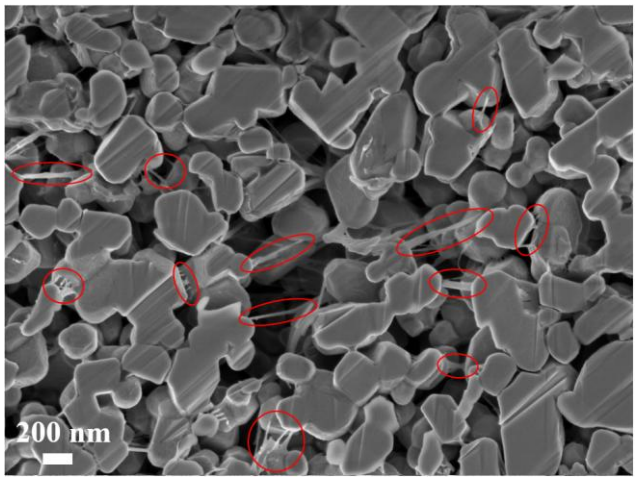


Figure 5.3: SEM cross-sectional image of a NCM-P particle in a dried electrode. PVDF fibers and bridges between the primary particles are visible. The binder causes additional crosslinking between the primary particles.

Since the binder is dissolved in the solvent, it is also assumed that the binder concentration in the pores of the particles and in the pore network between the particles is the same at the beginning of drying and corresponds to the initial slurry concentration.

To get an impression of the different porosity areas in electrodes containing porous particles and to link the electrode properties with the binder migration behavior, the following section investigates the differences in electrode microstructure between NCM-C and NCM-P electrodes.

### 5.2.3 Electrode Microstructure

To investigate the influence of particle morphology on electrode microstructure formation during drying, electrodes containing either NCM-C or NCM-P particles were prepared under identical processing conditions. The drying rate was systematically varied in the range between 0.75 and 3.5 g $m^{-2}s^{-1}$ using isothermal drying conditions. In order to achieve a maximum drying rate (see Section 2.3.1), the investigations were carried out at a heat transfer coefficient of 80 W $m^{-2}K^{-1}$.

Table 5.2 shows the characteristics of electrodes containing either compact particles or porous particles as active material.

Table 5.2: Dry film thickness, areal mass loading, and electrode porosity of non-calendered NCM electrodes made with compact (NCM-C) or porous (NCM-P) particles.

| Name | Dry film thickness / µm | Areal mass loading / g $m^{-2}$ | Electrode porosity / % |
|---|---|---|---|
| NCM-C | 78 ± 1 | 154 ± 4 | 51 ± 1 |
| NCM-P | 80 ± 3 | 105 ± 4 | 68 ± 1 |

Electrodes containing porous particles exhibit a significantly higher overall porosity compared to those with compact particles, which negatively affects volumetric energy density. This topic is addressed in Chapter 6 and optimized through the use of multilayer architectures.

SEM cross-sectional images of electrodes with either compact or porous active material particles are shown in Figure 5.4.

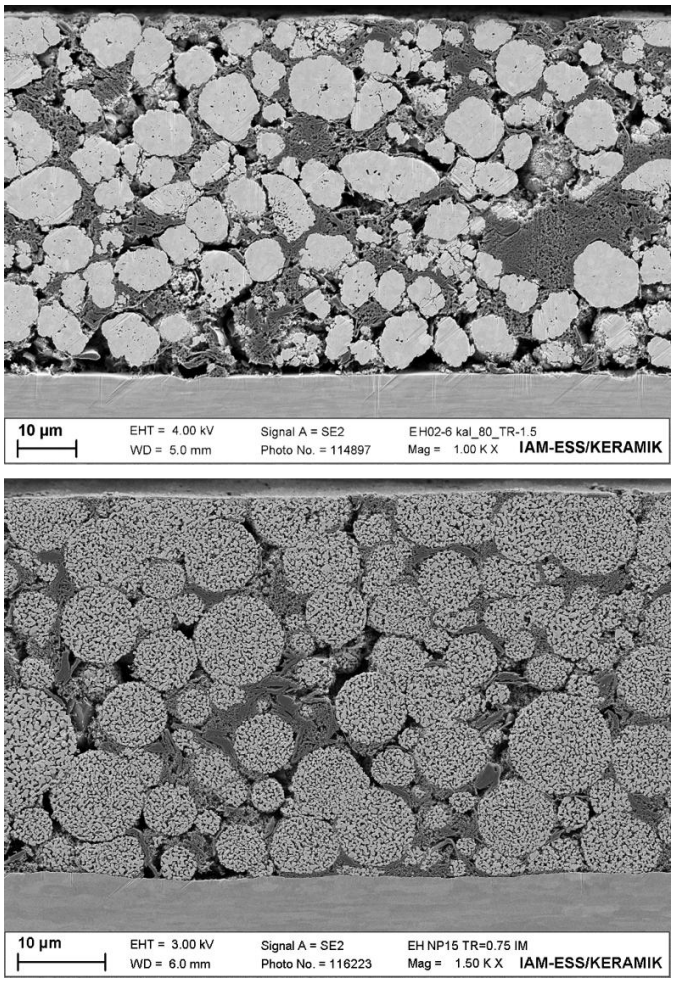


Figure 5.4: SEM cross-sectional image of dry electrodes with compact (upper image) or porous, nanostructured (lower image) particles.

Cross-sectional SEM images reveal that the porous particles form a highly open microstructure with both interparticle pores and intraparticle pores contributing to the total porosity. Given the pronounced differences in pore structure and solvent retention, the presence of intraparticle porosity is expected to alter binder mobility during drying. The following section therefore focuses on binder migration as a function of particle morphology and drying rate.

### 5.2.4 Binder Migration

Binder migration during the drying process was investigated using a combination of adhesion strength measurements, electrical resistivity analysis, and electrochemical characterization. In addition, visualization of the fluorine distribution as a marker for the PVDF binder enables a direct assessment of the spatially resolved component distribution. The objective of these investigations is to establish a relationship between the previously discussed penetration of solvent and binder into the particles and binder migration as a function of the drying rate.

The drying conditions were systematically varied to investigate the influence of the drying rate in a controlled manner. The drying rate was adjusted by modifying the temperature of the heated plate and the drying air, while maintaining a constant heat-transfer coefficient of the slot nozzle dryer. As discussed in the experimental section, the use of NMP as a solvent resulted in different drying temperatures compared to water-based slurries. An overview of the applied drying rates and corresponding drying temperatures is provided in Table 5.3, and further details on the experimental setup are given in Section 2.3.1.

Table 5.3: Overview of the applied drying rates and corresponding drying temperatues at a constant heat-transfer coefficient of 80 W $m^{-2}K^{-1}$.

| Drying rate / g $m^{-2}s^{-1}$ | Film temperature / °C |
|---|---|
| 0.75 | 61 |
| 1.50 | 73 |
| 1.70 | 75 |
| 2.00 | 79 |
| 3.50 | 85 |

Figure 5.5 shows the relationship between adhesion strength and drying rate for electrodes composed of either porous or compact particles.

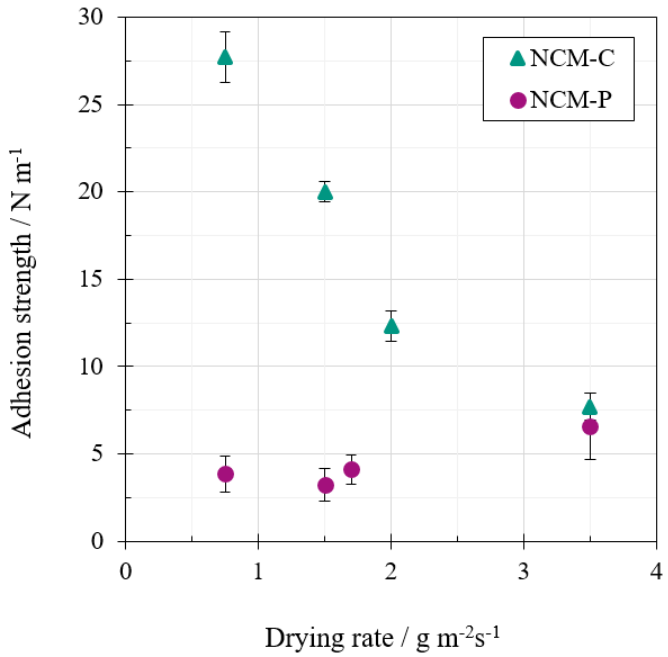


Figure 5.5: Adhesion strength as a function of the drying rate for NCM-C and NCM-P electrodes. As expected, NCM-C electrodes show a decrease in adhesion strength with increasing drying rate, indicating binder migration. NCM-P electrodes show rather low adhesion strength and, surprisingly, no further decrease for higher drying rates. The particle morphology influences the binder migration behavior.

For electrodes containing compact particles, adhesion strength decreases strongly with increasing drying rate, with an overall reduction of approximately 72 % over the investigated range. This behavior is consistent with drying-rate-induced binder migration towards the electrode surface, resulting in binder depletion near the current collector. In contrast, electrodes containing porous particles exhibit a significantly lower adhesion strength overall, but show only a weak dependence on drying rate. This indicates that a substantial fraction of the binder is immobilized within the intraparticle pores and does not participate in capillary-driven transport during drying.

The nearly constant adhesion strength across the investigated drying rates indicates altered binder mobility. One fraction of the binder appears to be permanently immobilized within the porous particles and is not transported even at higher drying rates, while another fraction is located in the interparticle pore network and is, in principle, available for capillary-driven transport. However, due to the overall low adhesion strength, it is assumed that the absolute binder mass in the interparticle pore space is too small for possible migration effets to be sensitively detected by adhesion strength measurements. Thus, the sensitivity of this method may be insufficient to identify binder migration in electrodes containing porous, nanostructured particles.

An alternative approach for detecting inhomogeneities is the measurement of the electrical resistivity of the electrodes. Electrical resistivity is influenced by the conductivity of the

active and inactive components as well as by their spatial distribution and contact resistances. An increase in resistivity often indicates increasing inhomogeneity in the distribution of conductive additives or binder within the electrode microstructure. Figure 5.6 shows the electrical resistivity as a function of drying rate.

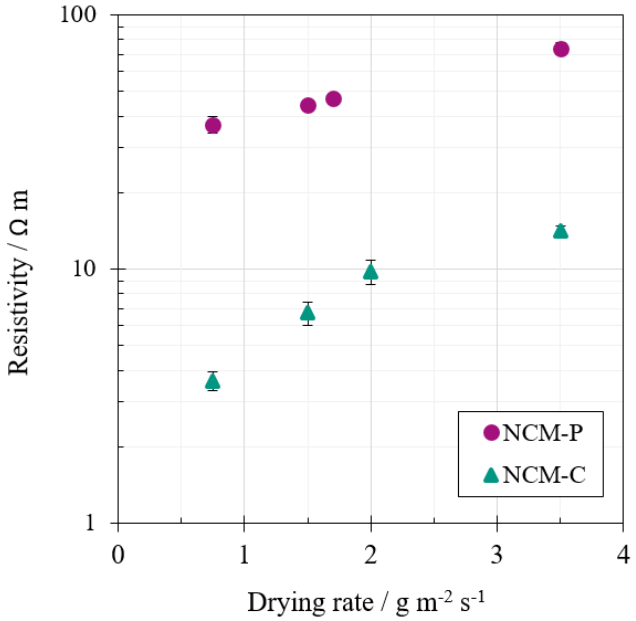


Figure 5.6: Electrical resistivity as a function of the drying rate for NCM-C and NCM-P electrodes. NCM-C and NCM-P electrodes show an increase in resistivity with increasing drying rate.

Due to their higher porosity and lower adhesion (low contacting) to the current collector, NCM-P electrodes exhibit higher absolute resistivity values which is consistent with findings in the literature.[109] For both electrode types, resistivity increases with increasing drying rate. However, the relative increase is significantly smaller for NCM-P electrodes than for NCM-C electrodes. This suggests that although some degree of component redistribution occurs in both systems, electrodes with porous particles are less sensitive to high drying rates.

The observed increase in resistivity for NCM-P electrodes was initially unexpected, as adhesion strength measurements did not indicate negative effects associated with binder migration. This supports the assumption that adhesion strength measurements lack sufficient sensitivity in this case. The stronger increase in resistivity observed for NCM-C electrodes suggests more pronounced binder and/or additive gradients at higher drying rates. However, electrical resistivity measurements alone do not allow a clear distinction between binder migration and conductive additive migration.[59,60]

To further quantify the measured influences of electrode properties behavior as a function of drying rate and to get a better insight into the underlying drying mechanism, energy-dispersive X-ray spectroscopy (EDS) analyses were carried out. EDS analyses enable a direct visualization of the spatial distribution of binder and conductive additives across the

electrode cross-section, with fluorine serving as a marker for the PVDF binder. This approach allows the influence of particle morphology on binder migration as a function of drying rate to be examined. Figure 5.7 shows the distributions of active material, conductive carbon additive, and fluorine in cross sections of NCM-C electrodes at the lowest and the highest drying rate investigated.

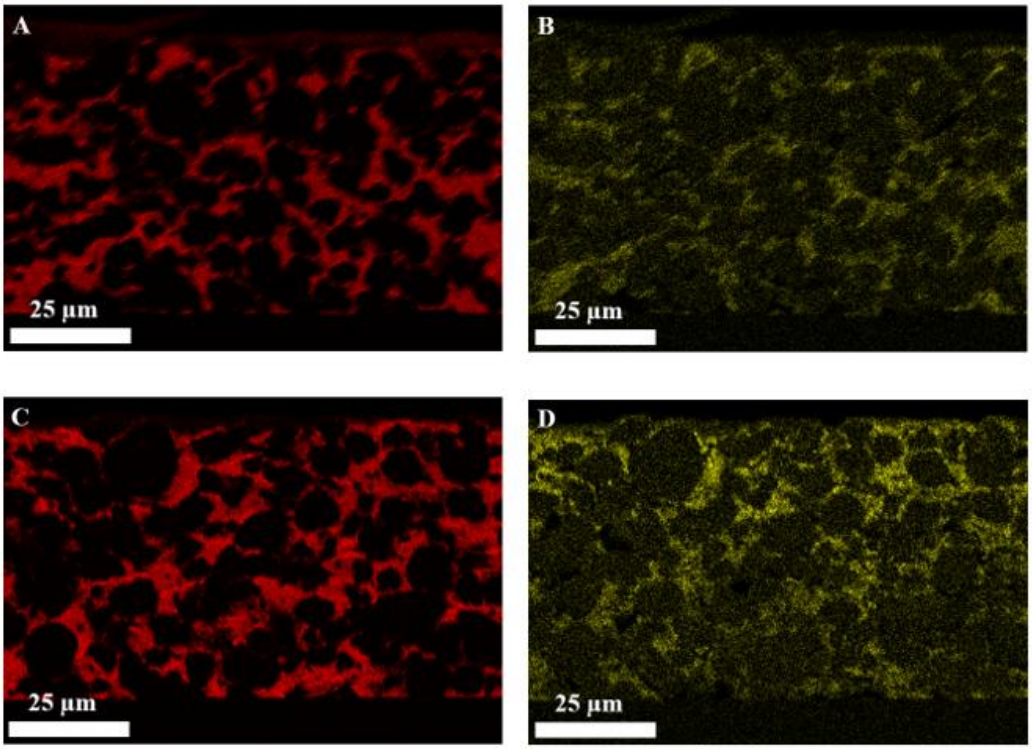


Figure 5.7: Carbon (A, C) and fluorine (B, D) EDS mapping of NCM-C electrodes for drying rates of 0.75 g $m^{-2}s^{-1}$ (A, B) and 3.5 g $m^{-2}s^{-1}$ (C, D). For the lower drying rate, the binder and conductive additives are located together in the pores between the active material particles. By drying at a higher rate, a binder gradient has been developed in the electrode. There is no evidence of migration of the conductive additives during faster drying.

The active material is composed of lithium, nickel, manganese, cobalt, and oxygen, without any presence of carbon or fluorine. The active material is represented by dark areas and is surrounded by the conductive additives and the PVDF binder in the interparticle pores. The fluorine distribution indicates that fluorine is also present in the compact particles. However, the reason for this is an overlay of EDS spectra of fluorine with manganese and cobalt, resulting in a virtually high fluorine concentration (so-called "fluorine noise").[18,109]

At low drying rates, a homogeneous distribution of all components is observed. The fluorine concentration is primarily located together with the conductive additives due to the high specific surface area.[100,126,127] At high drying rates, however, a depletion of the PVDF binder near the substrate and enrichment in the upper region of the electrode are evident, which can be attributed to increased capillary suction. A possible migration of conductive additives cannot be confirmed based on these EDS images by simple optical observation.

This shows that PVDF binder is transported separately in the electrode structure during drying.

Figure 5.8 shows the distribution of carbon additive and binder in electrodes containing porous particles.

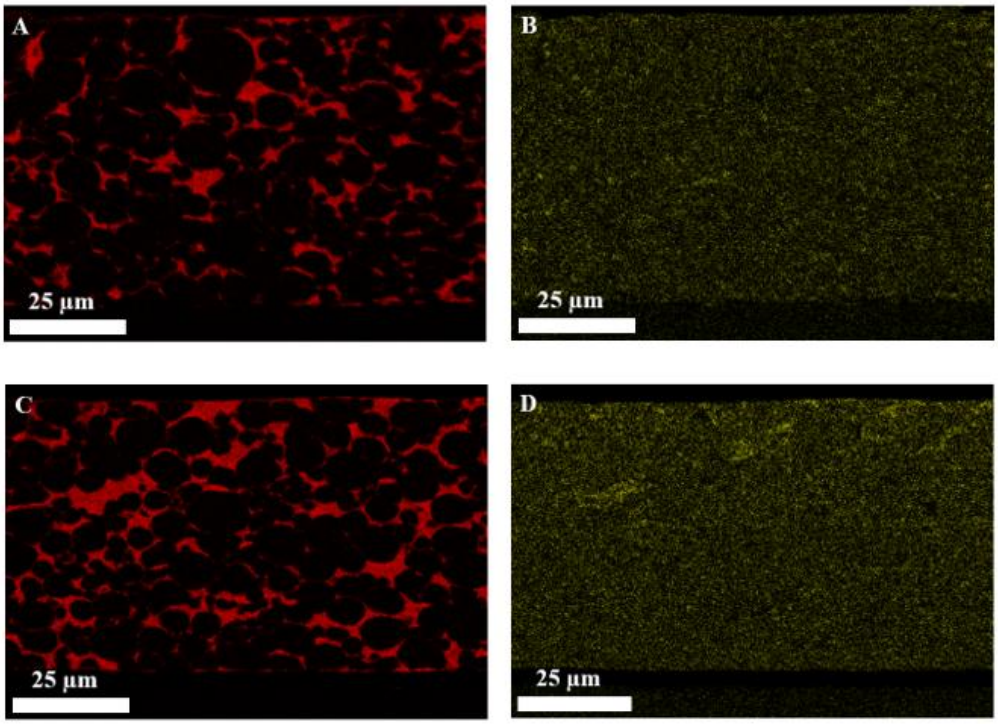


Figure 5.8: Carbon (A, C) and fluorine (B, D) EDS mapping of NCM-P electrodes for drying rates of 0.75 g $m^{-2}$ $s^{-1}$ (A, B) and 3.5 g $m^{-2}$ $s^{-1}$ (C, D). The binder is located within the active material particles, resulting in homogeneous binder distribution over the electrode cross-section. During faster drying, the binder is evenly distributed with slighty accumulation at the top side of the electrode.

Carbon is located in the interparticle pores between the clearly identifiable active material particles. Idependent of the drying rate, a homogeneous carbon distribution is observed within the interparticle pore space. The binder distribution, however, differs markedly from that observed in electrodes containing compact particles. Individual active material particles are barely distinguishable due to the accumulation of binder within the intraparticle pores of the porous secondary particles. This results in a homogeneous binder distribution throughout the entire electrode cross-section without significant accumulation in the interparticle pore space. Consequently, the pores between particles remain open, facilitating ion transport and leading to significant performance advantages. Even at high drying rates, the binder distribution remains largely homogeneous, although a slight enrichment in the upper region of the electrode is observed. The binder is present with the conductive additive and may therefore be misleading in appearance. However, a slightly binder redistribution would be consistent with the electrical resistivity measurements.

The measured increase in electrical resistivity for electrodes with porous particles raises the question of whether this increase is electrochemically relevant. To address this, half-cells containing electrodes composed of compact or porous particles were tested at different C-rates (Figure 5.9).

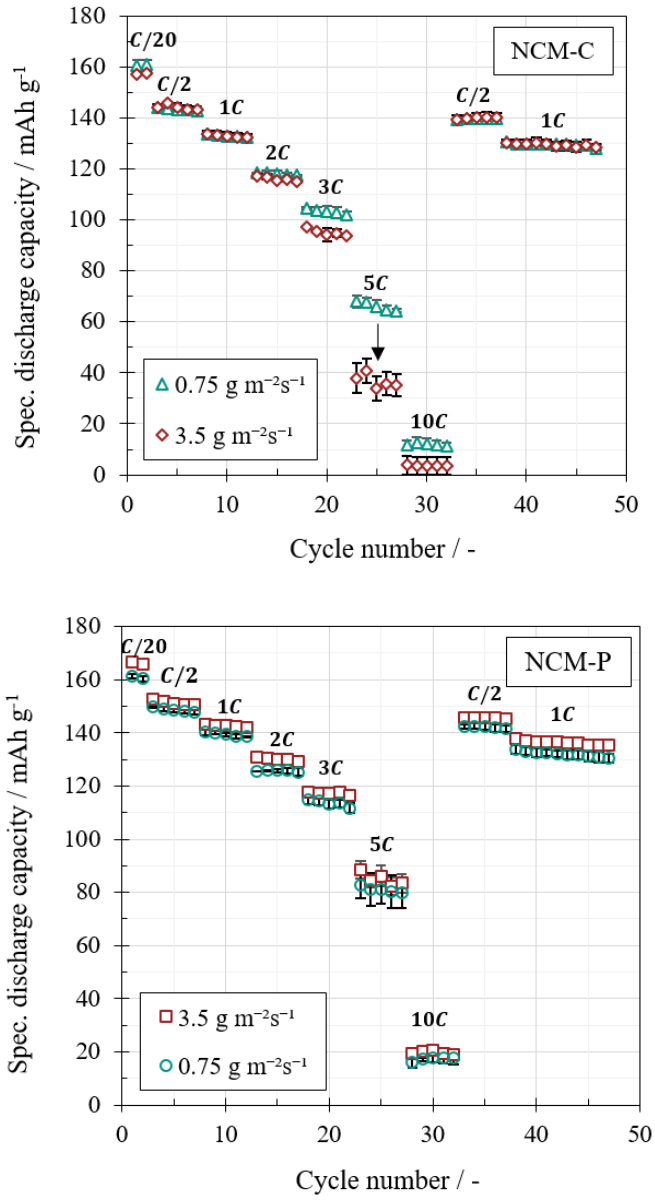


Figure 5.9: Comparison of the specific discharge capacity for cathodes with either NCM-C or NCM-P particles dried at lower and higher drying rate. For electrodes with compact particles, the expected behavior of decreasing C-rate capability due to binder migration is observed. In any case, electrodes with porous particles have a higher C-rate capability than electrodes with compact particles. In addition, it can be seen that there is no reduction in C-rate capability for electrodes manufactured with a higher drying rate.

For NCM-C cathodes, increasesing the drying rate leads to a pronounced reduction in C-rate capability. At a C-rate of 5C, the discharge capacity decreases by approximately 63 %. The pronounced binder concentration gradient observed with increasing drying rate has led

to an increase in resistivities, resulting in a reduction in C-rate capability. The accumulation of binder between particles has caused the pores to become clogged. The binder on the surface of the active material in the upper region of the electrode may increase the charge transfer resistance and enlarge the ion transport tortuosity for the lithium ions within the electrode porosity due to a reduced active exchange surface. These resistances increase the overpotential within the cell, the cut-off voltage is reached earlier, resulting in a lower discharge capacity.

In contrast, electrodes containing porous particles exhibit only a weak dependence of C-rate capability on drying rate. Even at the highest drying rate, a capacity of approximately 85 mAh $g^{-1}$ is achieved at 5C, corresponding to a 133 % higher capacity compared to NCM-C electrodes under the same conditions. The increased electrical resistivity does not result in performance limitations in this case, likely due to additional ionic transport pathways within the porous particles and the absence of binder-induced pore clogging in the interparticle pore network.

In summary, the results along the entire process chain demonstrate that the use of porous, nanostructured particles leads to a fundamentally different drying mechanism compared to conventional compact particles. The combined observations from adhesion strength measurements, electrical resistivity analysis, electrochemical characterization, and component distribution analyses cannot be fully explained by established drying models. These findings are consolidated into a sequential drying mechanism, which is presented and discussed in detail in the following section.

### 5.2.5 Sequential Drying Mechanism

Based on the experimental observations, a sequential drying mechanism is proposed for electrodes containing porous active material particles and using solvent-based binder as PVDF. During the slurry preparation process, the intraparticle pores of the active material are infiltrated with the solvent and dissolved PVDF binder by the capillary action of the small pore size within the particles. During the entire drying process, the conductive additives are located exclusively between the active material particles. Since no migration of conductive additives was detected, they are ignored in the visualization.

At the onset of drying, both the intraparticle and interparticle pore networks are fully saturated with solvent. As solvent evaporation proceeds, the wet film shrinkgs until particle rearrangement is no longer possible and the final film thickness is reached. This initial situation and the drying progress are shown in Figure 5.10.

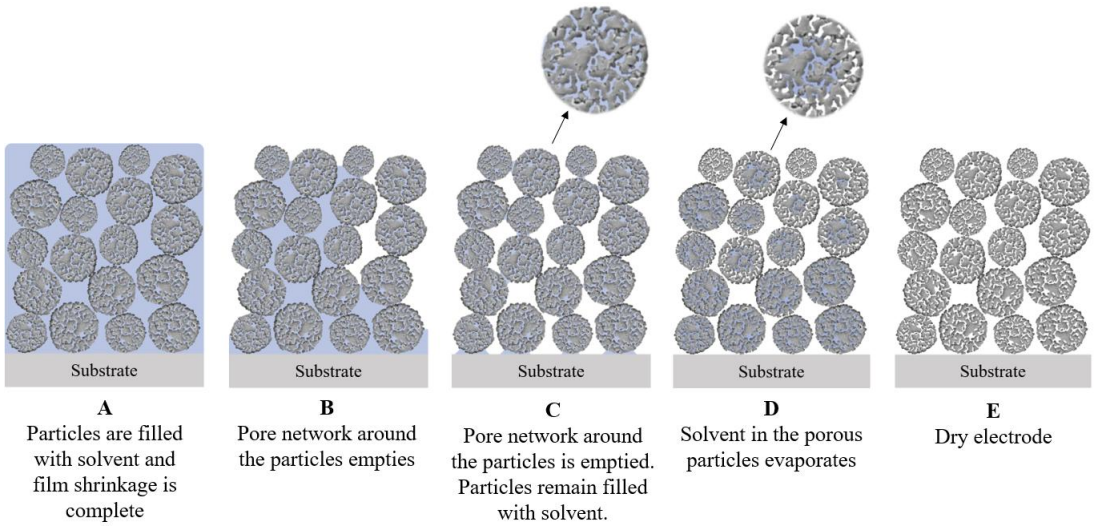


Figure 5.10: After film shrinkage, the capillary network between the active material particles (interparticle pores) empties. The active material pores remain filled due to capillary action. Emptying of porous particles starts when surrounding interparticle pores are emptied. Otherwise, the amount of evaporating solvent would be balanced by further uptake of solvent from another pore. Due to the immobilization of the solvent and binder in the small pores of the active material, the binder distribution over the electrode cross section is homogeneously distributed.

Subsequently, emptying of the interparticle capillary network begins. Larger capillaries empty first, while smaller capillaries remain filled and maintain a wet electrode surface. During this stage, binder can be transported towards the electrode surface by capillary liquid flow. However, the intraparticle pores remain filled due to their significantly higher capillary pressure, immobilizing a substantial fraction of the binder. The immobilized part of the binder and solvent does not take part in the emptying of the interparticle capillary network.

Solvent removal from the intraparticle pores can only occur once the connection to the surrounding solvent-filled pore netwok is lost. Otherwise, the amount of evaporating solvent would be balanced by further uptake of solvent from another pore. At this stage, solvent evaporates at the pore surface of the porous particles and is transported through the interparticle pores in the gas phase. This leads to a resistance within the electrode microstructure in addition to the resistance in the gas phase outside the electrode. This mechanism thus corresponds to a second drying stage with a reduced drying rate.

## 5.3 Conclusion

This chapter provides a comprehensive analysis of how porous, nanostructured cathode particles influence the entire electrode manufacturing chain for LIBs, ranging from slurry preparation and drying behavior to the resulting microstructure and electrochemical performance. Against the backdrop of emerging post-lithium battery systems, which increasingly rely on hierarchically structured and nanoscale active materials, this work addresses the

role of particle morphology as a unifying link between material design, process control, and electrode functionality.

By employing a strictly comparative experimental approach using compact and porous NCM111 particles of identical chemical composition, morphology-induced effects could be clearly isolated. The high intraparticle porosity and strongly increased specific surface area of the porous particles act as the initiator for a series of coupled effects that propagate consistently along the entire electrode manufacturing chain. Already at the slurry level, it becomes evident that porous particles fundamentally alter rheological behavior. Capillary uptake of solvent and dissolved binder into intraparticle pores reduces the amount of freely available liquid, effectively increases the solids volume fraction, and leads to a pronounced increase in viscosity over the entire shear-rate range. This shows a clear active-material-process relationship, and demonstrates that porous active materials cannot be regarded as a purely geometric modification, but instead fundamentally changes the physical basis of slurry processing.

This early interaction between particle morphology, binder, and solvent decisively governs microstructure evolution during drying. While in electrodes composed of compact particles the binder predominantly resides within the interparticle pore network, a substantial fraction of the binder in electrodes containing porous particles becomes immobilized within intraparticle pores. This immobilization results in reduced effective binder availability at the current collector interface and consequently lower adhesion strength.

Adhesion strength measurements reveal a strong sensitivity to drying rate for electrodes containing compact particles, which can be attributed to capillary-driven binder transport and binder depletion in the current-collector region. In contrast, electrodes with porous particles exhibit nearly constant adhesion strength across a wide processing window, even though at a lower absolute level. At the same time, these results indicate that adhesion strength alone is not a sufficiently sensitive measure for detecting binder redistribution in electrodes using porous, nanostructured particles. Electrical resistivity measurements provide a more sensitive measure and demonstrate that electrodes with porous particles show binder migration. EDS analyses show that electrodes containing porous particles maintain a largely homogeneous binder distribution, whereas electrodes with compact particles develop pronounced concentration gradients.

The infiltration and immobilization of binder within porous particles lead to reduced adhesion strength and a higher electrical resistivity compared to electrodes containing compact particles. However, this immobilization leads to homogeneous binder distribution, less clogging of interparticle pores, and significantly improved C-rate capability, even at higher drying rates.

Based on these experimental findings, a sequential, particle-morphology-dependent drying mechanism is proposed. In an initial stage, drying is dominated by capillary-driven emptying of the interparticle pore network, while intraparticle pores remain filled due to their

significantly higher capillary pressure, thereby effectively immobilizing binder wihtin the porous particles. Only in a subsequent stage does solvent removal from the intraparticle pores occur via evaporation at the particle surface and gas-phase transport through the interparticle pores. This extended model builds upon established drying mechanisms by explicitly accounting for the presence of porous active materials and provides a consistent mechanistic explanation for the observed differences in binder distribution and electrode performance.

In summary, this chapter demonstrates that porous, nanostructured active materials exert an influence far beyond their electrochemical function and fundamentally redefine the process-microstructure-property relationships in battery electrode manufacturing. The morphology of the particles is identified as a pivotal design parameter that exerts a significant influence on various parameters, including processability, drying mechanism, binder distribution, and the properties of electrodes. These findings underscore that the realization of high-performance and robust electrode manufacturing for future battery generations requires a strategic integration of active material development and process engineering.

Despite the demonstrated electrochemical advantages, the reduced adhesion strength and lower volumetric energy density of electrodes containing porous particles remain key challenges. A promising strategy to address these limitations is the construction of hirarchical multilayer electrode architectures, in which compact particles are employed near the current collector to enhance adhesion, while porous particles are used near the separator to maximize electrochemical performance.

The processing and drying behavior of such multilayer systems, particularly when using PVDF/NMP-based slurries and particles with different morphologies, is not yet understood. The following chapter builds upon the findings from this section by investigating multilayer electrodes in detail, thereby extending the identified active material-process-microstructure-property relationships to more complex electrode architectures, focusing on binder migration behavior and their implications for electrode performance.

# 6 Porous, Nanostructured Cathodes: Multilayer Architecture

As demonstrated in the previous chapter, the use of porous, nanostructured active material particles provides significant performance advantages, particularly with respect to rate capability. The penetration and fixation of the binder within the porous particle structure reduces pore clogging within the electrode pore network, thereby enabling a stable C-rate performance even at elevated drying rates during electrode manufacturing. Despite these advantages, electrodes containing porous NCM particles exhibit a pronounced drawback compared to conventional electrodes based on compact NCM, namely a reduced adhesion strength to the current collector. This trade-off between electrochemical performance and mechanical integrity represents a critical limitation for the industrial applicability of porous active materials.

A promising strategy to overcome this limitation is the use of multilayer electrode architectures with tailored formulations and particle morphologies in the individual layers.[17,19,128–132] By spatially separating functional requirements, multilayer electrodes offer the potential to combine the high volumetric energy density and adhesion strength of compact particles with the superior C-rate capability of porous particles.[p]

The objective of this chapter is to elucidate how multilayer electrode architectures can be used to tailor active material-process-microstructure-property relationships in order to overcome the inherent trade-off between electrochemical performance and mechanical integrity in electrodes containing porous, nanostructured active materials. In particular, this chapter investigates whether simultaneously coated multilayer electrodes can mitigate the reduced adhesion strength associated with porous NCM particles while preserving or enhancing their superior rate capability.

## 6.1 Motivation and State of the Art

Previous studies on multilayer coatings employing aqueous, two-component binder systems based on CMC/SBR have shown a linear dependence of the adhesion strength on the binder content in the bottom layer. In this case, the binder responsible for adhesion (SBR) can only be used in the bottom layer and completely reduced in the top player. It is assumed

[p] The results and discussion in this chapter are part from the following publication by the author:[62]
Klemens, J.; Burger, D.; Schneider, L.; Spiegel, S.; Müller, M.; Bohn, N.; Bauer, W.; Ehrenberg, H.; Scharfer, P.; Schabel, W. Drying of Compact and Porous NCM Cathode Electrodes in Different Multilayer Architectures: Influence of Layer Configuration and Drying Rate on Electrode Properties. *Energy Technology* **2023**, 2300267. https://doi.org/10.1002/ente.202300267.

that the drying process and migration of the binder will result in a quasi-homogeneous distribution of the binder throughout the layer thickness (assuming that the slurry is prone to binder migration).[133]

Comparable multilayer concepts have been investigated for cathodes using the one-component binder PVDF in the solvent NMP.[131] In these studies, the binder content in the top layer could not be reduced to zero, as PVDF also stabilizes the slurry and a minimum binder concentration is required to ensure sufficient slurry processability and guarantee the flowability of the suspension. Contrary to expectations, the authors found that the adhesion strength was lower than anticipated by intended layer-wise binder distribution. Notably, the specific influence of the thickness ratio between the top and bottom layers on binder migration has not yet been systematically clarified.

Importantly, it remains unclear how porous particle morphologies interact within simultaneously coated multilayer electrodes during drying depending on layer thickness ratio, overall binder contents, drying rates, and how this interaction affects binder redistribution, microstructure formation, and ultimately electrode properties.

The objective of the present chapter is to extend the current understanding of multilayer electrode processing and to systematically investigate the drying-induced binder migration in simultaneously coated multilayer electrodes as a function of particle morphology, layer thickness ratio, total binder content, and drying rate. The central hypothesis is that a deliberate combination of compact and porous particles in a multilayer architecture enables the formation of microstructural gradients that maximize adhesion strength at the current collector while preserving or enhancing the rate capability associated with porous particles. By testing these hypotheses experimentally, this chapter aims to provide mechanistic insight into how active material-process-microstructure-property relationships can be engineered to meet competing electrochemical and mechanical requirements in battery electrodes. To this end, compact particles with higher volumetric energy density are combined with porous particles exhibiting superior C-rate capability within a multilayer architecture for an efficient active material use.

## 6.2 Results and Discussion

The comparative investigations presented in this chapter were conducted under strictly controlled and identical processing conditions to isolate the influence of multilayer architecture on drying behavior, binder migration, and the resulting electrode properties. Mixing procedures, solid contents, and drying conditions were kept constant throughout all experiments. This approach ensures that observed differences can be attributed to particle morphology, layer configuration, and overall binder content rather than to variations in processing.

A particular focus of this chapter is on elucidating how multilayer electrode designs influence material-process-microstructure-property relationships when porous, nanostructured particles are combined with compact particles within one electrode architecture.

### 6.2.1 Particle Properties

Porous, nanostructured NCM622 particles were produced following the same manufacturing procedure as described in the literature and in Section 5.2.1 by the Insistute for Applied Materials at the KIT. Compact NCM622 particles were used as a reference material. An overview of the relevant particle properties is given in Table 6.1.

Table 6.1: Overview of the particle parameters of NCM622 with compact and porous particles.

| | Mean particle diameter / µm | BET surface area / $m^2\ g^{-1}$ | Density / $kg\ m^{-3}$ | Secondary particle porosity / % |
|---|---|---|---|---|
| NCM622 compact particles | 9.5 | 0.7 | 4640 | - |
| NCM622 porous particles | 8.4 | 3.5 | 4560 | 33 |

The significant higher BET surface area and the internal porosity of the porous particles are very similar to the investigated NCM111 particles in Chapter 5 and are expected to strongly influence slurry rheology, microstructure formation during drying, and binder migration.

### 6.2.2 Slurry Viscosity Profile

As shown in the previous chapter and in Appendix 11.8.1, slurries containing porous, nanostructured particles exhibit elevated viscosities compared to slurries based on compact particles. This behavior arises from the penetration of PVDF binder and NMP solvent into the internal pore structure of the porous particles during slurry preparation, which effectively increases the solid volume fraction.

During simultaneous coating of multilayer electrodes, a viscosity mismatch between the two slurries can result in displacement or intermixing of the layers.[134] To prevent this, the viscosity of the slurry containing porous particles was adjusted by reducing the PVDF content. The bottom layer slurry containing compact particles was prepared with 4.5 wt-% PVDF, while the top layer slurry containing porous particles was prepared with a reduced PVDF content of 3.0 wt-%. Both slurries were prepared with the same solid content of 55 wt-% and identical mixing procedures.

The compositions of the dry electrodes with compact and porous particles are summarized in Table 6.2.

Table 6.2: Composition of dry electrodes with compact and porous NCM622 particles.

| Name | NCM / wt-% | CB / wt-% | KS6L / wt-% | PVDF / wt-% | Solids / wt-% |
|---|---|---|---|---|---|
| NCM-C | 90.5 | 3.0 | 2.0 | 4.5 | 55 |
| NCM-P | 92.0 | 3.0 | 2.0 | 3.0 | 55 |

The resulting slurry flow curves as a function of shear rate are shown in Figure 6.1.

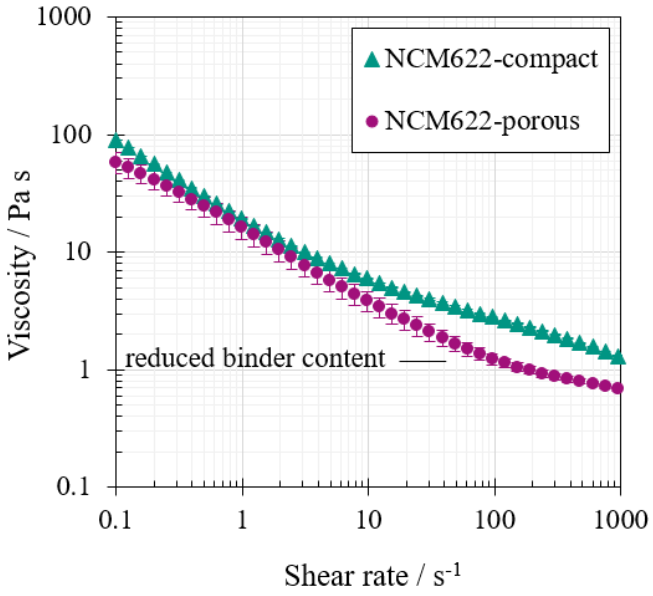


Figure 6.1: Viscosity profile as a function of shear rate for slurries containing compact or porous NCM622 particles. The slurry with porous particles exhibits a reduced binder content to adjust viscosity and to reduce the binder content in the multilayer electrodes compared to the single-layer electrode with only compact particles.

The viscosity of the slurry with porous particles was adjusted to be in the range and below the viscosity curve of the slurry with compact particles (see Appendix 11.8.1). With this flow behavior of the two slurries, intermixing of the two slurries during simultaneously coating is not expected.

This rheological adjustment not only enables stable multilayer coating, but also introduces a defined binder gradient and different overall binder contents, which must be considered in the interpretation of the subsequent results. The total binder content is adjusted by different layer thicknesses of the bottom and top layer (see Section 6.2.3 and 6.2.4).

### 6.2.3 Electrode Microstructure

To investigate the influence of particle morphology and multilayer configuration on microstructure formation during drying, electrodes containing either compact or porous NCM622 particles were prepared under identical processing conditions in single-layer and multilayer configurations.

In all multilayer electrodes, the lower layer adjacent to the current collector consists of compact particles, while the upper layer adjacent to the separator consists of porous particles. Layer configurations with different proportions of compact and porous layers were produced. Two multilayer configurations were realized: one with a higher fraction of compact particles (ML 1/3 porous particles) and one with a higher fraction of porous particles (ML 2/3 porous particles).

Representative cross sections of single-layer and multilayer electrodes are shown in Figure 6.2.

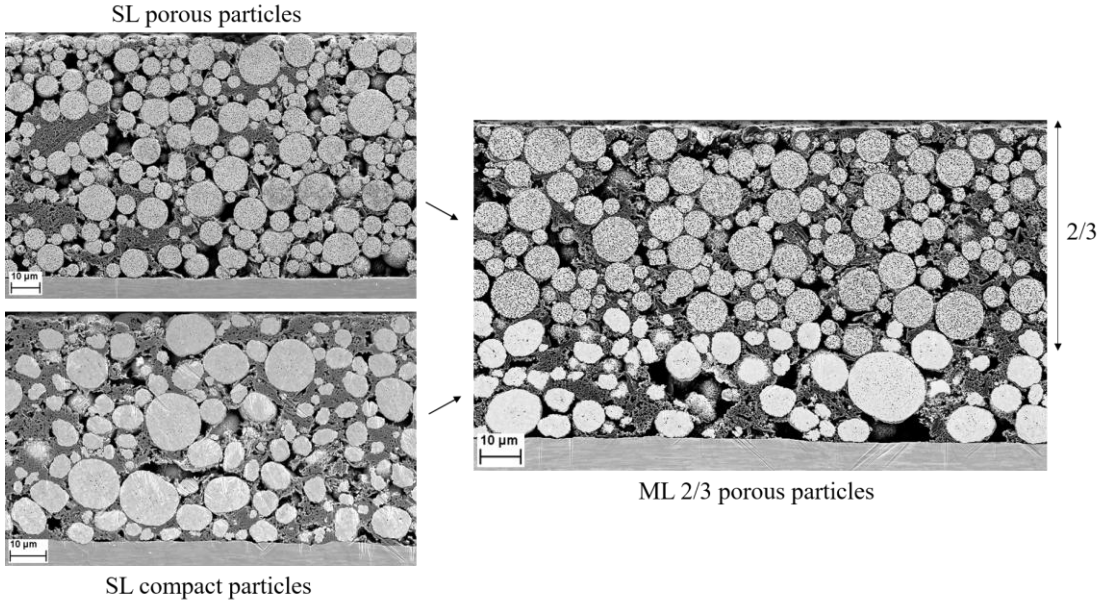


Figure 6.2: Cross-sectional images of single-layer electrodes with compact and porous particles (left) and a composite multilayer architecture (ML 2/3 porous particles) with porous particles near the separator and compact particles near the current collector (right).

The cross-sectional analysis confirms that adjusting the slurry viscosity prevents intermixing of the layers during simultaneous coating. A sharp interface between the layers is observed, along with good layer conformity and no evidence of cohesion failure.

Since coating thickness influences both drying behavior and adhesion strength, all electrodes were manufactured with comparable dry film thicknesses. Two drying rates were investigated: a lower drying rate of 0.75 g $m^{-2}s^{-1}$ at an isothermal drying temperature of

61 °C and a three times higher drying rate of 2.25 g $m^{-2}s^{-1}$ at an isothermal drying temperature of 81 °C. All drying experiments were carried out at a heat transfer coefficient of 80 W $m^{-2}K^{-1}$ using isothermal drying conditions (see Section 2.3.1).

An overview of the dry film thickness, areal mass loading, electrode porosity, and interparticle porosity of the single- and multilayer electrodes is given in Table 6.3. Given the areal mass loading and the solids content of 55 wt%, the drying rate increase results in a reduction of drying time from 207 ± 33 s to 69 ± 11 s.

Table 6.3: Dry film thickness, areal mass loading, electrode porosity, and interparticle porosity of single- and multilayer electrodes. The porosity of the porous particles is $\varepsilon_{\text{porous,particles}} = 33\ \%$.

| Name | Dry film thickness / µm | Areal mass loading / g $m^{-2}$ | Electrode porosity / % | Interparticle porosity / % |
|---|---|---|---|---|
| SL compact | 94 ± 1 | 220 ± 4 | 43 ± 1 | |
| SL porous | 97 ± 2 | 160 ± 4 | 60 ± 1 | 44 ± 1 |
| ML 1/3 porous | 101 ± 2 | 201 ± 1 | 51 ± 1 | 46 ± 1 |
| ML 2/3 porous | 102 ± 2 | 189 ± 1 | 55 ± 1 | 44 ± 1 |

The areal mass loading of the multilayer electrodes is increased due to the combination with the compact particles. The open porosity of the porous particles $\varepsilon_{\text{porous,particles}} = 33\ \%$ results in an increased electrode porosity of the single-layer (SL porous particles) and the multilayer electrodes in comparison to the single layer with compact particles (SL compact particles). When accounting for the internal porosity of the porous particles, the interparticle porosity is comparable for all electrodes, indicating that differences in performance are primarily governed by particle morphology and binder distribution during drying rather than interparticle-porosity variations.

### 6.2.4 Binder Migration: Influence of Overall Binder Content and Drying Rate

The influence of multilayer architecture and overall binder content on drying-induced binder migration was assessed using adhesion strength measurements, which serve as a sensitive indicator of binder redistribution towards or away from the current collector (Figure 6.3).

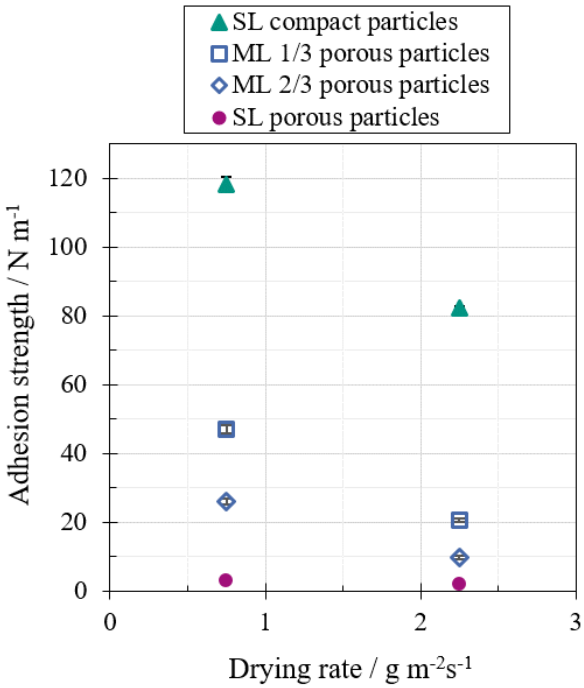


Figure 6.3: Adhesion strength measurements of single-layer electrodes (SL compact particles, SL porous particles) and multilayer electrodes (ML 1/3 porous particles, ML 2/3 porous particles) at a lower drying rate of 0.75 g $m^{-2}s^{-1}$ (61 °C isothermal drying temperature) and a higher drying rate of 2.25 g $m^{-2}s^{-1}$ (81 °C isothermal drying temperature).

As expected from the previous chapter, single-layer electrodes containing porous particles exhibit very low adhesion strengths of 2.55 ± 0.45 N $m^{-1}$, whereas single-layer electrodes containing compact particles show significantly higher values. Introducing a multilayer architecture with compact particles near the current collector leads to pronounced increase in adhesion strengths compared to single-layer electrodes containing only porous particles. The increase in adhesion strength is up to approximately 16-fold higher at lower drying rate and 10-fold higher at increased drying rate.

Although the multilayer electrodes show substantially improved adhesion compared to the single-layer electrodes with porous particles, their adhesion strength remains below that of the single-layer electrodes with compact particles. Since intermixing of the layers can be excluded based on microstructural analysis, it can be hypothesized that this discrepancy must be attributed to differences in overall binder content.

To quantify this effect, the adhesion strength is plotted as a function of total binder content in Figure 6.4. The overall binder content can be quantified by calculating the mass ratio and the binder content of each layer.

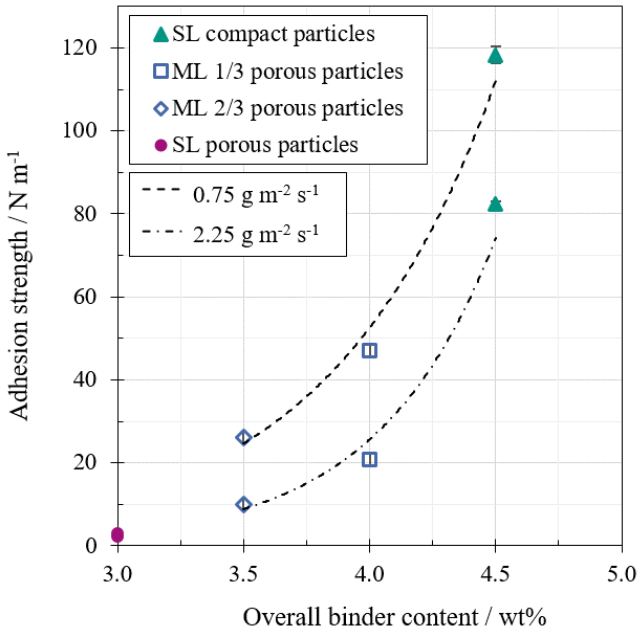


Figure 6.4: Adhesion strength of single-layer and multilayer electrodes as a function of overall binder content and drying rate.

The total binder content strongly affects adhesion strength. From a conceptual standpoint, it could have been expected that adhesion strength to be largely independent of electrode thickness, as a sufficiently high overall binder content should ensure adequade interfacial bonding regardless of the internal distribution. In this idealized scenario, a single-layer electrode composed of compact particles would exhibit similarly high adhesion strength as multilayer architecture. However, the experimental results indicate that this expection is not fully met. The results suggest that, despite the imposed binder gradient in multilayer electrodes, diffusive equilibration of PVDF concentration in NMP occurs prior to capillary-driven transport during drying.

Such diffusive homogenization is consistent with polymer film shrinkage governed by solvent diffusion.[94,135] This finding is of particular relevance for the processing of PVDF/NMP-based multilayer coatings, as it fundamentally differs from the behavior reported in the literature for aqueous multilayer coatings employing CMC/SBR binder system. In CMC/SBR-based electrodes, the adhesion strength of multilayer architectures is predominantly governed by the properties of the layer adjacent to the current collector, indicating that diffusive equilibration of the binder concentration across the electrode thickness does not play a decisive role in determining the final electrode properties.

Since the adhesion strength as a function of the overall binder content exhibits an exponential behavior, the increasing interactions of the binder with the particles and the current collector may play a significant role. As the drying rate increases, the exponential relationship between adhesion strength and overall binder content shifts to lower values. While the adhesion strength of the single layer with compact particles (4.5 wt-% PVDF) decreases by

approximately 30 %, the multilayers with lower binder contents show reductions of up to 62 % (3.5 wt-% overall binder content). This trend indicates that reduced binder-particle and binder-current collector interactions at lower binder contents facilitate binder transport away from the current collector during capillary transport.

The results of the adhesion tests have shown that binder migration is enhanced for multilayer electrodes dried at a higher drying rate. It is therefore to be expected that the C-rate capability of multilayer electrodes also depends on the drying rate.

The influence of the multilayer construction and higher drying rates on cell performance is investigated by coin-cell tests with increasing C-rate. It is expected that the use of porous particles in the vicinity of the separator will have a positive effect on the C-rate capability and that also multilayer electrodes show an influence of the higher applied drying rate. Figure 6.5 shows the specific discharge capacity of the single- and multilayer electrodes dried at the lower drying rate and the higher drying rate.

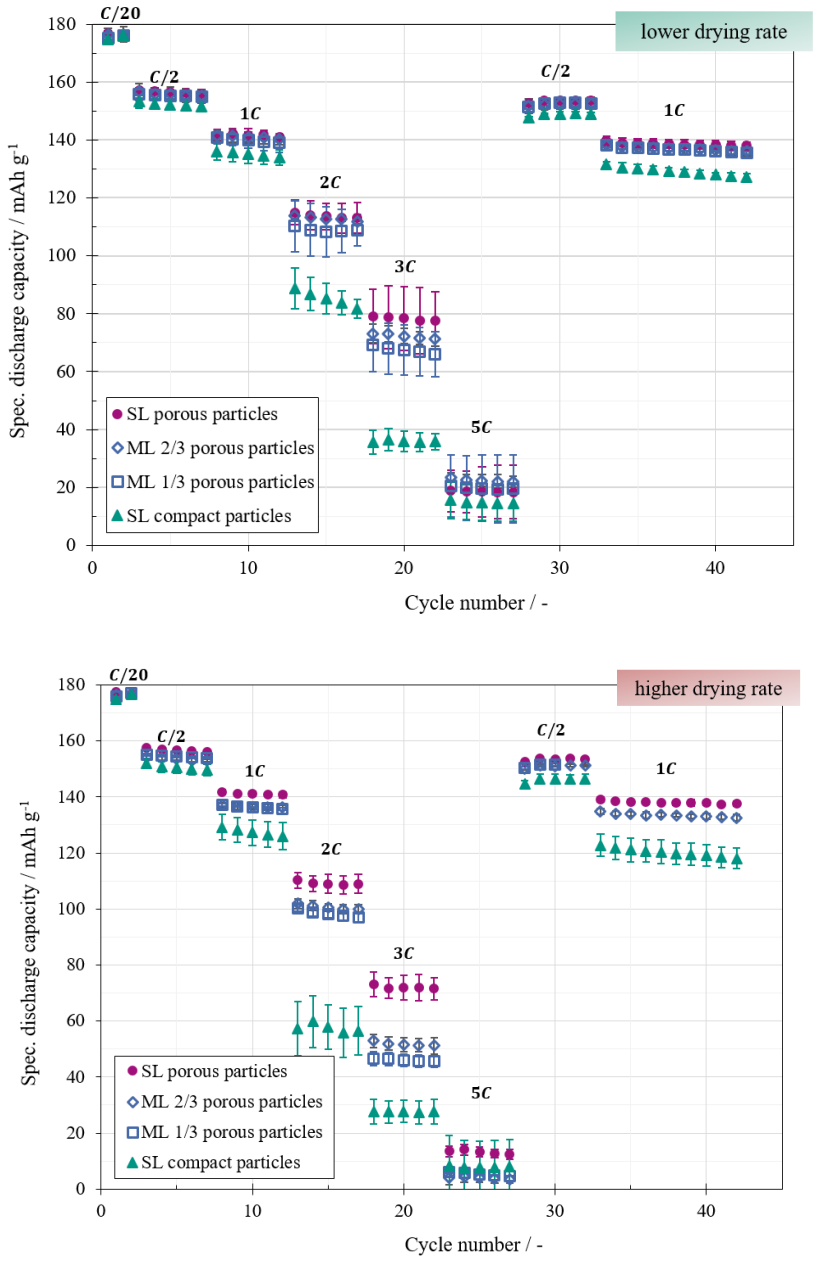


Figure 6.5: Specific discharge capacity of single-layer and multilayer electrodes dried at a lower and a higher drying rate as a function of the C-rate.

At elevated C-rates, the single- and multilayer electrodes with porous particles are shown to have higher specific discharge capacities than the single layer with compact particles. Remarkably, even a relatively small fraction of porous particles in the multilayer (ML 1/3 porous particles) results in a substantial increase in C-rate capability.

At 3C and low drying rate, the discharge capacity of the single-layer electrode with porous particles is approximately 118 % higher than that of the single-layer electrode with compact particles. The multilayer electrodes with 2/3 and 1/3 porous particles show increases of approximately 101 % and 88 %, respectively.

Impedance measurements (Appendix 11.8.2) indicate that the use of porous particles and reduced binder content lowers ionic resistance, while multilayer electrodes additionally benefit from reduced electrical resistivity (Appendix 11.8.3) compared to single-layer electrodes containing porous particles. Control experiments confirm that a reduction of binder content in electrodes with compact particles does not yield comparable improvements in C-rate capability (Appendix 11.8.4), demonstrating that the observed performance enhancement is intrinsically linked to particle morphology.

Figure 6.5 also shows the discharge capacities for the electrodes produced at a higher drying rate. The C-rate capability can be improved by using only porous particles or the multilayer architectures. The multilayer ML 2/3 porous provides an 88 % increase over the SL compact, but has a lower specific discharge capacity than the SL porous due to the binder migration. With a 67 % increase at 3C compared to the single layer with compact particles, the multilayer ML 1/3 porous shows a lower increase in C-rate capability than the ML 2/3 porous. This could be related to the lower proportion of porous particles.

Multilayer electrodes combine the advantages of both particle types: improved adhesion due to compact particles in the current-collector region and enhanced electrochemical performance due to porous particles in the upper electrode layers. At a discharge rate of 3C, multilayer cathodes outperform compact single-layer electrodes.

## 6.3 Conclusion

Multilayer electrodes were constructed in such a way that compact particles are present at the interface to the current collector foil and porous particles are present at the interface to the separator. Thus, the properties of both particles are successfully implemented in a multilayer. Furthermore, the influence of drying on the production of multilayer electrodes with the binder PVDF was investigated in order to improve the understanding of the microstructure formation.

The results show that a significant increase in adhesion strength compared to a single layer with porous particles and an increase in C-rate capability compared to a single layer with compact particles could be achieved by the multilayer structure.

Due to the simultaneous wet-on-wet application, a concentration compensation of the binder takes place during the drying process, so that the adhesion strength of the electrodes mainly depends on the total binder content. As the binder content increases, the adhesion increases exponentially, indicating that the interaction of the binder with the components in the slurry increases more than proportionally. Electrodes with a higher binder content show that less binder migration occurs during production at higher drying rates than electrodes with a lower binder content. This is also indicated by the fact that with a higher binder content the binder interactions are more pronounced and therefore less free binder could be transported by capillary transport and more binder could be fixated.

Half-cell tests have shown that despite binder migration during drying at the higher drying rate, the C-rate capability of the multilayer electrode with porous particles is increased. Compared to the single-layer electrode with compact particles, a higher proportion of porous particles shows an increase in specific discharge capacity.

Overall, the results demonstrate that multilayer electrode architecture enable a targeted tuning of active material-process-microstructrue-property relationships. This chapter highlights the strong interdependence of binder distribution, particle morphology, and process parameters, and provides clear optimization strategies for industrial implementation of porous, nanostructured battery active materials and in general multilayer electrodes.

The main advantage of the presented multilayer architecture results from the fact that the electrodes have compact and porous particles in a suitable combination. The adjusted binder gradient did not show the desired improvement with simultaneous multilayer coating. There was a compensation of the concentration gradient. In order to counteract this effect, the concept of sequential multilayer production for the optimization of electrodes with PVDF binder should be addressed in future work. The idea would be to coat and dry a first layer with a higher binder content. This fixes the binder, which determines the adhesion of the multilayer. A second coating with reduced binder content could be applied to reduce the overall binder content and maximize the overall electrode performance. An extreme case of this method would be the production of a very thin primer layer containing only binder and conductivity additive.

# 7 Summary and Outlook

The overarching objective of this thesis is to elucidate the relationships between active materials, binder systems, varying drying process conditions, microstructure formation, multilayer architectures, and resulting electrode properties. The outcomes achieved represent a significant advancement in understanding the processing of active materials for LIB and SIB systems.

The results demonstrate that the drop-in capability of SIB electrode manufacturing is not primarily constrained by machine compatibility, but by the interplay of material-specific properties and process conditions. A key lever for process optimization lies in the targeted design of particle properties, particularly particle size and internal structure. In summary, this dissertation provides the first systematic comparison of LIB and SIB materials from an electrode manufacturing perspective. It establishes a mechanistic understanding of binder migration, quantifies the impact of particle morphology on drying behavior, and delivers a scientifically validated methodology for assessing the drop-in capability of SIB technology. The insights gained in this work provide a foundation for rational process adaptation in emerging battery technologies and thereby bridging the gap between material development and industrially viable electrode manufacturing.

The conceptual framework of this work, as introduced in the Aim of this Work (Section 1.4), is structured along two complementary research areas that systematically address these interdependencies using distinct material systems and processing routes.

*Research area 1* focuses on water-based processing using the CMC/SBR binder system and investigates both LIB- and SIB-relevant materials, including LFP, graphite, and hard carbon with defined particle sizes. Within this approach, key aspects such as the identification of critical active material parameters, the role of particle size, and the influence of drying conditions on microstructure formation and binder migration are examined.

*Research area 2* extends this approach to NMP-based processing using PVDF and focuses on NCM as a model system. Here, the influence of particle morphology (compact vs. porous) and advanced electrode designs, such as multilayer architectures, on drying mechanisms and binder redistribution is analyzed.

Together, the research areas follow a consistent analytical approach based on active material-process-microstructure-property relationships. This structure enables both a comparative and a mechanistic understanding of how material properties and process parameters interact across different electrode systems.

Given this structured approach, the present chapter is organized into corresponding subchapters. Each subchapter provides a dedicated summary and outlook, in which the key

findings of the respective research focus are synthesized and critically discussed in the context of process design and future research directions. To avoid redundancy, the following sections deliberately focus on the consolidation and interpretation of results rather than repeating detailed discussions from the individual chapters.

## 7.1 Drop-In Capability: Material-Dependent Electrode Manufacturing of LIB vs. SIB

This chapter systematically investigates the extent to which SIBs can be regarded as a drop-in technology relative to established LIBs under realistic manufacturing conditions. The focus is not on a purely electrochemical comparison of cell chemistries, but rather on a manufacturing-oriented analysis that examines the role of active material properties along the electrode production chain. The objective was to illustrate the challenges and opportunities associated with processing SIB-active materials in comparison to LIB-active materials. It was demonstrated that all production processes for the manufacture of LIB electrodes can be applied to the production of SIB electrodes. However, the properties of the active material used affects the potential production speeds, drying process, adhesion properties, and, most importantly, binder migration during the drying process.

This thesis chapter provides a systematic, manufacturing-oriented assessment of the drop-in capability of SIB electrode manufacturing to established LIB technology. By applying strictly identical processing conditions across all investigated systems, the study isolates material-specific effects and identifies the governing active-material-process-microstructure-property relationships along the electrode manufacturing chain.

The results demonstrate that SIB electrode manufacturing cannot be regarded as a true drop-in replacement for LIB manufacturing. Although similar electrode architectures can be produced, the feasibility of direct transfer is fundamentally constrained by intrinsic differences in active material properties rather than by transferable process parameters alone.

At the process-dimensioning level, lower specific capacities of SIB active materials require higher areal mass loadings at identical areal capacity, resulting in systematically longer drying times. While increased drying rates can reduce absolute time differences, they do not eliminate the underlying material-induced constraints. Even minor differences in drying time translate into substantial variations in required dryer length or achievable production speed, highlighting the industrial relevance of material-dependent drying behavior.

Attempts to compensate for longer drying times through increased slurry solid content reveal slurry viscosity as a critical bottleneck. Despite identical solid contents and mixing procedures, SIB slurries exhibit significantly higher low-shear viscosities than LIB slurries due to smaller particle sizes, irregular morphologies, and lower particle densities, which

increase the active material volume fraction. These rheological differences constrain pumpability and air bubble removal, thereby necessitating process or equipment adaptions and further limiting true drop-in capability.

With respect to drying-induced microstructure formation, simultaneous measurements of film shrinkage and pore breakthrough reveal a material-invariant behavior: pore breakthrough consistently coincides with the end of film shrinkage for all investigated active material systems, drying rates and electrode thicknesses. This finding demonstrates that capillary forces dominate over viscous resistance during drying of water-based battery slurry and that the onset of pore breakthrough and binder migration is independent of active material properties. Consequently, material-dependent differences in binder redistribution must arise from mechanisms beyond the timing of pore breakthrough.

In contrast, the extent of binder migration is strongly material-dependent. Adhesion strength measurements reveal that absolute adhesion strength alone is not a reliable indicator of binder fixation. Graphite electrodes show pronounced binder migration with increasing drying rate, whereas hard carbon electrodes exhibit higher resistance. For LFP electrodes, binder migration occurs only once a critical drying-rate-induced capillary driving force is exceeded. These results indicate that binder migration is governed by the balance between capillary transport and binder fixation, which is controlled by binder-active material affinity and particle size rather than by adhesion strength alone.

Overall, this chapter establishes that the drop-in capability of SIB electrode manufacturing is fundamentally limited by interconnected active material-process-microstructure-property relationships. As a result, SIB electrode manufacturing requires a material-specific process design rather than a direct transfer of LIB manufacturing strategies.

The findings highlight several critical directions for future research and industrial implementation. First, the demonstrated particle-size-dependent resistance to binder migration indicates that particle engineering represents a promising lever for expanding the process window at high drying rates. Systematic variations of particle size within a single active material system, as initiated in the subsequent chapter, is essential to decouple particle-size effects from density or chemistry-related superposition effects and to derive quantitative design rules for binder migration.

Second, the strong influence of binder-active material affinity on binder migration sensitivity suggests that binder chemistry and surface functionalization strategies offer significant potential for mitigating drying-induced binder inhomogeneities. Future work should therefore focus on tailoring binder systems to surface modifications to enhance binder fixation without compromising slurry processability.

Third, while this study focuses on water-based CMC/SBR binder system, the identified active material and process dimensioning relationships are expected to be transferable to other binder systems and solvents. Extending the investigation of active material-process-

microstructure-property relationships to alternative binder chemistries and solvent systems would enable a broader generalization to the derived principles.

From an industrial perspective, the results underline that the successful implementation of SIB technology requires a paradigm shift from chemistry-based drop-in assumptions towards active material-based process design. Future work should therefore integrate the identified active material-process-microstructure-property relationships into scale-up models to quantitatively evaluate trade-offs between drying rate, slurry formulation, equipment design, and electrode performance.

Ultimately, the insights gained in this work provide a framework for rational process adaptions in emerging battery technologies and contribute to bridging the gap between material development and industrially viable electrode manufacturing.

## 7.2 Influence of Particle Size and Fast Drying on Binder Migration

This chapter systematically investigates the electrode processing of HC particles with different particle sizes at varying drying rates and comparatively analyzed with graphite electrodes reported in the literature under comparable conditions, including electrode compositions, slurry preparations, electrode fabrication, and drying conditions.

The results demonstrate that binder migration during the drying of water-based battery electrodes is governed by a coupled material-microstructure-process-property relationship. A key finding of this work is that binder migration can be effectively suppressed by reducing active material particle size. This enables fast drying of electrodes with state-of-the-art loadings within a few seconds, representing a substantial reduction in drying time and a significant increase in potential production speed.

The suppression of binder migration correlates with the gel-like rheological behavior of the corresponding slurries, which originates from enhanced particle-polymer interactions and the formation of a stabilized CMC network in the water-based CMC/SBR binder system. However, the results also show that rheological descriptors alone are insufficient to predict binder migration at a given drying rate. Binder transport arises from the competition between drying-rate-induced capillary transport and binder immobilization within the evolving microstructure. The size of the particles affects the immobilization or fixation of the binder.

Particle size plays a decisive role in this balance by influencing the degree of binder immobilization. Smaller particles promote stronger fixation of the binder, thereby increasing resistance to disruptive capillary transport. Nevertheless, even immobilized binder can become detached if the capillary driving force induced by the drying rate becomes sufficiently

large. This behavior highlights the complex interplay between CMC-particle interactions and SBR-CMC and SBR-particle interactions.

In addition to drying rate and particle size, film temperature during drying is identified as a parameter for increasing adhesion strength, regardless of material system or active material particle size.

Complementary impedance measurements confirm that binder migration and its suppression are also reflected in ionic transport properties. Variations in ionic resistance and tortuosity establish a direct link between adhesion strength and ionic transport during electrode processing.

Overall, this work provides a mechanistic foundation for controlling binder migration through targeted material design and process optimization, enabling robust fast-drying strategies for the manufacturing of water-based battery electrodes.

To predict binder migration behavior, a comprehensive mechanistic understanding must be developed. This requires quantitative validation of the interaction between binder system, active material, and other slurry additives. In particular, the interactions between CMC and the active material, as well as between SBR, CMC, and the active material, must be considered to describe the resistance to capillary transport. Such an understanding may enable future material and formulation design in which binder migration is prevented by targeted fixation and may further allow a simplification of process settings in multistage drying systems.

## 7.3 Porous, Nanostructured Cathodes: Microstructure Development

This chapter systematically investigates the influence of porous, nanostructured cathode particles on processing behavior, microstructure development, and electrochemical performance of LIB electrodes, and derives an extended drying model based on the experimental findings. The chapter addresses the critical yet previously underexplored question of how particle morphology affects slurry behavior, drying, binder migration, and the resulting electrode properties.

A strictly comparative experimental approach was employed using compact and porous NCM111 particles with identical chemical composition, comparable particle size, and similar density, ensuring that observed differences can be unequivocally attributed to intraparticle porosity. The porous secondary particles exhibit an intraparticle porosity of approximately 48 % and a more than sevenfold increase in specific surface area. These structural characteristics initiate a cascade of coupled effects along the entire electrode manufacturing process chain.

Already during slurry preparation, particle morphology exerts a pronounced influence on rheological behavior. Capillary infiltration of solvent and dissolved PVDF binder into the intraparticle pores of the porous particles reduces the volume of freely available solvent in the slurry phase. As a consequence, the effective solids volume fraction increases substantially, leading to elevated slurry viscosity over the entire shear-rate range. This observation constitutes a direct active material-process relationship and clearly demonstrates that porous particles cannot be treated purely as a geometric modification, but fundamentally alter slurry viscosity behavior.

The binder and solvent infiltration initiated during slurry preparation decisively governs subsequent microstructure formation during drying. In contrast to electrodes composed of compact particles, where the binder is predominantly located within the interparticle pore network, a significant fraction of the binder in electrodes with porous particles becomes immobilized within the intraparticle pores. This immobilization reduces the effective binder availability at the electrode–current collector interface, resulting in significantly lower adhesion strength.

Adhesion strength measurements reveal a strong decrease with increasing drying rate for electrodes containing compact particles, consistent with capillary-driven binder transport towards the electrode surface and binder depletion near the current collector. In contrast, electrodes containing porous particles exhibit nearly constant adhesion strength over a wide range of drying rates, although at a lower absolute level. This behavior indicates fundamentally altered binder mobility and, at the same time, highlights the limited sensitivity of adhesion measurements for detecting slight binder redistribution in electrodes containing porous particles.

Electrical resistivity measurements provide a more sensitive tool for microstructural inhomogeneities. While both electrode types exhibit increasing resistivity with increasing drying rate, the relative increase is significantly smaller for electrodes containing porous particles. In combination with EDS analyses, these results demonstrate that pronounced binder concentration gradients form in electrodes with compact particles, whereas a largely homogeneous binder distribution is maintained in electrodes with porous particles. The intraparticle accumulation of binder prevents clogging of the interparticle pore network and preserves open ionic transport pathways.

These microstructural differences translate directly into electrochemical performance. Electrodes containing compact particles exhibit a significant reduction in C-rate capability at high drying rates, which is attributed to increased resistivity, hindered ion transport, and elevated charge-transfer resistance caused by binder accumulation and pore blockage. In contrast, electrodes containing porous particles retain high rate capability even at elevated drying rates. Additional ionic transport pathways within the porous particles and open interparticle pores compensate for the increased electrical resistivity and enable superior high-rate performance.

Based on the experimental observations, a sequential, active material-particle-morphology-dependent drying mechanism is proposed. Initially, binder transport is governed by capillary-driven emptying of the interparticle pore network, while intraparticle pores remain filled due to their significantly higher capillary pressure, immobilizing a substantial fraction of the binder. Only in a subsequent drying stage does solvent removal from intraparticle pores occur via evaporation at the particle surface and gas-phase transport through the interparticle pores, introducing an additional internal drying resistance. This model extends established drying concepts by explicitly incorporating the role of porous active materials.

Overall, this chapter consistently demonstrates that porous, nanostructured active materials do not solely influence electrochemical performance but fundamentally influence the entire process-microstructure-property chain. Particle morphology emerges as a central design parameter governing slurry behavior, drying mechanism, binder distribution, and ultimately functional electrode properties.

The findings of this chapter highlight that porous active materials offer substantial performance advantages for cathode electrodes but simultaneously introduce new processing-related challenges. In particular, reduced adhesion strength and lower volumetric energy density represent critical trade-offs that currently limit straightforward industrial implementation.

A promising strategy to mitigate these limitations is the development of hierarchical multilayer electrode architectures, in which compact particles are placed near the current collector to enhance adhesion, while porous particles are employed in separator-near region to maximize electrochemical performance. However, the mechanisms identified in this chapter suggest that drying and binder migration in such heterogeneous systems will be considerably more complex than in single-layer electrodes.

Beyond LIB, the insights gained here are directly transferable to post-lithium systems such as SIB, where porous and hierarchically structured particles are even more critical. In this context, the coupling of active material design with process engineering will be a key enabler for the next generation of high-performance, sustainable battery technologies.

## 7.4 Porous, Nanostructured Cathodes: Impact of Multilayer Architecture

This dissertation chapter systematically investigates the potential of multilayer electrode architectures to overcome the inherent trade-off between electrochemical performance and mechanical integrity in battery cathodes containing porous, nanostructured active materials. By combining compact and porous NCM622 particles within a simultaneously coated multilayer architecture, the study aimed to elucidate how active material morphology, processing conditions, and drying behavior jointly govern electrode microstructure formation and, ultimately, electrode properties.

A central outcome of this work is the demonstration that multilayer electrode architectures enable a targeted tuning of active material-process-microstructure-property relationships. Porous particles provide pronounced advantages in terms of C-rate capability due to their internal pore structure, enhanced binder penetration, and improved pore-network accessibility. However, these benefits are intrinsically accompanied by a significant reduction in adhesion strength when porous particles are used in single-layer electrodes. This limitation represents a critical obstacle for the industrial implementation of porous active materials.

By spatially separating functional requirements within the electrode thickness, multilayer architectures were shown to effectively mitigate this limitation. Positioning compact particles with higher intrinsic adhesion strength adjacent to the current collector significantly improves the mechanical integrity of the electrode, while porous particles in the upper electrode layers preserve or enhance electrochemical performance. Importantly, even a relatively small fraction of porous particles in the multilayer architecture was sufficient to induce a substantial improvement in C-rate capability, highlighting the dominant role of particle morphology for electrode properties.

A key mechanistic insight gained from this work concerns the role of drying-induced binder migration in PVDF/NMP-based multilayer electrodes. Adhesion strength measurements revealed an exponential dependence on the overall binder content, with electrodes containing lower binder fractions being particularly sensitive to increased drying rates. Despite the deliberate imposition of a binder gradient through multilayer coating, the results indicate that diffusive equilibration of PVDF concentration in NMP occurs prior to capillary-driven binder transport during drying. As a consequence, the final adhesion strength is governed primarily by the total binder content rather than by the local binder concentration in the bottom layer alone.

This behavior fundamentally distinguishes PVDF/NMP-based multilayer systems from aqueous multilayer coatings employing CMC/SBR binder systems, for which literature reports suggest that binder gradients can be preserved and adhesion is predominantly controlled by the layer adjacent to the current collector. The present findings therefore highlight the strong binder-system-specific nature of multilayer electrode processing and underline the necessity of considering solvent-binder interactions when transferring multilayer concepts between different formulation chemistries.

Electrochemical characterization further demonstrated that multilayer electrodes retain a clear performance advantage over single-layer electrodes with compact particles, even under elevated drying rates that promote binder migration. While higher fractions of porous particles lead to superior rate capability, multilayer architectures provide a favorable compromise between electrochemical performance and mechanical robustness. Impedance and resistivity measurements confirm that this performance enhancement arises from a combined reduction in ionic and electronic transport resistances, which cannot be achieved by binder reduction alone in electrodes with compact particles.

Overall, this chapter establishes multilayer electrode architectures as an effective strategy to reconcile competing functional requirements in battery electrodes. The results provide mechanistic insight into how particle morphology, binder system, drying conditions, and electrode architecture interact to define the final electrode properties.

The findings of this work open several promising directions for future research and industrial application. From a scientific perspective, further studies are required to quantitatively resolve the individual contributions of diffusive and capillary transport mechanisms during drying in PVDF/NMP-based multilayer systems. Advanced in-situ or operando characterization techniques, such as spatially resolved spectroscopy could provide direct insight into transient binder concentration profiles and microstructure evolution during drying. Coupling experimental studies with physics-based drying and transport models could enable predictive process design and facilitate the identification of robust processing windows for multilayer electrodes.

From a materials perspective, the multilayer concept offers substantial flexibility for integrating additional functional gradients into electrode architectures. Beyond the combination of compact and porous active materials, future work may explore graded conductive additive distributions, hybrid binder systems, or particle-size gradients to further optimize transport pathways and mechanical stability. In particular, the use of mixed or dual binder systems may provide additional degrees of freedom to control binder mobility and mitigate diffusive equilibration effects observed for PVDF/NMP.

Another approach involves the use of very thin primer coatings as the initial layer. The specific challenge in the production of primers is the requirement for a thin layer with a thickness of less than 3 µm. To create this layer using a slot-die coating process, a wet film of at least 50 µm is necessary, which implies a high proportion of solvents in the slurry. This leads to a series of new questions regarding the optimization of primer coatings. At the same time, there are challenges in the areas of formulation optimization, understanding the suitability of such systems for coating, and the development of optimized drying strategies.

The insights gained in this dissertation are also highly relevant for emerging battery technologies beyond conventional lithium-ion systems. SIBs and other post-lithium technologies often rely on similar electrode processing routes and face comparable trade-offs between performance and mechanical integrity. Multilayer and functionally graded electrode designs may therefore represent a broadly applicable strategy to enhance the performance and manufacturability of next-generation battery electrodes.

In summary, this dissertation chapter contributes fundamental understanding of multilayer electrode processing and provides a framework for engineering active material-process-microstructure-property relationships. The presented results highlight multilayer architectures as a powerful and versatile tool for overcoming intrinsic material limitations and pave

the way toward more robust, high-performance battery electrodes suitable for industrial implementation.

# 8 References


(1) *Handbuch Lithium-Ionen-Batterien*; Korthauer, R., Ed.; Springer: Berlin, Heidelberg, 2013. https://doi.org/10.1007/978-3-642-30653-2.

(2) *Energiespeicher - Bedarf, Technologien, Integration*; Sterner, M., Stadler, I., Eds.; Springer: Berlin, Heidelberg, 2017. https://doi.org/10.1007/978-3-662-48893-5.

(3) Peters, J.; Peña Cruz, A.; Weil, M. Exploring the Economic Potential of Sodium-Ion Batteries. *Batteries* **2019**, *5* (1), 10. https://doi.org/10.3390/batteries5010010.

(4) *BGR - Deutsche Rohstoffagentur - Graphit*. https://www.bgr.bund.de/DERA/DE/Aktuelles/rohstoff_graphit.html (accessed 2024-02-20).

(5) Yabuuchi, N.; Kubota, K.; Dahbi, M.; Komaba, S. Research Development on Sodium-Ion Batteries. *Chem Rev* **2014**, *114* (23), 11636–11682. https://doi.org/10.1021/cr500192f.

(6) Fichtner, M.; Edström, K.; Ayerbe, E.; Berecibar, M.; Bhowmik, A.; Castelli, I. E.; Clark, S.; Dominko, R.; Erakca, M.; Franco, A. A.; Grimaud, A.; Horstmann, B.; Latz, A.; Lorrmann, H.; Meeus, M.; Narayan, R.; Pammer, F.; Ruhland, J.; Stein, H.; Vegge, T.; Weil, M. Rechargeable Batteries of the Future—The State of the Art from a BATTERY 2030+ Perspective. *Advanced Energy Materials* **2022**, *12* (17), 2102904. https://doi.org/10.1002/aenm.202102904.

(7) Alvira, D.; Antorán, D.; Manyà, J. J. Plant-Derived Hard Carbon as Anode for Sodium-Ion Batteries: A Comprehensive Review to Guide Interdisciplinary Research. *Chemical Engineering Journal* **2022**, *447*, 137468. https://doi.org/10.1016/j.cej.2022.137468.

(8) Tapia-Ruiz, N.; Armstrong, A. R.; Alptekin, H.; Amores, M. A.; Au, H.; Barker, J.; Boston, R.; Brant, W. R.; Brittain, J. M.; Chen, Y.; Chhowalla, M.; Choi, Y.-S.; Costa, S. I. R.; Crespo Ribadeneyra, M.; Cussen, S. A.; Cussen, E. J.; David, W. I. F.; Desai, A. V.; Dickson, S. A. M.; Eweka, E. I.; Forero-Saboya, J. D.; Grey, C. P.; Griffin, J. M.; Gross, P.; Hua, X.; Irvine, J. T. S.; Johansson, P.; Jones, M. O.; Karlsmo, M.; Kendrick, E.; Kim, E.; Kolosov, O. V.; Li, Z.; Mertens, S. F. L.; Mogensen, R.; Monconduit, L.; Morris, R. E.; Naylor, A. J.; Nikman, S.; O'Keefe, C. A.; Ould, D. M. C.; Palgrave, R. G.; Poizot, P.; Ponrouch, A.; Renault, S.; Reynolds, E. M.; Rudola, A.; Sayers, R.; Scanlon, D. O.; Sen, S.; Seymour, V. R.; Silván, B.; Sougrati, M. T.; Stievano, L.; Stone, G. S.; Thomas, C. I.; Titirici, M.-M.; Tong, J.; Wood, T. J.; Wright, D. S.; Younesi, R. 2021 Roadmap for Sodium-Ion Batteries. *J. Phys. Energy* **2021**, *3* (3), 031503. https://doi.org/10.1088/2515-7655/ac01ef.

(9) Baumann, M.; Häringer, M.; Schmidt, M.; Schneider, L.; Peters, J. F.; Bauer, W.; Binder, J. R.; Weil, M. Prospective Sustainability Screening of Sodium-Ion Battery Cathode Materials. *Advanced Energy Materials* **2022**, *12* (46), 2202636. https://doi.org/10.1002/aenm.202202636.

(10) Rudola, A.; Rennie, A. J. R.; Heap, R.; Meysami, S. S.; Lowbridge, A.; Mazzali, F.; Sayers, R.; Wright, C. J.; Barker, J. Commercialisation of High Energy Density Sodium-Ion Batteries: Faradion's Journey and Outlook. *J. Mater. Chem. A* **2021**, *9* (13), 8279–8302. https://doi.org/10.1039/D1TA00376C.

(11) Hasa, I.; Mariyappan, S.; Saurel, D.; Adelhelm, P.; Koposov, A. Y.; Masquelier, C.; Croguennec, L.; Casas-Cabanas, M. Challenges of Today for Na-Based Batteries of

the Future: From Materials to Cell Metrics. *Journal of Power Sources* **2021**, *482*, 228872. https://doi.org/10.1016/j.jpowsour.2020.228872.
(12) Stüble, P.; Müller, C.; Klemens, J.; Scharfer, P.; Schabel, W.; Häringer, M.; Binder, J. R.; Hofmann, A.; Smith, A. Enabling Long-Term Cycling Stability of Na3V2(PO4)3/C vs. Hard Carbon Full-Cells. *Batteries & Supercaps* **2024**, *7* (2), e202300375. https://doi.org/10.1002/batt.202300375.
(13) Buechele, S.; Binder, J. R. Partial Replacement of Manganese in Sodium Manganese Hexacyanoferrate for Long-Life Sodium-Ion Cathode Materials. *Meet. Abstr.* **2023**, *MA2023-02* (4), 589. https://doi.org/10.1149/MA2023-024589mtgabs.
(14) Klemens, J.; Wurba, A.; Burger, D.; Müller, M.; Bauer, W.; Büchele, S.; Leonet, O.; Blázquez, J. A.; Boyano, I.; Ayerbe, E.; Ehrenberg, H.; Fleischer, J.; Smith, A.; Scharfer, P.; Schabel, W. Challenges and Opportunities for Large-Scale Electrode Processing for Sodium-Ion and Lithium-Ion Battery. *Batteries & Supercaps* **2023**. https://doi.org/10.1002/batt.202300291.
(15) Diehm, R.; Weinmann, H.; Kumberg, J.; Schmitt, M.; Fleischer, J.; Scharfer, P.; Schabel, W. Edge Formation in High-Speed Intermittent Slot-Die Coating of Disruptively Stacked Thick Battery Electrodes. *Energy Technology* **2020**, *8* (2), 1900137. https://doi.org/10.1002/ente.201900137.
(16) Spiegel, S.; Heckmann, T.; Altvater, A.; Diehm, R.; Scharfer, P.; Schabel, W. Investigation of Edge Formation during the Coating Process of Li-Ion Battery Electrodes. *J Coat Technol Res* **2022**, *19* (1), 121–130. https://doi.org/10.1007/s11998-021-00521-w.
(17) Kumberg, J.; Bauer, W.; Schmatz, J.; Diehm, R.; Tönsmann, M.; Müller, M.; Ly, K.; Scharfer, P.; Schabel, W. Reduced Drying Time of Anodes for Lithium-ion Batteries through Simultaneous Multilayer Coating. *Energy Technology* **2021**. https://doi.org/10.1002/ente.202100367.
(18) Klemens, J.; Schneider, L.; Herbst, E. C.; Bohn, N.; Müller, M.; Bauer, W.; Scharfer, P.; Schabel, W. Drying of NCM Cathode Electrodes with Porous, Nanostructured Particles Versus Compact Solid Particles: Comparative Study of Binder Migration as a Function of Drying Conditions. *Energy Technology* **2022**, 2100985. https://doi.org/10.1002/ente.202100985.
(19) Diehm, R.; Kumberg, J.; Dörrer, C.; Müller, M.; Bauer, W.; Scharfer, P.; Schabel, W. In Situ Investigations of Simultaneous Two-Layer Slot Die Coating of Component-Graded Anodes for Improved High-Energy Li-Ion Batteries. *Energy Technology* **2020**, *8* (5), 1901251. https://doi.org/10.1002/ente.201901251.
(20) Goodenough, J. B.; Park, K.-S. The Li-Ion Rechargeable Battery: A Perspective. *J. Am. Chem. Soc.* **2013**, *135* (4), 1167–1176. https://doi.org/10.1021/ja3091438.
(21) Chen, T.; Ouyang, B.; Fan, X.; Zhou, W.; Liu, W.; Liu, K. Oxide Cathodes for Sodium-Ion Batteries: Designs, Challenges, and Perspectives. *Carbon Energy* **2022**, *4* (2), 170–199. https://doi.org/10.1002/cey2.153.
(22) Zhao, L.; Hu, Z.; Lai, W.; Tao, Y.; Peng, J.; Miao, Z.; Wang, Y.; Chou, S.; Liu, H.; Dou, S. Hard Carbon Anodes: Fundamental Understanding and Commercial Perspectives for Na-Ion Batteries beyond Li-Ion and K-Ion Counterparts. *Advanced Energy Materials* **2021**, *11* (1), 2002704. https://doi.org/10.1002/aenm.202002704.
(23) Liu, Y.; Merinov, B. V.; Goddard, W. A. Origin of Low Sodium Capacity in Graphite and Generally Weak Substrate Binding of Na and Mg among Alkali and

Alkaline Earth Metals. *Proc Natl Acad Sci U S A* **2016**, *113* (14), 3735–3739. https://doi.org/10.1073/pnas.1602473113.
(24) Hou, H.; Qiu, X.; Wei, W.; Zhang, Y.; Ji, X. Carbon Anode Materials for Advanced Sodium-Ion Batteries. *Advanced Energy Materials* **2017**, *7* (24), 1602898. https://doi.org/10.1002/aenm.201602898.
(25) Au, H.; Alptekin, H.; Jensen, A. C. S.; Olsson, E.; O'Keefe, C. A.; Smith, T.; Crespo-Ribadeneyra, M.; Headen, T. F.; Grey, C. P.; Cai, Q.; Drew, A. J.; Titirici, M.-M. A Revised Mechanistic Model for Sodium Insertion in Hard Carbons. *Energy Environ. Sci.* **2020**, *13* (10), 3469–3479. https://doi.org/10.1039/D0EE01363C.
(26) Chakraborty, A.; Kunnikuruvan, S.; Kumar, S.; Markovsky, B.; Aurbach, D.; Dixit, M.; Major, D. T. Layered Cathode Materials for Lithium-Ion Batteries: Review of Computational Studies on LiNi1–x–yCoxMnyO2 and LiNi1–x–yCoxAlyO2. *Chem. Mater.* **2020**, *32* (3), 915–952. https://doi.org/10.1021/acs.chemmater.9b04066.
(27) Jiang, M.; Danilov, D. L.; Eichel, R.-A.; Notten, P. H. L. A Review of Degradation Mechanisms and Recent Achievements for Ni-Rich Cathode-Based Li-Ion Batteries. *Advanced Energy Materials* **2021**, *11* (48), 2103005. https://doi.org/10.1002/aenm.202103005.
(28) Li, C.-C.; Chen, C.-A.; Chen, M.-F. Gelation Mechanism of Organic Additives with LiFePO4 in the Water-Based Cathode Slurries. *Ceramics International* **2017**, *43*, 765–770. https://doi.org/10.1016/j.ceramint.2017.05.315.
(29) Zhao, T.; Li, W.; Traversy, M.; Choi, Y.; Ghahreman, A.; Zhao, Z.; Zhang, C.; Zhao, W.; Song, Y. A Review on the Recycling of Spent Lithium Iron Phosphate Batteries. *Journal of Environmental Management* **2024**, *351*, 119670. https://doi.org/10.1016/j.jenvman.2023.119670.
(30) Wu, H.; Chen, Y.; Wen, T.; Chen, L.; Pu, X.; Chen, Z. Advances in Vanadium-Redoxed Polyanions for High-Voltage Sodium-Ion Batteries. *Batteries* **2023**, *9* (1), 56. https://doi.org/10.3390/batteries9010056.
(31) Akçay, T.; Häringer, M.; Pfeifer, K.; Anhalt, J.; Binder, J. R.; Dsoke, S.; Kramer, D.; Mönig, R. Na 3 V 2 (PO 4 ) 3 ─A Highly Promising Anode and Cathode Material for Sodium-Ion Batteries. *ACS Appl. Energy Mater.* **2021**, *4* (11), 12688–12695. https://doi.org/10.1021/acsaem.1c02413.
(32) Gourang Patnaik, S.; Escher, I.; Ferrero, G. A.; Adelhelm, P. Electrochemical Study of Prussian White Cathodes with Glymes – Pathway to Graphite-Based Sodium-Ion Battery Full Cells. *Batteries & Supercaps* **2022**, *5* (7), e202200043. https://doi.org/10.1002/batt.202200043.
(33) Titirici, M.-M.; Adelhelm, P.; Hu, Y.-S. *Sodium-Ion Batteries: Materials, Characterization, and Technology*, 1st ed.; Titirici, M.-M., Adelhelm, P., Hu, Y. S., Eds.; Wiley-VCH: Weinheim, 2022.
(34) CATL, C. A. T. Co., Ltd. *CATL Unveils Its Latest Breakthrough Technology by Releasing Its First Generation of Sodium-ion Batteries*. https://www.catl.com/en/news/665.html (accessed 2024-02-19).
(35) Vekic, N. *LITHIUM-IONEN-BATTERIEN FÜR DIE ELEKTROMOBILITÄT: STATUS, ZUKUNFTSPERSPEKTIVEN, RECYCLING THINKTANK Industrielle Ressourcenstrategien*; 2020. https://doi.org/10.13140/RG.2.2.14824.70406.
(36) Chayambuka, K.; Mulder, G.; Danilov, D. L.; Notten, P. H. L. From Li-Ion Batteries toward Na-Ion Chemistries: Challenges and Opportunities. *Advanced Energy Materials* **2020**, *10* (38), 2001310. https://doi.org/10.1002/aenm.202001310.
(37) Placke, T.; Kloepsch, R.; Dühnen, S.; Winter, M. Lithium Ion, Lithium Metal, and Alternative Rechargeable Battery Technologies: The Odyssey for High Energy

Density. *J Solid State Electrochem* **2017**, *21* (7), 1939–1964. https://doi.org/10.1007/s10008-017-3610-7.
(38) *Potentials of 46 mm cylindrical cells: On the way to the new standard format*. Fraunhofer Institute for Systems and Innovation Research ISI. https://www.isi.fraunhofer.de/en/blog/themen/batterie-update/46-mm-rundzellen-potenziale-standardformat-batteriezellen.html (accessed 2024-02-23).
(39) *Innovative Technology*. https://www.catl.com/en/research/technology/ (accessed 2024-02-21).
(40) Bauer, A.; Song, J.; Vail, S.; Pan, W.; Barker, J.; Lu, Y. The Scale-up and Commercialization of Nonaqueous Na-Ion Battery Technologies. *Advanced Energy Materials* **2018**, *8* (17), 1702869. https://doi.org/10.1002/aenm.201702869.
(41) *Strong Performance - Faradion*. https://faradion.co.uk/technology-benefits/strong-performance/, https://faradion.co.uk/technology-benefits/strong-performance/ (accessed 2024-02-21).
(42) Liu, H.; Baumann, M.; Dou, X.; Klemens, J.; Schneider, L.; Wurba, A.-K.; Häringer, M.; Scharfer, P.; Ehrenberg, H.; Schabel, W.; Fleischer, J.; Aßen, N.; Weil, M. Tracing the Technology Development and Trends of Hard Carbon Anode Materials - A Market and Patent Analysis. *Journal of Energy Storage* **2022**, *56*, 105964. https://doi.org/10.1016/j.est.2022.105964.
(43) Bauer, W.; Müller, M.; Schneider, L.; Häringer, M.; Bohn, N.; Binder, J. R.; Klemens, J.; Scharfer, P.; Schabel, W.; Ehrenberg, H. Using Hierarchically Structured, Nanoporous Particles as Building Blocks for NCM111 Cathodes. *Nanomaterials* **2024**, *14* (2), 134. https://doi.org/10.3390/nano14020134.
(44) Wagner, A. C.; Bohn, N.; Geßwein, H.; Neumann, M.; Osenberg, M.; Hilger, A.; Manke, I.; Schmidt, V.; Binder, J. R. Hierarchical Structuring of NMC111-Cathode Materials in Lithium-Ion Batteries: An In-Depth Study on the Influence of Primary and Secondary Particle Sizes on Electrochemical Performance. *ACS Applied Energy Materials* **2020**, *3* (12), 12565–12574. https://doi.org/10.1021/acsaem.0c02494.
(45) Schneider, L.; Klemens, J.; Herbst, E. C.; Müller, M.; Scharfer, P.; Schabel, W.; Bauer, W.; Ehrenberg, H. Transport Properties in Electrodes for Lithium-Ion

Batteries: Comparison of Compact versus Porous NCM Particles. *J. Electrochem. Soc.* **2022**, *169* (10), 100553. https://doi.org/10.1149/1945-7111/ac9c37.
(46) He, M.; Mejdoubi, A. EL.; Chartouni, D.; Morcrette, M.; Troendle, P.; Castiglioni, R. High Power NVPF/HC-Based Sodium-Ion Batteries. *Journal of Power Sources* **2023**, *588*, 233741. https://doi.org/10.1016/j.jpowsour.2023.233741.
(47) Hurlbutt, K.; Wheeler, S.; Capone, I.; Pasta, M. Prussian Blue Analogs as Battery Materials. *Joule* **2018**, *2* (10), 1950–1960. https://doi.org/10.1016/j.joule.2018.07.017.
(48) Reid, M. *Sodium-ion batteries: disrupt and conquer?* https://www.woodmac.com/news/opinion/sodium-ion-batteries-disrupt/.
(49) Küpper, D.; Kuhlmann, K.; Wolf, S.; Pieper, C.; Gang Xu; Ahmad, J. The Future of Battery Production for Electric Vehicles. *BCG Global*. September 11, 2018. https://www.bcg.com/publications/2018/future-battery-production-electric-vehicles.
(50) Mohsseni, A. M. *Pathways to Reduce Energy Consumption in Li-ion Battery Cell Manufacturing*. https://www.ukbic.co.uk/white-paper-pathways-to-reduce-energy-consumption-in-lithium-ion-battery-cell-manufacturing (accessed 2024-06-01).
(51) Kwade, A.; Haselrieder, W.; Leithoff, R.; Modlinger, A.; Dietrich, F.; Droeder, K. Current Status and Challenges for Automotive Battery Production Technologies. *Nat Energy* **2018**, *3* (4), 290–300. https://doi.org/10.1038/s41560-018-0130-3.
(52) Kaiser, J.; Wenzel, V.; Nirschl, H.; Bitsch, B.; Willenbacher, N.; Baunach, M.; Schmitt, M.; Jaiser, S.; Scharfer, P.; Schabel, W. Prozess- und Produktentwicklung von Elektroden für Li-Ionen-Zellen. *Chemie Ingenieur Technik* **2014**, *86* (5), 695–706. https://doi.org/10.1002/cite.201300085.
(53) Pillot, C. The Rechargeable Battery Market and Main Trends 2011-2020. **2021**.
(54) Brückner, L.; Frank, J.; Elwert, T. Industrial Recycling of Lithium-Ion Batteries—A Critical Review of Metallurgical Process Routes. *Metals* **2020**, *10* (8), 1107. https://doi.org/10.3390/met10081107.
(55) BMBF-Dachkonzept Batterieforschung – Souveränität für eine nachhaltige Wertschöpfung von morgen.
(56) Gaines, L.; Dai, Q.; Vaughey, J. T.; Gillard, S. Direct Recycling R&D at the ReCell Center. *Recycling* **2021**, *6* (2), 31. https://doi.org/10.3390/recycling6020031.
(57) Mauler, L.; Duffner, F.; Leker, J. Economies of Scale in Battery Cell Manufacturing: The Impact of Material and Process Innovations. *Applied Energy* **2021**, *286*, 116499. https://doi.org/10.1016/j.apenergy.2021.116499.
(58) Müller, M.; Pfaffmann, L.; Jaiser, S.; Baunach, M.; Trouillet, V.; Scheiba, F.; Scharfer, P.; Schabel, W.; Bauer, W. Investigation of Binder Distribution in Graphite Anodes for Lithium-Ion Batteries. *Journal of Power Sources* **2017**, *340*, 1–5. https://doi.org/10.1016/j.jpowsour.2016.11.051.
(59) Pfaffmann, L.; Jaiser, S.; Müller, M.; Scharfer, P.; Schabel, W.; Bauer, W.; Scheiba, F.; Ehrenberg, H. New Method for Binder and Carbon Black Detection at Nanometer Scale in Carbon Electrodes for Lithium Ion Batteries. *Journal of Power Sources* **2017**, *363*, 460–469. https://doi.org/10.1016/j.jpowsour.2017.07.102.
(60) Jaiser, S.; Müller, M.; Baunach, M.; Bauer, W.; Scharfer, P.; Schabel, W. Investigation of Film Solidification and Binder Migration during Drying of Li-Ion

Battery Anodes. *Journal of Power Sources* **2016**, *318*, 210–219. https://doi.org/10.1016/j.jpowsour.2016.04.018.
(61) Li, C.-C.; Wang, Y.-W. Binder Distributions in Water-Based and Organic-Based LiCoO2 Electrode Sheets and Their Effects on Cell Performance. *J. Electrochem. Soc.* **2011**, *158* (12), 1361. https://doi.org/10.1149/2.107112jes.
(62) Klemens, J.; Burger, D.; Schneider, L.; Spiegel, S.; Müller, M.; Bohn, N.; Bauer, W.; Ehrenberg, H.; Scharfer, P.; Schabel, W. Drying of Compact and Porous NCM Cathode Electrodes in Different Multilayer Architectures: Influence of Layer Configuration and Drying Rate on Electrode Properties. *Energy Technology* **2023**, 2300267. https://doi.org/10.1002/ente.202300267.
(63) Morasch, R.; Landesfeind, J.; Suthar, B.; Gasteiger, H. A. Detection of Binder Gradients Using Impedance Spectroscopy and Their Influence on the Tortuosity of Li-Ion Battery Graphite Electrodes. *Journal of The Electrochemical Society* **2018**, *165* (14), 3459–3467. https://doi.org/10.1149/2.1021814jes.
(64) Baunach, M.; Jaiser, S.; Schmelzle, S.; Nirschl, H.; Scharfer, P.; Schabel, W. Delamination Behavior of Lithium-Ion Battery Anodes: Influence of Drying Temperature during Electrode Processing. *Drying Technology* **2016**, *34* (4), 462–473. https://doi.org/10.1080/07373937.2015.1060497.
(65) Westphal, B.; Bockholt, H.; Gunther, T.; Haselrieder, W.; Kwade, A. Influence of Convective Drying Parameters on Electrode Performance and Physical Electrode Properties. *ECS Transactions* **2015**, *64* (22), 57–68. https://doi.org/10.1149/06422.0057ecst.
(66) Westphal, B. G.; Kwade, A. Critical Electrode Properties and Drying Conditions Causing Component Segregation in Graphitic Anodes for Lithium-Ion Batteries. *Journal of Energy Storage* **2018**, *18*, 509–517. https://doi.org/10.1016/j.est.2018.06.009.
(67) Rahani, E. K.; Shenoy, V. B. Role of Plastic Deformation of Binder on Stress Evolution during Charging and Discharging in Lithium-Ion Battery Negative Electrodes. *J. Electrochem. Soc.* **2013**, *160* (8), A1153. https://doi.org/10.1149/2.046308jes.
(68) Liu, W.-R.; Yang, M.-H.; Wu, H.-C.; Chiao, S. M.; Wu, N.-L. Enhanced Cycle Life of Si Anode for Li-Ion Batteries by Using Modified Elastomeric Binder. *Electrochem. Solid-State Lett.* **2004**, *8* (2), A100. https://doi.org/10.1149/1.1847685.
(69) Jaiser, S.; Funk, L.; Baunach, M.; Scharfer, P.; Schabel, W. Experimental Investigation into Battery Electrode Surfaces: The Distribution of Liquid at the Surface and the Emptying of Pores during Drying. *Journal of Colloid and Interface Science* **2017**, *494*, 22–31. https://doi.org/10.1016/j.jcis.2017.01.063.
(70) Jaiser, S.; Kumberg, J.; Klaver, J.; Urai, J. L.; Schabel, W.; Schmatz, J.; Scharfer, P. Microstructure Formation of Lithium-Ion Battery Electrodes during Drying – An Ex-Situ Study Using Cryogenic Broad Ion Beam Slope-Cutting and Scanning Electron Microscopy (Cryo-BIB-SEM). *Journal of Power Sources* **2017**, *345*, 97–107. https://doi.org/10.1016/j.jpowsour.2017.01.117.
(71) Schlünder, E.-U. Drying of Porous Material During the Constant and the Falling Rate Period: A Critical Review of Existing Hypotheses. *Drying Technology* **2004**, *22* (6), 1517–1532. https://doi.org/10.1081/DRT-120038738.
(72) Schlünder, E.-U. Über Den Mechanismus Des Ersten Trocknungsabschnittes Und Seine Mögliche Bedeutung Für Diffusionskontrollierte Katalytische Gasphasen-

Reaktionen. *Chemie Ingenieur Technik* **1988**, *60* (2), 117–120. https://doi.org/10.1002/cite.330600209.
(73) Gnielinski, V.; Mersmann, A.; Thurner, F. *Verdampfung, Kristallisation, Trocknung*; Springer Berlin Heidelberg: Berlin, Heidelberg; s.l., 1993. https://doi.org/10.1007/978-3-642-58073-4.
(74) Krischer, O. *Die Wissenschaftlichen Grundlagen Der Trocknungstechnik*, Zweite erweiterte Auflage.; Springer Berlin Heidelberg: Berlin, Heidelberg; s.l., 1963. https://doi.org/10.1007/978-3-662-26011-1.
(75) Scherer, G. W. Theory of Drying. *Journal of the American Ceramic Society* **1990**, *73* (1), 3–14. https://doi.org/10.1111/j.1151-2916.1990.tb05082.x.
(76) Kumberg, J.; Baunach, M.; Eser, J. C.; Altvater, A.; Scharfer, P.; Schabel, W. Investigation of Drying Curves of Lithium-Ion Battery Electrodes with a New Gravimetrical Double-Side Batch Dryer Concept Including Setup Characterization and Model Simulations. *Energy Technology* **2021**, *9* (2), 2000889. https://doi.org/10.1002/ente.202000889.
(77) Metzger, T.; Tsotsas, E. Influence of Pore Size Distribution on Drying Kinetics: A Simple Capillary Model. *Drying Technology* **2005**, *23* (9–11), 1797–1809. https://doi.org/10.1080/07373930500209830.
(78) Metzger, T.; Irawan, A.; Tsotsas, E. Isothermal Drying of Pore Networks: Influence of Friction for Different Pore Structures. *Drying Technology* **2007**, *25* (1), 49–57. https://doi.org/10.1080/07373930601152640.
(79) Lehmann, P.; Assouline, S.; Or, D. Characteristic Lengths Affecting Evaporative Drying of Porous Media. *Phys Rev E Stat Nonlin Soft Matter Phys* **2008**, *77* (5 Pt 2), 056309. https://doi.org/10.1103/PhysRevE.77.056309.
(80) Shokri, N.; Lehmann, P.; Or, D. Evaporation from Layered Porous Media. *J. Geophys. Res.* **2010**, *115* (B6). https://doi.org/10.1029/2009JB006743.
(81) Jaiser, S.; Sanchez Salach, N.; Baunach, M.; Scharfer, P.; Schabel, W. Impact of Drying Conditions and Wet Film Properties on Adhesion and Film Solidification of Lithium-Ion Battery Anodes. *Drying Technology* **2017**, *35* (15), 1807–1817. https://doi.org/10.1080/07373937.2016.1276584.
(82) Kumberg, J.; Baunach, M.; Eser, J. C.; Altvater, A.; Scharfer, P.; Schabel, W. Influence of Layer Thickness on the Drying of Lithium-Ion Battery Electrodes—Simulation and Experimental Validation. *Energy Technology* **2021**, *9* (5), 2100013. https://doi.org/10.1002/ente.202100013.
(83) Kind, M.; Martin, H. *VDI-Wärmeatlas*; Springer, 2013.
(84) Klemens, J.; Schneider, L.; Burger, D.; Zimmerer, N.; Müller, M.; Bauer, W.; Ehrenberg, H.; Scharfer, P.; Schabel, W. Process and Drying Behavior Toward Higher Drying Rates of Hard Carbon Anodes for Sodium-Ion Batteries with Different Particle Sizes: An Experimental Study in Comparison to Graphite for Lithium-Ion-Batteries. *Energy Technology* **2023**, 2300338. https://doi.org/10.1002/ente.202300338.
(85) Hawley, W. B.; Parejiya, A.; Bai, Y.; Meyer, H. M.; Wood, D. L.; Li, J. Lithium and Transition Metal Dissolution Due to Aqueous Processing in Lithium-Ion Battery Cathode Active Materials. *Journal of Power Sources* **2020**, *466*, 228315. https://doi.org/10.1016/j.jpowsour.2020.228315.
(86) Bockholt, H.; Haselrieder, W.; Kwade, A. Intensive Dry and Wet Mixing Influencing the Structural and Electrochemical Properties of Secondary Lithium-Ion

Battery Cathodes. *ECS Trans.* **2013**, *50* (26), 25–35. https://doi.org/10.1149/05026.0025ecst.
(87) Mezger, T. *Das Rheologie Handbuch: Für Anwender von Rotations- Und Oszillations-Rheometern*; Vinzentz Network: Hannover, 2016.
(88) Malkin, A. Y.; Derkach, S. R.; Kulichikhin, V. G. Rheology of Gels and Yielding Liquids. *Gels* **2023**, *9* (9), 715. https://doi.org/10.3390/gels9090715.
(89) Altvater, A.; Heckmann, T.; Eser, J. C.; Spiegel, S.; Scharfer, P.; Schabel, W. (Near-) Infrared Drying of Lithium-Ion Battery Electrodes: Influence of Energy Input on Process Speed and Electrode Adhesion. *Energy Technology* **2022**, 2200785. https://doi.org/10.1002/ente.202200785.
(90) Fuller, E. N.; Schettler, P. D.; Giddings, J. Calvin. New Method for Prediction of Binary Gas-Phase Diffusion Coefficients. *Ind. Eng. Chem.* **1966**, *58* (5), 18–27. https://doi.org/10.1021/ie50677a007.
(91) Kumberg, J.; Müller, M.; Diehm, R.; Spiegel, S.; Wachsmann, C.; Bauer, W.; Scharfer, P.; Schabel, W. Drying of Lithium-Ion Battery Anodes for Use in High-Energy Cells: Influence of Electrode Thickness on Drying Time, Adhesion, and Crack Formation. *Energy Technology* **2019**, *7* (11), 1900722. https://doi.org/10.1002/ente.201900722.
(92) Lippke, M.; Ohnimus, T.; Heckmann, T.; Ivanov, D.; Scharfer, P.; Schabel, W.; Schilde, C.; Kwade, A. Simulation of Structure Formation during Drying of Lithium-Ion Battery Electrodes Using Discrete Element Method. *Energy Technology* **2023**, *11* (5), 2200724. https://doi.org/10.1002/ente.202200724.
(93) Oehler, D.; Seegert, P.; Wetzel, T. Modeling the Thermal Conductivity of Porous Electrodes of Li-Ion Batteries as a Function of Microstructure Parameters. *Energy Technology* **2021**, *9* (6), 2000574. https://doi.org/10.1002/ente.202000574.
(94) Eser, J. C.; Deichmann, B.; Wirsching, T.; Merklein, L.; Müller, M.; Scharfer, P.; Schabel, W. Diffusion Kinetics of Water in Graphite Anodes for Li-Ion Batteries. *Drying Technology* **2022**, *40* (6), 1130–1145. https://doi.org/10.1080/07373937.2020.1852568.
(95) Heckmann, T.; Eser, J. C.; Altvater, A.; Streller, N.; Scharfer, P.; Schabel, W. Experimental Investigation of the Temperature, Pressure, and Binder System Influence on Vacuum Postdrying Processes and Moisture Management of Li-Ion Battery Electrodes. *Energy Technology* **2022**, *11* (5), 2200859. https://doi.org/10.1002/ente.202200859.
(96) BRUGGEMAN DAG. The Calculation of Various Physical Constants of Heterogeneous Substances. I. The Dielectric Constants and Conductivities of Mixtures Composed of Isotropic Substances. *Annals of Physics* **1935**, *416*, 636–791.
(97) Zehner, P.; Schlünder, E. U. Wärmeleitfähigkeit von Schüttungen Bei Mäßigen Temperaturen. *Chemie Ingenieur Technik* **1970**, *42* (14), 933–941. https://doi.org/10.1002/cite.330421408.
(98) Zehner, P.; Schlünder, E. U. Die Effektive Wärmeleitfähigkeit Durchströmter Kugelschüttungen Bei Mäßigen Und Hohen Temperaturen. *Chemie Ingenieur Technik* **1973**, *45* (5), 272–276. https://doi.org/10.1002/cite.330450509.
(99) Landesfeind, J.; Ebner, M.; Eldiven, A.; Wood, V.; Gasteiger, H. A. Tortuosity of Battery Electrodes: Validation of Impedance-Derived Values and Critical

Comparison with 3D Tomography. *J. Electrochem. Soc.* **2018**, *165* (3), 469–476. https://doi.org/10.1149/2.0231803jes.

(100) Landesfeind, J.; Eldiven, A.; Gasteiger, H. A. Influence of the Binder on Lithium Ion Battery Electrode Tortuosity and Performance. *Journal of The Electrochemical Society* **2018**, *165* (5), 1122–1128. https://doi.org/10.1149/2.0971805jes.

(101) Landesfeind, J.; Hattendorff, J.; Ehrl, A.; Wall, W. A.; Gasteiger, H. A. Tortuosity Determination of Battery Electrodes and Separators by Impedance Spectroscopy. *J. Electrochem. Soc.* **2016**, *163* (7), 1373–1387. https://doi.org/10.1149/2.1141607jes.

(102) Jinasena, A.; Burheim, O. S.; Strømman, A. H. A Flexible Model for Benchmarking the Energy Usage of Automotive Lithium-Ion Battery Cell Manufacturing. *Batteries* **2021**, *7* (1), 14. https://doi.org/10.3390/batteries7010014.

(103) Michaelis, S.; Schütrumpf, J.; Kampker, A.; Heimes, H.; Dorn, B.; Wennemar, S.; Scheibe, A.; Wolf, S.; Smulka, M.; Ingendoh, B.; Thielmann, A.; Neef, C.; Wicke, T.; Weymann, L.; Hettesheimer, T.; Kwade, A.; Gottschalk, L.; Boeselager, C.; Blömeke, S.; Diener, A.; Horstig, M.-W.; Husmann, J.; Kouli, M.; Mund, M.; Ventura Silva, G.; Weber, M.; Podbreznik, M.; Schmetz, A. *Roadmap Battery Production Equipment 2030. Update 2023*; VDMA Verlag, 2023.

(104) d'Ambrosio, E.; Gilbert, D.; Blanc, F.; Cohen, C.; Lemaire, E. Rheology of Suspensions of Cubic Particles. *J. Rheol.* **2025**, *69* (6), 807–828. https://doi.org/10.1122/8.0001045.

(105) Spiegel, S.; Hoffmann, A.; Klemens, J.; Scharfer, P.; Schabel, W. Optimization of Edge Quality in the Slot-Die Coating Process of High-Capacity Lithium-Ion Battery Electrodes. *Energy Technology* **2022**, 2200684. https://doi.org/10.1002/ente.202200684.

(106) Hoffmann, A.; Spiegel, S.; Heckmann, T.; Scharfer, P.; Schabel, W. CFD Model of Slot Die Coating for Lithium-Ion Battery Electrodes in 2D and 3D with Load Balanced Dynamic Mesh Refinement Enabled with a Local-Slip Boundary Condition in OpenFOAM. *J Coat Technol Res* **2022**, 1–12. https://doi.org/10.1007/s11998-022-00660-8.

(107) Hawley, W. B.; Li, J. Electrode Manufacturing for Lithium-Ion Batteries—Analysis of Current and next Generation Processing. *Journal of Energy Storage* **2019**, *25*, 100862. https://doi.org/10.1016/j.est.2019.100862.

(108) Schweizer, P. M. Specific Properties of Slot Coating. In *Premetered Coating Methods*; Springer, Cham, 2022; pp 511–593. https://doi.org/10.1007/978-3-031-04180-8_17.

(109) Müller, M.; Schneider, L.; Bohn, N.; Binder, J. R.; Bauer, W. Effect of Nanostructured and Open-Porous Particle Morphology on Electrode Processing and

Electrochemical Performance of Li-Ion Batteries. *ACS Applied Energy Materials* **2021**, *4* (2), 1993–2003. https://doi.org/10.1021/acsaem.0c03187.
(110) Lim, S.; Ahn, K. H.; Yamamura, M. Latex Migration in Battery Slurries during Drying. *Langmuir* **2013**, *29* (26), 8233–8244. https://doi.org/10.1021/la4013685.
(111) Bird, R. B.; Stewart, W. E.; Lightfoot, E. N. *Transport Phenomena*, Revised second edition.; John Wiley & Sons, Inc: New York ; Chichester ; Weinheim ; Brisbane ; Singapore ; Toronto, 2007.
(112) Stein, M.; Mistry, A.; Mukherjee, P. P. Mechanistic Understanding of the Role of Evaporation in Electrode Processing. *J. Electrochem. Soc.* **2017**, *164* (7), A1616. https://doi.org/10.1149/2.1271707jes.
(113) Zihrul, C.; Lippke, M.; Kwade, A. Model Development for Binder Migration within Lithium-Ion Battery Electrodes during the Drying Process. *Batteries* **2023**, *9* (9), 455. https://doi.org/10.3390/batteries9090455.
(114) Font, F.; Protas, B.; Richardson, G.; Foster, J. M. Binder Migration during Drying of Lithium-Ion Battery Electrodes: Modelling and Comparison to Experiment. *Journal of Power Sources* **2018**, *393*, 177–185. https://doi.org/10.1016/j.jpowsour.2018.04.097.
(115) Keim, N.; Weber, A.; Müller, M.; Burger, D.; Bauer, W.; Scharfer, P.; Schabel, W.; Ehrenberg, H. CMC Staining Method for the Visualization of the Binder Distribution in Water-Based Electrodes with EDS. *ACS Appl. Energy Mater.* **2025**, *8* (7), 4501–4505. https://doi.org/10.1021/acsaem.5c00048.
(116) Buqa, H.; Holzapfel, M.; Krumeich, F.; Veit, C.; Novák, P. Study of Styrene Butadiene Rubber and Sodium Methyl Cellulose as Binder for Negative Electrodes in Lithium-Ion Batteries. *Journal of Power Sources* **2006**, *161* (1), 617–622. https://doi.org/10.1016/j.jpowsour.2006.03.073.
(117) Jeschull, F.; Brandell, D.; Wohlfahrt-Mehrens, M.; Memm, M. Water-Soluble Binders for Lithium-Ion Battery Graphite Electrodes: Slurry Rheology, Coating Adhesion, and Electrochemical Performance. *Energy Technol.* **2017**, *5* (11), 2108–2118. https://doi.org/10.1002/ente.201700200.
(118) Chang, W. J.; Lee, G. H.; Cheon, Y. J.; Kim, J. T.; Lee, S. I.; Kim, J.; Kim, M.; Park, W. I.; Lee, Y. J. Direct Observation of Carboxymethyl Cellulose and Styrene-Butadiene Rubber Binder Distribution in Practical Graphite Anodes for Li-Ion Batteries. *ACS Appl. Mater. Interfaces* **2019**, *11* (44), 41330–41337. https://doi.org/10.1021/acsami.9b13803.
(119) Lim, S.; Kim, S.; Ahn, K. H.; Lee, S. J. The Effect of Binders on the Rheological Properties and the Microstructure Formation of Lithium-Ion Battery Anode Slurries. *Journal of Power Sources* **2015**, *299*, 221–230. https://doi.org/10.1016/j.jpowsour.2015.09.009.
(120) Gordon, R.; Orias, R.; Willenbacher, N. Effect of Carboxymethyl Cellulose on the Flow Behavior of Lithium-Ion Battery Anode Slurries and the Electrical as Well as Mechanical Properties of Corresponding Dry Layers. *J Mater Sci* **2020**, *55* (33), 15867–15881. https://doi.org/10.1007/s10853-020-05122-3.
(121) Kumberg, J.; Bauer, W.; Schmatz, J.; Diehm, R.; Tönsmann, M.; Müller, M.; Ly, K.; Scharfer, P.; Schabel, W. Reduced Drying Time of Anodes for Lithium-Ion Batteries through Simultaneous Multilayer Coating. *Energy Technol.* **2021**, *9* (10), 2100367. https://doi.org/10.1002/ente.202100367.
(122) Froboese, L.; Titscher, P.; Westphal, B.; Haselrieder, W.; Kwade, A. Mercury Intrusion for Ion- and Conversion-Based Battery Electrodes – Structure and

Diffusion Coefficient Determination. *Materials Characterization* **2017**, *133*, 102–111. https://doi.org/10.1016/j.matchar.2017.09.002.

(123) Li, X.; Liu, J.; Banis, M. N.; Lushington, A.; Li, R.; Cai, M.; Sun, X. Atomic Layer Deposition of Solid-State Electrolyte Coated Cathode Materials with Superior High-Voltage Cycling Behavior for Lithium Ion Battery Application. *Energy Environ. Sci.* **2014**, *7* (2), 768–778. https://doi.org/10.1039/C3EE42704H.

(124) Landesfeind, J.; Gasteiger, H. A. Temperature and Concentration Dependence of the Ionic Transport Properties of Lithium-Ion Battery Electrolytes. *J. Electrochem. Soc.* **2019**, *166* (14), 3079–3097. https://doi.org/10.1149/2.0571912jes.

(125) Hein, S.; Danner, T.; Westhoff, D.; Prifling, B.; Scurtu, R.; Kremer, L.; Hoffmann, A.; Hilger, A.; Osenberg, M.; Manke, I.; Wohlfahrt-Mehrens, M.; Schmidt, V.; Latz, A. Influence of Conductive Additives and Binder on the Impedance of Lithium-Ion Battery Electrodes: Effect of Morphology. *J. Electrochem. Soc.* **2020**, *167* (1), 013546. https://doi.org/10.1149/1945-7111/ab6b1d.

(126) Marks, T.; Trussler, S.; Smith, A. J.; Xiong, D.; Dahn, J. R. A Guide to Li-Ion Coin-Cell Electrode Making for Academic Researchers. *Journal of The Electrochemical Society* **2011**, *158* (1), 51. https://doi.org/10.1149/1.3515072.

(127) Liu, G.; Zheng, H.; Kim, S.; Deng, Y.; Minor, A. M.; Song, X.; Battaglia, V. S. Effects of Various Conductive Additive and Polymeric Binder Contents on the Performance of a Lithium-Ion Composite Cathode. *Journal of The Electrochemical Society* **2008**, *155* (12), 887. https://doi.org/10.1149/1.2976031.

(128) Yang, J.; Li, Y.; Mijailovic, A.; Wang, G.; Xiong, J.; Mathew, K.; Lu, W.; Sheldon, B. W.; Wu, Q. Gradient Porosity Electrodes for Fast Charging Lithium-Ion Batteries. *J. Mater. Chem. A* **2022**, *10* (22), 12114–12124. https://doi.org/10.1039/D2TA01707E.

(129) Dai, Y.; Srinivasan, V. On Graded Electrode Porosity as a Design Tool for Improving the Energy Density of Batteries. *J. Electrochem. Soc.* **2016**, *163* (3), 406–416. https://doi.org/10.1149/2.0301603jes.

(130) Neidhart, L.; Fröhlich, K.; Eshraghi, N.; Cupid, D.; Winter, F.; Jahn, M. Aqueous Manufacturing of Defect-Free Thick Multi-Layer NMC811 Electrodes. *Nanomaterials* **2022**, *12* (3), 317. https://doi.org/10.3390/nano12030317.

(131) Liu, D.; Chen, L.-C.; Liu, T.-J.; Chu, W.-B.; Tiu, C. Improvement of Lithium-Ion Battery Performance by Two-Layered Slot-Die Coating Operation. *Energy Technol.* **2017**, *5* (8), 1235–1241. https://doi.org/10.1002/ente.201600536.

(132) Chen, L.-C.; Liu, D.; Liu, T.-J.; Tiu, C.; Yang, C.-R.; Chu, W.-B.; Wan, C.-C. Improvement of Lithium-Ion Battery Performance Using a Two-Layered Cathode by Simultaneous Slot-Die Coating. *Journal of Energy Storage* **2016**, *5*, 156–162. https://doi.org/10.1016/j.est.2015.12.008.

(133) Diehm, R.; Kumberg, J.; Dörrer, C.; Müller, M.; Bauer, W.; Scharfer, P.; Schabel, W. In Situ Investigations of Simultaneous Two-Layer Slot Die Coating of Component-Graded Anodes for Improved High-Energy Li-Ion Batteries. *Energy Technol.* **2020**, *8* (5), 1901251. https://doi.org/10.1002/ente.201901251.

(134) Hoffmann, A.; Klemens, J.; Raupp, S.; Hanske, C.; Lawrenz, N.; Machate, M.; Scharfer, P.; Schabel, W. Optimized Battery Electrodes with Primer Layers by Simultaneous Two-Layer Slot-Die Coating. *Eur. Phys. J. Spec. Top.* **2025**, *234* (11), 3065–3076. https://doi.org/10.1140/epjs/s11734-024-01398-7.

(135) W. S. Schabel; P. S. Scharfer; M. K. Kind. Messung Und Simulation von Konzentrationsprofilen Bei Der Trocknung von Dünnen Filmen Mit Hilfe Der

Konfokalen-Mikro-Raman-Spektroskopie. *Chemie Ingenieur Technik* **2003**, *75* (8), 1105–1106. https://doi.org/10.1002/cite.200390274.
(136) Huggins, R. A. *Advanced Batteries*; Springer US: Boston, MA, 2009. https://doi.org/10.1007/978-0-387-76424-5.
(137) Doppelbauer, M. *Grundlagen der Elektromobilität: Technik, Praxis, Energie und Umwelt*; Springer Fachmedien: Wiesbaden, 2025. https://doi.org/10.1007/978-3-658-44828-8.
(138) Orikasa, Y.; Gogyo, Y.; Yamashige, H.; Katayama, M.; Chen, K.; Mori, T.; Yamamoto, K.; Masese, T.; Inada, Y.; Ohta, T.; Siroma, Z.; Kato, S.; Kinoshita, H.; Arai, H.; Ogumi, Z.; Uchimoto, Y. Ionic Conduction in Lithium Ion Battery Composite Electrode Governs Cross-Sectional Reaction Distribution. *Sci Rep* **2016**, *6* (1), 26382. https://doi.org/10.1038/srep26382.
(139) Nayak, P. K.; Yang, L.; Brehm, W.; Adelhelm, P. From Lithium-Ion to Sodium-Ion Batteries: Advantages, Challenges, and Surprises. *Angew Chem Int Ed Engl* **2018**, *57* (1), 102–120. https://doi.org/10.1002/anie.201703772.
(140) Winter, M.; Besenhard, J. O.; Spahr, M. E.; Novák, P. Insertion Electrode Materials for Rechargeable Lithium Batteries. *Advanced Materials* **1998**, *10* (10), 725–763. https://doi.org/10.1002/(SICI)1521-4095(199807)10:10<725::AID-ADMA725>3.0.CO;2-Z.
(141) Li, D.; Danilov, D.; Zhang, Z.; Chen, H.; Yang, Y.; Notten, P. H. L. Modeling the SEI-Formation on Graphite Electrodes in LiFePO4 Batteries. *J. Electrochem. Soc.* **2015**, *162* (6), A858. https://doi.org/10.1149/2.0161506jes.
(142) Kurzweil, P.; Dietlmeier, O. K. *Elektrochemische Speicher: Superkondensatoren, Batterien, Elektrolyse-Wasserstoff, Rechtliche Rahmenbedingungen*; Springer Fachmedien: Wiesbaden, 2018. https://doi.org/10.1007/978-3-658-21829-4.
(143) Thompson, M.; Xia, Q.; Hu, Z.; Zhao, X. S. A Review on Biomass-Derived Hard Carbon Materials for Sodium-Ion Batteries. *Mater. Adv.* **2021**, *2* (18), 5881–5905. https://doi.org/10.1039/D1MA00315A.
(144) Hu, H.-Y.; Xiao, Y.; Ling, W.; Wu, Y.-B.; Wang, P.; Tan, S.-J.; Xu, Y.-S.; Guo, Y.-J.; Chen, W.-P.; Tang, R.-R.; Zeng, X.-X.; Yin, Y.-X.; Wu, X.-W. A Stable Biomass-Derived Hard Carbon Anode for High-Performance Sodium-Ion Full Battery. *Energy Technology* **2021**, *9* (1), 2000730. https://doi.org/10.1002/ente.202000730.
(145) Kumaresan, T. K.; Masilamani, S. A.; Raman, K.; Karazhanov, S. Zh.; Subashchandrabose, R. High Performance Sodium-Ion Battery Anode Using Biomass Derived Hard Carbon with Engineered Defective Sites. *Electrochimica Acta* **2021**, *368*, 137574. https://doi.org/10.1016/j.electacta.2020.137574.
(146) Dou, X.; Hasa, I.; Saurel, D.; Vaalma, C.; Wu, L.; Buchholz, D.; Bresser, D.; Komaba, S.; Passerini, S. Hard Carbons for Sodium-Ion Batteries: Structure, Analysis, Sustainability, and Electrochemistry. *Materials Today* **2019**, *23*, 87–104. https://doi.org/10.1016/j.mattod.2018.12.040.
(147) Fondard, J.; Irisarri, E.; Courrèges, C.; Palacin, M. R.; Ponrouch, A.; Dedryvère, R. SEI Composition on Hard Carbon in Na-Ion Batteries After Long Cycling: Influence of Salts (NaPF6, NaTFSI) and Additives (FEC, DMCF). *J. Electrochem. Soc.* **2020**, *167* (7), 070526. https://doi.org/10.1149/1945-7111/ab75fd.
(148) Müller, C.; Wang, Z.; Hofmann, A.; Stueble, P.; Liu-Théato, X.; Klemens, J.; Smith, A. Influences on Reliable Capacity Measurements of Hard Carbon in Highly

Loaded Electrodes. *Batteries & Supercaps* **2023**. https://doi.org/10.1002/batt.202300322.

(149) *Lithium nickel manganese cobalt oxide powder; CAS-number: 346414-97-8*. http://www.sigmaaldrich.com/ (accessed 2024-02-20).

(150) Shaju, K. M.; Subba Rao, G. V.; Chowdari, B. V. R. Performance of Layered Li(Ni1/3Co1/3Mn1/3)O2 as Cathode for Li-Ion Batteries. *Electrochimica Acta* **2002**, *48* (2), 145–151. https://doi.org/10.1016/S0013-4686(02)00593-5.

(151) Weber, A.; Keim, N.; Gyulai, A.; Muller, M.; Colombo, F.; Bauer, W.; Ehrenberg, H. The Role of Surface Free Energy in Binder Distribution and Adhesion Strength of Aqueously Processed LiNi0.5Mn1.5O4 Cathodes. *J. Electrochem. Soc.* **2024**. https://doi.org/10.1149/1945-7111/ad3a24.

(152) Weichel, M.; Reder, M.; Daubner, S.; Klemens, J.; Burger, D.; Scharfer, P.; Schabel, W.; Nestler, B.; Schneider, D. Modeling the Drying Process in Hard Carbon Electrodes Based on the Phase-Field Method. *Phys. Rev. Mater.* **2025**, *9* (3), 035403. https://doi.org/10.1103/PhysRevMaterials.9.035403.

(153) Diehm, R.; Müller, M.; Burger, D.; Kumberg, J.; Spiegel, S.; Bauer, W.; Scharfer, P.; Schabel, W. High-Speed Coating of Primer Layer for Li-Ion Battery Electrodes by Using Slot-Die Coating. *Energy Technology* **2020**, *8* (9), 2000259. https://doi.org/10.1002/ente.202000259.

# 9 List of Figures

# 10 List of Tables

# 11 Appendix

## 11.1 Capacity and Transport Resistances in Electrodes

### Capacity

The specific theoretical capacity $q$ in Ah kg$^{-1}$ of an active material is calculated using equation (11.1) by taking into account the number of transferred charges per ion $z$, the Faraday constant $F$ (96485 C mol$^{-1}$ = 96485 · 3600$^{-1}$ Ah mol$^{-1}$), and the molar mass $\widetilde{M}$ of the active material. For both lithium and sodium, the number of transferred charges per ion is identical ($z = 1$, $1 \cdot e^-$).[136]

$$q_{theoretical} = \frac{z \cdot F}{\widetilde{M}} \qquad (11.1)$$

The ion transfer rate through the electrode and electrolyte is limited by diffusion at higher currents. Diffusion limitations caused by higher currents can lead to reversible capacity losses during insertion of ions into or out of the active material or electrodes. If not all ions are de- or intercalated from or into the active material within a certain voltage range, the actual capacity $q_{\text{practical}}$ does not match the theroretical capacity.[9] The practical capacity (equation (11.2)) depends on the current $I$ (Ampere, A), the charging or discharging time t (hour, h), and the mass of active material (kg).

$$q_{practical} = \frac{I \cdot t}{m_{active\ material}} = \frac{I}{C \cdot m_{active\ material}} \qquad (11.2)$$

In the context of investigating the fast-charging capabilities of materials and the resistances of electrodes, the $C$ rate is typically used. The $C$ rate is the inverse of the charging and discharging times. A $C$ rate of 1C means that the discharge current is chosen to fully discharge the cell within one hour. In addition, irreversible capacity losses can occur due to side reactions or changes in electrode volume.[20]

### Transport resistances in electrodes

The potential between the two electrodes ($\Delta E^0 = E^0_{\text{Cathode}} - E^0_{\text{Anode}}$) drives the electrochemical reaction process and is referred to as the Open Circuit Voltage (OCV) at an infinitesimally small current $I$. It arises from the different electrochemical potentials of lithium or sodium in the active material of the cathode and anode. The difference in the chemical potential of lithium or sodium between the anode and cathode is expressed as the difference

in free enthalpy $\Delta_r\tilde{G}$. In contrast to the electrochemical series, in LIB and SIB, the respective metal serves as the reference state for the chemical potential. Equation (11.3) shows the OCV.

$$U_{\mathrm{OCV}} = -\frac{\Delta_r\tilde{G}}{z \cdot F} = E^0_{\mathrm{Cathode}} - E^0_{\mathrm{Anode}} \qquad (11.3)$$

Since the chemical potential of lithium or sodium in the anode and cathode is dependent on the concentration, the cell voltage also varies according to the State of Charge (SoC) of the cell. This dependence is represented by charge and discharge curves. This potential curve depends on the active materials used, transport properties in the electrode and the applied current.

The following section will initially examine the impact of the resistances on the potential curve. An exemplary discharge curve, i.e. the voltage over the capacity, as a function of the set current or C-rate is shown in Figure 11.1. Subsequently, a comprehensive analysis of the underlying causes will be conducted (Figure 11.2). The acquired knowledge can be employed to enhance the performance of active materials and electrodes. Furthermore, the impact of inhomogeneous component distributions resulting from electrode fabrication can be investigated.

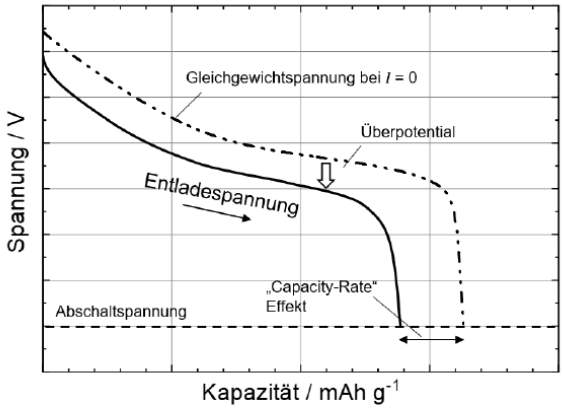


Figure 11.1: Potential-capacity curve for a NCM cathode against metallic lithium. Depending on the applied current, the cut-off voltage is reached early and the discharge capacity is lower. This overpotential can be more pronounced for an inhomogeneous binder distribution. The figure was taken from a student thesis related to this dissertation (see Chapter 14). The figure is based on the illustrations found in the literature.[137]

During the charging and discharching, the electrode's microstructure, binder, network of conductive additive, active material, and particle design create an internal cell resistance $R$ to ions and charge carriers. Accordingly, this resistance can be considered to be the sum of individual resistances. According to Ohm's Law, an potential result as a kinetic phenomena from the resistances multiplied by the corresponding current ($U_{transport} = R \cdot I$). Due to resistances, the actual cell voltage differs from the $U_{OCV}$ (equation (11.3)) as current flows. The overpotential represent a voltage difference between potential profiles of different C-

rates. It increases with increasing current and with increasing electrical and ionic resistances. At high C-rates, a voltage limit is reached at a lower capacity during charging ($U = U_{OCV} + U_{transport}$) or discharging ($U = U_{OCV} - U_{transport}$). A cell with low capacity loss during fast discharge exhibits high C-rate stability or capability.

The transport of ions and electrons is opposed by individual resistances that depend on the current or C-rate and the state of charge. Figure 11.2 shows an electrode and the individual transport resistances as an overview.

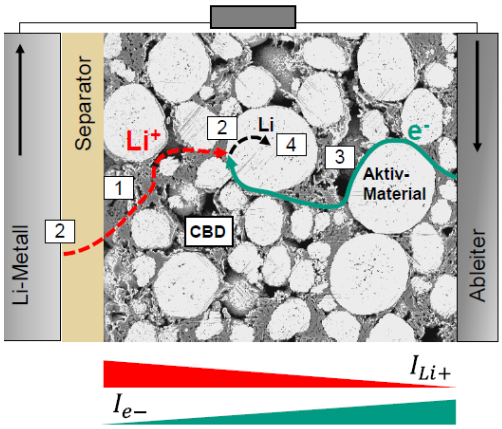


Figure 11.2: Schematic representation of ion and electron transport through an electrode in a half cell configuration (cathode against Li-metal). During battery operation, multiple resistances occur that affect the potential or overpotential. Processing affects these resistances and must be optimized to achieve the best possible performance of the active material. The figure was taken from a student thesis related to this dissertation (see Chapter 14). The figure is based on the illustrations found in the literature.[138]

The overpotentials result from the transition of ions from the electrolyte to the active material (charge transfer), the ohmic resistance during the transport of charge carriers (ohmic resistance), and a concentration gradient during the diffusive transport of ions in the electrolyte and the diffusion within the active material (concentration overpotential):

- Charge transfer overpotential: Ion transfer from the electrolyte into the active material
- Concentration overpotential: Compensation of the lithium or sodium concentration in the electrolyte and in the active material occurs by diffusion
- Ohmic resistance during the transport of charge carriers

## 11.2 LIB and SIB Active Materials

Table 11.1 compares the properties. Both ions belong to the first group of the periodic table and have a weakly bound electron in their outermost electron shell.

Table 11.1: Comparison of the properties of lithium and sodium and their corresponding ions ($Li^+$, $Na^+$).[5] The cost of lithium carbonate ($Li_2CO_3$) and sodium carbonat ($Na_2CO_3$), which are utilized as raw materials in the production of active materials, is also provided.

| | Lithium / $Li^+$ | Sodium / $Na^+$ |
|---|---|---|
| Atomic mass / g $mol^{-1}$ | 6.94 | 23.00 |
| Ionic radius[q] / Å | 0.76 | 1.02 |
| $E^0$ (vs. RHE[r]) / V = W/A | -3.04 | -2.71 |
| Theoretical capacity of metal electrode / mAh $g^{-1}$ | 3861 | 1166 |
| Occurrence in the earth's crust / ppm | 17 | 23600 |
| Cost of alkali carbonate / € $kg^{-1}$ | 35.3 | 0.4 |

Na-ions have one more electron shell than Li-ions, they are 34 % larger and more than three times as heavy as Li-ions. The larger size of the ions results in increased stresses in the material during intercalation and deintercalation. This necessitates the development of new materials and particle morphologies. In addition, sodium also has a lower electrochemical standard potential $E^0$, resulting in a lower energy density compared to lithium.[5,139] The difference is more pronounced when referring to the pure element than when referring to the respective active material.

**Anode material**

On the anode side, Graphite for LIB is compared to Hard Carbon (HC) for SIB, as both are considered state-of-the-art materials. Graphite is the most commonly used anode material for LIB. The intercalation of Li-ions into the graphene layers of the graphitic structure causes an increase in the volume of the active material particles by ~ 10 %.[140] The specific capacity can be calculated from the molar mass (72 g $mol^{-1}$)[141] to 372 mAh $g^{-1}$.[1,136] During the first subsequent deintercalation process, up to ~ 95 % of the Li-ions are recovered, while the remaining amount is irreversibly reacted. This is caused by the formation of a so-called SEI (Solid Electrolyte Interface) layer. The SEI acts as a passivation layer for the graphite anode and is permeable to Li-ions, allowing for the reversible operation of a LIB by preventing further reactions with the electrolyte.[142] After the formation of the SEI, there are no further capacity losses at the graphite electrode when the battery is operated.[140] The literature reports a practical capacity of 360 mAh $g^{-1}$.[9]

In contrast to LIB, graphite is not suitable as an anode material for SIB, because the formation of a Na-graphite intercalation bond is energetically unfavorable and has a very low capacity of 35 - 130 mAh $g^{-1}$.[22–24] Instead, HC (Hard Carbon) can be used and is currently considered as a reference material for SIB in terms of energy density. It is mainly produced through the pyrolysis (e.g. temperatures of 500 - 1500 °C) of oxygen-rich precursors such

[q] 1 Å = $10^{-10}$ m = 0.0001 µm

[r] Reference hydrogen electrode (RHE)

as biomass or synthetic organic materials.[11,143–146] In contrast to graphite, the carbon structure in HC is disordered and exhibits randomly oriented graphitic domains. The structure and properties of HC are influenced by the precursor used and the chosen manufacturing conditions. The different structures allow for the intercalation of Na-ions. For instance, ion storage can occur between the graphene layers in the graphite-like domains or in the micropores. However, the mechanism of Na-ion insertion into HC is still a topic of discussion.[25] A high capacity loss in the first cycles remains a challenge. The side reactions and formation of the SEI layer are still under investigation.[12,147,148]

Practically measured capacities for HC are typically evaluated against metallic sodium in half-cells and range from 200 to 450 mAh $g^{-1}$. The majority of values reported in the literature average at 300-330 mAh $g^{-1}$.[9,14]

**Cathode materials**

Lithium layered transition metal oxides are the largest and most successful group of cathode materials for commercial LIB. An important representative is Lithium-Nickel-Cobalt-Aluminium Oxide (NCA), with high practical capacity of 188 mAh $g^{-1}$ and a high potential of 3.7 V. It is used from Panasonic for the Tesla Model S (2017) with an energy density of 260 Wh $kg^{-1}$.[35] Another important representatives in this material class are the Lithium-Nickel-Manganese Oxides ($LiNi_xCo_yMn_zO_2$, NCM). The numerical sequence of the corresponding material is indicated depending on the stoichiometric ratio of Ni, Mn, and Co. Two examples are the materials $LiNi_{0.33}Mn_{0.33}Co_{0.33}O_2$ (NCM111) and $LiNi_{0.6}Mn_{0.2}Co_{0.2}O_2$ (NCM622), with a high potential of 3.7 V. The included Mn stabilizes the crystal lattice, while Co improves the electrical conductivity and thus the cell performance, and Ni increases the capacity.[1,26] The market trend is moving towards nickel-rich material compositions to increase energy density.[27] With the molar mass of 96.4 g $mol^{-1}$ (NCM111)[149] a theoretical capacity of 278 mAh $g^{-1}$ is obtained. However, due to structural instabilities, only ~ 66 % of the available lithium can deintercalate, resulting in a practical specific capacity of ~ 150 - 160 mAh $g^{-1}$.[9,150] To enhance the performance of NCM cells, particle morphology can be optimized. This work investigates hierarchically structured particles that allow electrolyte penetration into their pore structure. For example, a comparison of ion diffusion in the active material and diffusion in the electrolyte indicates that the diffusion coefficients are much higher in the electrolytic phase (LP30, e.g. $10^{-6}$ $cm^2$ $s^{-1}$) than in the solid phase NCM with ~ $10^{-10}$ $cm^2$ $s^{-1}$.

Layered oxides are used as cathode material for SIB, for example by the company Faradion (United Kingdom) or HiNa Battery Technology Co., Ltd. (China). An example of a layered oxide as a cathode material for SIB that does not contain cobalt is P2-$Na_{0.67}MnO_2$ (NMO). The practical capacity of this material class is with 175 mAh $g^{-1}$ similar to that of layered oxide for LIB. However, due to the lower cell voltage (2.8 V), the specific energy is lower. Higher capacities and potentials can be achieved by optimizing material compositions.[9]

Lithium-Iron-Phosphate ($LiFePO_4$ or LFP) is considered one of the cathode materials for the next generation of LIB due to its electrochemical properties, durability, safety, and the fact that it is made from non-toxic and non-critical raw materials.[28,29] According to the literature, Tesla has switched to LFP batteries for the Model 3 and Model Y since 2021. Similarly, the Volkswagen Group and Ford Group have gradually incorporated LFP batteries into their electric vehicles (EV).[29] LFP exhibits high cycle stability due to the low volume expansion of the active material during battery operation.[1] One challenge in using LFP as a cathode material is its low electronic and ionic conductivity. To increase electronic conductivity, a carbon coating is applied to the LFP particles. To enhance ion conductivity within the LFP active material particles, LFP is produced as primary particles with a diameter of 200 nm and agglomerated into secondary particles (hierarchically structured particles) with a particle size of ~ 5-10 µm.[1] By this special particle design a capacity of ~ 165 mAh $g^{-1}$ at a potential of ~ 3.5 V can be achieved in practical operation. This corresponds to 97 % of the theoretical capacity of 170 mAh $g^{-1}$.[1] Similar to LFP, there is also Sodium-Iron-Phosphat ($NaFePO_4$, NFP), which however has a low potential (~2.7 V) and lower practical capacity of 152 mAh $g^{-1}$. Another representative of phosphates for SIB is $Na_3V_2(PO_4)_3$ (NVP), which belongs to the NASICON (sodium(NA) Super Ionic CONductors) structures. It is characterized by excellent cycle stability and rate capability at higher currents, as well as a high voltage of 3.4 V.[12] The theoretical capacity is 118 mAh $g^{-1}$, while its practical capacity is around 112 mAh $g^{-1}$.[14,30,31] The theoretical and practical capacity can be increased by integrating fluorine to 134 mAh $g^{-1}$. Similar to LFP, NVP also exhibits low electrical conductivity. Therefore, a special particle design is required for optimal performance, which includes nanostrucutring as well as carbon to enable the electrolyte filling up to the core of the material.

Prussian Blue Analogues (PBA) are also polyanion types and promising candidates as cathode materials for SIB, due to promising capacity, discharge potential (2.9-3.5 V) and production with available, low-cost raw materials (e.g. CATL, Natron Energy, Altris).[32,33] The robust three-dimensional lattice structure allows for high conductivity of the alkali ions, making PBA particularly suitable for high-performance applications. However, their low electric conductivity and the low cycle stability still limits their further application and needs adjustment.[13] Depending on the exact composition of the material, practical values of for example 103 - 170 mAh $g^{-1}$ can be achieved.[9,14] Prussian White (PW) $Na_2Fe[Fe(CN)_6]$ has a theoretical capacity of 171 mAh $g^{-1}$.[32] Because of the low density, only a lower volumetric energy density can be achieved.[11,47] A special characteristic is that the active material particles have a cubic shape.

## 11.3 Local Heat and Mass Transfer

A new experimental drying setup for simultaneous measurement of film shrinkage and pore emptying during drying was developed. During drying, the film is subjected to a lateral hot-

air flow, resulting in initially position-dependent local heat and mass transfer coefficients due to boundary layer development.

The local mass transfer coefficient ($\beta_{\mathrm{s,g,local}}$) depending on the overflow length x is calculated using the local Sherwood-number ($Sh_{\mathrm{x}}$, equations (11.4) and (11.5)).

$$Sh_{\mathrm{x}} = \frac{\beta_{\mathrm{s,g,local}} \cdot x}{D_{\mathrm{s,g}}} = 0.332 \cdot \sqrt{Re_{\mathrm{x}}} \cdot \sqrt[3]{Sc} \qquad (11.4)$$

The Schmidt number $Sc$ and the Reynolds number $Re$ are calculated using the kinematic viscosity $v$, the air velocity $u$ and the diffusion coefficient $\mathrm{D_{1,g}}$. Note that the Schmidt number is independent of the overflow length.

$$Sc = \frac{v}{\delta_{s,g}} \; and \; Re_{\mathrm{x}} = \frac{u\,x}{v} \qquad (11.5)$$

The Lewis analogy can be used to calculate the heat transfer coefficient from the mass transfer coefficient (equation (2.12) and (2.13)). The course of the heat and mass transfer coefficient is shown in Figure 11.3.

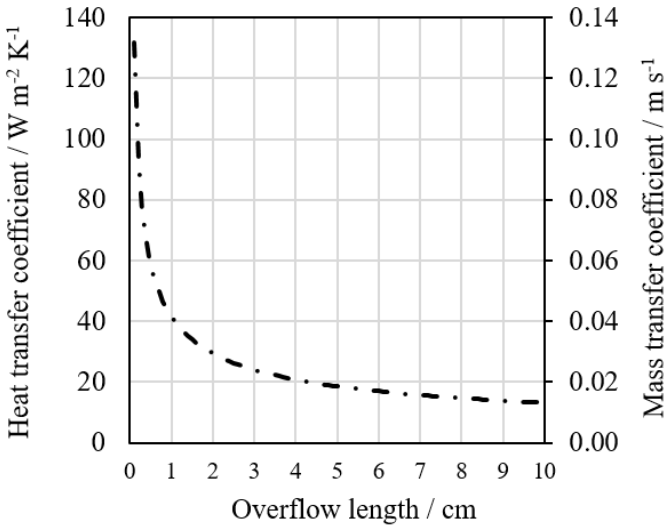


Figure 11.3: Local heat transfer coefficient depending on the overflow length. It is assumed that the thermal and mass boundary layers begin at the same position.

After an initial distance (start-up phase), the dependence of the heat transfer coefficient on the distance (direction of air flow) decreases. The measurement is made at a point where the heat and mass transfer coefficient is approximately constant.

## 11.4 Drop-In Capability: Material-Dependent Electrode Manufacturing of LIB vs. SIB

### 11.4.1 Wet Film Thickness

The aim is to describe the course of the film drying process (film shrinkage profile) as it depends on the material system and to identify the parameters that are crucial. A comprehensive understanding for the application of a process control for an industrial drying process based on the material properties of the active material is to be achieved.

The production of electrodes requires consideration of several parameters, including the necessary wet film thickness, which depends on the areal mass loading of the required dry electrode. The wet film thickness can be calculated by the desired areal mass loading divided by the solid content of the slurry and the density of the slurry, as shown in equation (11.6).

$$h_{\mathrm{wet}} = \frac{m_{\mathrm{areal}}^{\mathrm{dry}}}{x_{\mathrm{solids}}} \cdot \frac{1}{\rho^{slurry}} \qquad (11.6)$$

Figure 11.4 shows the wet film thickness of coated slurries for LIB and SIB anode and cathode electrodes as a function of the areal capacity.

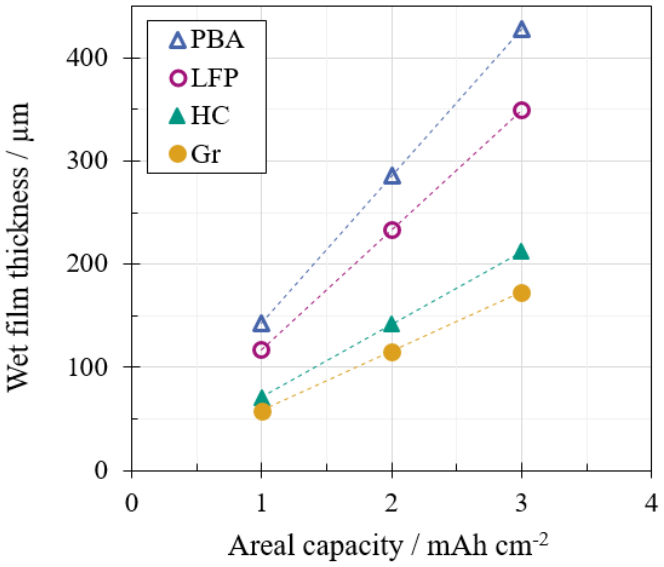


Figure 11.4: The wet film thickness is calculated as a function of areal capacity. As the areal capacity increases, the difference in wet film thickness between LIB and SIB increases. In addition to the capacity and electrode composition, the wet film thickness is also dependent on the density of the active material. For different areal capacity, the wet film thickness of SIB anodes is about 23% higher and of SIB cathodes about 22 % higher than for LIB.

The necessary thickness of the wet coating to achieve a specified areal mass loading is directly proportional to the required areal capacity ($h_{wet} \sim c_{area}$). For all areal capacities, the

wet coating thickness is 22-23% higher for SIB cathodes and anodes than for LIB ones. However, the absolute differences in wet coating thickness increase as the areal capacities become higher. It is noteworthy that the wet film thicknesses of PBA and LFP are more different from each other than would be suggested by the required areal mass loading. Compared to the areal mass loading shown in Figure 3.2, differences between the materials are more pronounced as the wet film thickness depends on the volume fraction and, consequently, on the density of the active material.

The difference in particle density affects not only the slurry viscosity but also the required coating thickness. Higher areal mass loadings or wet film thicknesses may require additional investment in larger mixers, feed tanks, and pumping system. If a production line has been configured for high-capacity electrodes, producing larger volumes or pumping higher volume flows should not be a challenge. In general, a reduction in wet film thickness for the same areal mass loading of the electrode can be achieved by increasing the active material content, solid content, specific capacity, or density of the active material.

### 11.4.2 End of Film Shrinkage

To illustrate the relationship of film shrinkage and solvent mass fraction for all material systems used, Figure 11.5 shows the normalized decrease in film thickness during drying.

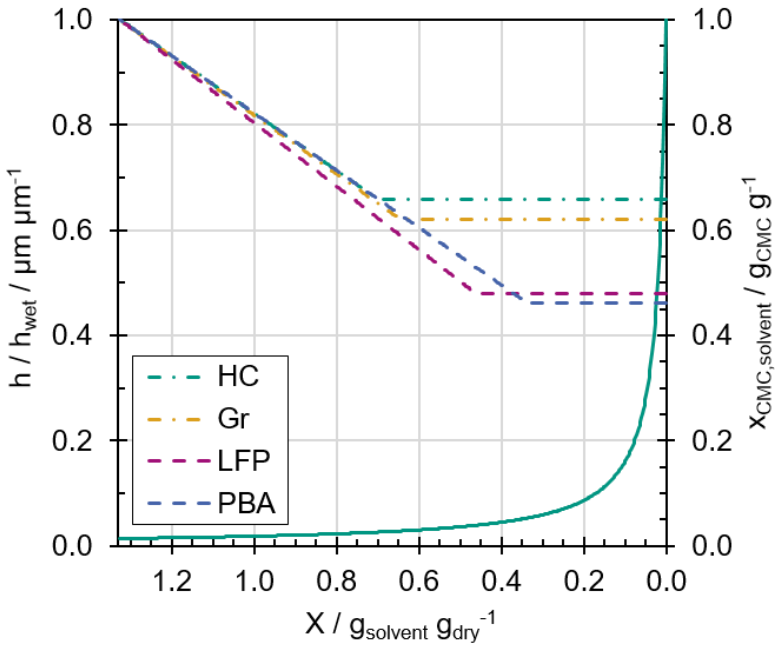


Figure 11.5: Drying progress: Reduction in film thickness as a function of the solvent content for water-based slurry drying depending on different active materials. The end of film shrinkage terminates for anodes and for cathodes at different level of solvent content. Lower solvent contents appear for lower electrode porosity and/or higher density (cathodes) of the active material.

Two regimes appear, one for the anodes and one for the cathodes. It can be seen that the solvent content at the end of film shrinkage is different for all material systems. The solvent

content at the end of film shrinkage for Graphite and HC ranges from 39 wt-% to 41 wt-%. For LFP, this value of about 32 wt-% is considerably lower due to the higher density of the dry mixture. With regard to the cathode, NCM (e.g. NCM622, 4.6 g $cm^{-3}$)[62] represents an example of an active material with an even higher density compared to LFP. The solvent mass fraction at the end of film shrinkage is only about 17 wt-% (assumed same electrode composition as for LFP and an electrode porosity of 45 %[62]).

With the knowledge of the end of film shrinkage for the different active material systems, the CMC concentration at the beginning of the pore emptying can be calculated (see Section 11.4.3).

## 11.4.3 CMC-Concentration Depending on End Film Shrinkage

To assess the viscosity conditions within the actual pore structures investigated in this work, calculations of the end of film shrinkage and the viscosity of the CMC solution within the pores are provided in this section. These results are incorporated into the subsequent discussion of the experimental findings on pore emptying.

In order to develop a hypothesis regarding the onset of pore emptying and to gain insight into the conditions that prevail during this process, the concentration of the CMC solution within the pores at the end of the film shrinkage is examined. This is done on the basis of the data presented in Figure 11.5, which illustrates the solvent content at the end of the film shrinkage.

**Viscosity of CMC-solution**

Figure 11.6 illustrates how the viscosity of CMC-water solutions changes depending on the concentration of CMC. Furthermore, the figure illustrates the calculated concentrations of the CMC-water solutions at the end of film shrinkage, which are dependent on the active material.

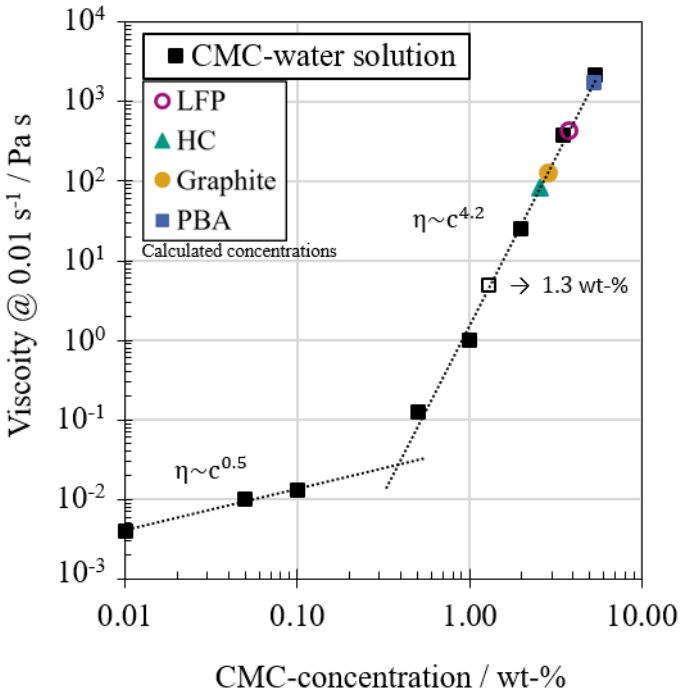


Figure 11.6: Viscosity of CMC-water solutions with increasing CMC concentration. Two distinct regions are observed, wherein the viscosity exhibits an exponential increase with concentration. At a specific concentration, referred to as the overlap concentration, there is an entanglement of the polymer chains, which has a notable impact on the viscosity of the system. The CMC-water solution used has an overlap concentration of 0.4 wt-%. The initial concentration of the CMC in the slurries is 1.3 wt-%, based on the water content. This means that the CMC is already entangled at the beginning of the drying process, which will be discussed further in Section 3.2.5. The calculated CMC concentrations are given for LFP and Graphite at the time of the end of film shrinkage, assuming a fully saturated pore network.

The relationship between the concentration and the viscosity of the CMC solution is exponential. The viscosity increase slope seems to change at a concentration of 0.4 wt-%, which is known as the overlap concentration. At the beginning of the drying process, the concentration of CMC in all slurries is 1.3 wt-% (based on the water content), which exceeds the overlap concentration. Section 3.2.5 will provide a more detailed examination of the relationship between this phenomenon and the migration of binders.

The CMC concentration for HC and Graphite is about 2.4 - 2.7 wt-%, while for LFP and PBA it is 3.9 - 5.2 wt-%. It needs to be investigated whether this affects the capillary pore emptying mechanism. A comparatively higher viscosity of the liquid in the capillary network could increase the flow resistance. Based on the examination of the viscosity of the CMC-water solutions, this could mean that the pore breakthrough for slurries containing LFP as an active material, for example, occurs with a delay than for slurries containing graphite.

### 11.4.4 Pore Breakthrough Depending on Drying Rate and Electrode Thickness

The end of film shrinkage is measured experimentally, simultaneously with the beginning of pore emptying to show potential effects of the active material and drying conditions on the pore breakthrough. The results are summarized in Figure 11.7 as the measured ratio of the time of first visible pore emptying on the underside of the wet film ($t_{1st\ pore}$) to the time at which film shrinkage is completed ($t_{EOFS}$) for a dry film thickness of approximately 100 µm for the different material systems.

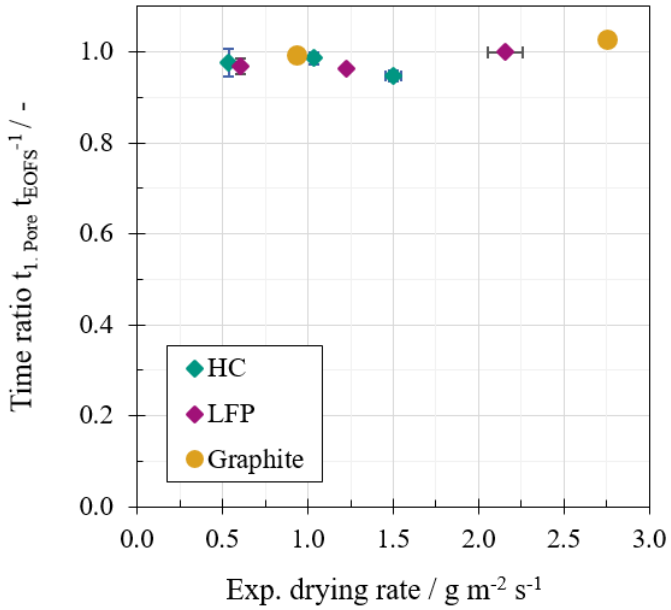


Figure 11.7: Ratio of the time of first visible pore emptying on the underside of the wet film ($t_{1st\ pore}$) to the time at which film shrinkage is completed ($t_{EOFS}$) for different active material systems and drying rates. For all investigated active materials and drying rates, pore breakthrough coincides with the end of film shrinkage ($t_{1st\ pore} = t_{EOFS}$), demonstrating the onset of pore emptying is independent of material system and drying rate.

For all investigated active material systems and drying rates, pore breakthrough consistently occurs at the completion of film shrinkage ($t_{1st\ pore} = t_{EOFS}$), indicating that the onset of pore emptying is independent of both the material system and the applied drying conditions.

It could be also assumed that with thicker electrodes, the pore breakthrough occurs with a delay, because increasing the distance between the electrode surface and the bottom of the electrode results in a compensation of capillary forces by higher friction losses and retard the pores from breaking through. In contrast, the experimental examination of pore breakthrough for thick graphite anodes in high-energy applications suggested that a breakthrough

can occur before the theoretical end of film shrinkage[82] but the drying experiment to determine the drying rate and the observation pore breakthrough were conducted in separate experiments, which introduces the possibility of errors.

LFP and HC electrodes with approximately double the thickness of the layer show simultaneous onset of pore breakthrough with the end of film shrinkage at a drying rate of 1 g $m^{-2}s^{-1}$. For HC, a mean time ratio of 0.99 is obtained at a mean layer thickness of ~200 µm. LFP also shows a mean time ratio of 1.01 at a layer thickness of ~180 µm. This holds even for an extreme case with a layer thickness of ~350 µm examined for LFP, with a time ratio of 1.00 determined. Thus, the occurrence of pore breakthrough before the end of film shrinkage cannot be confirmed.

## 11.4.5 Electrode Characterization

Dry film thickness, areal mass loading, and electrode porosity of non-calendered graphite electrodes for a target areal capacity of 1, 2 and 3 mAh $cm^{-2}$. Values represent averages over all electrodes produced at drying rates of 0.75 to 3 g $m^{-2}s^{-1}$.

Table 11.2: Dry film thickness, areal mass loading, and electrode porosity of non-calendered graphite electrodes for a target areal capacity of 1, 2 and 3 mAh $cm^{-2}$. Values represent averages over all electrodes produced at drying rates of 0.75 to 3 g $m^{-2}s^{-1}$.

| | Gr | | | HC | | | LFP | | | PBA | | |
|---|---|---|---|---|---|---|---|---|---|---|---|---|
| Areal capacity / mAh $cm^{-2}$ | 1 | 2 | 3 | 1 | 2 | 3 | 1 | 2 | 3 | 1 | 2 | 3 |
| Dry coating thickness / µm | 36 ± 3 | 67 ± 3 | 101 ± 3 | 56 ± 5 | 93 ± 1 | 143 ± 4 | 70 ± 4 | 104 ± 2 | 152 ± 5 | 72 ± 6 | 128 ± 2 | 162 ± 7 |
| Areal mass loading / g $m^{-2}$ | 29 ± 1 | 60 ± 1 | 91 ± 1 | 40 ± 2 | 76 ± 1 | 118 ± 2 | 79 ± 9 | 130 ± 2 | 200 ± 2 | 77 ± 1 | 155 ± 3 | 210 ± 4 |
| Density dry mixture / kg $m^{-3}$ | 2136 | | | 1970 | | | 2992 | | | 1959 | | |
| Electrode porosity / % | 62 ± 1 | 58 ± 2 | 57 ± 1 | 64 ± 1 | 58 ± 1 | 58 ± 1 | 62 ± 2 | 58 ± 1 | 56 ± 1 | 47 ± 1 | 38 ± 1 | 33 ± 2 |
| Solvent loading $X_{EOFS}$ / g $g^{-1}$ | 0.77 | 0.64 | 0.63 | 0.88 | 0.70 | 0.70 | 0.55 | 0.46 | 0.43 | 0.44 | 0.31 | 0.25 |

## 11.4.6 Adhesion Strength Depending on Areal Mass Loading

Figure 11.8 shows the adhesion force for increasing areal capacity. The anode ad cathode electrodes were manufactured using the same drying rate (0.75 g $m^{-2}s^{-1}$).

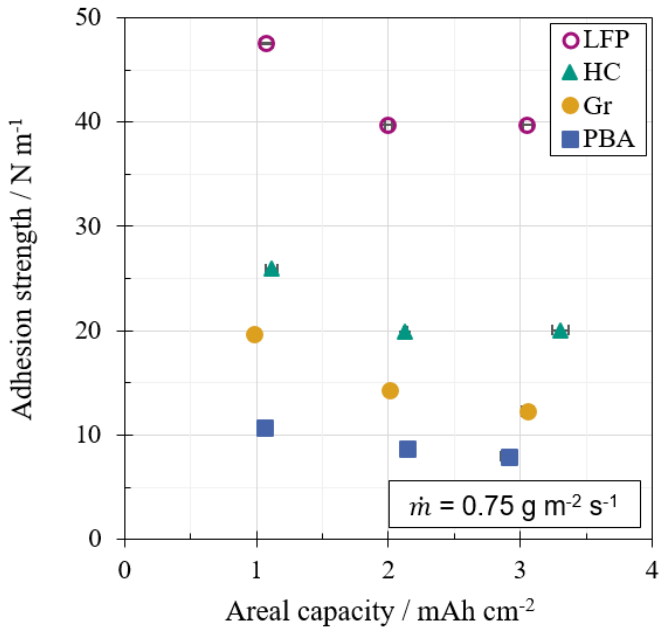


Figure 11.8: Adhesion strength (90° peel test) as a function of areal capacity for LIB and SIB anodes and cathodes manufactured at a low drying rate of 0.75 g $m^{-2}s^{-1}$.

The results demonstrate that electrodes with lower areal mass loading exhibit superior adhesion strength compared to electrodes with higher areal mass loading. Increasing the layer thickness appears to cause the failure mechanism at the interface to the current collector foil to occur at lower force. There may be an effect due to pore emptying and binder migration. It is possible that the capillary action within the network increases due to the higher layer thickness, resulting in more binder being carried away. However, differentiation is required with regard to the course of adhesion strength in relation to increasing areal mass loading. The adhesion strength decreases approximately linearly for Graphite and PBA. When comparing the adhesion strength curves of LFP and HC electrodes, an increase in areal capacity results in a plateau formation in both cases. It may indicate that the binder is better fixed for HC and LFP electrodes, as further increasing the layer thickness does not lead to a further decrease in adhesion strength. It could be hypothesized that LFP and HC electrodes exhibit better fixation compared to Graphite, resulting in a lower decrease in adhesion strength with increasing drying rate. In other words, based on the results, it could be assumed that binder migration is reduced when using LFP and HC compared to Graphite.

## 11.5 Hard Carbon Electrodes

### 11.5.1 Particle Size Distribution

The particle size was determined by laser diffraction (Horiba LA950, Retsch Technology). For this purpose, the active materials are dispersed in 2-propanol.

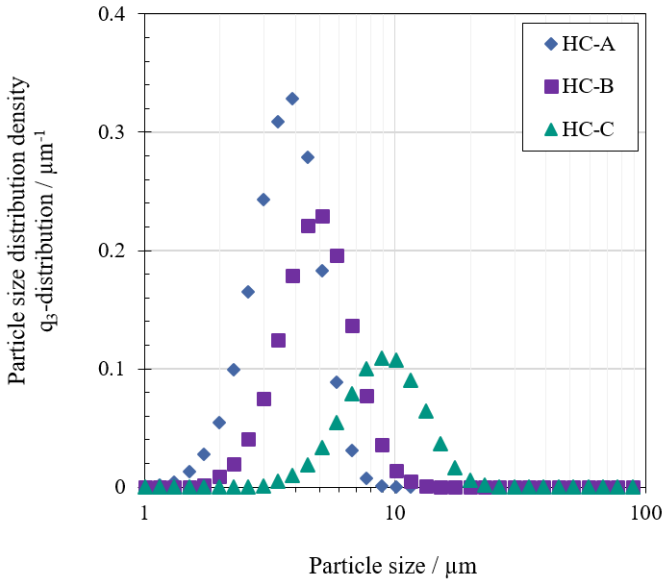


Figure 11.9: Particle size distribution of the different HC investigated.

### 11.5.2 Adhesion

It is assumed that the course of the adhesion strength is also influenced by the current collector. There are hardly any studies on this in the current literature, although an influence of the surface energy is suspected.[151] Therefore, it is assumed that the adhesion strength profiles of the electrodes made from different materials and coated on the same current collector are highly comparable.

Figure 11.10 shows the reference adhesion strength of Graphite, HC-A, and HC-C electrodes coated on copper current collector foil and dried with a drying rate of 0.75 g $m^{-2}s^{-1}$. The data is compared to HC-A and HC-C electrodes on an aluminum current collector foil.

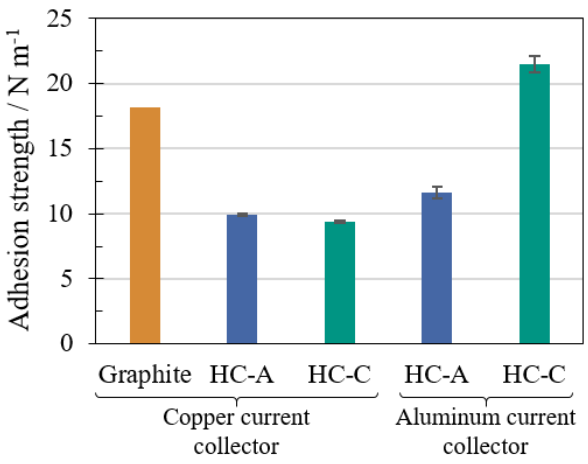


Figure 11.10: Reference adhesion strength of Graphite, HC-A and HC-C electrodes coated on the same copper current collector with the areal capacity of about 2.2-2.3 mAh $cm^{-2}$. The electrodes consisting of HC-A and HC-C active material exhibit the same adhesion strength on copper current collectors. However, on aluminum current collectors, HC-C electrodes show an increased adhesion strength.

The comparison of the adhesive strength values of HC-A and HC-C on the aluminum current collector shows a significant influence on the absolute adhesion strength.

### 11.5.3 Porosity and Pore Size Distribution Depending on Drying Rate

The HC slurries were dried at different drying rates and geometric porosity was determined from the dry electrodes by area weight and film thickness (see Figure 11.11).

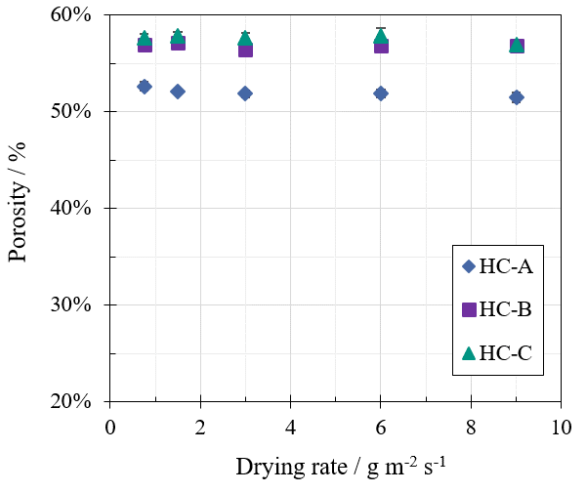


Figure 11.11: Porosity of HC-A, HC-B, and HC-C electrodes dried at different drying rates.

The porosity of the electrodes is observed to remain approximately constant, despite their fabrication being conducted at significantly different drying rates.

Figure 11.12 shows the pore size distribution for electrodes made with HC-A, HC-B, and HC-C to show the influence of the particle size on the pore size. The figure also shows the pore size distribution of HC-A and HC-C electrodes which were produced using different drying rates.

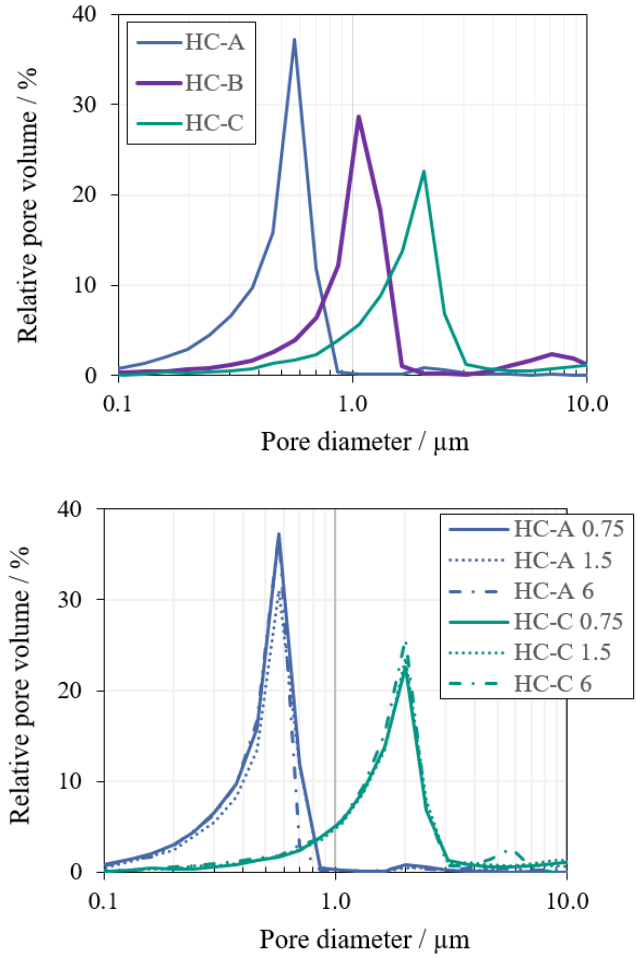


Figure 11.12: Pore size distribution measured by mercury intrusion for HC-A, HC-B, and HC-C electrodes. The HC-A electrodes are dominated by pores at 0.6 µm, HC-B at 1.1 µm, and HC-C at 2 µm. The pore size distribution for HC-A and HC-C electrodes which are dried at three different drying rates is also shown. The pore size distribution is not influenced by the drying rate.

The pore size distribution remains unchanged with increasing drying rate. As particle size increases, the dominant pore size of the electrodes also increases (HC-A $x_{50}$ = 3.7 µm corresponds to $d_{pore,peak}$ = 0.6 µm and HC-C $x_{50}$ = 9.4 µm to $d_{pore,peak}$ = 2 µm).

shows an overview of the geometric porosity by determining the areal mass loading and the electrode thickness as well as the porosity from Hg-porosimetry.

Table 11.3: Overview of the geometric porosity and porosity measured by Hg-intrusion.

| Name | Geometric porosity / % | Porosity (Hg-intrusion) / % |
|---|---|---|
| HC-A | 52.0 ± 0.3 | 43.0 |
| HC-B | 56.8 ± 0.3 | 46.6 |
| HC-C | 57.5 ± 0.6 | 47.1 |

The porosity determined by the mercury intrusion method is lower than the geometrically calculated porosity for all electrodes, since the measurement is incapable of determining closed pores.[122] The SEM cross-sectional image of an HC-C electrode (Figure 11.13) demonstrates the presence of closed pores within the active material, thereby supporting the hypothesis derived from existing literature on the subject.

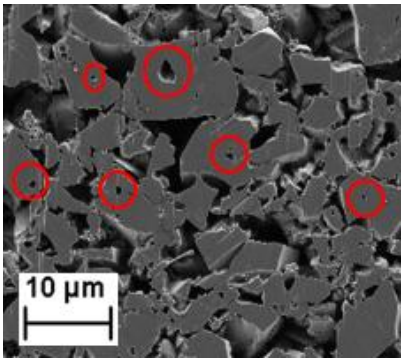


Figure 11.13: SEM cross-sectional image of an HC-C electrode. The pores present in the active material particles are indicated by the red circles.

A cross-sectional image of a graphite electrode with a non-spherical graphite (SMGA, Hitachi Chemical Co. Ltd., Japan) with a particle size of $x_{50}$ = 18.4 µm is shown in Figure 1 to facilitate comparison of the particles and microstructure between graphite and hard carbon.

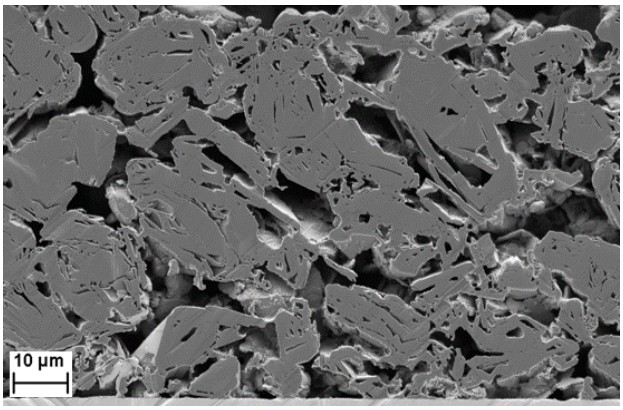


Figure 11.14: SEM cross-sectional image of a graphite anode with non-spherical SMGA particles with a particle diameter of $x_{50}$ = 18.4 µm.

The fabrication of this electrode was conducted in accordance with the identical procedures and electrode composition as the HC electrodes examined in this study. A significant difference in the morphology of the particles and the size of the pores is evident when compared to the HC electrodes examined (see Figure 4.4).

### 11.5.4 Pore Breakthrough Depending on Particle Size

The end of film shrinkage is measured experimentally, simultaneously with the beginning of pore emptying to show potential effects of the active material and drying conditions on the pore breakthrough. The results are summarized in Figure 11.15 as the measured time ratio $t_{1st\,pore}\ t_{EOFS}^{-1}$ depending on the active materials.

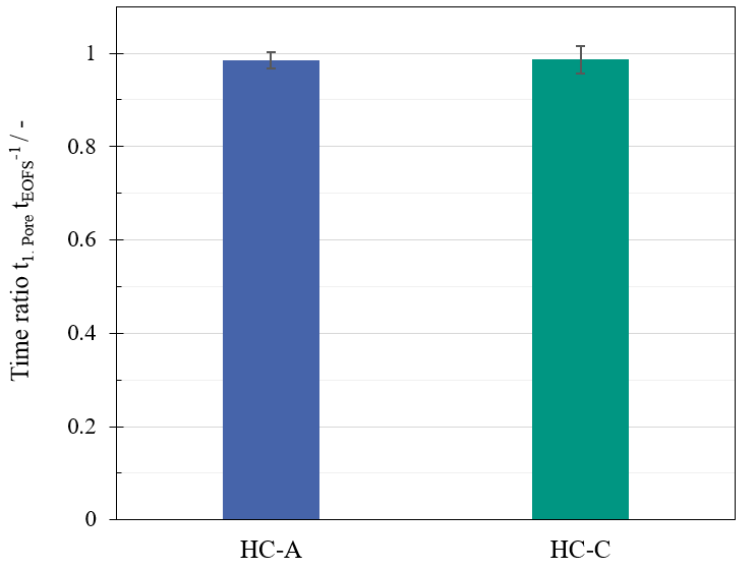


Figure 11.15: The first pore appears at the bottom of the microstructure coincides with the end of film shrinkage the material systems investigated. A time range is specified to account for accuracy in determining the end of film shrinkage and the beginning of pore emptying.

The first pore is visible on the bottom of the substrate, if the film shrinkage is finished ($t_{EOFS} \approx t_{1st\,pore}$) for HC-A and HC-C. Thus, the onset of capillary transport during drying coincides with the end of film shrinkage.

Further investigations using simulations of pore emptying showed that the pore size or the behavior of pore emptying is only influenced by the pore size if the viscosity of the liquid in the pores is greatly reduced. If the viscosity of the liquid in the pore spaces is reduced, emptying occurs as a liquid front. No pore breakthrough to the lower end of the electrode structure can be observed.[152]

### 11.5.5 Binder Migration: Influence of Binder System

The aim of the following investigations is to examine whether the observed differences in the drying behavior of electrodes with different particle sizes depend primarily on the binder system used. For this purpose, electrodes based on two hard carbon materials with different mean particle sizes (HC-A and HC-C) were prepared using the binder PVDF. NMP was used as the solvent. The adhesion strength of the electrodes was investigated as a function of the drying rate (see Figure 11.16).

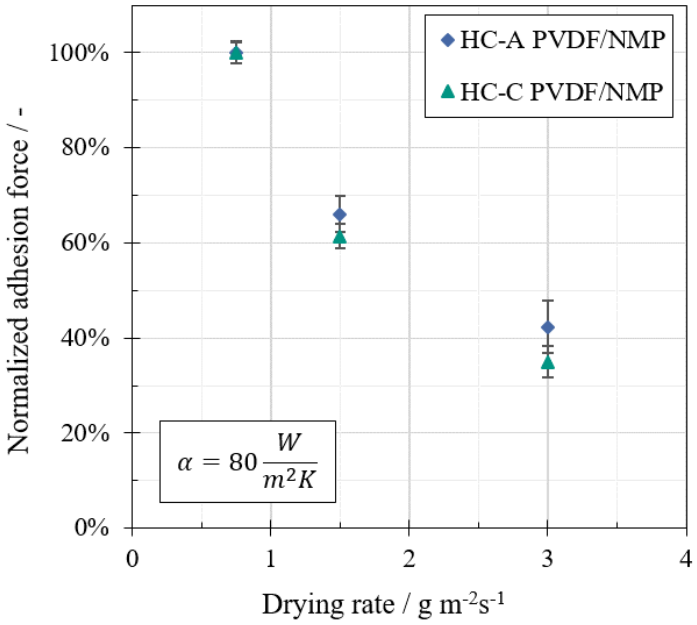


Figure 11.16: Normalized adhesion strength of HC-A and HC-C electrodes with increasing drying rate. The slurry composition is shown in. The dry film thickness of the electrodes is 94.3 ± 4.0 µm. The adhesion strength of the PVDF-based electrodes are normalized to 5.1 ± 0.2 N m$^{-1}$ (HC-A ) and 13.1 ± 0.3 N m$^{-1}$ (HC-C). With increasing drying rate, the same trend towards lower adhesion strength is obtained for both particle sizes.

The results show that the adhesion strength decreases with increasing drying rate for electrodes with both smaller and larger particle sizes. The relative reduction in adhesion strength is comparable for both electrodes. This indicates that, when using the PVDF/NMP binder system, binder migration is mainly governed by the drying rate and is less influenced by structural parameters such as pore size or porosity of the electrode.

The capillary suction, which is strongly affected by the drying rate due to mass conservation, is therefore similar for both electrodes. Consequently, the transport of the mobile binder fraction is also comparable. In contrast, water-based HC-A and HC-C electrodes using the CMC/SBR binder system (see Figure 4.5) exhibit suppressed binder migration, which can be attributed to specific interactions between the binder system and the particle surfaces.

The adhesion strength for both particle sizes decreases with increasing drying rate, resulting in equal percentage changes. This indicates that the binder migration depends on the drying rate in particular and less on the pore size or porosity for electrodes with PVDF/NMP. The capillary suction, which is determined especially by the drying rate due to mass conservation, appears to be the same for both electrodes, and thus, the transport of the mobile binder fraction. Thus, for water-based HC-A and HC-C electrodes using the bindersystem CMC/SBR in Figure x, the suppression of binder migration must have resulted from interaction with the binder system with the particles.

### 11.5.6 Annealing

The present study investigates the influence of an annealing step subsequent to the drying process. To this end, samples were placed between two metal plates to avoid bending and ensure a homogenous heat input. The samples were transferred into a preheated vacuum furnace and subjected to annealing conditions for 10 min at 10 mbar and at varying annealing temperatures. This procedures aligns with the methods outlined in the extant literature for water-based graphite anodes.[91] The dried HC-A and HC-C electrodes were subsequently subjected to an annealing process, after which the adhesion strength was measured (see Figure 11.17).

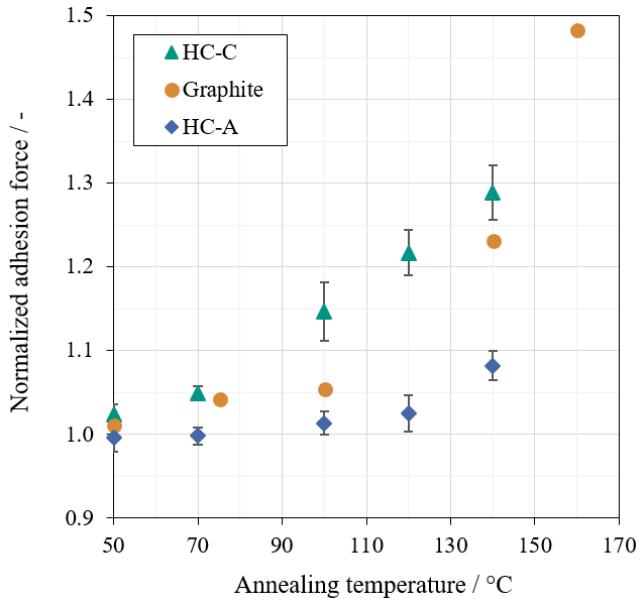


Figure 11.17: Normalized adhesion strength as a function of annealing temperature for HC-A, HC-C, and graphite electrodes. The electrodes were dried at a drying rate of 0.75 g $m^{-2}s^{-1}$ with a heat transfer coefficient of 80 W $m^{-2}K^{-1}$ and then undergo a 10 min annealing process at the appropriate temperature. The data for graphite have been obtained from existing literature.[91] Annealing has been shown to increase of the adhesion strength, with an observed increase starting from 70 °C for HC-C and graphite electrodes, and from 100 – 120 °C for HC-A electrodes.

The study found that HC-C electrodes exhibit an approximate 29% increase in adhesion strength at an annealing temperature of 140 °C, while the HC-A electrodes demonstrate an

approximately 8% increase. The effect of annealing on adhesion strength is only observable at annealing temperatures of 70 °C (HC-C) or 100 - 120 °C (HC-A). In the drying tests carried out in this study for water-based HC anodes, a maximum isothermal drying temperature of approximately 70 °C was established. Consequently, an increase in adhesion strength with increasing temperature cannot be ascribed to an annealing effect. However, with increasing annealing temperature, the adhesion strength of all electrodes nevertheless increases, indicating the effectiveness for post-treatment of electrodes.

### 11.5.7 Binder Migration and Ionic Transport Resistance

The adhesion strength of electrodes represents an indirect measure of binder migration. However, it provides information only about the binder distribution in the vicinity of the current collector. For a more comprehensive analysis of binder distribution after the drying process, impedance spectroscopy under blocking conditions is particularly suitable. While this approach has already been applied in the literature to investigate binder migration in PVDF-based electrodes, no corresponding studies exist for water-based binder systems such as CMC/SBR. In the corresponding publication by the author, this relationship is demonstrated and published experimentally for the first time.[85]

To investigate the influence of binder migration on ionic transport resistance and the resulting electrical tortuosity, impedance measurements under blocking conditions were carried out on hard carbon electrodes. An electrolyte was used that does not contain any ions capable of intercalating into the active material, ensuring that only ionic transport through the electrolyte within the electrode pore structure is probed.

Since HC-A and HC-C electrodes exhibit opposite trends in adhesion strength as a function of drying rate, a corresponding inverse behavior is expected for the ionic transport resistance and the electrical tortuosity. The impedance spectra were analyzed using a transmission line model (TLM), which describes ion transport in the electrolyte within the porous electrode structure. From the fitted spectra, the ionic transport resistance $R_{ion}$ was extracted.

Figure 11.18 shows exemplarily the Nyquist plots for HC-A and HC-C produced with the lowest and highest drying rates investigated.

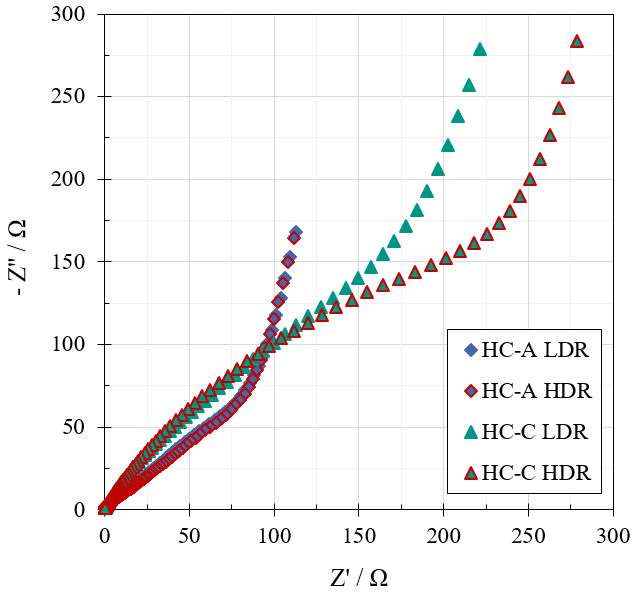


Figure 11.18: Nyquist plots of HC-A and HC-C electrodes produced with lowest drying rate (LDR 0.75 g $m^{-2}s^{-1}$) and the highest drying rate (HDR 9 g $m^{-2}s^{-1}$) investigated. The ionic transport resistance of the HC-C electrode is higher than that of the HC-A electrode. As the drying rate increases, the HC-C electrode's ionic transport resistance also increases, indicating a change in binder distribution.

Independent of the drying rate, HC-A electrodes exhibit a lower ionic transport resistance than HC-C electrodes. This behavior can be attributed to the higher number of pores and, consequently, a larger number of possible ion transport pathways through the electrode. The ionic transport resistance of HC-A electrodes remains nearly constant over the investigated drying rates, ranging from 268 to 249 Ohm. Since no increase in resistance is observed with increasing drying rate, these results confirm the conclusions drawn from the adhesion strength measurements, indicating a suppression of binder migration in HC-A electrodes.

In contrast, HC-C electrodes exhibit a significantly higher ionic transport resistance, which increases from 605 Ω at low drying rates to 802 Ω at high drying rates, corresponding to an increase of approximately 33%. Literature reports on graphite anodes with PVDF binder show that enhanced binder migration and an inhomogeneous binder distribution lead to an increase in ionic resistance. Consistent with these findings, an extension of the mid-frequency region in the impedance spectra is observed for HC-C electrodes at higher drying rates. This behavior suggests the formation of a binder gradient, characterized by a reduced binder content near the current collector and an increased binder content toward the separator.

To directly correlate impedance spectroscopy with the adhesion strength measurements shown in Figure 4.6, the ionic transport resistances of HC-A and HC-C electrodes were determined over the entire range of investigated drying rates and converted into electrical

tortuosity values using Equation (2.28). Figure 11.19 compares the electrical tortuosity as a function of drying rate with the corresponding adhesion strength.

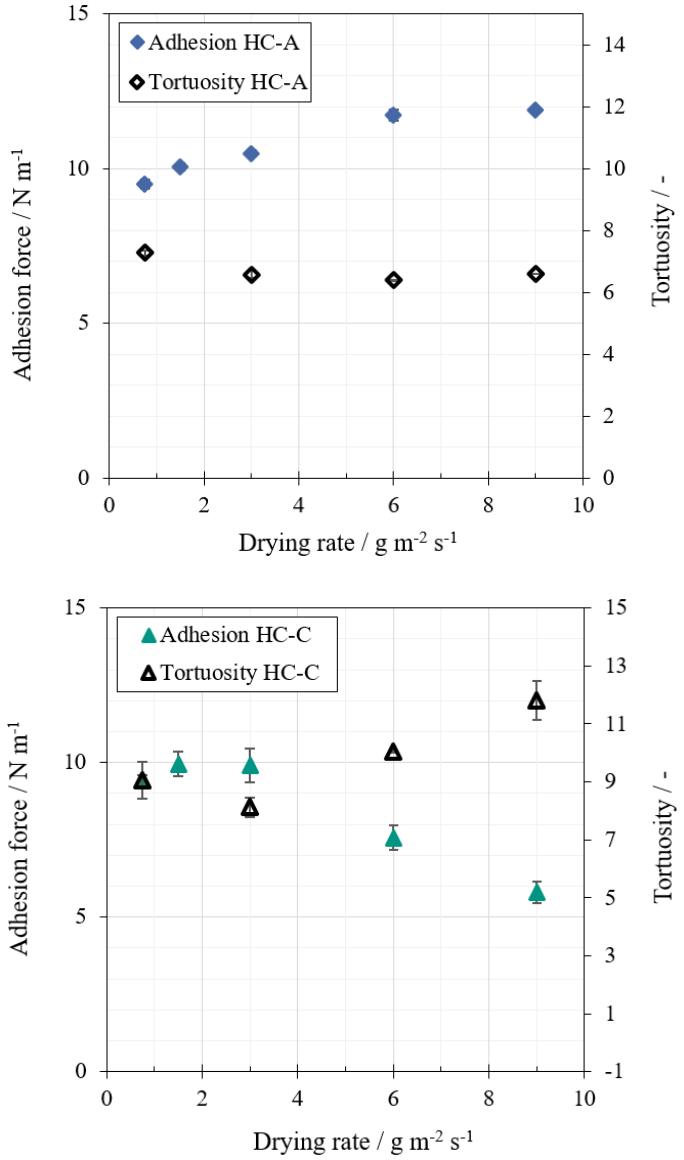


Figure 11.19: Adhesion strength and electrical tortuosity from impedance spectroscopy measurements of HC-A (left) and HC-C (right) electrodes as a function of the drying rate. The tortuosity curve shows an inverse trend to the adhesion strength for both HC active materials.

For both material systems, the electrical tortuosity values are significantly higher than those estimated from heat or mass transport measurements or from analytical models for geometrical tortuosity, such as the Bruggeman ($\tau = \varepsilon\gamma$ with $\gamma = 0.5$)[96] relation or the Zehner–Bauer–Schlünder ($\tau = \varepsilon / (1-(1-\varepsilon)-1.5)$)[97,98] model. The calculated geometrical tortuosity is in the range between 1.5 to 1.7 for the two different analytical models used.

The substantially higher electrical tortuosity values indicate that the resistance encountered by ions during transport through the electrolyte within the microstructure is considerably greater than would be expected based solely on geometric effects. The magnitude of the

electrical tortuosity determined for both hard carbon electrodes is consistent with values reported in the literature for graphite anodes with CMC/SBR binder obtained by impedance spectroscopy. [100]With increasing drying rate, an inverse correlation between adhesion strength and electrical tortuosity is observed for both material systems. This demonstrates that adhesion strength measurements and impedance spectroscopy provide equivalent information regarding binder migration.

In order to improve ionic transport properties and reduce electrical tortuosity, a reduction in binder content is generally recommended. However, this approach adversely affects electrode adhesion. To reduce the binder content without compromising adhesion strength, multilayer electrodes can be employed, in which the binder distribution is deliberately tailored. Nevertheless, little is currently known about the influence of different particle sizes in a multilayer architecture on microstructure formation, pore emptying, and binder migration.

A highly promising strategy for optimizing electrode properties is therefore the fabrication of multilayer electrodes using at least two different slurries. These slurries may differ in binder content or particle size. This approach enables a reduction in overall binder content or the creation of an optimized pore size distribution, thereby decreasing ionic resistance without sacrificing adhesion strength. However, only limited data are available in the literature on the processing and effects of binder migration in multilayer electrodes with varying binder contents or pore gradients employing different particle sizes in each layer.

### 11.5.8 Hierarchically Structured Multilayer Electrodes and Manipulation of Pore Breakthrough

The fabrication of multilayer electrodes with intentionally designed gradients in binder content and porosity offers significant potential for enhancing electrode properties. In addition to improving adhesion strength and electrochemical performance, such architectures can also increase manufacturing productivity.[15,17,134,153] Previous studies on water-based, simultaneously coated electrodes with different binder contents have shown, for example, that adhesion strength is primarily determined by the binder content in the bottom layer adjacent to the current collector. A nearly linear relationship between the binder content in the bottom layer and the adhesion force measured by a 90° peel test has been reported. Importantly, the binder gradient between a bottom layer with high binder content and a top layer with reduced binder content is not fully equalized during drying and can therefore be exploited to improve electrode performance. It is hypothesized that binder from the lower layer is partially transported during pore emptying without completely leveling the gradient.[19] For graphite anodes, it is further well established that multilayer concepts employing different particle morphologies can be used to create a porosity gradient that influences the drying mechanism. However, for water-based systems combining different particle sizes with an additional binder gradient, a comprehensive understanding of binder migration and the resulting microstructure formation is still lacking.[17]

A key objective of this section is therefore to elucidate the pore emptying behavior of hierarchically structured electrodes featuring a pore size gradient. In particular, it aims to clarify the consequences for the emptying process when either smaller pores or larger pores are located in the lower region of the electrode, i.e., in the vicinity of the current collector.

The multilayer architecture enables a targeted investigation of the pore emptying behavior of a capillary system with a pore size gradient. Multilayer electrodes were analyzed in which either smaller particles (corresponding to smaller capillaries) or larger particles were positioned near the current collector (see Figure 11.20).

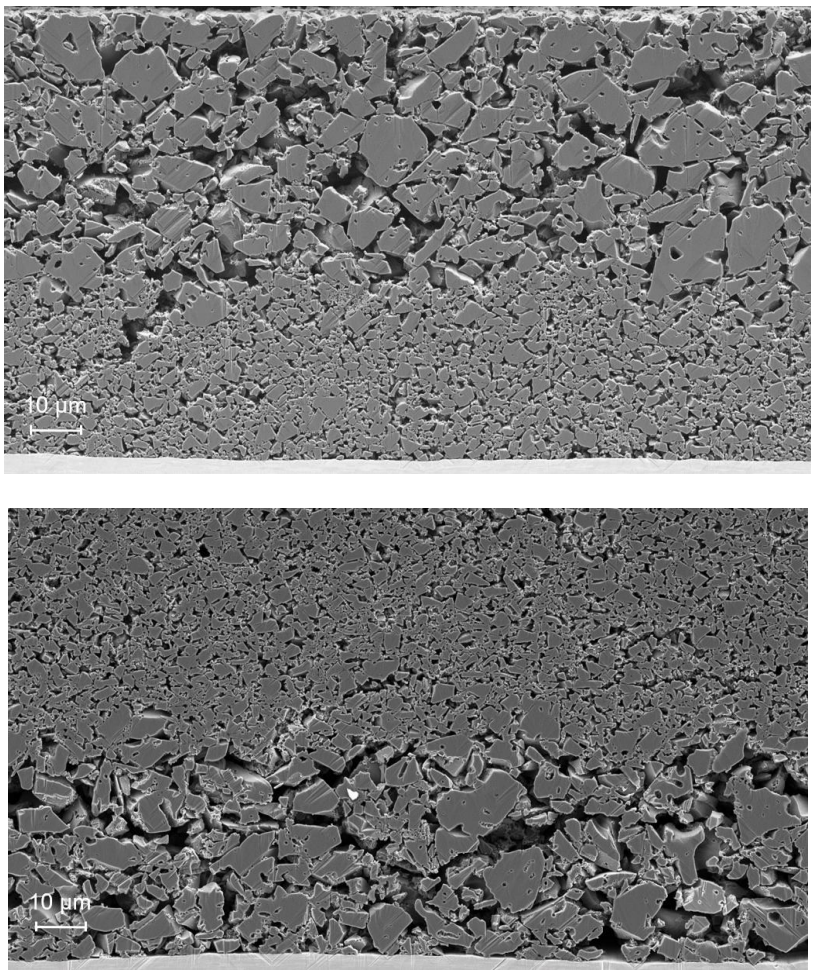


Figure 11.20: SEM of multilayer structured electrodes with smaller particles near the current collector or bigger particles near the current collector. A multilayer with 1/3 of the film thickness with smaller particles in the bottom layer and with 1/3 larger particles in the bottom layer is shown.

The influence of the pore gradient on pore breakthrough behavior was examined by simultaneously measuring film shrinkage, determined from the reduction in layer thickness from the wet to the dry film, and the onset of pore emptying from the bottom side of the electrode. The latter was identified by coating the electrode onto a glass substrate. Figure 11.21 compares the time of pore breakthrough with the end of film shrinkage.

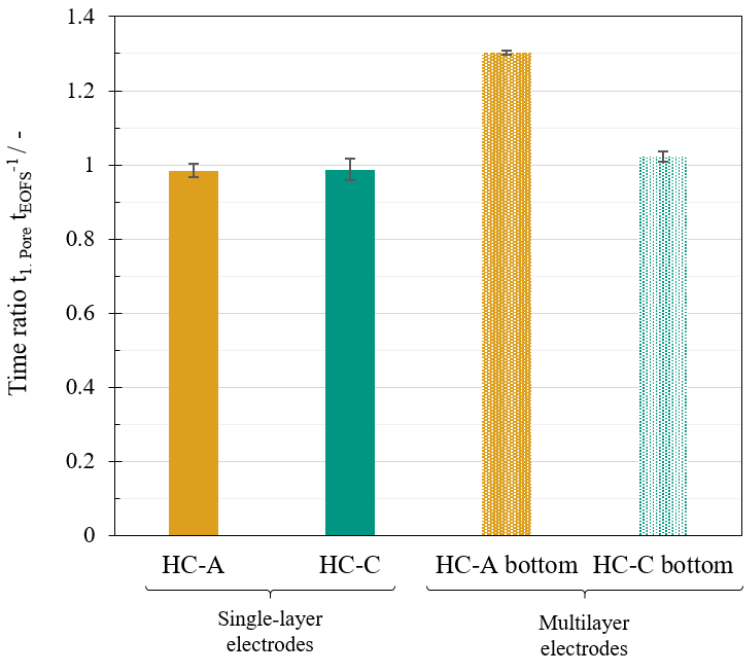


Figure 11.21: Investigation of the pore breakthrough of multilayer electrodes with either smaller pores or larger pores in the vicincy of the current collector. Smaller pores at the bottom of the microstructure leads to a delay in the breakthrough of the pores.

When smaller pores are present in the bottom layer of the multilayer electrode, the solvent is retained within the electrode for a longer period. This behavior can be attributed to the fact that the solvent remains trapped in the smaller capillaries until the pore system above, consisting of larger pores, has been nearly completely emptied. Nevertheless, pore emptying still follows the principle of capillary emptying rather than that of a continuously advancing drying front. This sequential emptying of the capillary system is referred to as “moving pore emptying”. This behavior is consistent with findinds in the literature about pore network modeling in structures with pore size gradient.[80]

A hypothesis proposed in the literature, suggesting that a layer of smaller particles (often referred to as a consolidation layer) in the upper region of the electrode could induce earlier pore breakthrough, was disproven in this work. The presence of smaller particles or smaller pores in the upper region of the microstructure did not lead to an earlier pore breakthrough.

Figure 11.22 schematically illustrates the pore breakthrough behavior of multilayer electrodes with different pore size gradients.

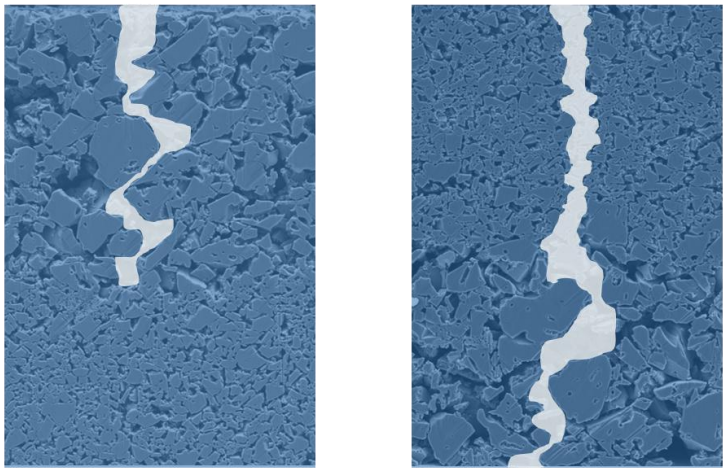


Figure 11.22: Schematic illustration of the pore breakthrough of multilayer electrodes with different pore size gradients. The multilayer architecture comprises either smaller pores or larger pores in the region near to the current collector. When smaller pores are present in the first layer at the current collector side, a temporal delay in pore breakthrough is observed. The smaller pores act as a capillary barrier, thereby hindering solvent emptying and delaying the breakthrough process.

If the multilayer electrode contains smaller pores in the bottom layer near to the current collector, a temporal delay in pore breakthrough is observed. The smaller pores act as a capillary barrier, thereby delaying the emptying process.

It remains to be investigated whether the altered pore emptying behavior observed in multilayer electrodes affects binder migration at higher drying rates.

For this purpose, adhesion strength measurements of multilayer electrodes are presented for comparison (see Figure 11.23). The multilayer systems comprise either small or large particles in the bottom layer near to the current collector. For each configuration, the adhesion strength is shown for both a lower (0.75 g $m^{-2}s^{-1}$) and a higher drying rate (6 g $m^{-2}s^{-1}$). In addition, reference data from previous chapters for single-layer electrodes with small (HC-A) and large (HC-C) particles, respectively, are included for comparison.

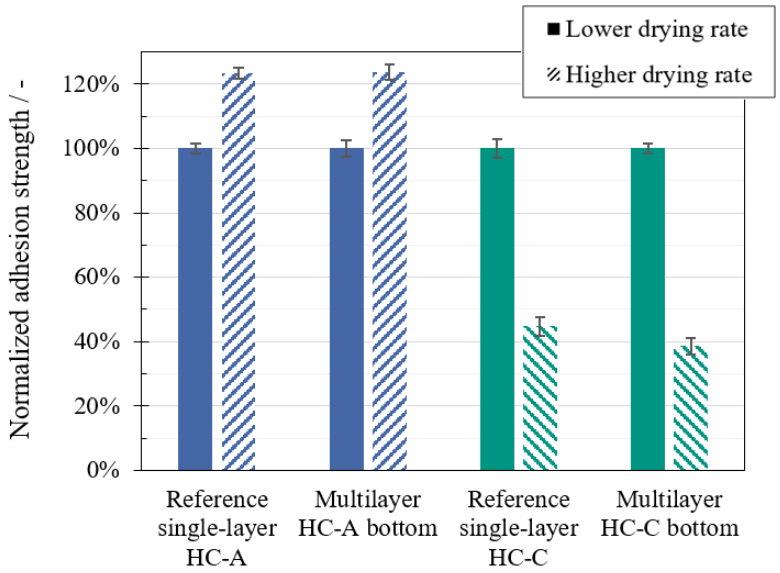


Figure 11.23: Normalized adhesion strength as a function of drying rate for single-layer and multilayer electrodes. Single-layer HC-A and HC-C electrodes are included as reference. All electrodes were fabricated at a constant heat transfer coefficients of 35 W $m^{-2}K^{-1}$, while the drying rate was varied by adjusting the isothermal drying temperature. Both single-layer and multilayer electrodes exhibit the same trend in adhesion strength with increasing drying rate. No additional effect on adhesion strength is observed for the multilayer electrode containing HC-A particles in the bottom layer, despite the delayed pore breakthrough.

Based on the findings established in Chapters 3 and 4 of this work, no significant influence of a modified pore emptying behavior on binder migration at higher drying rates is expected. It has been demonstrated that smaller hard carbon particles effectively suppress binder migration, which was attributed to enhanced interactions between the active material particles and the binder system.

For multilayer architectures with smaller particles in the bottom layer, a delayed pore breakthrough toward the current collector has been observed. It may therefore be hypothesized that this delayed pore breakthrough also postpones binder transport in the lower layer, potentially leading to a further reduction in binder migration. However, since the system with smaller particles already exhibits strongly suppressed binder migration, the delayed pore breakthrough is not expected to result in any additional beneficial effects with respect to binder migration.

### 11.5.9 Half Cell Test

The anodes (13 mm) were electrochemically examined in CR2032 coin cells against sodium-metal (16 mm) counter electrodes. $NaClO_4$ in EC:DMC 1:1 with 2% FEC (100 µL) is used as the electrolyte. As separator a glass-microfiber fleece (GF/C, Whatman) with a diameter of 16 mm is used. The half-cells were assembled in an argon filled glovebox and sealed with a MSK-11 press (MTI, KJ Group) and 750 psi. The cycling was carried out in

a BT2000 battery cycler (Arbin Instruments) in constant current mode inside a voltage range of 0 V to 1.5 V.

Identical current density is used for charging and discharging. The current density for the two cycles (Figure S7) was 5 mA $g^{-1}$. Figure 11.24 shows the voltage profiles of the first charging and discharging cycle of electrodes with the different particles (HC-A and HC-C).

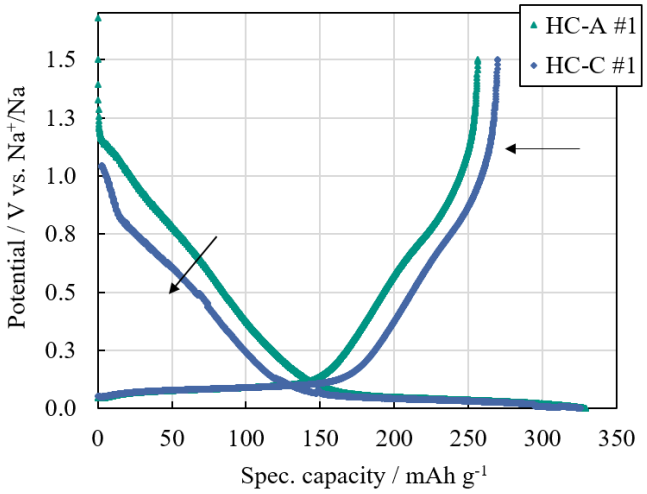


Figure 11.24: Comparison of voltage profiles of the first charge and discharge step of two different HC at a current density of 5 mA $g^{-1}$.

The voltage profile of HC-A is at higher voltages than for HC-C. HC-C half-cell show a higher over-potential. The maximum in charge capacity for HC-A is at ~ 330 mAh $g^{-1}$ and for HC-C at ~ 325 mAh $g^{-1}$. The discharge capacity is at ~ 255 mAh $g^{-1}$ (HC-A) and at ~ 270 mAh $g^{-1}$ (HC-C).

Figure 11.25 shows a comparison of HC-A and HC-C half-cells for the first and second cycle.

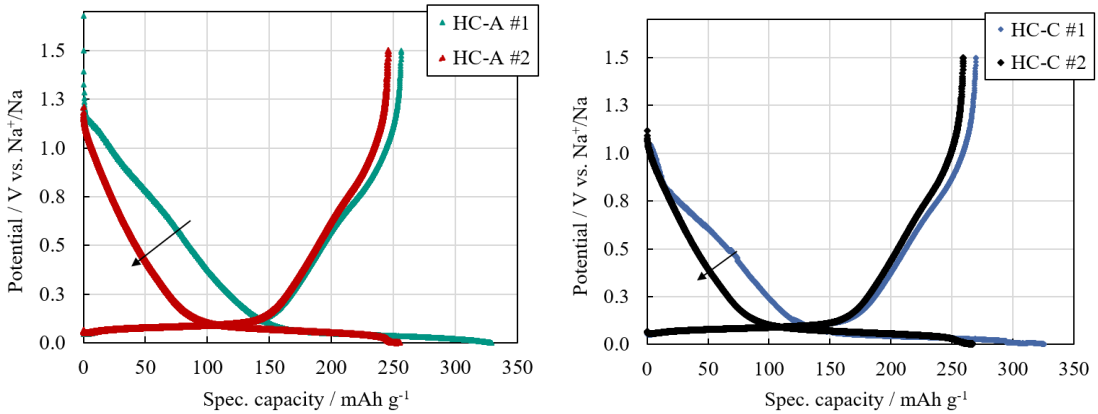


Figure 11.25: Comparison of voltage profiles of the first and second charge and discharge step of two different HC at a current density of 5 mA $g^{-1}$.

The voltage profile of the second charging cycle is at lower potential in comparison to the first cycle. This can be attributed to the SEI building in the first charging cycle.

## 11.6 LFP Electrodes: Influence of Particle Size on Binder Migration Behavior

To evaluate the general applicability of particle size effects on binder migration, LFP with different particle sizes was investigated as an active material. The mean particle diameter of LFP200 is 6 µm and of LFP400 is 11 µm. To isolate particle size as the sole variable, LFP from a single manufacturer was used and provided in two distinct particle size fractions.

### Slurry viscosity and stability

The influence of particle size on the viscosity behavior of the slurries was investigated.

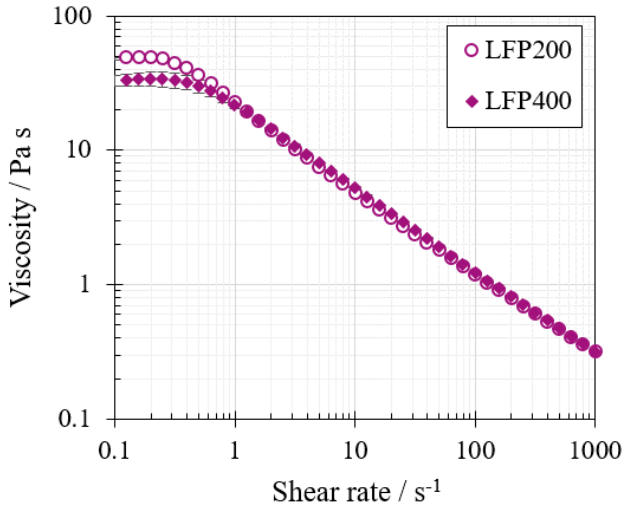


Figure 11.26: Viscosity as a function of increasing shear rate depending on the active material and, respectively, the particle size. LFP200, exhibiting a comparatively smaller particle size, results in a slightly increased viscosity at low shear rates. With increasing shear rate, the viscosity profiles of both slurries converge.

The results indicate that a comparatively smaller particle size leads to an increased viscosity in the low shear rate regime. With increasing shear rate, the viscosity curves of the slurries containing different particle sizes converge. This behavior is consistent with previous observations reported for various material systems (see Section 3.2.3) and was also observed for the same material system (HC) when different particle sizes were employed (see Section 4.2.2). The increased viscosity at low shear rates can be attributed to enhanced particle-particle interactions and a higher effective surface area associated with smaller particles.

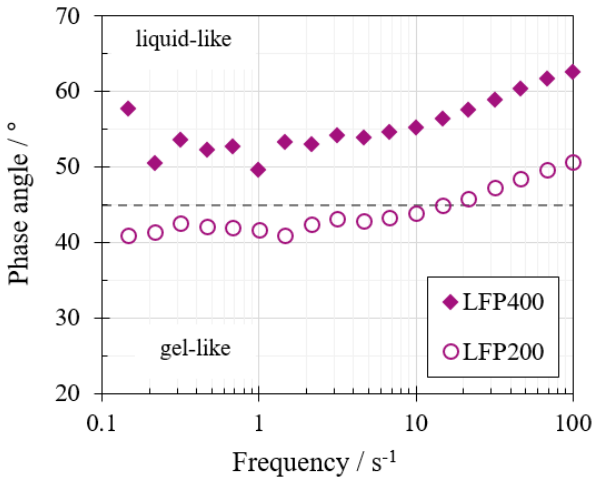


Figure 11.27: Stability behavior of LFP slurries with different particle sizes. Slurries containing smaller particles exhibit a gel-like character.

The stability measurements further demonstrate that the use of active materials with smaller particle sizes promotes a gel-like behavior of the slurry. This tendency is indicative of the formation of a percolated particle network, which contributes to enhanced structural stability and reduced sedimentation.

**Electrode microstructure**

To investigate binder migration behavior, electrodes were produced from both active materials at different drying rates. The resulting electrode properties in terms of dry film thickness, areal mass loading, and porosity are summarized in Table 11.4.

Table 11.4: Dry film thickness, areal mass loading, and electrode porosity of non-calendered LFP electrodes with different particle sizes. Values represent averages over all electrodes produced at drying rates between 0.5 - 2 g $m^{-2}s^{-1}$.

| Name | Dry film thickness / µm | Areal mass loading / g $m^{-2}$ | Electrode porosity / % |
|---|---|---|---|
| LFP200 | 98 ± 5 | 133 ± 7 | 55 ± 1 |
| LFP400 | 102 ± 3 | 126 ± 6 | 59 ± 3 |

Similar to the behavior observed for HC electrodes with different particle sizes, LFP electrodes prepared with smaller particles exhibit a reduced electrode porosity. This can be attributed to the more efficient packing of smaller particles.

**Binder migration behavior**

Binder migration was assessed by adhesion strength measurements of electrodes dried at different drying rates.

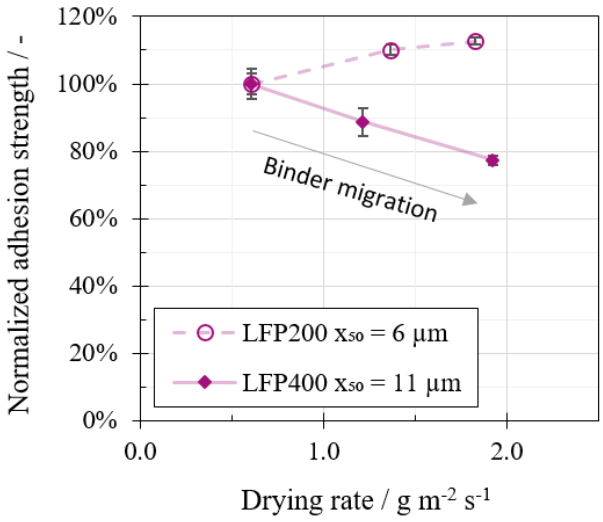


Figure 11.28: Adhesion strength as a function of drying rate and particle size of the employed active material.

The results reveal that, also for LFP electrodes, the use of smaller particle sizes leads to a suppression of binder migration. Consequently, particle size emerges as a key parameter linking active material properties, slurry rheology, microstructure evolution, and final electrode adhesion behavior.

## 11.7 NCM111 Electrodes

### 11.7.1 Particle Size Distribution

The particle size distribution of the investigated NCM111 with either compact or porous, nanostructured particles is shown in Figure 11.29.

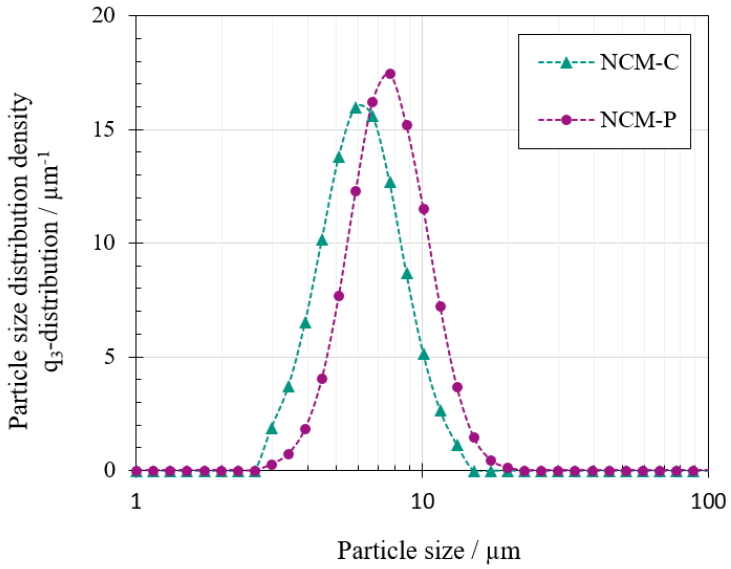


Figure 11.29: Particle size distribution of the investigated NCM111 with either compact (NCM-C) or porous, nanostructured (NCM-P) particles.

The particle size distributions of the two particle systems differ only in a shift of the mean particle diameter due to the processing of the nanoporous structured particles.

## 11.8 NCM622 Electrodes

### 11.8.1 Viscosity Profiles

The flow behavior of the slurries with compact particles and porous particles with the same and reduced binder content is shown in Figure 11.30.

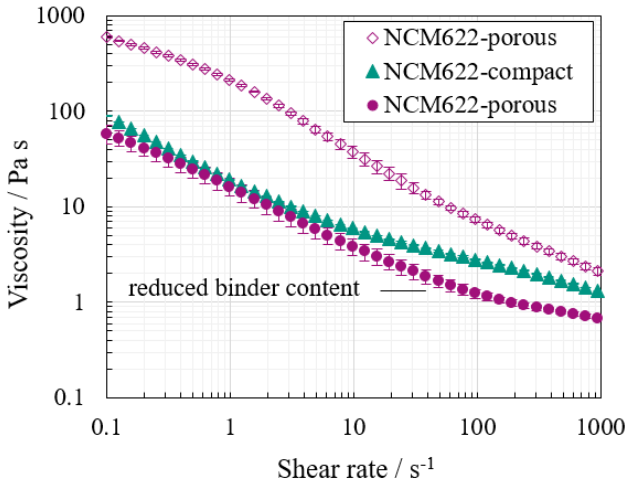


Figure 11.30: Viscosity of NCM622-compact (green triangles), NCM622-porous with 4.5 wt-% PVDF (red dots) and NCM-622-porous with reduced binder content of 3 wt-% (red rhombus) as a function of shear rate at 25 °C.

### 11.8.2 Binder Migration and Overall Binder Content

To verify that the results discussed in Section 6.2.4 originate from the overall binder content rather than from the multilayer architecture itself, a multilayer electrode composed exclusively of slurries containing compact active material particles was fabricated. This approach enables a systematic investigation of binder migration as a function of total binder content and drying rate.

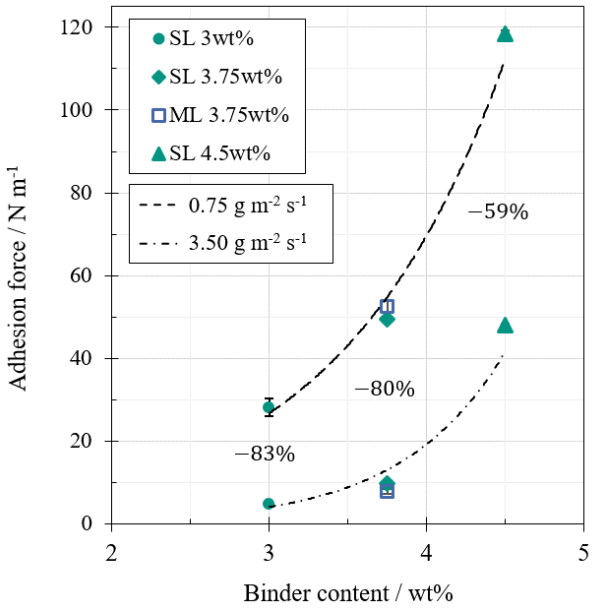


Figure 11.31: Binder migration as a function of the overall binder content and the drying rate for single-layer and a multilayer electrode fabricated with only compact active material particles. The single-layer and multilayer electrodes with an overall binder content of 3.75 wt-% show the same adhesion strength and binder migration behavior, demonstrating the overall binder content as governing parameter for simultaneously coated multilayer electrodes with PVDF/NMP.

The comparison demonstrates that a simultaneously coated multilayer electrode processed with the PVDF binder and NMP solvent exhibits the same binder migration behavior as a single-layer electrode when the overall binder content is identical. This finding confirms that, under the investigated conditions, the overall binder content is the governing parameter for binder redistribution, independent of whether the electrode is structured as a single layer or as a simultaneously coated multilayer.

For further optimization, wet-on-dry coating strategies should be investigated. Such approaches may suppress diffusive equilibration of binder concentration by utilizing of the already dried bottom layer, potentially leading to increased adhesion strength. However, it remains to be clarified whether wet-on-dry coating induces partial redissolution of the underlying dried layer, which could in turn affect binder migration and adhesion behavior.

### 11.8.3 Resistivity

Resistivity measurements were carried out to investigate the influence of the coating configuration on the electrical conductivity as a function of the drying rate. The resistivity for the single- and multilayer electrodes with increasing drying rate is shown in Figure 11.32.

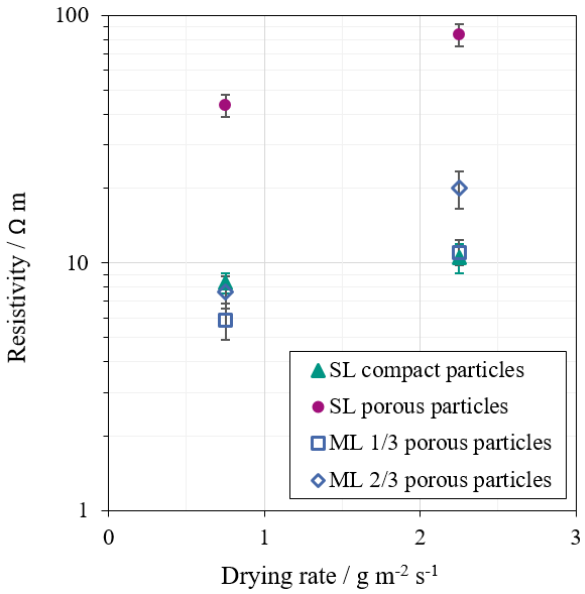


Figure 11.32: Resistivity as a function of the drying rate for single- and multilayer electrodes with compact and porous particles in different layer configurations.

For all electrodes, the electrical resistivity increases with increasing drying rate, which could be related to the binder migration in all layers. The resistivity is significantly higher for the porous single layers, which is consistent with the literature and Chapter 5.

The measured resistivity for the multilayer electrodes is more oriented towards the resistivity of the single layer with compact particles. The resistivity increases by 26% for the single-layer electrode SL compact particles (4.5 wt-% PVDF), 88% for multilayer ML 1/3 porous particles (4 wt-% PVDF), and 160% for multilayer ML 2/3 porous particles (3.5 wt-% PVDF).

## 11.8.4 Reduced Binder Content with NCM622-Compact Particles

The influence of binder content of the single-layer with compact particles on the cell performance is shown in Figure 11.33 for the lower drying rate. The electrode SL compact particles with reduced binder content has a PVDF content of 3 wt-% and about the same film thickness of 95 µm and an areal mass loading of 220 g $m^{-2}$.

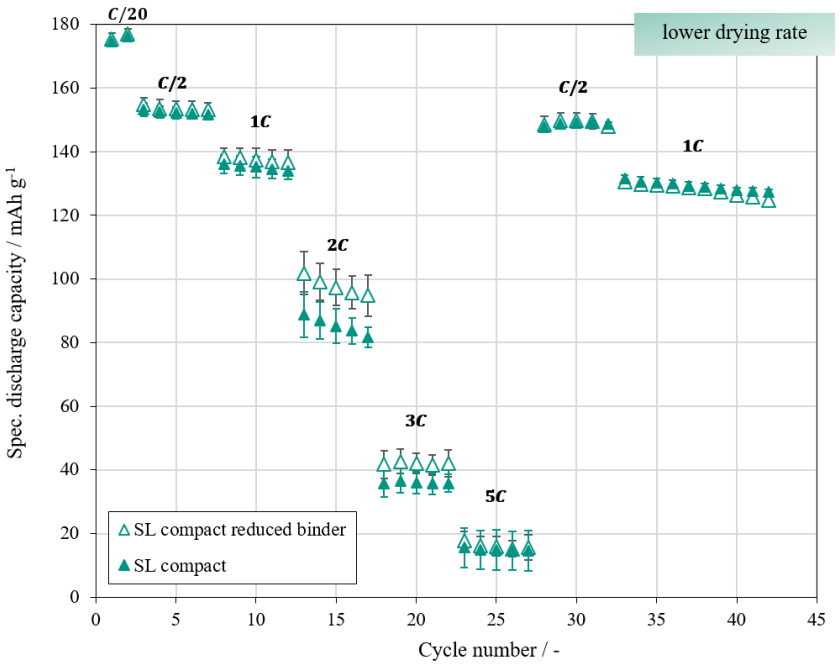


Figure 11.33: Specific discharge capacities of half cells with non-calendered SL compact (4.5 wt-% PVDF) and SL compact reduced binder (3 wt-% PVDF) at the lower drying rate (0.75 g $m^{-2}s^{-1}$).

# 12 Publications

As first author

1. **J. Klemens**, L. Schneider, D. Burger, N. Zimmerer, M. Müller, W. Bauer, H. Ehrenberg, P. Scharfer, W. Schabel (2023): *Process and Drying Behavior Toward Higher Drying Rates of Hard Carbon Anodes for Sodium-Ion Batteries with Different Particle Sizes: An Experimental Study in Comparison to Graphite for Lithium-Ion-Batteries.* In: Energy Technol., DOI: 10.1002/ente.202300338.
2. **J. Klemens**, D. Burger, L. Schneider, S. Spiegel, M. Müller, N. Bohn, W. Bauer, H. Ehrenberg, P. Scharfer, W. Schabel (2023): *Drying of Compact and Porous NCM Cathode Electrodes in Different Multilayer Architectures: Influence of Layer Configuration and Drying Rate on Electrode Properties.* In: Energy Technol., DOI: 10.1002/ente.202300267.
3. **J. Klemens**, L. Schneider, E. C. Herbst, N. Bohn, M. Müller, W. Bauer, P. Scharfer, W. Schabel (2022): *Drying of NCM Cathode Electrodes with Porous, Nanostructured Particles Versus Compact Solid Particles: Comparative Study of Binder Migration as a Function of Drying Conditions.* In: Energy Technol., DOI: 10.1002/ente.202100985.
4. **J. Klemens**, A.-K. Wurba, D. Burger, M. Müller, W. Bauer, S. Büchele, O. Leonet, J. A. Blázquez, I. Boyano, E. Ayerbe, H. Ehrenberg, J. Fleischer, A. Smith, P. Scharfer, W. Schabel (2023): *Challenges and Opportunities for Large-scale Electrode Processing for Sodium-Ion and Lithium-Ion Battery: Comparison of PBA/Hard Carbon vs. LFP/Graphite.* In: Batteries & Supercaps, DOI: batt.202300291

As Co-author

1. M. Weichel, M. Reder, S. Dauber, **J. Klemens**, D. Burger, P. Scharfer, W. Schabel, B. Nestler, D. Schneider (2025): *Modeling the drying process in hard carbon electrodes based on the phase-field method*. In: Physical Review Materials, DOI: 10.1103/PhysRevMaterials.9.035403
2. A. Hoffmann, **J. Klemens**, S. Raupp, C. Hanske, N. Lawrenz, M. Machate, P. Scharfer, W. Schabel (2024): *Optimized battery electrodes with primer layers by simultaneous two-layer slot-die coating*. In: The European Physical Journal, Special Topics, DOI: 10.1140/epjs/s11734-024-01398-7
3. D. Burger, **J. Klemens**, N. Keim, M. Müller, W. Bauer, J. Schmatz, J. Kumberg, P. Scharfer, W. Schabel (2024): *Additive Influence on Binder Migration in Electrodes Drying.* Energy Technol., DOI: 10.1002/ente.202400057
4. P. Stüble, C. Müller, N. Bohn, M. Müller, A. Hofmann, T. Akcay, **J. Klemens**, A. Koeppe, S. Kolli, R. Deepalaxmi, H. Geßwein, W. Schabel, P. Scharfer, M. Selzer, J. R. Binder, A. Smith (2024): *From Powder to Pouch Cell: Setting up a Sodium-Ion*

*Battery Reference System Based on Na3V2(PO4)3/C and Hard Carbon*. In: Batteries & Supercaps, DOI: 10.1002/batt.202400406

5. A. Altvater, **J. Klemens**, J. Borho, A. Smith, T. Heckmann, P. Scharfer, W. Schabel (2023): *Application of Multi-Stage Drying Profiles for Accelerated Production of Li-Ion Battery Anodes Using Infrared Radiation – Validation with Electrochemical Performance and Structural Properties.* In: Energy Technol., DOI: 10.1002/ente.202301272
6. W. Bauer, M. Müller, L. Schneider, M. Häringer, N. Bohn, J. R. Binder, **J. Klemens**, P. Scharfer, W. Schabel, H. Ehrenberg (2023): *Using Hierarchically Structured, Nanoporous Particles as Building Blocks for NCM111 Cathodes*. In: MDPI Nanomaterials, DOI: nano14020134
7. S. Spiegel, A. Hofmann, **J. Klemens**, P. Scharfer, W. Schabel (2023): *High-Speed Slot-Die Coating of Primer for Li-Ion Battery Electrodes: Influence of Coating Gap and Viscosity on the Extended Coating Window.* In: Journal of Coating Technology and Research, DOI: 10.1007/s11998-023-00877-1
8. P. Stüble, C. Müller, **J. Klemens**, P. Scharfer, W. Schabel, M. Häringer, J. R. Binder, A. Hofmann, A. Smith (2023): *Enabling Long-term Cycling Stability of Na3V2(PO4)3/C vs. Hard Carbon Full Cells.* In: Batteries & Supercaps, DOI: batt.202300375
9. C. Müller, Z. Wang, A. Hofmann, P. Stüble, X. Liu-Théato, **J. Klemens**, A. Smith (2023): *Influences on Electrochemical Performance of Hard Carbon in Sodium-Ion Half-Cells.* In: Batteries & Supercaps, DOI: batt.202300322
10. A.-K. Wurba, **J. Klemens**, D. Mayer, C. Reusch, L. Altmann, O. Leonet, J. A. Blázquez, I. Boyano, E. Ayerbe, P. Scharfer, W. Schabel, J. Fleischer (2022): *Methodology of the characterization and understanding of longitudinal wrinkling during calendaring of lithium-ion and sodium-ion battery electrodes*. In: Elsevier Procedia CIRP, DOI: j.procir.2023.08.056
11. L. Schneider, **J. Klemens**, E. C. Herbst, M. Müller, P. Scharfer, W. Schabel, W. Bauer, H. Ehrenberg (2022): *Transport Properties in Electrodes for Lithium-Ion Batteries: Comparison of Compact versus Porous NCM Particles.* In Journal of the Electrochemical Society, DOI: 10.1149/1945-7111/ac9c37.
12. S. Spiegel, A. Hofmann, **J. Klemens**, P. Scharfer, W. Schabel (2022): *Optimization of Edge Quality in the Slot-Die Coating Process of High-Capacity Lithium-Ion Battery Electrodes.* In Energy Technol., DOI: 10.1002/ente.202200684.
13. H. Liu, M. Baumann, X. Dou, **J. Klemens**, L. Schneider, A.-K. Wurba, M. Häringer, P. Scharfer, H. Ehrenberg, W. Schabel, J. Fleischer, N. von der Aßen, M. Weil (2022): *Tracing the technology developement and trends of hard carbon anode materials – A market and patent analysis.* In Journal of Energy Storage, DOI: 10.1016/j.est.2022.105964
14. J. Ruhland, T. Storz, F. Kößler, A. Ebel, J. Sawodny, J. Hillenbrand, P. Gönnheimer, L. Overbeck, Gisela Lanza, M. Hagen, J. Tübke, J. Gandert, S. Paarmann, T. Wetzel,

J. Mohacsi, A. Altvater, S. Spiegel, **J. Klemens**, P. Scharfer, W. Schabel, K. Nowoseltschenko, P. Müller-Welt, K. Bause, A. Albers, D. Schall, T. Grün, M. Hiller, A. Schmidt, A. Weber, L. de Biasi, H. Ehrenberg, J. Fleischer (2022). *Development of a Parallel Product-Production Co-design for an Agile Battery Cell Production System. In: A.-L. Andersen et al. Towards Sustainable Customization: Bridging Smart Products and Manufacturing Systems*. CARV MCPC 2021 2021. Lecture Notes in Mechanical Engineering. Springer, Cham. DOI: 10.1007/978-3-030-90700-6_10.

15. J. Hofmann, A.-K. Wurba, S. Maliha, P. Schollenmeyer, J. Fleischer, **J. Klemens**, P. Scharfer, W. Schabel (2021): *Investigation of Parameters Influencing the Producibility of Anodes for Sodium-Ion Battery Cells.* In: Congress of the German Academic Association for Production Technology, Springer, DOI: 10.1007/978-3-662-62138-7_18.

# 13 Conference Contributions

1. **J. Klemens**, D. Burger, S. Spiegel, P. Scharfer, W. Schabel, *Drying of structure-optimized multilayer electrodes with different particle morphologies for sodium-ion batteries* (**Talk**), 21th International Coating Science and Technology Symposium, ISCST 2022, 11.-14. September 2022, Minneapolis, Minnesota, USA
2. S. Spiegel; A. Hoffmann; **J. Klemens**; P. Scharfer; W. Schabel, *Simultaneous double-sided coating of Li-ion battery electrodes: Investigation of edge formation for conventional and tensioned-web slot die coating* (**Talk**), 21th International Coating Science and Technology Symposium, ISCST 2022, 11.-14. September 2022, Minneapolis, Minnesota, USA
3. A. Hoffmann, S. Spiegel; D. Burger; **J. Klemens**; P. Scharfer; W. Schabel, *About the slot die coating process of lithium-ion battery electrodes with regard to an optimized layer structure and edge quality* (**Poster**) Dechema Jahrestagung 09/2022, Aachen, Germany, Chemie Ingenieur Technik, DOI: 10.1002/cite.202255273
4. D. Burger, A. Hoffmann, **J. Klemens**, P. Scharfer, W. Schabel, *Optimizing the production of Li-ion batteries: Efficient drying of electrodes and savings by multilayer approach* (**Poster**), Dechema Jahrestagung 09/2022, Aachen, Germany, Chemie Ingenieur Technik, DOI: 10.1002/cite.202255278
5. **J. Klemens**, D. Burger, S. Spiegel, P. Scharfer, W. Schabel, *Processing of structure-optimised lithium- and sodium-ion-battery electrodes* (**Talk**), 6th Thin Film Technology Forum, 05/2022, online
6. S. Spiegel, T. Heckmann, A. Hoffmann, **J. Klemens**, P. Scharfer, W. Schabel, *Recent Advances in Battery-Electrode Coating and Experimental and Simulative Edge Formation Aspects* (**Poster**), Batterieforum Deutschland 2022, 25. Januar 2022, online, Germany
7. **J. Klemens**, E. Herbst, D. Burger, P. Scharfer, W. Schabel, *Drying mechanisms of single- and multilayer battery electrodes with porous and compact particles* (**Talk**), Jahrestreffen ProcessNet-Fachgruppe Trocknungstechnik, 10.-11.03.2022, Frankfurt
8. **J. Klemens**, A. Smith, P. Scharfer, W. Schabel, *Electrode processing and developement of sodium-ion cells* (**Talk**), POLiS (Post Lithium Storage Cluster of Excellence) –Emerging Technologies – From Research to Manufacturing (online)
9. **J. Klemens**, L. Schneider, E. Herbst, N. Bohn, M. Müller, W. Bauer, P. Scharfer, W. Schabel, *Investigation of binder migration for NCM cathode slurries with compact and nanoporous particles* (**Talk**), International Battery Production Conference (IBPC), 01.-02. November 2021, Braunschweig, Germany
10. **J. Klemens**, P. Scharfer, W. Schabel, *Processing of post-Li battery electrodes and challenges to enhance electrode properties* (**Talk**), Karlsruhe Institute of Technology, Zentrum Energie, Vortragsreihe ENERGIE – Forschung. Forum. Fragen, 19.10.2021 (online)

11. **J. Klemens**, P. Scharfer, W. Schabel, *Film processing of battery electrodes for sodium-ion batteries along the process chain in relation to particle properties* (**Talk**), European Coating Symposium (ECS), 06. - 09.09.2021, Belgium
12. **J. Klemens**, Philip Scharfer, Wilhelm Schabel, *Influence of particle properties on battery processing* (**Talk**), 5th Thin Film Technology Forum, 24-25. June 2021, Karlsruhe
13. W. Schabel, P. Scharfer, **J. Klemens**, S. Spiegel, *Coating Technologies for Battery Electrodes (**Talk**)*, Kompetenznetzwerk Lithium-Ionen-Batterien (KLiB), 19.05.2021, Germany
14. **J. Klemens**, N. Zimmerer, E. Herbst, P. Scharfer, W. Schabel, *Influence of particle properties on the processing of hard carbon anodes and nanostructured cathode materials for use in sodium-ion batteries* (**Poster**), Kraftwerk Batterie, 27.-29.04.2021
15. **J. Klemens**, N. Zimmerer, P. Scharfer, W. Schabel, L. Schneider, M. Häringer, M. Müller, W. Bauer, H. Ehrenberg, A. Wurba, J. Hofmann, J. Fleischer, *Investigation of future electrode materials processability* (**Poster**), Batterieforum Deutschland, 2.2.2021
16. **J. Klemens**, N. Zimmerer, E. Herbst, P. Scharfer, W. Schabel, *Investigation of drying and microstructure formation for sodium-ion-battery electrodes as a function of particle properties* (**Poster**), Jahrestreffen ProcessNet-Fachgruppen; Fachausschuss Trocknungstechnik, 15.-16.03.2021, online, Germany
17. **J. Klemens**, P. Scharfer, W. Schabel, *Coating and Drying of Sodium-Ion-Battery Electrodes* (**Talk**), International Sodium Battery Symposium 2021 (digital event), 13.-14.01.2021, Fraunhofer IKTS, Dresden
18. **J. Klemens**, N. Zimmerer, P. Scharfer, W. Schabel, *Post Lithium Storage – Processing of Sodium Ion Battery Electrodes* (**Poster**), International Battery Production Conference (IBPC), 02.-03. November 2020, Braunschweig, Germany
19. A. Wurba, J. Hofmann, J. Fleischer, **J. Klemens**, P. Scharfer, W. Schabel, *Identifying the influence of the particle size and morphology of electrode materials on the process of calendaring*, International Battery Production Conference (IBPC), 02.-03. November 2020, Braunschweig, Germany
20. A. Altvater, S. Spiegel, **J. Klemens**, P. Scharfer, W. Schabel, *FlexCAD – Flexible Coater and Dryer for Battery Electrodes* (**Poster**), International Battery Production Conference (IBPC), 02.-03. November 2020, Braunschweig, Germany
21. **J. Klemens**, P. Scharfer, W. Schabel, *Coating and Drying of Sodium-Ion-Battery Electrodes* (**Poster**), Material Science Conference (MSE), 21.-25. September 2020, Germany.
22. **J. Klemens**, S. Spiegel, A. Altvater, P. Scharfer, W. Schabel, *Post Lithium Storage – Potential and Challenges* (**Poster**), International Battery Production Conference (IBPC), 03.-05. November 2019, Braunschweig, Germany
23. A. Altvater, S. Spiegel, **J. Klemens**, T. Storz, J. Fleischer, P. Scharfer, W. Schabel, *Invenstigation of format-flexible coating processes with quality impact on electrodes* (**Poster**), International Battery Production Conference (IBPC), 03.-05. November 2019, Braunschweig, Germany

24. **J. Klemens**, J. Hofmann, S. Maliha, J. Fleischer, P. Scharfer, W. Schabel, *Post Lithium Storage – Scale-up of materials and cell producibility* (**Poster**), POLiS Conclave, 10.-11. Oktober 2019, Ulm, Germany
25. **J. Klemens**, S. Spiegel, A. Altvater, P. Scharfer, W. Schabel, *Energy Storage beyond Lithium – Challenges of Processing* (**Poster**), European Coating Symposium (ECS), 08.-11. September 2019, Heidelberg, Germany
26. A. Altvater, S. Spiegel, **J. Klemens**, T. Storz, J. Fleischer, P. Scharfer, W. Schabel, *SmartBatteryMaker (SMB) – Developement of a flexible coating and drying process* (**Poster**), European Coating Symposium (ECS), 08.-11. September 2019, Heidelberg, Germany

# 14 Supervised Student Work

Principal Supervisor:

1. Linus Janning: Investigation of Microstructure Formation and Pore Emptying in Relation to Slurry Properties and Drying Conditions (2023, Master's Thesis)
2. Lisa Frankenhauser: Investigation of the relation of pore emptying and drying curve of battery electrodes (2023, Master's Thesis)
3. David Burger: Investigation of the structural optimisation and drying behaviour of multilayer electrodes with different particle morphology of cathodes for Li-ion batteries (2022, Master's Thesis)
4. Carolyn Reinhold: Investigation of the processing and structural optimization of electrodes for lithium-ion and sodium-ion batteries (2022, Master's Thesis)
5. Eike Christian Herbst: Investigation of the drying behaviour of battery slurries with nano pouros particles for cathodes of Li-ion batteries (2022, Master's Thesis)
6. Chaima Hamrita: Electrochemical investigation of hard carbon as active material of the anode for the sodium ion battery (2021, Masterarbeit)
7. Nadine Zimmerer: Investigation of the drying behaviour and the formation of the microstructure of anodes for sodium ion batteries (2020, Master's Thesis)
8. Jara Abu Tayeh: Investigation of the influence of slurry formulation and process conditions on the production of hirarchically structured electrodes for sodium-ion-batteries (2021, Master's Thesis)
9. Stefan Wacker: Investigation of material properties of the anode of sodium-ion-batteries with variation of solid content and additive fraction (2020, Bachelor's Thesis)
10. Ziying Wen: Investigation and comparison of active components of the anode of lithium-ion and sodium-ion-batteries with regard to their processing (2020, Bachelor's Thesis)

Second Supervisor:

1. Yasmin Grübbel: Investigation of the influence of the formulation and drying parameters on the thermal conductivity of porous electrodes (2024, Bachelor's Thesis)
2. Niklas Könnecke: Investigating the influence of particle morphology of LFP cathode materials for lithium-ion batteries on processing and electrode properties (2023, Master's Thesis)
3. Julian Borho: Investigation of the influence of process and material parameters during the drying of battery electrodes of different material systems with radiation-based energy input (2022, Master's Thesis)
4. Wenhan Deng: Investigation of the slot coating of simultaneous multilayers for lithium-ion batteries (2021, Master's Thesis)

5. August Gladik: Investigation of different dispersing systems for the pro-duction of nanoparticle-based coating inks for fuel cells (2020, Bachelor's Thesis)